

University of Mississippi

eGrove

Electronic Theses and Dissertations

Graduate School

1-1-2020

Incorporation Of Acoustic And Chemical Modifications To Biochar For Pollution Abatement

Riya Chatterjee

Follow this and additional works at: <https://egrove.olemiss.edu/etd>

Recommended Citation

Chatterjee, Riya, "Incorporation Of Acoustic And Chemical Modifications To Biochar For Pollution Abatement" (2020). *Electronic Theses and Dissertations*. 1844.

<https://egrove.olemiss.edu/etd/1844>

This Dissertation is brought to you for free and open access by the Graduate School at eGrove. It has been accepted for inclusion in Electronic Theses and Dissertations by an authorized administrator of eGrove. For more information, please contact egrove@olemiss.edu.

INCORPORATION OF ACOUSTIC AND CHEMICAL MODIFICATIONS TO BIOCHAR
FOR POLLUTION ABATEMENT

A Thesis
presented in partial fulfillment of requirements
for the degree of Doctor of Philosophy
in the Department of Chemical Engineering
The University of Mississippi

by

RIYA CHATTERJEE

May 2020

Copyright © 2020 by Riya Chatterjee

All rights reserved

ABSTRACT

A series of my researches aim to develop an advanced suitable carbon activation techniques using ultrasound waves, and chemical functionalization for the application of environmental remediation. Ultrasound irradiation exfoliates the graphitic layers of biochar, and creates new/opens the blocked pores, thus creating active sites for chemical activation using amine. CO₂ is one of the major air pollutants and a leading cause of the global warming. Thus, it is imperative to establish a proper CCS technology. Reductive photocarboxylation could be an effective way to attach CO₂ on carbonaceous structure such as biochar. Biochars have highly porous structure, high surface area and graphitic oxide clusters that consist of the reactive oxygen functional groups such as- COOH, C=O,- OH that are susceptible to amine functionalization. Amine, a nucleophile, can react with CO₂, which is an electrophile, to boost adsorption efficiency of the biochar. Furthermore, to identify the impact of amination, the work was carried out in the presence of two different activating agents carbodiimide-benzotriazole and potassium hydroxide and five different amines - tetraethylenepentamine, diethanolamine, monoethanolamine, polyethylenimine, piperazine and their binary and ternary mixtures. The work was further extended to investigate the role of different biomass origin on CO₂ capture. Biochars were synthesized from herbaceous, agro-industrial and crop based biomasses and were subjected to three different treatment conditions that involved- I. physical activation, II. chemical activation and III. integrated ultrasonic-amine activation. The last step of this series of works involved investigating the synergistic and antagonistic impact of pyrolysis temperature (in the range of 500-800 °C) on ultrasound activation and the subsequent CO₂ adsorption. It is worth to

mention that the conventional carbon activation requires elevated temperature ($>700\text{ }^{\circ}\text{C}$) and prolonged activation time ($>3\text{ hrs}$). While the method discussed in this dissertation was conducted at near ambient temperature for a very short duration ($\sim 30\text{-}60\text{sec}$) and consumes a significantly lower level of energy than conventional carbon activation processes. In addition, this advanced carbon modification method can be adopted for other environmental applications, in addition to CO_2 capture and pollutant removal from water and air.

DEDICATION

In the loving memory of my dad, without his constant support, love, and encouragement I wouldn't have been able to complete my journey. I would also like to say, thanks Mom, for being with me, in every step of my life.

LIST OF ABBREVIATIONS

As	Arsenic
Ca	Calcium
CCS	Carbon Capture and Storage
Cd	Cadmium
CO	Carbon Monoxide
CO ₂	Carbon Dioxide
Cr	Chromium
CS	Corn Stover
DCC	Dicyclohexylcarbodiimide
DEA	Diethanolamine
DETA	Diethylenetriamine
EDA	Ethylenediamine
EDC	Ethyl-3-(3-dimethylaminopropyl) Carbodiimide
ESA	Electric Swing Adsorption
FP	Fluor Process
H ₂ O ₂	Hydrogen Peroxide
H ₂ SO ₄	Sulfuric Acid
HCl	Hydrochloric Acid
Hg	Mercury
HOBt	Hydroxybenzotriazole

K	Potassium
KMnO ₄	Potassium Permanganate
KOH	Potassium Hydroxide
MEA	Monoethanolamine
MP	Morphysorb Process
MS	Miscanthus
Na	Sodium
NaNO ₃	Sodium Nitrate
NaOH	Sodium Hydroxide
PAH	Polycyclic Aromatics Hydrocarbons
Pb	Lead
PEI	Polyethylenimine
PP	Purisol Process
PSA	Pressure Swing Adsorption
PZ	Piperazine
RH	Rice Husk
RP	Rectisol Process
RS	Rice Straw
SB	Sugarcane Bagasse
Se	Selenium
SG	Switchgrass

Si	Silicon
SP	Selexol Process
SR	Sorghum
TEPA	Tetraethylenepentamime
TETA	Triethylenetetramine
TSA	Temperature Swing Adsorption
US	Ultrasound
VSA	Vacuum Swing Adsorption
WS	Wheat Straw

ACKNOWLEDGMENTS

First and foremost, I would like to express my sincere gratitude to my advisors, Dr. Baharak Sajjadi and Prof. Wei-Yin Chen for their valuable guidance, support, encouragement and patience throughout my studies. I am truly thankful to them for teaching me importance of scientific ethics and without their help this thesis wouldn't be completed. I am sincerely grateful to my thesis committee members, Prof. Daniell L Mattern and Dr. Sasan Nouranian for accepting the invitation to become members of my committee. Their valuable suggestions and scientific criticism are respectfully acknowledged.

I would also like to acknowledge the Department of Chemical Engineering, Department of Chemistry and Biochemistry and School of Pharmacy of the University of Mississippi for helping me in conducting the analyses.

I am grateful to National Science Foundation Grant (NSF EPSCoR RII Grant No. OIA-1632899) for their financial support during the whole period of my studies in the United States of America.

Last but not the least I would like to express my heart-felt gratitude to my wonderful family members and friends for their understanding, encouragement, unconditional love and support throughout my entire endeavor.

TABLE OF CONTENTS

ABSTRACT	ii
DEDICATION	iii
LIST OF ABBREVIATIONS	iv
ACKNOWLEDGEMENTS.....	viii
LIST OF TABLES	xv
LIST OF FIGURES.....	xvii
1 Chapter I: Literature Review	1
1.1 CO ₂ Emissions: Effects on Global Warming and Climate Change	1
1.2 CO ₂ Capture Technologies.....	3
1.2.1 Pre-Combustion Technology.....	3
1.2.2 Oxyfuel Combustion Technology	4
1.2.3 Post-Combustion Technology	4
1.3 Post-Combustion CO ₂ Capture Techniques.....	5
1.4 CO ₂ Adsorption by Carbonaceous Adsorbents.....	8
1.4.1 Activated Carbon.....	8
1.4.2 Ordered Porous Carbons	9
1.4.3 Activated Carbon Fibers (ACFs).....	11
1.4.4 Graphene Oxide.....	11
1.4.5 Metal Oxyhydroxide–Carbon Composites	12
1.4.6 Carbon Nanomaterials.....	13

1.4.7 Biochar	13
1.5 Objective of the Present Work.....	21
2 Chapter II: Implications of Ultrasound Activation and Amine Functionalization for Enhanced CO ₂ Adsorption	22
2.1 Abstract.....	22
2.2 Introduction.....	23
2.3 Materials and Methods.....	25
2.3.1 Materials.....	25
2.3.2 Experimental Method.....	26
2.3.3 Characterizations.....	27
2.3.4 CO ₂ Adsorption Study.....	27
2.4 Results and Discussions.....	28
2.4.1 Physical Activation of Biochar.....	28
2.4.2 Mechanism of Chemical Activation of Biochar.....	31
2.4.3 Effect of Physicochemical Activation on Elemental Composition of Biochar.....	33
2.4.4 Effect of Physicochemical Activation on Functional Groups of Biochar.....	36
2.4.5 Effect of Physicochemical Activation on Graphitic Structure of Biochar.....	37
2.4.6 CO ₂ Capture Study of Physicochemical Activated Biochar.....	41
2.4.7 Effect of Temperature.....	43
2.4.8 Effect of CO ₂ Concentration.....	44
2.4.9 Cyclic Adsorption-Regeneration of Adsorbent.....	46

2.5 Selectivity.....	47
2.6 Conclusions.....	48
3. Chapter III: Ultrasound Promoted Dual Amination of Biochar for Preparing Efficient CO ₂ Adsorbent.....	50
3.1 Abstract.....	50
3.2 Introduction.....	51
3.3 Materials and Methods.....	56
3.3.1 Materials.....	56
3.3.2 Experimental Method.....	56
3.4 Results and Discussions.....	59
3.4.1 Physicochemical Properties of Raw and Modified Biochar Samples.....	59
3.4.2 CO ₂ Adsorption Studies.....	72
3.5 Conclusions.....	78
4 Chapter IV: Impact of Biomass Sources on Acoustic Based Chemical Functionalization of Biochars for Improved CO ₂ Adsorption.....	80
4.1 Abstract.....	80
4.2 Introduction.....	82
4.3 Materials and Methods.....	87
4.3.1 Materials.....	87
4.3.2 Experimental Method.....	87
4.4 Results and Discussions.....	91

4.4.1 Surface Area Analysis	92
4.4.3 Elemental Analysis	99
4.4.5 Raman Analysis	110
4.4.6 Adsorption Study	116
4.4.7 Mechanism of Physicochemical Activation of Char and Interactions with CO ₂	121
4.4.8 Regeneration Study.....	123
4.5 Conclusions.....	125
5. Chapter V: Determination the Impact of Pyrolysis Temperature on PhysicoChemical Properties and Ultrasound-Promoted Amination of Biochar for CO ₂ Capture.....	
5.1 Abstract.....	125
5.2 Introduction.....	128
5.3 Materials and Methods.....	132
5.3.1 Materials	132
5.3.2 Experimental Method	132
5.4 Results and Discussions.....	135
5.4.1 Surface Morphology Analysis	135
5.4.2 Surface Area Analysis	138
5.4.3 Elemental Analysis	142
5.4.4 FTIR Analysis.....	147
5.4.5 Raman Analysis	149
5.4.6 Thermal Stability Analysis	152

5.4.7 XRD Analysis	154
5.4.8 CO ₂ Adsorption Study	155
5.5 Conclusions.....	158
6. Chapter VI: Acoustic Treatment of Coal Gasification Residue for Extraction of Selenium..	158
6.1 Abstract.....	158
6.2 Introduction	159
6.3 Materials and Methods.....	159
6.4 Results and Discussions.....	160
6.4.1 Effects of Ultrasound Amplitude, Energy and Irradiation Duration.....	160
6.4.2 Effect of Dissolved CO ₂	162
6.4.3 Effect of Water Washing	163
6.4.4 Effects of Ultrasound Amplitude, Energy and Irradiation Duration.....	164
6.5 Conclusions	167
7 Chapter VII: Conclusions and Future Recommendations	168
7.1 Conclusions	168
7.2 Recommendations for Future Work	169
7.2.1 Plasma Activation of Biochar	169
7.2.2 Simultaneous Pyrolysis and Activation.....	170
Bibliography	171
Appendix A: Experimental Set Up and Schematic Diagram	195
Appendix B: Details of Experimental Procedure.....	197

Appendix C: Maintenance and Calibration Procedures of the Experimental Set Up.....	199
Appendix D: Data Acquisition and Analysis	203
Appendix E: Sample Preparations and Parameters Settings for Characterization Techniques	205
Appendix F: Elemental Compositions of Raw and Activated Samples with Mineral Free and Dry Basis.....	207
Appendix G: FTIR Spectrums of Raw and Activated Samples after Baseline Correction in Origin	209
Appendix H: Breakthrough Plots of Raw and Activated Samples.....	213
Appendix I: FTIR Spectrums of Raw and Activated Samples after Baseline Correction in Origin	217
VITAE	218

LIST OF TABLES

Table 1.1 Different absorption and adsorption strategies for Post-Combustion CO ₂ capture	6
Table 2.1. DR-CO ₂ and BET-N ₂ surface area of raw biochar, only ultrasound treated, and ultrasound treated -amine modified biochar	32
Table 2.2. Elemental Analysis of Raw Biochar and Physico-Chemical Activated Biochar	34
Table 2.3. Summary of intensity ratio for raw biochar and ultrasonicated amine functionalized biochar samples	40
Table 2.4. Effect of Process Parameters on CO ₂ Adsorption Capacity	43
Table 2.5. Comparison of Present Adsorption Capacity with Literature	45
Table 3.1. Structures and Properties of Different Amines	54
Table 3.2. DR-CO ₂ and BET-N ₂ Surface Area of Raw Biochar and Physicochemically Activated Biochars	61
Table 3.3. Elemental Analysis of Raw and Activated Biochars (Dry Basis)	64
Table 3.4. Elemental Analysis of Biochars as Percentage of Organic Constituents, Omitting Ash Contribution	65
Table 3.5. Raman Intensity ratios I _D /I _G of raw biochar and physico-chemically activated biochars	68
Table 3.6. CO ₂ Adsorption Capacities (in mmol/g) of Biochars (raw and functionalized) at 70 °C and 10 vol.% CO ₂ (effects of EDC-HOBt-activated amines and amine mixtures)	73
Table 3.7. Effect of KOH-Amine Mixture on CO ₂ Adsorption Capacity at 70 °C and 10 vol% CO ₂ Concentration	76
Table 3.8. Comparison of Adsorption Capacity Obtained in Present Study with Literature	77
Table 4.1. Lignino-cellulosic Compositions of Different Biomasses	82
Table 4.2. Physicochemical Properties of Different Biochars obtained from Literatures	84
Table 4.3. Surface Area Analysis of Different Biochar Samples (Raw, Ultrasonically, Chemically and Sono-Chemically Activated	91

Biochars)	
Table 4.4. Elemental compositions (dry basis) of Different Biochar Samples (Raw, Ultrasonically, Chemically and Sono-Chemically Activated Biochars)	101
Table 4.5. Organic compositions (dry ash free basis) of Different Biochar Samples (Raw, Ultrasonically, Chemically and Sono-Chemically Activated Biochars)	102
Table 4.6. Raman Intensity Ratios of Biochars Samples (Raw and Activated under Different Conditions)	109
Table 5.1 Literature Review on Physico-Chemical Properties of Biochars Synthesized at Different Pyrolysis Temperatures	127
Table 5.2. Surface Area Analysis of Raw and Sono-Chemically Activated Biochars Samples Synthesized at Different Pyrolysis Temperatures	138
Table 5.3. Elemental Compositions (dry basis) of Raw and Activated Biochar Samples Synthesized at Different Pyrolysis Temperatures	142
Table 5.4. Organic Compositions (dry ash-free basis) of Raw and Activated Biochar Samples Synthesized at Different Pyrolysis Temperatures	144
Table 5.5. Raman Intensity Ratios of Biochars Samples (Raw and Ultrasound Amine Activated Samples Synthesized at Different Pyrolysis Temperatures)	148
Table 6.1. Changes in Elemental Metal Concentration of the Residue upon Treatment	161
Table 6.2. Treatment of Residue	164
Table 6.3. Elemental compositions of the raw and treated residues (dry basis)	166

LIST OF FIGURES

Figure 2.1. SEM images of raw biochar	28
Figure 2.2. SEM image of a) physically activated biochar under ultrasound irradiation of 20kHz for 30Sec, b) physio-chemically activated biochar after both ultrasound irradiation and amine functionalization	29
Figure 2.3. EDC-HOBt coupling reaction and subsequent amine functionalization of biochar	33
Figure 2.4. IR spectrum of R, US3-EH1:1-T10, and US3-EH0-T0	36
Figure 2.5. IR spectrum of R, US3-EH1:1-T2.5, US3-EH1:1-T5, US3-EH1:1-T10, and US3-EH0-T0	37
Figure 2.6: Raman spectra of R, US3-EH1:1-T10, US3-EH1:0.75-T10, and US3-EH0.75:1-T10	38
Figure 2.7. Raman spectra of R, US3-EH1:1-T2.5, US3-EH1:1-T5, US3-EH1:1-T10, and US3-EH0 T0	39
Figure 2.8. Raman spectra of R, US0.5-EH1:1-T2.5 , US1-EH1:1-T2.5, and US3-EH1:1-T2.5	40
Figure 2.9 Cyclic Adsorption-Desorption Behavior of Sonicated-TEPA-Modified Biochar	46
Figure 3.1. Nitration of Carbonaceous Compounds	53
Figure 3.2. Amine Treatment of Carbonaceous Compounds	53
Figure 3.3. SEM images of (a) raw biochar (cross sectional view), (b) raw biochar (longitudinal view), (c) ultrasound activated biochar, (d) ultrasound-EDC-HOBt-binary amine (DEA-TEPA) activated biochar US0.5-EH1:1-DT1:1.	60
Figure 3.4. Raman spectra of raw biochar, US0.5-EH1:1-M2.5, US0.5-EH1:1-PZ2.5, US0.5-EH1:1-D2.5 and US0.5-EH1:1-P2.5	67
Figure 3.5. Raman spectra of raw biochar, US0.5-EH1:1-MT1:1, US0.5-EH1:1-DT1:1, US0.5-EH1:1-DP1:1, US0.5-EH1:1-TP1:1 and US0.5-EH1:1-DTP1:1:1	69
Figure 3.6. Raman spectra of raw biochar, US0.5-K1.5-M2.5, US0.5-K1.5-T2.5 and US0.5-K1.5-DT1:1	70
Figure 3.7. FTIR spectra of raw biochar, US0.5-EH1:1-M2.5, US0.5-EH1:1-	70

	PZ2.5, US0.5-EH1:1-D2.5 and US0.5-EH1:1-P2.5	
Figure 3.8.	FTIR spectra of raw biochar, US0.5-EH1:1-MT1:1, US0.5-EH1:1-DT1:1, US0.5-EH1:1-DP1:1, EH1:1-TP1:1 and US0.5-EH1:1-DTP1:1:1	71
Figure 3.9.	FTIR spectra of raw biochar, US0.5-K1:5-M2.5, US0.5-K1:5-T2.5 and US0.5-K1:5-DT1:1	72
Figure 4.1.	Schematic Representation of Biomass Classifications and the Corresponding Biochar.	82
Figure 4.2.	SEM images of Herbaceous Biochars (a) R-MS; (b) US-MS; (c) R-SG and (d) US-SG.	94
Figure 4.3.	SEM images of Agro-Industrial Biochars (a) R-CS; (b) US-CS; (c) R-SB and (d) US-SB	95
Figure 4.4.	SEM images of Crop Biochars (a) R-SR; (b) US-SR; (c) R-WS; (d) US-WS; (e) R-RH; (f) US-RH; (g) R-RS; (h) US-RS	96
Figure 4.5.	FTIR Spectra of Raw Biochar Samples	103
Figure 4.6.	FTIR Spectra of Physically Activated Biochar Samples	104
Figure 4.7.	FTIR Spectra of Chemically Activated (no US) Biochar Samples	105
Figure 4.8.	FTIR Spectra of Sono-Chemically Activated Biochar Samples	106
Figure 4.9.	Raman Spectra of Raw Biochar Samples	110
Figure 4.10.	Raman Spectra of Physically Activated (no amine) Biochar Samples.	111
Figure 4.11.	Raman Spectra of Chemically Activated (no US) Biochar Samples	112
Figure 4.12.	Raman Spectra of Sono-Chemically Activated Biochar Samples	113
Figure 4.13.	Adsorption capacities of different biochars at 70 °C and 10 vol% CO ₂ inlet concentration	115
Figure 4.14.	Mechanism of Physicochemical Activation of Char and Interactions with CO ₂	120
Figure 4.15.	Mechanism of Zwitterion and Alkyl Carbamate formation during the Interaction between Biochar Chemical Structure (C and N) with CO ₂	121

Figure 4.16. Cyclic adsorption-desorption behavior of ultrasono-aminated Herbaceous residue based chars (MS, SG), Agro-industrial based biochars (CS and SB) and Crop residue based biochars (SR, WS, RH and RS)	123
Figure 5.1. SEM images of (a) R-MS 700 and (b) US-MS 700	138
Figure 5.2. SEM images of (a) R-SG 700 and (b) US-SG 700	139
Figure 5.3. SEM images of (a) R-CS 700 and (b) US-CS 700	140
Figure 5.4. SEM images of (a) R-SB 700 and (b) US- SB 700	141
Figure 5.5. FTIR Spectra of Raw and Activated Samples (a) Miscanthus, (b) Switchgrass, (c) Corn Stover and (d) Sugarcane Bagasse Synthesized at Different Pyrolysis Temperatures	146
Figure 5.6. Raman Spectra of Raw and Activated Samples (a) Miscanthus, (b) Switchgrass, (c) Corn Stover and (d) Sugarcane Bagasse Synthesized at Different Pyrolysis Temperatures	149
Figure 5.7 TGA-DTG plots of (a) Raw and (b) Activated Miscanthus Samples Synthesized at 500, 600, 700 and 800 °C	151
Figure 5.8. XRD plots of (a) Raw and (b) Activated Miscanthus Samples Synthesized at 500, 600, 700 and 800 °C	152
Figure 5.9. CO ₂ Adsorption Capacities of both Raw and Sono-Chemically Activated Biochar Samples Synthesized at Different Pyrolysis Temperatures	154

CHAPTER I
LITERATURE REVIEW

1.1 CO₂ Emissions: Effects on Global Warming and Climate Change

Global climate is projected to change continuously over this century and the magnitude of this change depends on the amount of heat-trapping gases (greenhouse gas) emitted globally and how sensitive the earth's climate is to those emissions. The primary sources of the greenhouse gases are energy sectors [1]. In the United States, 40% of total energy is consumed in electrical form, of which 55-60% comes from fossil fuels (coal, oil, and natural gas), 20% from nuclear plants, and the remaining comes from renewables (mainly hydro) [1]. Major sources of CO₂ are thermoelectric power plants and industrial plants (such as steel mills and refineries) [2], combustion of fossil fuels etc. [3]. The burning of the fossil fuels generates pollutant gases, such as SO₂, CO, NO_x, and CO₂ that cause environmental pollution [1]. The most dominant effect of fossil fuel burning is the global warming that is mainly caused by CO₂, which traps the solar heat in the atmosphere (greenhouse effect). According to the Intergovernmental Panel on Climate Change (IPCC), 2007, elevated CO₂ concentration due to anthropogenic activities is responsible for the global warming [4, 5] and resulted to increase the average world temperature by 0.74% in the past 100 years and is expected to increase by another 6.4% by the end of the twenty-first century [2, 6]. The IPCC also estimated that atmospheric temperature will rise typically between 1.1 and 6.4 °C in the next 100 years due to greenhouse gases if no remedial actions are taken [1]. The deleterious impact of global warming can be listed as droughts, melting of ice in the

Antarctic, Greenland, the Himalayas, and thousands of glaciers around the world [1]. Considering the serious consequences of global warming, the United Nations called a series of international meetings to discuss the challenges posed by global temperature and climate change. As a result, Kyoto Protocol emerged in 1997 [7] where it was decided to reduce GHG emissions below 5–8% of the 1990 levels by 2012. In addition several other options are explored to reduce anthropogenic carbon footprint, from increasing household energy efficiency to sequestering carbon in soils [8]; some studies even focus on capturing CO₂ from ambient air [9]. Since majority of the fossil fuel combustion is used to produce electricity contributing 37% of all anthropogenic CO₂ released, thus, power plants have been proposed as important locations for CO₂ capture [10]. Currently, there is also ongoing research on clean coal technologies, which can be classified as carbon capture and sequestration (CCS). CCS has a great potential to be a green technology in the future [2]. The International Energy Agency and Organization for Economic Co-operation and Development and United States forecast that the CCS market will grow to its full capacity by 2020, and there is a need to obtain better insights into the techno-economic possibilities of CO₂ capture [2].

The basic concept of CCS is to capture CO₂ emissions without releasing them into the atmosphere; they include sequestration or storage which is a comprehensive technology for direct reduction of CO₂ [2]. CO₂ capture is a core technology and accounts for 70–80% of the total costs of CCS technologies. It is classified as (i) post-combustion, (ii) pre-combustion, and (iii) oxy-fuel combustion. Post-combustion capture technology involves collecting CO₂ from the emission gases of a power plant [11, 12, 13].

1.2 CO₂ Capture Technologies

1.2.1 Pre-Combustion Technology

Pre-combustion is primarily associated with integrated gasification combined cycle power plants, in which coal is normally first gasified to CO and hydrogen (syngas) prior to combustion in a gas turbine [14]. If the water-gas shift (WGS) reaction is used to convert CO to CO₂ and more hydrogen, the CO₂ can instead be separated out before combustion of hydrogen (with a diluent such as nitrogen) in the turbine [14]. The most developed form of the pre-combustion process is complex and comes with several energy losses besides the relatively efficient solvent-based capture step, including the steam demand of the WGS reaction, the low operating temperature of the capture solvents (which requires inefficient cooling and reheating and loss of water from the fuel gas), and reduced gas turbine efficiency [15].

Among pre-combustion technology, sorbents and sorbent-enhanced water gas shift is an important technique. However, of most interest is the integration of the CO₂ capture step with the shift reaction in a process known as sorbent-enhanced water gas shift (SEWGS) which, by continuously removing CO₂ product from the reactor, helps drive the equilibrium to completion and reduce the demand for steam reagent [14]. Membranes are well suited to pre-combustion separation as well, as the CO₂ is retained on the high pressure side while the small hydrogen molecule passes through the membrane, and the hydrogen diluent (usually nitrogen) can be used as a sweep gas to help drive the process [14]. However, elevated temperature of syngas (250°C) is a problem for most of the polymer membranes. Thus, membranes are needed to withstand high temperature that comes at the expense of cost. Other materials which can be used in H₂/CO₂ separation include porous inorganic materials and metal alloys based on palladium, which are even more costly to produce than polymers [16].

1.2.2 Oxyfuel Combustion Technology

The principle of oxyfuel combustion is to fire coal in oxygen rather than air, producing a flue gas stream consisting of mostly CO₂ and water, from which CO₂ can be purified relatively easily [17]. Large-scale air separation to produce oxygen is a highly developed commercial process which can be readily applied to a power plant, however, the costs and energy penalties associated with this process are not significantly different from commercial post-combustion capture [14]. Investigation of less energy intensive air separation methods has focussed on ceramic membranes, but these currently remain some distance from the necessary scale or performance [18]. The most widely investigated approach is to carry out combustion at high pressures, enabling the significant latent heat of water vaporisation in the flue gases to be recovered as useful work, along with other benefits including smaller equipment, reduced air ingress, and improved heat transfer [14].

1.2.3 Post-Combustion Technology

Post-combustion capture describes any carbon capture technique which is applied to the separation of CO₂ from the flue gases of a conventional fossil fuel-fired power plant. Owing to their inherent suitability for retrofit to existing plant and compatibility with standard power plant technologies, post-combustion capture technologies have been subject to significantly more research than other approaches to carbon capture, and have reached a mature stage of development in the form of commercially available amine-based solvents. However, the fundamental task of separating a relatively low concentration of CO₂ (<15%) from mainly nitrogen at atmospheric pressure is challenging to achieve without significant energy consumption. A diverse range of gas separation technologies have been applied to the problem, including chemical solvents, physical and chemical solid sorbents, membranes, cryogenic processes, and fuel cells etc. Post-combustion capture uses wet/dry adsorbents, which are used

for gas separation, and separates and collects CO₂ by adsorption/desorption [2].

1.3 Post-Combustion CO₂ Capture Techniques

According to the most recent version (August 2015) of the Carbon Dioxide Capture Handbook published by the National Energy Technology Laboratory (NETL), the CO₂ capture technology can be divided into i) solvent based process (absorption), ii) sorbent based process (adsorption), and iii) membrane based process [19]. Different strategies of post-combustion (including absorption and adsorption) technique and their advantages/disadvantages are illustrated in Table 1. Another classification for CO₂ capture is based on the type of sorbent used [20]. Sorbent-based CO₂ capture involves primarily three types of adsorbents: i) inorganic adsorbents, ii) organic and organic-inorganic hybrids, and iii) metal organic frameworks. Inorganic adsorbents are further categorized as physisorbents (such as zeolites, activated carbon) and chemisorbents (such as metal-based and hydrotalcite-like compounds). Organic and organic-inorganic hybrid sorbents consist of amines supported on various oxides. Therefore, they can be grouped based on the type of support used. These include: i) amine physically adsorbed on oxide support, ii) amine covalently attached to oxide support, and iii) amine supported on solid organic materials. Post-combustion capture uses wet/dry adsorbents, which are used for gas separation, and separates and collects CO₂ by adsorption/desorption. The post-combustion technologies have been shown in Table 1.

Advantages	Efficiency	Disadvantages	Cost effectiveness	Ref
Absorption				
<p>1) <u>Physical Absorption</u></p> <ul style="list-style-type: none"> • SP- low VP, toxicity, less corrosive solvent • RP- solvent is less corrosive and more stable • PP- low energy consumption • MP- easy to operate • FP- used to remove high concentration CO₂ <p>2) <u>Chemical Absorption</u></p> <p>• Amine absorption - Since CO₂ reacts chemically with amine, it can be used to process gas streams with low CO₂ partial pressure</p> <p>• Aqua ammonia absorption - Used for multi pollutant removal - Equipment corrosion negligible - No degradation of absorbent - Byproducts (NH₄NO₃ & sulfate) used as fertilizer</p> <p>• Dual alkali absorption - Better replacement of the Solvay process - Absorption capacity better than amine process</p> <p>• Ionic Liquid - Applied either physically or chemically - Low vapor pressure, good thermal stability, high polarity, and non-toxicity - Chemical absorption of IL is higher than physical one</p>	<p>85 % of the CO₂ from flue gas can be captured efficiently</p> <p>CO₂ removal: 0.4 kg CO₂/kg monoethanol amine</p> <p>CO₂ removal: 1.20 kg CO₂/kg ammonia is satisfactory</p> <p>CO₂ removal: 0.54 kg CO₂/kg methylaminoethanol</p> <p>CO₂ removal: 0.20 mole of CO₂ per mole of IL</p>	<p>- Needs high pressure 2.07-13.8 MPa</p> <p>- Solvent disposal is a problem</p> <p>- Reaction of solvents with constituent</p> <p>- Operating temperature is very low</p> <p>- Solvent regeneration not fully achieved</p> <p>- Energy intensive process</p> <p>- Waste stream can be hazardous</p> <p>- Flue gas must be cooled to 15–27° C due to volatility of ammonia</p> <p>- Solids formation upon CO₂ capture; equipment plugging</p> <p>- Ammonia vapor losses during stripping</p> <p>- Gas stream must be cooled to 25° C</p> <p>- Removal of NO_x-SO_x prior to absorption</p> <p>- Solvent regeneration not yet achieved</p> <p>- ILs are highly viscous thus needed blended solution with alkanolamine</p> <p>- Supported ILs to improve efficiency of the process</p>	<p>Because of high pressure and low temperature, the process is not cost effective</p> <p>Not economic: i) Not complete solvent regeneration ii) high energy demand</p> <p>Not economically attractive because energy lose during the cooling of feed</p> <p>Solvent regeneration is not possible to achieve- not cost effective</p> <p>Not economic because of low absorption rate and use of blended solution</p>	<p>[21, 22]</p> <p>[23]</p> <p>[23]</p> <p>[23]</p> <p>[23]</p>
Adsorption				

<p>1) <u>Traditional adsorbents</u></p> <ul style="list-style-type: none"> • Carbonaceous adsorbents - High thermal stability; favorable adsorption kinetics - Cheaper feedstock sources - Desorption is accomplished by the PSA 	<p>CO₂ adsorption: 0.1-1.13 g CO₂/g activated carbon</p>	<ul style="list-style-type: none"> - Unable to treat high pressure gases - Needs separate characterizations depending feedstock - Adsorption rate reduces when exposed to NO_x, SO_x & H₂O 	<p>The CO₂ capture costs are such that the carbon-based systems can be applicable when CO₂ purity is not more than 90 %</p>	<p>[23]</p>
<ul style="list-style-type: none"> • Zeolites - CO₂/N₂ selectivity is much higher than activated carbon - Enhanced capacity and selectivity than physical sorbents • Mesoporous silica - High surface area; high pore volume - Tunable pore size - Good thermal and mechanical stability • Metal Organic Frameworks - High thermal stability; high surface area - Adjustable chemical functionality - High adsorption capacity at elevated pressure - Easily tunable pore characteristics 	<p>CO₂ adsorption: 0.004 to 0.216 g CO₂/g zeolite</p> <p>Adsorption capacity is not sufficient</p> <p>CO₂ adsorption: 1.13 g CO₂/g adsorbent</p>	<ul style="list-style-type: none"> - Efficiency reduces in presence of H₂O - Regeneration temperature high (>300°C) - Needs chemical modification - Adsorption capacity not good at atmospheric pressure - Silica has lower adsorption capacity and selectivity toward CO₂ - Adsorption capacities reduce in exposure to a gas mixture of NO_x, SO_x, and H₂O - Low CO₂ selectivity in CO₂/N₂ gas streams and PS and TS have not been thoroughly understood 	<p>The high regeneration temperature makes the process less cost effective</p> <p>Low adsorption capacity makes the process less economic</p> <p>Due to low sorbent regeneration, the technique is not cost effective</p>	<p>[23]</p> <p>[23]</p> <p>[23]</p>
<p>2) <u>Advanced adsorbents</u></p> <ul style="list-style-type: none"> • Fly-ash carbon enriched by 3-chloropropylamine-hydrochloride • Modified mesocellular silica foams impregnated with Tetraethylenepentamine (TEPA) • Amine functionalized adsorbents - CO₂ partial pressure does not affect adsorption capacity - Moisture facilitates adsorption; favorable kinetics • Biochar 	<p>CO₂ adsorption: 174.6 μmol/g</p> <p>CO₂ adsorption: 26.4-193.6 mg/g</p> <p>CO₂ adsorption: 0.089-1.1 mmol/g adsorbent</p> <p>CO₂ adsorption: 1.67 mmol/g</p>	<ul style="list-style-type: none"> - Needs chemical modification - Adsorption capacity very low - Degrade at temperatures around 100° C - Irreversible reactions with NO_x-SO_x - Loss in capacity after desorption - Surface functionalization may be required 	<p>Not cost effective</p> <p>Not cost effective</p> <p>The process not fully economic for large scale operation</p> <p>Cost effective and viable</p>	<p>[4]</p> <p>[24]</p> <p>[23]</p> <p>[25]</p>

1.4 CO₂ Adsorption by Carbonaceous Adsorbents

Inorganic porous carbons are common adsorbent for the CO₂ adsorption. The group of carbonaceous material-based adsorbents encompasses a large variety of materials that include activated carbon obtained from a range of materials, graphene, mesocarbon and carbon nanotubes (CNTs) [26, 27], activated carbon, activated carbon fiber etc. [28].

1.4.1 Activated Carbon

CO₂ adsorption capacity is strongly sensitive to the textural properties and surface groups of carbon-based adsorbents [29-31]. The pore size distributions of activated carbons vary from micropore to macropore; therefore, activated carbons are inappropriate for selective adsorption of a specific gas. The typical CO₂ adsorption capacity of an activated carbon is 5 wt. % at 298 K and 0.1 bar [32, 33]. The pore structures of activated carbons can be easily controlled by varying the preparation and activation conditions [34]. Moreover, the functional groups on the activated carbon surface can also be easily controlled using various treatments [35]. Zhao et al. showed in their study that K⁺ ions attached to microporous carbon material (KNC-A-K) showed superior CO₂ capture performances (17.8 wt.% at 0.1 bar and 298 K) [36]. Lee et al. prepared heat-treated carbons by pyrolysis of poly (vinylidene fluoride) at various heat-treatment temperatures and evaluated the CO₂ adsorption capacities. The CO₂ adsorption capacity increased with increasing heat-treatment temperature up to 873 K (15.5 wt. % at 298 K and 1 bar) and then decreased at 973 K; this correlated with their micropore volumes. It was found that ultra-micropores (<0.65 nm) were strongly preferred sites for CO₂ [2]. Sevilla et al. prepared sustainable porous carbons synthesized using polysaccharides and biomass by hydrothermal carbonization and chemical activation. A very high CO₂ adsorption capacity of 21.2 wt. % was achieved at 298 K and 1 bar. They observed that the porous carbon samples obtained using mild activating conditions had

smaller specific surface areas; however, the mildly activated carbons had the best CO₂ adsorption capacities because of the presence of abundant narrow micropores of size less than 1 nm [37]. Balsamo et al. explained the importance of microporous structure of activated carbon in improving CO₂ capture ability where they synthesized the adsorbent from activated carbon using a mixture of coal tar pitch and furfural (50/50 wt.%) followed by steam activation. They reported CO₂ adsorption capacity was 2.68 wt.% at 303 K under typical flue gas conditions (with CO₂ partial pressure 0.15 bar) [2]. According to the study by Meng et al., the N-doped activated carbon prepared from polypyrrole functionalized nanoporous carbon material and subsequently activated by NaOH provided high specific surface area (2169 m²/g) that aided to exhibit a high CO₂ adsorption capacity of 17.7 wt. % at 298 K and 1 bar. The CO₂ adsorption capacity was attributable to the presence of narrow micropores, together with a high density of N basic groups [38]. Meng et al. synthesized porous carbons with well-developed pore structures, using a weak-acid cation-exchange resin (CER), by the carbonization of mixtures containing different amounts of magnesium acetate. As the magnesium acetate/CER ratio increased, the specific surface area increased from 326 to 1276 m²/g; the CO₂ adsorption capacities were 16.4 and 104.5 wt.% at 1 and 30 bar, respectively, at 298 K [39]. Jang et al. demonstrated that metal oxide (such as nickel oxide) grafting at elevated temperature (573 K) in presence of air stream produced oxidized activated carbon with high CO₂ adsorption capacity of 49.9 cm³/g at 298 K and 1 bar. They also confirmed that the NiO acted as electron donors on the carbon surface, enhancing the adsorption of CO₂, which is an electron acceptor, because of the acid–base properties [40].

1.4.2 Ordered Porous Carbons

These adsorbents have attracted much research interest because of their widespread applications in gas storage, and as catalysts and supports, electrode materials, etc. [2]. Many

synthetic methods for ordered porous carbons have been reported including (i) direct synthesis by organic–organic self-assembly, involving a combination of carbon precursors and block copolymers as soft templates and (ii) nanocasting using silica materials as structural directing hard templates [41]. Ordered porous carbons are expected to act as CO₂ adsorbents because of their high specific surface areas, large pore volumes, large adsorption capacities, high chemical stabilities, ease of tuning of pore sizes or channels, and ease of surface modification [41]. In particular, their pore size distributions are quite narrow and uniform compared with commercially available high-surface-area carbons making them suitable CO₂ adsorbents. Bin et al. reported the importance of soft-templating method to prepare ordered mesoporous carbon that had CO₂ adsorption capacity of 13.2 wt.% at 278 K and 1 bar [42]. N-doped porous carbon fabricated by carbonization of melamine-formaldehyde resins had a CO₂ adsorption capacity of 9.9 wt. % at 298 K and 1 bar [43]. The N-doping in porous carbon using facile one-pot evaporation-induced self-assembly method synthesized sorbent material with high specific surface area of 1979 m²/g and a high %N content of 4.32 wt.% which also increased CO₂ adsorption capacity of 18.9 wt.% at 298 K and 1 bar [44]. Mahurin et al. investigated a material produced by grafting amidoxime functional groups onto a hierarchical porous carbon framework, synthesized using a soft-templating method, for the selective capture and removal of CO₂ from combustion streams. The best adsorbent showed a CO₂ adsorption capacity of 10.9 wt. % at 298 K and 1 bar [45]. Yoo et al. investigated the effect of elevated carbonization temperature to improve CO₂ capture capacity of ordered nanoporous carbon that exhibited CO₂ adsorption capacities of 15.8 wt.% and 68.5 wt.% at 298 K and 1 and 30 bar respectively [46].

1.4.3 Activated Carbon Fibers (ACFs)

ACFs are promising adsorbent materials, based on their nanostructures, abundant micrometer porosities, and properties such as high specific surface areas and narrow pore size distributions [2]. The fibrous shape of ACFs makes them easier to handle than granular and powdered adsorbents [47], [48]. Lee et al. [49] demonstrated that the ACF pore structure can be designed to enhance the CO₂ adsorption capacity by controlling the concentration of KOH intercalated into the graphitic lattice. The highest CO₂ adsorption capacity was 25.0 wt. % at 298 K and 1 bar achieved using KOH/ACF with a ratio of 3:1. Thiruvengkatachari et al. prepared large honeycomb-shaped carbon fiber composite adsorbents for large-scale CO₂ capture tests (the adsorbent mass in one column was 4.486 kg). The average CO₂ adsorption capacity was 11.9 wt.% for a simulated flue gas consisting of 13% CO₂, 5.5% O₂, and the balance N₂, at 293 K. They also showed that the CO₂ capture efficiency of HMCFC adsorbents is more effective in a combined vacuum and thermal decomposition process [50].

1.4.4 Graphene Oxide

GO is a derivative of graphene and can be synthesized with various functional groups on the basal planes and edges [51]. The surface modification of GO with various functional groups and the synthesis of new types of GO-like derivatives with light weight frameworks has been widely researched for applications such as gas storage and separation, energy conversion, and sensors [2]. For instance, GO functionalized with ethylenediamine (EDA) showed a CO₂ adsorption capacity of 4.65 wt. % at 303 K and 1 bar [52]. The performance of different amines such as ethylenediamine, diethylenetriamine (DEA) and triethylenetetramine (TETA) on CO₂ adsorption were determined. The results indicated that the adsorption capacity of GO sample functionalized with EDA had higher adsorption capacity than those of GO modified with DETA

or TETA [52]. Additionally, literature showed that GO prepared using isothermal exfoliation using PS technique exerted sufficient pressure to overcome the GO-interlayer Van der Waals binding energy, thus promoting high surface area ($547 \text{ m}^2/\text{g}$) and pore volume ($2.468 \text{ cm}^3/\text{g}$) and consequently high CO_2 adsorption capacity of 28.2 wt. % at 298 K and 30 bar [53]. Another study demonstrated that thermal exfoliation of graphene nanoplates had induced high CO_2 capture capacity of 24.8 wt. % at 298 K and 30 bar which was attributed to the larger inter-layer spacing and high pore volume [39].

1.4.5 Metal Oxyhydroxide–Carbon Composites

The addition of metal oxides and/or hydroxides (i.e., oxyhydroxides) to the surface of porous carbon adsorbents has been shown to enhance CO_2 capture ability by increasing surface area, increasing the basicity of the material, and even promoting the production of carbonates with the reaction of CO_2 . [54, 55]. Most synthesis methods for metal oxyhydroxide carbon are designed to produce a composite with high surface area and good dispersion of nanosized or colloidal oxide or hydroxide on the surface within the porous carbon network. When used for CO_2 capture, the mechanisms of both chemisorption (from the addition of some metal oxyhydroxides) and physisorption (from increased surface area of the structure) may be involved in the process. Typically, samples with added metals, such as Ca, Mg, Al, Fe oxides and hydroxides, will have capacities for CO_2 that are higher than those of the unmodified samples. Metal oxyhydroxides, themselves, have been shown to be effective CO_2 trappers. For example, Pierre-Louis et al. studied the ability of Al/Fe oxyhydroxide to capture CO_2 [56]. Several studies have focused on producing MgO/C composites to capture CO_2 at both high and low temperatures [10, 54]. Bhagiyalakshmi [55] carbonized a mixture of magnesium nitrate along with other solvents (HCl, sucrose, H_2SO_4 , H_2O) after evaporation. This led to the production of a thermally

stable mesoporous supported MgO that is capable of adsorbing up to $92 \text{ mg g}^{-1} \text{ CO}_2$ at $25 \text{ }^\circ\text{C}$. Liu et al. [57] developed MgO nanoparticles that were stabilized by mesoporous carbon. MgCl_2 was obtained in low concentrations from seawater, mixed in solution with biomass, and pyrolyzed to produce an efficient CO_2 capture material. The excellent CO_2 capture is attributed to the porous structure along with the presence of basic $-\text{OH}$ groups.

1.4.6 Carbon Nanomaterials

Carbon nanomaterials have at least one dimension between 1 and 100 nm in size and are found in many different forms. They possess a large diversity of properties, leading to their use in many applications; including catalyst supports, energy conversion and storage, filtration, and sorption [58]. These materials have been highly studied because of their unique thermal, electrical, mechanical, and chemical properties [58]. Carbon nanomaterials when amalgamated with chitosan hybrid aerogels decorated with graphene oxide nanosheets high CO_2 capture capacity ($1.92\text{-}4.14 \text{ mmol g}^{-1}$) [59]. Although they might be more intensive and expensive to produce than other carbon materials, can be produced precisely for optimal CO_2 capture with high selectivity and capacity. Additionally, study shows that carbon nanostructures not only have very high CO_2 capture ability ($>4 \text{ mmol g}^{-1}$ at $25 \text{ }^\circ\text{C}$ and 1 atm.) but also possess high thermal stability and good regeneration properties [10].

1.4.7 Biochar

Biochar is an eco-friendly adsorbent that is produced from natural biomass or agricultural waste which is nearly ten times cheaper than other CO_2 adsorbents because of the wide availability of biomass. Raw biochar exhibits a low adsorption capacity towards CO_2 , but modified biochar has shown enhanced CO_2 adsorption in many studies. Several modification methods have been tested and applied with varying degrees of success. The CO_2 adsorption

capacity of biochar, which is the amount of CO₂ adsorbed per unit weight of biochar, mainly depends on the physicochemical properties of the biochar, such as the surface area, pore size, pore volume, basicity of biochar surface, presence of surface functional groups, presence of alkali and alkali earth metals, hydrophobicity, polarity, and aromaticity [60]. These physical and chemical properties of biochar are closely related to the type of feedstock used and the thermochemical conditions of biochar production [61, 62].

1.4.7.1 Structure and Properties of Biochar

Biochars have structural similarity with graphene oxide [63]. GO has two-dimensional structure that contains atomic sheet of graphite decorated by several oxygenated functional groups on its basal planes and at its edges, resulting in a hybrid structure comprising a mixture of sp² and sp³ hybridized carbon atoms [64]. The outstanding properties of biochar arises from its hybrid electronic structure as it contains both the conducting p states from the sp² carbon domains and also the σ states from the sp³ carbon domains [65]. The graphitic cluster of biochar is made of honeycomb crystal lattice [66, 67] that has a strong π-π interactions [68]. According to the literature, the GO sheets of biochars are rough with an average roughness of 0.6 nm and the structure is predominantly amorphous due to distortions from the high fraction of sp³ C-O bonds [69]. In the amorphous biochar matrix, some local crystalline structures of cross-linked and highly conjugated aromatic sheets are observed. At elevated preparation temperature, the size of biochar crystallites increases, and the structure becomes more ordered [70].

1.4.7.2 Physical Properties of Biochars

Carbon dioxide adsorption occurs through van der Waals forces between gas molecules and the solid phase (biochar), which is associated with the specific surface area, pore size, and

pore volume of the biochar [71].

Specific surface area: The specific surface area of biochar can be defined as the ratio between the total surface area and the total mass of the biochar [72]. Several studies have assessed the effects of the specific surface area of biochar on its capacity of CO₂ adsorption [73]. The specific surface area of biochar is strongly related to the carbon content of the material, which may vary depending on the feedstock [72, 74]. Whereas, high mineral content can reduce the specific surface area by blocking the pores on the biochar surface [75]. Thus the differences in the Brunauer–Emmett–Teller (BET) specific surface area can be attributed to the different lignin, cellulose, and hemicellulose contents of the feedstock, which may also contribute to different decomposition rates [76]. The surface area of the biochar increases with increasing pyrolysis temperature and residence time, possibly because of the release of volatile matter, which increases the pore volume [77].

Total pore volume and pore size: The pore volume and pore size also play a vital role in CO₂ adsorption. The release of volatile organic matter from the polymeric backbone of the feedstock causes the formation of porous structures in biochar, and a larger total pore volume provides more active sites for interaction between CO₂ and the biochar [72, 78]. Generally, the CO₂ capture capacity of porous carbon strongly depends on the presence of micropores with a diameter of less than 1 nm [33, 79]. The pore volume of biochar usually increases with the increase of heating rate. When the heating rate of the process is low, pyrolysis products/volatile organic matter has enough time to diffuse from the biochar particles. Nevertheless, with the increase of heating rate, the time for discharging volatile organic matter reduces resulting in the accumulation of volatiles within and between particles blocking the pore entrance [80].

1.4.7.3 Chemical Properties of Biochar

The adsorption of CO₂ onto the biochar surface is also affected by the chemical properties of the biochar such as alkalinity, mineral composition, and presence of surface functional groups, hydrophobicity, and non-polarity [73, 79]. The CO₂ adsorption capacity of biochar can be enhanced by increasing the alkalinity of the biochar surface [81].

Functional groups: The properties of biochar and the adsorption reactions are related to functional groups, mainly oxygen-containing groups. The oxygen complexes include carboxylic, hydroxyl, phenolic (hydroxyl), carbonyl, lactone, carboxylic acid anhydride, and cyclic peroxide groups [82]. These surface oxides may exist in the original biomass or be formed either during the pyrolysis or the subsequent activation stage that involves oxidation. Oxygen containing functional groups have been considered as the major active sites for adsorption [83]. This oxygen-containing acidic functional groups such as hydroxyl groups, carboxyl groups, and carbonyl groups also increase CO₂ adsorption on carbonaceous surfaces by facilitating hydrogen bonding between the CO₂ molecules and the carbon surface [84, 85].

On the other hand, basic surface functional groups contribute to surface basicity, which enhances the affinity of the biochar for CO₂ [86]. Nitrogen-containing functional groups (e.g., amide, imide, pyridinic, pyrrolic, and lactam groups) are the contributors to the surface basicity of biochar. They can be introduced to the biochar surface through reaction with different *N*-containing reagents such as ammonia, amines, and nitric acid or by the activation of biochar with nitrogen-containing precursors (a precursor is a compound that participates in a chemical reaction while producing another compound), such as melamine or polyacrylonitrile [87, 88]. Xing et al. [84] suggested that the basicity of *N*-containing functional groups is very weak compared to that of organic amines, but this has rarely been studied.

Alkaline and alkaline earth metals: The presence of alkali metals and alkaline earth

metals (e.g., Na, K, Ca, Mg, and Li) can enhance the formation of basic sites with a strong affinity for CO₂, which has an acidic nature [73]. Thus, the presence of alkaline metals and alkaline earth metals may enhance the CO₂ adsorption capacity of biochar. Additionally, decrease in the specific surface area and pore volume have been observed with the incorporation of metal ions due to localized deposition of metals on the biochar surface and blockage of micropore entrance by alkaline metal oxide [81].

Hydrophobicity, polarity, and aromaticity: Studies have revealed that the CO₂ adsorption capacity of carbonaceous materials may be reduced under humid environments because of the high affinity for H₂O of most porous materials [89, 90]. Low H/C and O/C ratios (<0.2), suggest a high degree of aromaticity and fixed carbon, which are chemically stable [72]. Increasing pyrolysis temperature can separate H and O due to the fracture of chemical bonds. The molar ratio of O/C and H/C decreases as the increase of pyrolysis temperature, possibly due to loss of volatile organic compounds and increase in dehydrogenation and deoxygenation reactions resulting formation of aromatic structures and reduce the polarity of biochar while increasing the hydrophobicity [60].

1.4.7.4 Modification of Biochar for CO₂ Adsorption

Biochar has excellent inherent characteristics for capturing CO₂ because of its polar and hydrophilic nature with a highly porous structure and high specific surface area [60]. At present, the focus is on the production of engineered/designer biochar through modification with novel structures to yield different surface properties and increase the sorption capacity [60]. The modification of biochar can be achieved through various methods, such as the use of different activation conditions, precursors, and additives [91]. The feedstock can be treated either prior to pyrolysis or after pyrolysis to achieve the desired changes to the biochar [91]. The modification

of biochar can be categorized as physical modification and chemical modification [92].

Physical Activation of Biochar: Physical activation, a green activation way, that increases the porosity of biochar, introduces functional groups (O-containing functional groups through O₂, H₂O and CO₂ activation and N-containing functional groups through NH₃ activation), and improves the polarity [93]. CO₂ is the most popular activating agent, which mainly develops narrow micropores [94]. Whereas steam activation generates narrow micropores, and also creates mesopores [95]. In addition, NH₃ activation has received wide attention, as it could develop micropores and dope N-containing functional groups at the same time. Air or O₂ activation often obtained lower carbon yield, as the seriously exothermic reaction of biochar with O₂ is difficult to control, which would lead to the excessive burn-off [96]. Further details explanation on physical activation techniques are provided in the following sections-

I. Carbon dioxide Modified Biochar: Gas purging or the modification of biochar with CO₂ is a physical modification method [60]. Several studies have proven that CO₂ activation enhances micropores, which favors CO₂ adsorption [60]. During CO₂ modification, CO₂ reacts with the C of biochar to form CO (known as hot corrosion) and creates a more microporous structure [92]. Moreover, the gas purging facilitates the thermal degradation of carbonaceous material and enhances the aromaticity of the biochar [60]. Studies have revealed that the capacity of CO₂ adsorption in CO₂-modified biochar is significantly higher than that of unmodified biochar [60]. In addition, CO₂-modified biochar has a higher surface area and pore volume than unmodified and NH₃-modified biochar, and CO₂ adsorption capacity shows a significant linear relationship with the micropore volume [60]. Studies have revealed that the CO₂ adsorption capacity shows an increasing trend with increasing activation temperature [97].

II. Steam Modified Biochar: During steam activation, biochar is subjected to partial

gasification with steam, which enhances the devolatilization and the formation of a crystalline structure [98]. The oxygen from water molecules in carbon surface sites, create surface oxides and H_2 . Then, the produced H_2 reacts with C surface sites, forming surface hydrogen complexes and activating the biochar surface [98]. Even though CO_2 -activated biochar and steam-activated biochar have similar micropore volumes, steam-activated biochar has a higher total pore volume than that of CO_2 -activated biochar [99]. Steam-activated carbon has a higher graphitic carbon content and lower content of oxygen-containing functional groups than that of KOH-activated carbon [99]. However, it was found that the adsorption capacity of steam-activated carbon begins to reduce after few cycles, which indicates that the steam-activated biochar may not be suitable for multicycle CO_2 adsorption [99].

Chemical Activation of Biochar: Chemical activation, in which char is doped with a chemical agent, is the most common method to modify surface functional groups. In this process, the biochar is impregnated with the chemical agent and then the mixture is thermally treated. During this process, the chemical agent dehydrates the sample, inhibits the tar formation and volatiles compounds evolution, and therefore increases the yield of the carbonization process [100]. The distribution of chemical agents in the precursor prior to carbonization plays a key role in porosity development and functionality of the final products [101]. Modifications of biochar with acid, alkali and amines are the widely used chemical activation techniques.

I. Acid Modified Biochar: H_3PO_4 is a common acid activator, which can generate micropores and introduce phosphorous-containing functional groups into the biochar [102]. It promotes dehydration reaction (including cyclization and condensation reactions) of biochar during activation, which reduces the particle dimensions [96]. Concentrated nitric acid which is another common oxidizing agent helps to increase the N-O bonds and introduces nitrogen groups

into the biochar structure [100]. Another common acidic treatment with HCl increases the quantity of weak acidic and single-bonded oxygen functional groups such as phenols, ethers, and lactones [103, 104]. However, the acidic treatments are primarily used to modify biochar for heavy metal adsorption.

II. Alkali-Modified Biochar: The activation of biochar using KOH or NaOH dissolves ash and compounds like lignin and cellulose, which increases the O content and surface basicity of the biochar. Two-stage KOH activation of pre-carbonized precursors may create a higher surface area with more surface hydroxyl groups than that of pristine biochar [105, 106]. Moreover, during the KOH activation process, different potassium species, including K_2O and K_2CO_3 , are formed and diffuse into the internal structure of the biochar matrix, which increases the width of the existing pores and generates new pores [60]. Nevertheless, the effect of alkali treatment on the formation of $-OH$ in biochar depends on the type of feedstock, charring method, and treatment conditions, such as the activation temperature and ratio between alkali and C [73]. KOH-activated biochar exhibits higher adsorption capacities than CO_2 and steam-activated biochar because of its higher surface area and micropore volume, irrespective of the presence of more oxygen-containing functional groups [60]. Moreover, Igalavithana et al. found that the development of micropores by KOH activation significantly increased the CO_2 adsorption [107].

III. Amino-Modified Biochar: Ammonia modification or the introduction of basic functional groups such as *N*-containing functional groups onto biochar surface increases the affinity of biochar for adsorbing acidic CO_2 as a result of the increase in alkalinity. The classic surface amination technique involves a pre-oxidation process because the graphitic surface of biochar is not highly reactive toward ammonia. Pre-oxidized biochar is then exposed to ammonia (NH_3) at high temperature ($\sim 200^\circ C$) that promotes the generation of amides, lactams, and imides

functionalities through dehydration, decarboxylation, or decarbonylation reactions and enhance CO₂ adsorption capacity. The adsorption capacity further increases with the increase of activation temperature up to 800 °C. However, a slight reduction in CO₂ adsorption could be observed in biochar activated with 900 °C compared to that of 800 °C [71]. Although pre-oxidation and nitration by ammonia can effectively introduce amino groups onto the carbonaceous surface, it suffers from high consumption of energy. Alternatively, chemical modification using some amino-containing reagents such as diethanolamine (DEA), methyl diethanolamine (MDEA), and tetraethylenepentamine (TEPA) is also used for the surface amination of biochar. It has been proven that the -OH, C=O, and especially -COOH groups located on the surfaces of carbonaceous compounds can be chemically transformed into amino groups that facilitate CO₂ adsorption of aminated biochar.

1.4.8. Objective of the Present Work

The present study aimed to develop a novel acoustic based chemical activation technique to modify biochar for its application in CO₂ adsorption. At first the mechanism of sono-chemical modification was developed that employed low frequency ultrasound and amine (TEPA) functionalization. Following this, the effect of synergistic interaction of ultrasound with blended amination was determined. To achieve this five different amines such as (i) MEA, (ii) PZ, (iii) DEA, (iv) TEPA and (v) PEI and their binary and ternary mixtures: (1) MEA-TEPA, (2) DEA-TEPA, (3) DEA-PEI, (4) TEPA-PEI, and (5) DEA-TEPA-PEI were selected in presence of two different sets of activating agents I. EDC and HOBt and II. KOH. In addition to this, the present study also assessed the importance of biomass origin (primarily lignocellulosic compositions) on physico-chemical properties, activation conditions and CO₂ removal capacity of biochar. To accomplish this, biochars were synthesized from eight different biomasses which were obtained

from three different feedstocks: herbaceous (miscanthus, switchgrass), agro-industrial (corn stover and sugarcane bagasse), and crop based residues (sorghum, wheat straw, rice husk, and rice straw). The final step of the work focused to identify the interactions of pyrolysis temperatures on activation conditions that govern physicochemical properties and CO₂ removal ability of biochars. Therefore, biochars were synthesized under four different temperature ranges 500, 600, 700 and 800 °C from potential four biomass sources that exhibited highest carbon capture capacity as obtained from the last study. Furthermore, it is important to highlight that the ultrasonic-amine activation was conducted near ambient conditions (room temperature) under a short exposure of ultrasound making the process energy and time efficient. Therefore, the work identified the best possible set of parameters for functionalizing biochars as a CO₂ capture material.

CHAPTER II

Implications of Ultrasound Activation and Amine Functionalization for Enhanced CO₂ Adsorption

Riya Chatterjee, Baharak Sajjadi, Daniell L. Mattern, Wei-Yin Chen, Tetiana Zubatiuk, Danuta Leszczynska, Jerzy Leszczynski, Nosa O. Egiebor, Nathan Hammer, Ultrasound cavitation intensified amine functionalization: A feasible strategy for enhancing CO₂ capture capacity of biochar. *Fuel*, 2018. **225**: p. 287-298

2.1 Abstract

This study describes a two-stage biochar activation process for CO₂ capture, which includes acoustic treatment and amination. The rationale behind the study is the basic interaction mechanism between PAH and CO₂ through reductive photocarboxylation. Literature reveals that biochar contains carboxylic acids, epoxy and hydroxyl groups often serve as the active sites for amine grafting through functionalization. Thus these oxygen functionalities can be utilized for CO₂ adsorption when functionalized with amine. Hence, the present study focuses on maximizing the CO₂ capture capacity by manipulating the physicochemical structure of a pinewood-derived biochar. In this two-stage process, 30 s sonication at ambient temperature was applied to physically activate biochar prior to functionalization. Low-frequency ultrasound irradiation exfoliates and breaks apart the irregular graphitic layers of biochar, and creates new/opens the blocked micropores, thus enhancing the biochar's porosity and permeability that

are the keys in functionalization and subsequent CO₂ capture. The sono-modified biochar was then functionalized with tetraethylenepentamine (TEPA) in the presence of two activating agents. The changes in surface characteristics, functional groups, graphene-like structure, and functionalization using activating agents were examined in detail and the capacity of the final products in CO₂ removal was tested. The experimental results revealed that CO₂ capture capacity, from a flow containing 10 and 15 vol% CO₂, was almost 7 and 9 times higher, respectively, for ultrasound-treated amine-activated biochar, compared to raw biochar. The optimum capacity was 2.79 mmol/g at 70°C and 0.15 atm CO₂ partial pressure. Cyclic adsorption and desorption tests revealed that the CO₂ capture capacity decreased 44% after 15 cycles.

2.2 Introduction

The boon of rapid industrialization has elevated standards of living but at the expense of environmental deterioration. During the span of a century, there has been an unprecedented increase in the level of greenhouse gases such as CO₂, CH₄, N₂O, etc., among which CO₂ plays a critical role in climate change and global warming. Increased anthropogenic activities such as flue gas emission from fossil-fuel fired power plants and industrial facilities have resulted in elevated concentration of carbon dioxide in the atmosphere. Statistics reveal that CO₂ contributes more than 60% to global warming [21]. Thus it is of utmost importance to establish CCS technology.

Carbonaceous adsorbents are attractive for CO₂ sequestration. In recent years, biochar, which is derived from organic carbonaceous sources, has been gaining increasing attention as a carbon sequestration medium and potent soil amendment. Biochar is produced by pyrolysis that involves burning of (waste) biomass under oxygen-free conditions, which makes it less susceptible to degradation. It can also be derived as a byproduct during bio-oil production in

inert atmosphere at elevated temperature. Biochar has a highly porous structure with a high surface area, and since it is produced from easily available, natural biomass it is an eco-friendly adsorbent. The abundance of feedstock source for biochar makes it almost ten times cheaper than other CO₂ adsorbents. Biochar is a potential adsorbent of CO₂, but the adsorption capacity of raw biochar is not very high. Hence, to maximize the CO₂ capture capacity, surface modification is required. This can include both physical modification and chemical modification.

Biochar structure consists of graphite clusters that contain graphene oxide (GO) layers. The graphene oxide layers have reactive oxygen functional groups such as carboxyl, epoxy, and hydroxyl. However, these oxygen functionalities are accessible only for exfoliated biochar. Biochar is produced at elevated temperature, and its pristine graphitic oxide structure prevents any interaction, so that the graphene oxide layers remain inaccessible. But exfoliated biochar has oxygen functionalities available for further interaction. Interaction or activation with appropriate basic functional groups such as amine is desired due to the following reasons [108]. The carbon atom in CO₂ is electrophilic (electron deficient) because of the high electron negativity of the oxygen atoms. Amines are nucleophilic because of the presence of a lone pair of electrons and therefore can interact with CO₂. Thus, the amine-modified biochar has improved adsorption capacity compared to raw char. On the other hand, the graphitic cluster (basic structure of biochar) tends to agglomerate in the presence of water, blocking the pores that are active sites for CO₂ adsorption. This reduces the adsorption capacity by reducing the specific surface area. To overcome this problem, biochar needs to be mixed homogeneously into the water. Ultrasonic irradiation can prevent the formation of an agglomerated graphitic sheet by exfoliation of biochar.

Previous work [109] suggested that reductive photo-carboxylation of biochar's

polyaromatic hydrocarbons (PAH) edge carbons enhances its hydrogen content (up to 24%) and that in turn increases its energy content (up to 50%). The work also demonstrated that biochar was exfoliated into graphitic and graphene oxide clusters in the (CO₂+H₂O) system under ultrasound irradiation and this facilitated the reactivity of edge carbons of these platelets. The presence of CO₂ favors the ability of PAH to capture and convert CO₂ to carboxylic acid products, as demonstrated by Chateauneuf et al. [110]. Biochar with exfoliated basic graphene oxide clusters is expected to be more susceptible to chemical modification since more surface is available for modification. In other words, the improvement of biochar structure can be further boosted by irradiation under low-frequency ultrasound. Moreover, the cavitation effect of ultrasound makes a uniform biochar suspension, activates the binding sites, and leads to better grafting of functional groups. A similar trend was observed in work conducted by Park *et al.* [111] where ultrasound facilitated the preparation of a homogeneous colloidal suspension of polyanilineamine (PAA)-modified graphene oxide sheets. Previous work by our research group formed the basis of our current study and served as a motivation for economically modifying and functionalizing biochar with amine groups and utilizing it as a potent CO₂ adsorbent. To achieve this goal, the carbonaceous structure of biochar was improved both physically under ultrasound irradiation and chemically through amine functionalization. The effectiveness of physicochemical-activated (ultrasound treated-amine functionalized) biochar was determined by comparison with: I) raw biochar, and II) currently available commercial or modified CO₂ adsorbents.

2.3 Materials and Methods

2.3.1 Materials

Raw biochar was supplied by Biochar Now (Berthoud Colorado, U.S.A.). The feedstock

used for this biochar is pine (soft wood biomass). The biomass is pyrolyzed (heated in oxygen-deprived environment) at elevated temperature (between 550 and 600 °C) in a kiln reactor with a multi-zone combustion chamber. After pyrolysis, the biochar is exposed to nitrogen to stop the process. The raw biochar pieces are too large for practical use, so they are resized at crushing and screening sections. Biochar with a size range of 26 to 50 mesh was selected for our present work and was further ground and sieved before activation.

The reagents used in chemical functionalization were methanol, EDC (98% purity), HOBt (97% purity), and TEPA, which were obtained from Sigma Aldrich. The chemicals used in filtration were HCl (37%) from Sigma-Aldrich, DI water, NaOH from Fisher Scientific, and acetone from Sigma-Aldrich. All chemicals used were of analytical grade.

2.3.2 Experimental Method

2.3.2.1 Functionalization and Ultrasound Treatment of Biochar

Before modification, biochar was sieved using Tyler standard screens; a particle size of range 75-106 micron was selected. Physical modification of biochar was achieved under 20 kHz low power ultrasound irradiation (Sonicator model no. XL2010 with maximum power of 475 Watts) and high-power ultrasound irradiation (QSonica sonicator model no. Q700 with maximum power of 700 Watts). The specified amount of raw biochar was treated under different ultrasound irradiation durations (30 sec, 1, and 3 min). The ultrasonically-modified biochar was then subjected to chemical activation consisting of two steps. In the first step, the potential functional groups of biochar were activated with the activating agents EDC and HOBt in three different ratios (0.75:1, 1:1, and 1:0.75) in water. The mixture was stirred for 24 hours at 35°C, then filtered and dried under vacuum at 60°C overnight. In the second step, the dried sample was suspended in methanol and amine (TEPA) was added in an amount ranging from 2.5 times to 15 times the weight of the activated biochar. The mixture was stirred for 24 hours with gentle

heating as before. Then it was cooled to room temperature, filtered with repeated washing first with 1N NaOH, then with 1N HCl, and finally with acetone, dried as before, and stored in a desiccator.

2.3.3 Characterizations

The physico-chemically modified biochar was characterized using Raman (LabRam HR Evolution) and Fourier Transform Infrared (FTIR, Cary 660 FTIR Agilent) spectroscopies to determine the surface functional groups and chemical species. The elemental compositions of biochar samples were analyzed before and after physico-chemical modification (Huffman Hazen Laboratory, Colorado, USA). The effects of ultrasound activation on micro and macro surface area and porosity were investigated by surface analyzer (Quantachrome 2000E series). Surface morphology of both raw and activated biochar was examined using SEM (JSM-5600 Scanning Electron Microscope, JEOL USA Inc., Peabody, MS).

2.3.4 CO₂ Adsorption Study

Adsorption experiments were conducted in a tubular reactor made of alumina oxide (Al₂O₃) of 12 cm length and 1.5 cm inner diameter. The experimental set-up has been shown in Figures A1-A2 in Appendix A. The adsorption column, containing 2 g of the functionalized biochar, was placed into a temperature-controlled furnace. CO₂ was diluted with helium gas (99.99%) at a flowrate of 50° C m³ min⁻¹ at 378 K for 1 hour, and then cooled to 333 K. The helium flow was then switched to a CO₂-containing simulated flue gas of 10 vol% at a flow rate of 50° C m³ min⁻¹. The final concentration of CO₂ after adsorption was measured by a CO₂ analyzer (ZRH Infrared Gas Analyzer, CAI), connected on-line via the adsorption column outlet. The adsorption capacity of CO₂ after a certain time was then calculated using the following equation:

$$q_a = \frac{1}{M} \times \left[\int_0^t Q \times (C_0 - C) dt \right] \times \frac{1}{V_m} \quad (2.1)$$

where, q_a is the adsorption capacity for CO_2 , mmol g^{-1} ; M is the mass of adsorbent, g ; Q is the gas flow rate, $\text{cm}^3 \text{min}^{-1}$; C_0 and C are influent and effluent CO_2 concentrations, $\text{vol.}\%$; t denotes the time, min ; and V_m is $22.4 \text{ mL mmol}^{-1}$.

2.4 Results and Discussions

2.4.1 Physical Activation of Biochar

Effectiveness of sonication in this study was initially investigated by comparing SEM images of raw and sonicated biochar as shown in Figures 2.1 and 2.2, respectively.

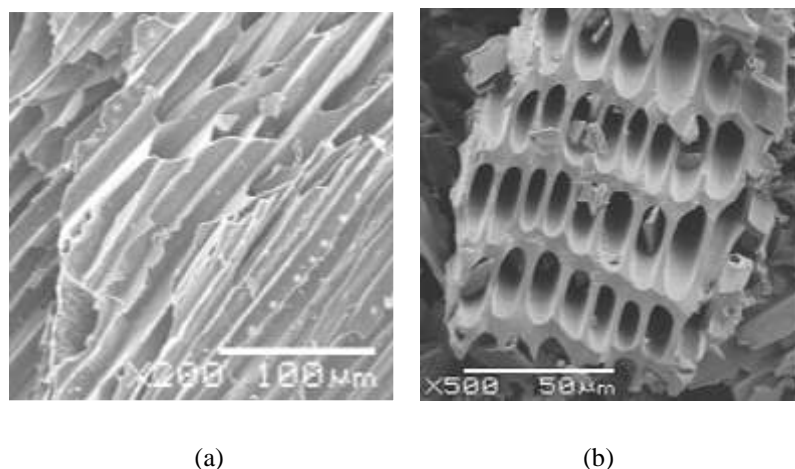


Figure 2.1. SEM images of raw biochar. a) Longitudinal view, b) Cross-sectional view

Cavitation under ultrasound consists of 3 steps: nucleation, growing of bubbles, and finally collapse of bubbles with high energy and pressure. High energy increases temperature, and high pressure produces microjets within the liquid. These phenomena in the biochar-water mixture lead to chemical excitation of the biochar during which the materials inside the porous structure of biochar leach out, creating empty pores [109]. The empty pores then act as active sites for either adsorption or chemical functionalization (with particular focus on amine groups in

this study). From both longitudinal view in Figure 2.1a and cross-sectional view in Figure 2.1b, it can be clearly seen the pores were blocked.

Therefore, the structure remained inaccessible for modification. In traditional activating processes, a secondary pyrolysis, or a thermal treatment with high temperature (very energy consuming) are usually used for surface and structural modification. In this study it has been shown that sonication can play a pivotal role to clear the blockage. It can be proposed that micro-jets formed during sonication impinged with and penetrated through the biochar surface, thus clearing the pores. The results related to the effect of ultrasound irradiation on biochar structure are shown in Figure 2.2a. The figure clearly portrays that the pores were exposed due to sonication. This helped in linking amine to the biochar in the subsequent functionalization step.

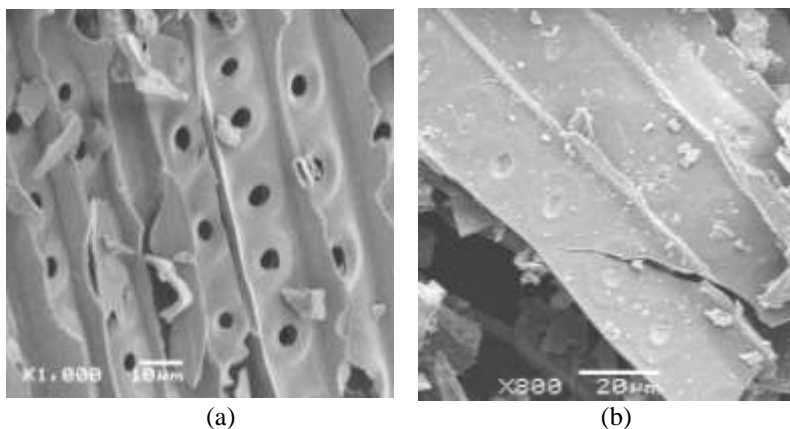


Figure 2.2. SEM image of a) physically activated biochar under ultrasound irradiation of 20kHz for 30Sec, b) physio-chemically activated biochar after both ultrasound irradiation and amine functionalization

Ultrasound also aided in enhancing surface area, as shown in Table 2.1. As summarized in the table, the surface area and porosity changed with sonication for both micropores (described by DR-CO₂) and macropores (described by BET-N₂). Raw biochar's microporous surface area of 312.31 m²/g increased to 354 m²/g after 30 sec of sonication. In contrast, the macroporous surface area reduced from 13.30 m²/g for raw biochar to 10.13 m²/g for 30 sec sonicated biochar. The micropore behavior can be explained as an effect of microjet formation

during cavitation. These micro-jets impinge on the surface and create more micropores, thus enhancing the microporous surface area. However, upon further increase of sonication duration to 1 min, the microporous surface area reduced to 268.82 m²/g. This demonstrated that cavitation negatively affected the biochar structure at longer durations.

Table 2.1. DR-CO₂ and BET-N₂ surface area of raw biochar, only ultrasound treated, and ultrasound treated -amine modified biochar

Sample Name	Micro-Porosity			Macro & Meso Porosity		
	Surface area (m ² /g)	Pore volume(cm ³ /g)	Pore Radius(nm)	Surface area(m ² /g)	Pore volume(cm ³ /g)	Pore radius(nm)
R	312.31	0.11	0.60	13.30	0.005	0.80
US0.5-EH0-T0	354.37	0.12	0.58	10.13	0.01	2.30
US1.0-EH0-T0	268.82	0.09	0.62	18.15	0.02	1.30
US0.5-EH1:1-T2.5	261.68	0.09	0.63	9.39	0.02	4.80

Note: R: Raw; US: Ultrasound; EH: EDC-HOBt; T: TEPA. Number beside US denotes sonication time in minutes; Number beside EH denotes ratio of activating agents; Number beside T denotes amine loading

As sonication time increased, cavitation intensity increased, and intensified cavitation disarranged the orientation of the layered structure of biochar, consequently blocking the pores and reducing adsorption capacity. Similar phenomena were observed by Verma et al. [112] and Hamdaoui et al. [113] where, in both cases, very high sonication times reduced the surface area, cumulatively reducing adsorption capacity. The high-pressure acoustic waves could further break the particles into smaller ones. These particles agglomerate and block pores, thus reducing the surface area. Particularly, low frequency ultrasound (20-100 kHz) induces particle size reduction, efficient mixing, and mass transport through cavitation [114].

Literature suggests that graphene oxide can be completely exfoliated under ultrasound irradiation, producing single-layer GO [115]. Since biochar has structural similarity with graphene oxide, it was expected to behave similarly under ultrasound irradiation, as discussed in the subsequent Raman analysis section (section 2.4.5). Novelty of the present work lies in using

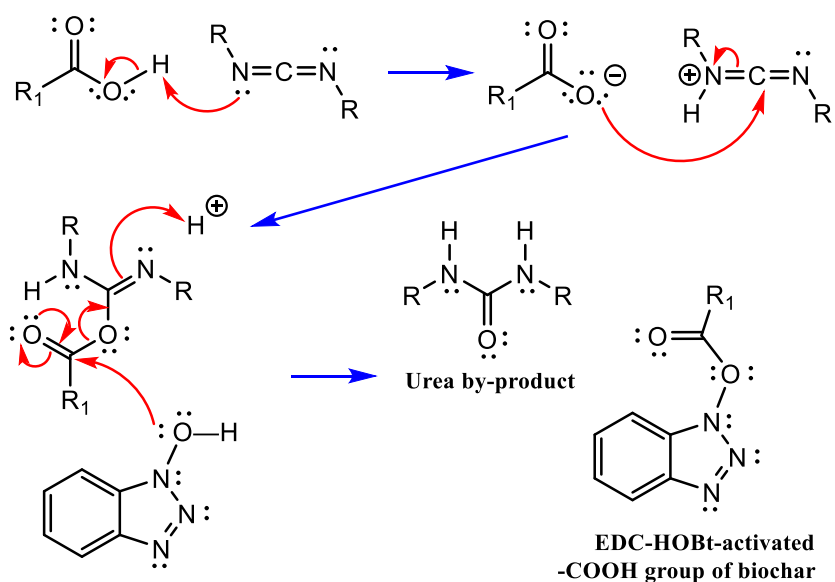
ultrasonic exfoliation to physically activate biochar. Other exfoliation techniques include the use of surfactants, strong acids, or other chemical reagents [116]. Using chemical agents for exfoliation increases the risk of toxicity and chemical hazard and leads to waste disposal problems; such treatment also consumes a high amount of energy if it is applied at elevated temperature. Therefore, sonication provides an easy, environmental friendly, economical and promising method of exfoliation.

2.4.2 Mechanism of Chemical Activation of Biochar

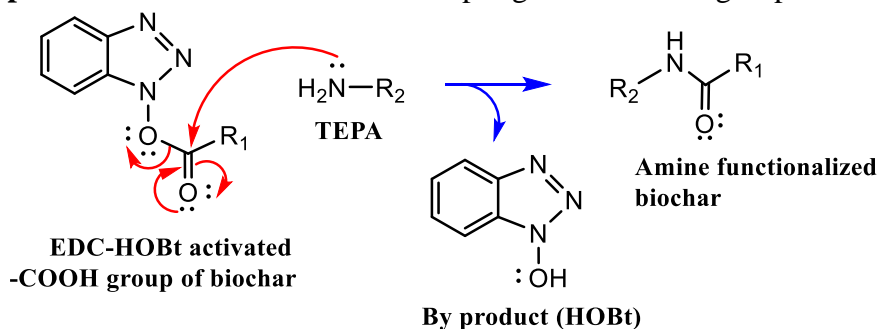
The treatment of biochar with amines leads to amination that result in elevated adsorption capacity. The amine functionalization can take place in two ways where amine can replace oxygen functionalities of biochar. The first mechanism is conversion of a -COOH (carboxyl) group, the most suitable group for amination located at edge carbon, to a -CONHR (amide) group, where R contains an amine group. First of all, the carboxyl group must be chemically activated in order to react with an amine. The second mechanism is attachment of amine by ring opening of an epoxide group. For last few decades, EDC-benzotriazole based coupling has provided efficient activation of carboxyl groups. The reagents and the EDC-benzotriazole by-products are water soluble. The basic chemistry of the amination reaction is depicted in Figure 2.3. In step 1 and step 2 of Figure 2.3 the reaction mechanism of the -COOH group with EDC-HOBT-TEPA is shown, and in step 3 the reaction of the epoxy group with amine is presented.

As shown in step 1, the coupling agent (EDC) activates the carboxylic acid group to form O-acylisourea as an intermediate. This intermediate could be displaced by nucleophilic attack from amino groups in the reaction mixture, producing amide and releasing iso-urea as a byproduct [117]. Another side reaction could be O-N migration of the activated carboxyl functional group forming an N-acyl urea [117]. Incorporation of appropriate additives prevents

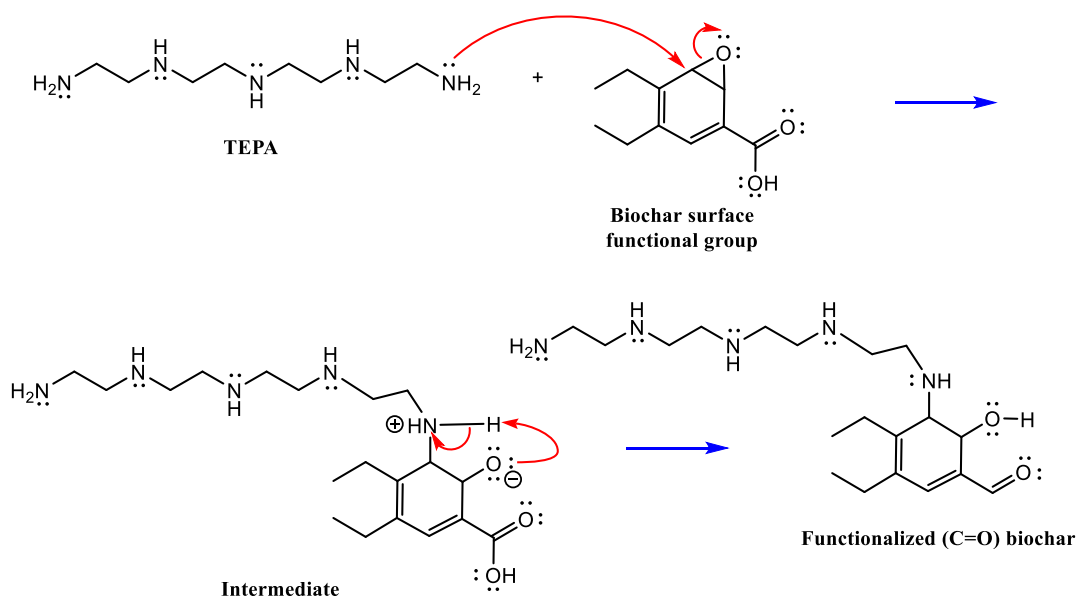
these side reactions and enhances the yield [117]. HOBt is a widely-used additive that prevents urea formation very effectively [118]. Besides, isolation of products from unreacted reagents can be done by simple filtration since urea is soluble in water [119]. Therefore, the chemical activation in this study incorporates HOBt as shown in Figure 2.3. In Step 2 the amination of the activated carboxyl group by TEPA is shown. The second mechanism involves interaction of epoxy group with TEPA (Figure 3, Step 3). However, in the presence of coupling agents, the former reaction is much faster than the latter one.



Step 1. Mechanism of EDC-HOBt coupling with -COOH group of biochar



Step 2. Mechanism of TEPA functionalization of activated carbonyl group of biochar



Step 3. Mechanism of TEPA functionalization of epoxy group of biochar

Figure 2.3. EDC-HOBt coupling reaction and subsequent amine functionalization of biochar

2.4.3 Effect of Physicochemical Activation on Elemental Composition of Biochar

The effects of chemical activating agents and ultrasonication on elemental compositions were shown by the organic elements C, N, O and S, and ash content (Table 2.2). Since the ash content varied widely the elemental composition of the organic material alone was also calculated, omitting the contribution of ash; this is shown in Table F1 of the Appendix F. Finally, it can be noted that the %C and %O of these samples varied in a way that suggested differing amounts of absorption of CO₂ by the samples. For now, the compositions, under the assumption that any oxygen in the final samples above the amount in raw biochar came from absorbed CO₂ has been also calculated which are displayed in Table F2 of the Appendix.

The activating reagents for amination, EDC and HOBt, were successful in promoting grafting of amine onto biochar whenever they were employed, as shown by the %N analyses (Table 2.2).

Table 2.2. Elemental Analysis of Raw and PhysicoChemical Activated Biochar (Dry Basis)

Entry	Sample Name	Ultrasound Power	EDC:HOBt: TEPA wt:wt:wt	C (% w/w)	H (% w/w)	N (% w/w)	O (% w/w)	S (% w/w)	Ash (% w/w)
1	Raw	-	-	65.36	1.97	0.18	11.22	0.05	23.95
2	US0-EH1:1-T2.5	-	1:1:2.5	62.21	2.31	0.93	15.24	0.02	18.86
3	US3-EH0-T0	Low	-	62.62	2.32	0.24	15.56	0.02	19.43
4	US0.5-EH1:1-T2.5	Low	1:1:2.5	69.61	2.61	1.63	11.36	0.02	13.93
5	US1-EH1:1-T2.5	Low	1:1:2.5	66.56	2.47	0.80	14.81	0.02	15.60
6	US3-EH1:1-T2.5	Low	1:1:2.5	66.68	2.32	0.83	15.43	0.02	15.30
7	US0.5-EH1:1-T2.5	High	1:1:2.5	65.11	2.54	0.51	20.08	0.02	13.63
8	US1-EH1:1-T2.5	High	1:1:2.5	64.95	2.40	0.63	19.56	0.02	14.63
9	US3-EH1:1-T2.5	High	1:1:2.5	57.75	2.32	0.64	22.81	0.01	20.10
10	US3-EH1:0.75-T10	Low	1:0.75:10	63.53	2.26	0.75	14.12	0.02	17.70
11	US3-EH1:1-T10	Low	1:1:10	63.18	2.45	0.75	17.95	0.01	16.83
12	US3-EH0.75:1-T10	Low	0.75:1:10	67.21	2.29	0.87	14.35	0.01	15.37
13	US3-EH1:1-T15	Low	1:1:15	67.71	2.27	1.01	14.26	0.02	14.60

The %N increased from 3 to 8 times its initial value in raw biochar. In contrast, and as expected, the use of ultrasound alone (entry 3) showed no significant increase in %N. The effectiveness of ultrasound in promoting chemical amination reactions gave inconsistent results, with no clear trends. For example, the use of 30 sec of low-energy ultrasound (entry 4) gave the highest %N incorporation, but similar treatment with high-energy ultrasound (entry 7) gave the lowest.

In entries 4-6 and 7-9, we compare the effects on amination of exposure duration (0.5, 1, or 3 min) to low-power and high-power ultrasound, respectively. There were no significant differences in %N seen within these series, although the average incorporation of nitrogen seems somewhat higher under low-power ultrasound (1.09%) than high-power (0.59%).

The effect of using one of the two activating reagents in excess was also examined (entries 10-12); there was no significant change in the amount of nitrogen grafted into the biochar structure whether the ratio of activating agents, EDC: HOBt, was 1:0.75, 1:1, or 0.75:1.

The effect of increasing the loading of the amine TEPA from a relative mass of 2.5 (entry 6) to 10 (entry 11) to 15 (entry 13) was investigated, all under 3 min of low-power ultrasound. As expected, the %N incorporation increased as the loading increased, consistent with the literature [120].

All treatments lowered the amount of sulfur in the biochar, from 0.05% to $\leq 0.02\%$. Ultrasound and amination had similar effects, and there was no apparent advantage to using both. This suggests that ultrasound could help lead to the production of sulfur-free, cleaner fuel. Finally, the residual ash in the treated biochars was also examined, which varied widely. Three min of low-power ultrasound lowered the ash content from 23.95% (entry 1) to 19.43% (entry 3). The turbulence created by ultrasound enhances mass transfer and promotes the efficient leaching of minerals such as Ca, Mg and P [121]. However, the chemical amination procedure alone lowered the % ash even further, to 18.86% (entry 2). All but one of the combination treatments were more effective in lowering ash than ultrasound or chemical activation alone. There were no obvious trends, but there was a suggestion, contrary to expectations, that shorter ultrasound durations (e.g., entry 7) were more effective than longer ones (entry 9). This will be an area of further study.

Reduction of ash content is important in increasing the heating value of biochar, but these amination experiments are directed towards CO₂ capture; amination would not be a cost-effective way to add fuel to biochar. It can also be noted that as the %N increases due to the incorporation of TEPA, the %C of samples will decrease and the %H will increase, in the direction of the composition of TEPA. These consequences are seen most clearly in Table F2, and do not indicate a change in the underlying structure of the biochar. Table F2 also shows no significant change in the %C of biochar due to sonication alone (entry 3).

2.4.4 Effect of Physiochemical Activation on Functional Groups of Biochar

The results of FTIR spectroscopy of raw and functionalized biochar with ultrasonic and chemical activation (US3-EH1:1-T10) and with ultrasonic activation alone (US3-EH0-T0), are depicted in Figure 2.4. FTIR helps in identifying major functional groups that take part in activation. The overall FT-IR spectrum shape is similar for all the biochar samples. The IR spectrum of R was consistent with the presence of -COOH/-OH and C=O groups at 3400 and 1600 cm^{-1} respectively. A new peak in US3-EH1:1-T10 at 1100 cm^{-1} could be attributed to the vibration absorption of C-N of the incorporated amines. A strong peak around 3400 cm^{-1} was seen for OH stretching in US3-EH0-T0; amine N-H stretch around 3400 cm^{-1} was not distinguishable from O-H stretch.

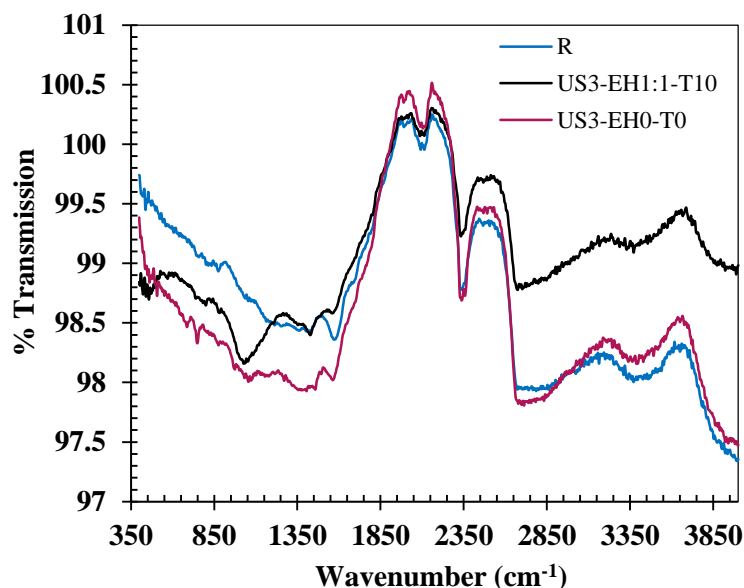


Figure 2.4. IR spectrum of R, US3-EH1:1-T10, and US3-EH0-T0

Note:R-Raw; R: Raw; US: Ultrasound; EH: EDC-HOBt; T: TEPA; Number beside US denotes sonication time in minutes; Number beside EH denotes ratio of activating agents; Number beside denotes amine loading

The IR spectra of raw, US3-EH1:1-T2.5, US3-EH1:1-T5, US3-EH1:1-T10 and US3-EH0-T0 are shown in Figure 2.5. The peak around 1100 cm^{-1} which could be attributed to the

vibration of C-N becomes more intense as the amine loading is increased from 2.5 to 10. A peak at 1423 cm^{-1} is not found for either R or US3-EH0-T0, but appeared in all amine activated samples; it is attributed to CH_2 bending vibrations introduced by the TEPA structure [122]. The efficacy of amine as a functionalizing agent was further demonstrated from the SEM image shown in Figure 2.2b. The reaction with amine was facilitated due to the presence of pores. The SEM image portrayed that the porous structure as well as the surface were covered with amine.

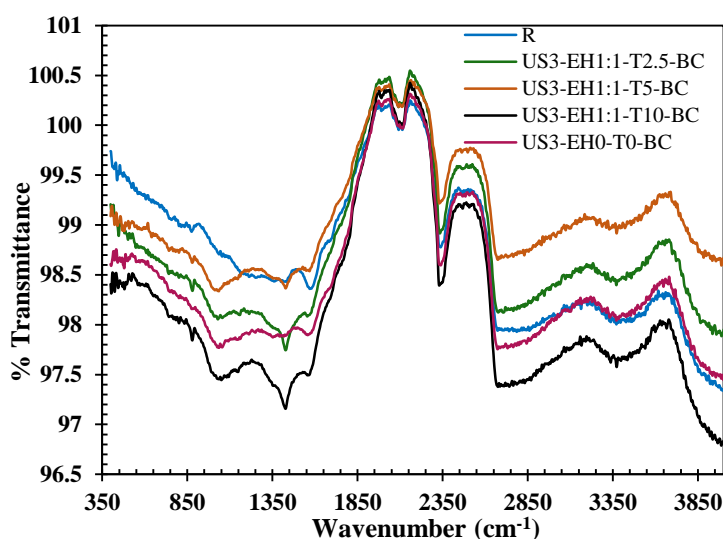


Figure 2.5. IR spectrum of R, US3-EH1:1-T2.5, US3-EH1:1-T5, US3-EH1:1-T10, and US3-EH0-T0

2.4.5 Effect of Physiochemical Activation on Graphitic Structure of Biochar

Raman spectroscopy provides useful information for characterizing carbonaceous compounds including graphitic oxide. Biochar has structural similarity with graphene oxide. So, Raman spectroscopic analysis is a useful tool for describing important characteristics of raw and modified biochar samples under different conditions. The Raman spectra for raw biochar (R) and biochar activated with different activating agent ratios (US3-EH1:1-T10, US3-EH1:0.75-T10, US3-EH0.75:1-T10) are shown in Figure 2.6. Sonication duration and amine concentration for all the samples were the same; they differed in the ratios of chemical activators. For the Raman spectrum of R (raw biochar), a strong peak is observed in the range $2500\text{-}2800\text{ cm}^{-1}$. This

confirms the structural similarity of biochar and graphene oxide, since this peak is a signature peak of graphitic sp^2 structure [123]. The characteristic D band is observed at 1394 cm^{-1} , 1356 cm^{-1} , 1366 cm^{-1} , 1382 cm^{-1} for R, US3-EH1:1-T10, US3-EH0.75:1-T10 and US3-EH1:0.75-T10, respectively.

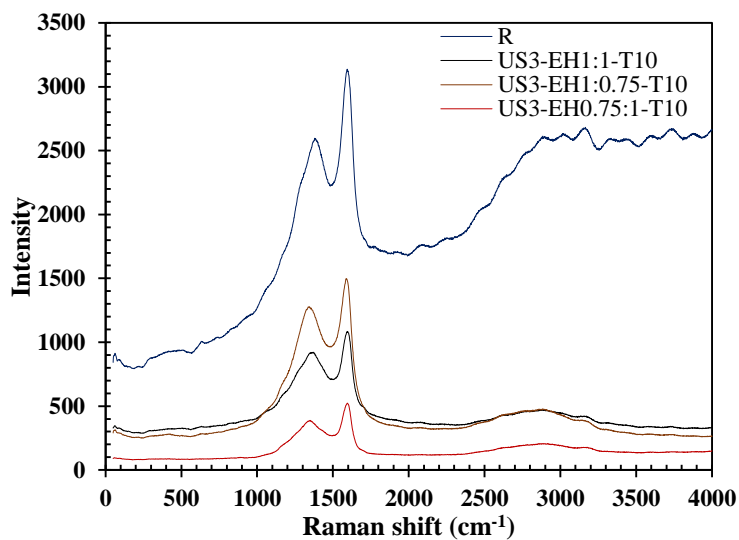


Figure 2.6. Raman spectra of R, US3-EH1:1-T10, US3-EH1:0.75-T10, and US3-EH0.75:1-T10

The broader D band of raw biochar also signifies the presence of oxygen functional groups that lead to reduced size of the sp^2 domain of biochar by creating defects and distortions [123]. The characteristic G band, due to C-C bond stretch, is located at 1606 cm^{-1} , 1599 cm^{-1} , 1625 cm^{-1} and 1605 cm^{-1} for R, US3-EH1:1-T10, US3-EH0.75:1-T10 and US3-EH1:0.75-T10 respectively. Disorder of the sp^2 crystal structure can be determined from the intensity ratio between the D and G bands (I_D/I_G) [124]. The I_D/I_G ratio for raw biochar was 0.82; this value increased to 0.87 and 0.85 for 1:1 and 1:0.75 respectively, and reduced to 0.75 for 0.75:1. The D peak was higher than G peak in all the spectra which indicates transition from sp^2 to sp^3 material [123]. The I_D/I_G ratio was higher for activated samples than for R, which signifies that the activated samples have more defects on carbon, presumably in the form of oxygen functionality

[123]. The maximum departure of the I_D/I_G ratio was found for the 1:1 ratio, suggesting the maximum defects resulting from aminations.

Next in Figure 2.7 the Raman spectra for R, US3-EH1:1-T2.5, US3-EH1:1-T5, US3-EH1:1-T10, and US3-EH0-T0 are represented. The D band appeared at 1367 cm^{-1} , 1417 cm^{-1} , 1365 cm^{-1} and 1371 cm^{-1} for US3-EH1:1-T2.5, US3-EH1:1-T5, US3-EH1:1-T10, and US3-EH0-T0, respectively.

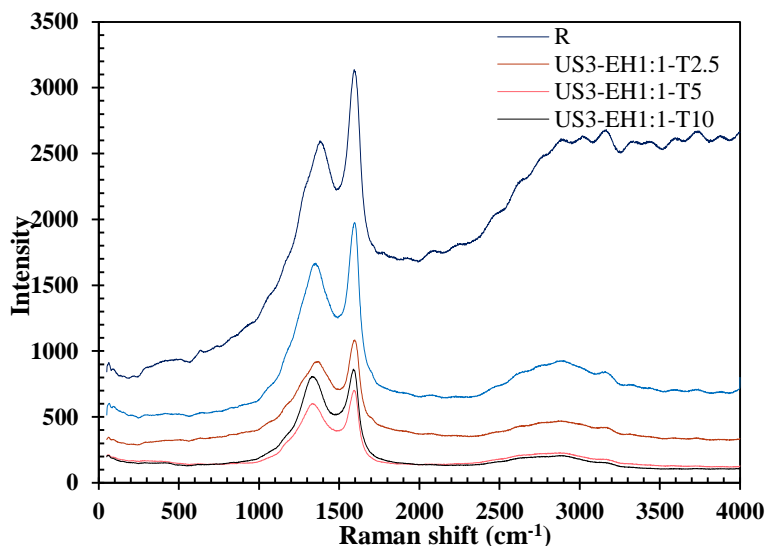


Figure 2.7. Raman spectra of R, US3-EH1:1-T2.5, US3-EH1:1-T5, US3-EH1:1-T10, and US3-EH0 T0

The G peak appeared at 1651 cm^{-1} , 1614 cm^{-1} , 1577 cm^{-1} , and 1602 cm^{-1} . As was discussed earlier, the D peak is associated with nanocrystalline carbon while the G peak corresponds to amorphous carbon materials. The I_D/I_G ratios for US3-EH1:1-T2.5, US3-EH1:1-T5, US3-EH1:1-T10, and US3-EH0-T0 were 0.85, 0.86, 0.87 and 0.83, respectively. This illustrates that more distortion was introduced into biochar surface upon more extensive activation, since the I_D/I_G ratio increased.

Further, the Raman spectra of samples sonicated for different times are shown in Figure 2.8. For US0.5-EH1:1-T2.5, US1-EH1:1-T2.5 and US3-EH1:1-T2.5, the D peak was observed at

1382 cm^{-1} , 1355 cm^{-1} and 1374 cm^{-1} ; and the G peak appeared at 1606 cm^{-1} , 1608 cm^{-1} and 1611 cm^{-1} , respectively.

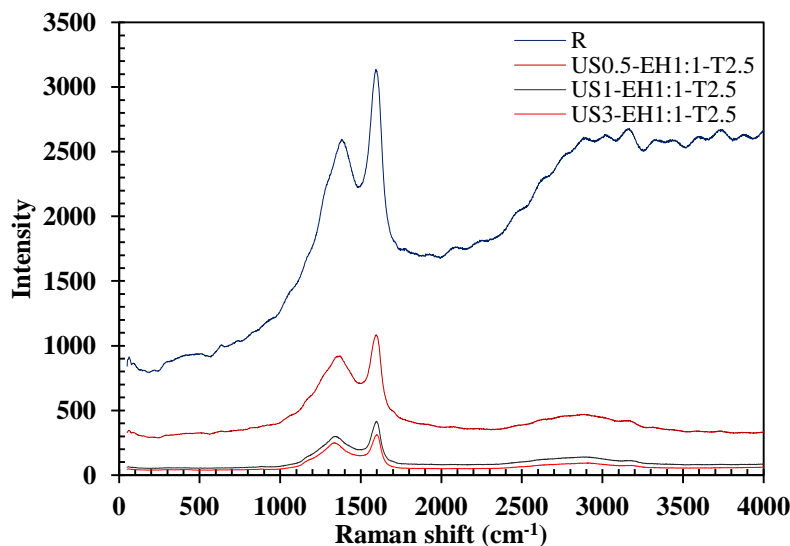


Figure 2.8. Raman spectra of R, US0.5-EH1:1-T2.5, US1-EH1:1-T2.5, and US3-EH1:1-T2.5. The I_D/I_G ratios were 0.85, 0.76 and 0.85. This is further evidence that the sonication time

Table 2.3. Summary of intensity ratio for raw biochar and ultrasonicated amine functionalized biochar samples

Sample Name	Intensity Ratio Value
R	0.82
US3-EH1:1-T10	0.87
US3-EH0.75:1-T10	0.75
US3-EH1:0.75-T10	0.85
US3-EH1:1-T2.5	0.85
US3-EH1:1-T5	0.86
US3-EH0-T0	0.83
US0.5-EH1:1-T2.5	0.85
US1-EH1:1-T2.5	0.76

The I_D/I_G ratios were 0.85, 0.76 and 0.85. This is further evidence that the sonication time of 30 sec provided the optimum value of adsorption capacity, since it had the maximum intensity ratio. The values of intensity ratios for all the biochar samples have been summarized in Table 2.3.

2.4.6 CO₂ Capture Study of Physicochemical Activated Biochar

The adsorption capacities of ultrasound treated-amine functionalized biochar synthesized under different conditions are summarized in Table 2.4. Firstly, the effect of activating agents was investigated. Experiments were carried out with three different ratios of EDC:HOBt, namely 1:1, 1:0.75 and 0.75:1. The biochar samples activated with 1:1 EDC:HOBt exhibited the highest CO₂ capture capacity. Therefore, this ratio was chosen for all subsequent experiments. Confirmation was also obtained from Raman spectra (Figure 2.6), showing the highest I_D/I_G ratio for 1:1 EDC:HOBt, attributed to the greatest conversion of acid functionalities to amide. The requirement for a 1:1 ratio is consistent with the mechanism described in Figure 2.3. EDC attaches to the -COOH group in the first step and then HOBt replaces EDC completely to activate the carboxyl group. So, an equal amount of HOBt is required to substitute EDC completely. The second factor which contributed to improving adsorption capacity was amine loading. The amine loading was varied from 2.5 to 15 times the weight of biochar, keeping the activating agents at their optimum ratio. The adsorption capacity of the biochar steadily increased with amine loading up to 10 times weight, and then reduced at 15. Therefore, an amine loading at 10 times the biochar weight was considered as the optimum loading capacity.

Additionally, elemental analysis pointed out enhancement in nitrogen content with increasing amine loading. The effect of amine loading can be substantiated from the surface area analysis results. Both DR-CO₂ and BET-N₂ analysis results indicate reductions in surface area due to amine attachment (Table 1.1). The reasoning behind this trend is that the number of oxygen functional groups on the biochar surface are fixed. Therefore, addition of excess amine would not assure its complete reaction with oxygen functionalities. Rather, excess amine would decrease CO₂ capture because of inaccessible surface area, formed by blocking pores to prevent intercalation of more amines. A similar trend was observed by Zhao et al. [120]. They treated

their graphene oxide sample with 10%, 50% and 100% amine loading. Adsorption capacity increased from 10% to 50% loading. But further increase negatively affected the adsorption capacity. In this study, the nitrogen content increases with amine loading, as seen from the elemental analysis.

From Table 2.4, it can be observed that the adsorption capacity increases gradually as the activating agent ratio and amine loading are optimized. But additional improvement was observed when the duration of sonication was optimized. In fact, ultrasound irradiation had a predominant effect in improving CO₂ capture capacity. Biochar-water mixtures were exposed to ultrasound irradiation times of 30 s, 1 min and 3 min. From no ultrasonication time to 30 s the adsorption capacity enhanced, but longer sonication times reduced the capture capacity. Similar results obtained with either low-energy or high-energy ultrasound. As sonication time progresses, the temperature of the biochar-water mixture increases. Consequently, the surface tension of the medium decreases and vapor pressure inside the microbubbles increases; this in turn reduces shock waves [121]. This foils the formation and collapse of microbubbles and reduces sonication efficiency. Thus, the adsorption capacity reduced. The results are also consistent with the surface area analysis where micropore surface area reduced as sonication time increased. For 60 s of sonication, the micropore surface area reduced from 354 m²/g to 268.8 m²/g. However, 30 s of sonication significantly increased the adsorption capacity of the modified biochar compared with samples functionalized without ultrasound. This can be explained based on the mass transport phenomena mentioned earlier. The mass transport inside the pores was expedited by ultrasound due to increased turbulence caused by sonication. Advantages of sonication as a physical activation technique include its use at ambient temperature and its very short time requirement.

Table 2.4. Effect of Process Parameters on CO₂ Adsorption Capacity

Sample Name	Adsorption capacity (mmol/g)	Temp. (°C)	CO ₂ Conc. (vol %)
Raw Biochar			
R	0.3	70	10
Effect of Activating agents			
Low energy ultrasound			
US3-EH1:0.75-T10	0.61	70	10
US3-EH1:1-T10	0.67	70	10
US3-EH0.75:1-T10	0.59	70	10
Effect of Amine Concentration			
US3-EH0-T0	0.55	70	10
US3-EH1:1-T2.5	0.69	70	10
US3-EH1:1-T5	0.72	70	10
US3-EH1:1-T10	0.75	70	10
US3-EH1:1-T15	0.70	70	10
Effect of ultrasound			
Low energy ultrasound			
US0-EH1:1-T2.5	0.56	70	10
US0.5-EH1:1-T2.5	1.69	70	10
US1-EH1:1-T2.5	0.78	70	10
US3-EH1:1-T2.5	0.69	70	10
High energy ultrasound			
US0-EH1:1-T2.5	0.55	70	10
US0.5-EH1:1-T2.5	2.04	70	10
US1-EH1:1-T2.5	1.73	70	10
US3-EH1:1-T2.5	1.58	70	10
Effect of Temperature			
High energy ultrasound			
US0.5-EH1:1-T2.5-25°	1.32	25	10
US0.5-EH1:1-T2.5-50°	1.48	50	10
US0.5-EH 1:1-T2.5-70°	2.04	70	10
US0.5-EH 1:1-T2.5-90°	1.10	90	10
Effect of CO₂ concentration (vol.%)			
US0.5-EH 1:1-T2.5-70°-C10	2.04	70	10
US0.5-EH1:1-T2.5-70°-C13	2.31	70	13
US0.5-EH 1:1-T2.5-70°-C15	2.79	70	15

Note: C-inlet CO₂ concentration; Number beside C denotes inlet CO₂ concentration in vol.%

2.4.7 Effect of Temperature

Adsorption experiments were carried out at different temperatures ranging from 25 °C to 90 °C (Table 2.4). The results indicated a gradual increase in adsorption capacity with temperature up to 70 °C, while a higher temperature negatively affected CO₂ adsorption. At the optimum temperature, 70 °C, the adsorptive capacity was 63% higher than at room temperature (25 °C). Following amine activation, the main adsorption process is expected to be

chemisorption. Chemisorption involves higher activation energy than physisorption. Hence, the initial increase of adsorption capacity with temperature is due to the higher activation energy requirement of chemisorption. But later it reduced due to exothermic nature of adsorption [125]. A similar phenomenon was observed by Heydari-Gorji et al. [125] where CO₂ uptake was favored at a higher temperature (75 °C) than at a lower temperature (25 °C) for polyethyleneimine (PEI) supported on mesoporous silica. Similarly, a study by Jadhav et al. [126] demonstrated that CO₂ adsorption by monoethanolamine (MEA) modified Zeolite 13X was favored at a higher temperature (120 °C) than at a lower temperature (30 °C). They explained this behavior using diffusion theory and demonstrated the dispersion state of amine within the porous system of their adsorbent mesoporous silica.

2.4.8 Effect of CO₂ Concentration

Inlet CO₂ concentration is a driving force for improving CO₂ capture capacity. To determine the effect of inlet CO₂ concentration on adsorption capacity, experiments were carried out with different concentrations of CO₂. Usually, flue gas from power plants contains 10-15 vol% of CO₂. Accordingly, and in order to determine the effect of CO₂ concentration on the adsorption capacity of the modified biochar, 10, 13 and 15 vol% of inlet CO₂ concentrations were selected in this study [127, 128]. The adsorption capacity increased with the CO₂ concentration in inlet flow (Table 2.4). The optimum capacity was achieved for 15% inlet CO₂ with the value of 2.79 mmol/g. The diffusion theory can explain this well. When inlet concentration increases, the diffusion velocity of adsorbate increases through the pores of the adsorbent, thus enhancing the resulting adsorption capacity. A similar trend was observed by Shiue et al. [129], where increasing CO₂ concentrations from 800 to 1200 ppm led to increases in CO₂ adsorption capacity from 2.1 to 2.77 mmol/g.

Table 2.5. Comparison of Present Adsorption Capacity with Literature

Adsorbent	Capacity (mmol/g)	Activating Agent	Activation Condition	Adsorption T (°C)	CO ₂ %	Ref.
Hickory wood Biochar	1.67	-	-	25	100	[3]
Perilla Biochar	2.31	-	-	50	40	[109]
Saw dust biochar	1.02	MEA	Room Temp	30	100	[108]
Pig manure Biochar	0.78	-	-	25	100	[130]
Rubber wood Biochar	0.40	-	-	25	100	[131]
PEI on mesoporous carbon	4.82	KOH	700°C,0.1MPa	75	15	[24]
Aminated graphene oxide	1.10	EDA, DETA,TETA	80 °C	30	100	[120]
Fly carbon	1.56	DETA, PEHA, PEI	60°C,300 mbar	30	100	[132]
KOH modified activated carbon	4.54	KOH	800 °C	25	100	[133]
Commercial carbon molecular sieve	4.06	Acetylene	600-900 °C	25	30	[134]
Pine Wood Biochar(raw)	0.30	-	-	70	10	This study
Pine Wood Biochar ¹	1.69	TEPA	Room Temp	70	10	This study
Pine Wood Biochar ²	2.04	TEPA	Room Temp	70	10	This study
Pine Wood Biochar ²	2.79	TEPA	Room Temp	70	15	This study

Note: ¹Low energy ultrasound system, ²High energy ultrasound system

According to the literature, for the biochar samples that have high microporous surface are, the micropores serve the active sites for adsorption where physisorption occurs [25, 135, 136]. This physisorption is a weak interaction arising from intermolecular forces (e.g. Van der Waals forces). D'Alessandro et al. [137] in their study also highlighted that the adsorbent materials with high surface area and microporosity primarily exhibit physical adsorption mechanism. Because of the physical adsorption mechanism, surface area is a significant determinant of CO₂ adsorption; nevertheless, the presence of nitrogenous groups also played a role, when the surface area is sufficient [25]. The similar result is obtained in the present study where the high surface area microporous biochar impregnated with amine functionality promotes physisorption of CO₂. Another confirmatory result about physisorption can be obtained from regeneration study. The present work used 180 °C as regeneration temperature to desorb the adsorbate from the adsorbent. This relatively low desorption temperature further proves the mechanism of physisorption where the CO₂ was desorbed from the biochar when the sample was

heated at 180 °C [25, 136].

Additionally, the values of adsorption capacity of raw biochar and both low-energy and high- energy ultrasound-irradiated amine-functionalized biochars obtained in the present study are compared with commonly available adsorbents found in the literature in Table 2.5. As observed that the adsorption capacity of the modified biochar in our present study is within a very good range, considering that, for most of the sorbents, the maximum capacity was reached with pure CO₂ gas, whereas we used a CO₂-He gas-mixture with only 10% to 15% CO₂. Also, the activation for the present study takes place at room temperature with only 30 secs of ultrasonic exposure. On the contrary, many of the traditional activation techniques require very high temperature, usually above 700 °C. Therefore, this study proved to be an effective technique of functionalizing biochar, utilizing a minimum energy from ultrasonic irradiation and a moderate quantity of amine, and still providing a high adsorption capacity — higher than any other biochar in Table 2.5. To improve the adsorption capacity further, the present work will be extended using different amine and dual amine techniques to attain maximum adsorption capacity.

2.4.9 Cyclic Adsorption-Regeneration of Adsorbent

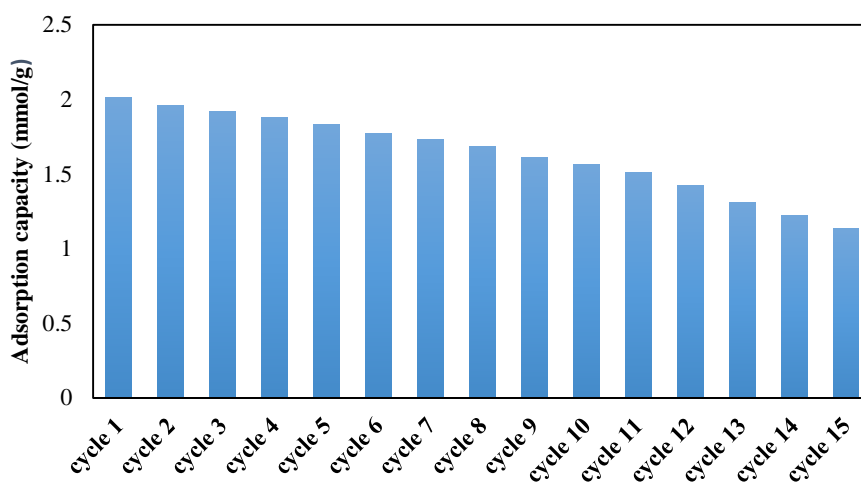


Figure 2.9 Cyclic Adsorption-Desorption Behavior of Sonicated-TEPA-Modified Biochar

Regeneration of adsorbent is necessary from an economic point of view and for long term use. A regeneration experiment was conducted by heating the adsorbent (US0.5-EH1:1-T2.5) at the elevated temperature of 180 °C under He gas flow for 60 minutes. The adsorbent after regeneration was reused in the CO₂ adsorption experiment. After 15 cycles of adsorption-regeneration, the adsorptive capacity was reduced by 44% as shown in Figure 2.9.

The regeneration processes are usually applied at very high temperatures, ranging from 200 to 500°C [138, 139]. However, in the present study 180°C was used to make the process less energy intensive and more economic. Higher temperature ascertains the better desorption rate but at the expense of high energy. Moreover, desorption behavior of the prepared adsorbent can be further enhanced by employing a suitable catalyst that improves the regeneration ability at a low desorption temperature which are the focuses of our coming works.

2.5 Selectivity

An ideal CO₂ adsorbent should exhibit high selectivity toward CO₂ over N₂ and other exhaust components (CO, NH₃, and light hydrocarbons, such as CH₄) [135]. The CO₂ adsorption capacity is strongly influenced by the adsorbent structural features and the operating conditions and that various mechanisms may be involved [135]. In carbon-based adsorbents, the main parameters governing both the CO₂ uptake capacity and selectivity at low partial pressures and ambient temperature are the microporosity (volume and size) and functionalization of the pores [140, 141]. At low pressure, the adsorption is favored in narrow micropores and the mechanism is based on short-range nonspecific interactions between the gas and adsorbent. At higher pressures, the surface coverage is the predominant mechanism and, therefore, wider micropores become more relevant. According to the literature uptake of N₂ and CH₄ is much lower than that of CO₂, indicating that the biochars are good materials for the separation of these gases [135].

It is well-known that carbon adsorbents display a much lower affinity for nitrogen than carbon dioxide; in the case of methane, the lower uptake is attributed to the pore structure of the biochars, because methane is slightly bulkier than CO₂ [135]. Therefore, biochars with maximum microporosity are suitable for CO₂ storage and separation. In order to explain the selectivity of biochars in presence of different oxides of sulphur and nitrogen, Beckman and co-workers studied the adsorption of weak acidic gases such as CO₂, SO₂, NO₂ and NO [142, 143]. They found that the thermal reversibility of the capture process decreased in the order CO₂ > SO_x > NO_x. The adsorbent simultaneously adsorbed CO₂ and NO_x where the amount of CO₂ adsorbed was significantly higher than that of NO_x. Therefore, the microporous biochar possess higher selectivity towards CO₂ than any other components of flue gas.

2.6 Conclusions

The current study aimed at introducing a fast, economically feasible and efficient physico-chemical method for the modification of biochar. In this process, biochar was first treated under ultrasonic irradiation with an optimum exposure time of only 30 secs, followed by chemical amination at room temperature. From the characterization of activated biochar, it became clear that ultrasound exfoliated the graphene clusters of biochar, cleaned and opened blocked micropores, and increased its surface area. All these factors intensified the chemical functionalization of biochar with TEPA. The ultrasound-treated, amine-modified biochar was then used for adsorption of CO₂. The interaction between the nucleophilic active sites on the modified biochar surface and the electrophilic CO₂ molecules facilitated adsorption through the formation of covalent bonding. The present study revealed that the combination of a physical activation method with chemical amine modification can lead to a very high adsorption capacity. Raw biochar had a very limited adsorption capacity of 0.3 mmol/g, but its capacity increased to 2.79 mmol/g (at

70 °C with 0.15 atm partial CO₂ pressure and 15 vol% inlet CO₂) after both physical modification with low frequency ultrasound and chemical activation with amine (TEPA). The adsorption capacity of physico-chemical activated biochar was over 9 times that of raw biochar. In addition, the adsorbent was undergone in a cyclic adsorption-regeneration experiment, which revealed that the adsorption capacity after 15 cycles retained 56% of the initial adsorption capacity. Aside from the promising results obtained in terms of CO₂ adsorption, the developed ultrasonic treatment process was very efficient in terms of energy and time. Biochar was exposed to ultrasound irradiation for only 30 secs at room temperature. Moreover, amine functionalization of ultrasono-treated biochar was accomplished with little warming at 35°C. Hence, the technique applied for modifying biochar proved very efficient, and the produced biochar is a potential sorbent for CO₂ adsorption.

Author Contributions

Riya Chatterjee: Conducting the experiments, interpreting the results and writing the manuscript

Baharak Sajjadi: Idea of the work, interpreting the results and writing the manuscript

Wei-Yin Chen: Idea of the work and revise the manuscript

Daniell L Mattern: Interpreting the results and revise the manuscript

Tetiana Zubatiuk: Revising the manuscript

Danuta Leszczynska: Revising the manuscript

Jerzy Leszczynski: Revising the manuscript

Nosa O. Egiebor: Revising the manuscript

Nathan Hammer: Conducting Raman Analysis

CHAPTER III

Ultrasound Promoted Dual Amination of Biochar for Preparing Efficient CO₂ Adsorbent

Riya Chatterjee, Baharak Sajjadi, Wei-Yin Chen, Daniell L. Mattern, Nosa O. Egiebor, Nathan Hammer, Vijayasankar Raman. Low Frequency Ultrasound Enhanced Dual Amination of Biochar: A Nitrogen-Enriched Sorbent for CO₂ Capture. *Energy & fuels*, 2019. **33**(3): p. 2366-2380.

3.1 Abstract

The present study discusses a novel biochar activation technique consisting of physical modification using low frequency ultrasound and chemical functionalization with five different amines and their blended mixtures in presence of two activating agents. Acoustic treatment under ultrasonic irradiation exfoliates the biochar's graphitic clusters, create new micropores, open the blocked pores and enhance the functionalization efficiency. In a subsequent chemical modification step, functionalization with amine moieties further boosted the adsorption capacity. The present study of sonochemical activation of biochar also investigates the effect of 5 different amines: (i) MEA (1°), (ii) PZ (2°), (iii) DEA (2°), (iv) TEPA (1° and 2°), and (v) PEI (1°, 2° and 3°), and several binary and ternary mixtures: (1) MEA-TEPA, (2) DEA-TEPA, (3) DEA-PEI, (4) TEPA-PEI, and (5) DEA-TEPA-PEI with the activating agents EDC - HOBt or KOH. The results revealed that ultrasonically treating biochar samples for 30 s, followed by chemical activation with either EDC-HOBt-TEPA-MEA or KOH-MEA, gave materials possessing

intensified adsorption capacities at 0.10 atm CO₂ partial pressure and 70°C of 1.91 and 1.62 mmol/g, respectively, compared to raw biochar (0.3 mmol/g).

3.2 Introduction

Amination of carbonaceous materials has received significant attention because of the following applications- enhanced adsorption of pollutants (such as Ni, Cd, methylene blue, and ibuprofen), manufacturing of carbon quantum dots [144], site specific drug delivery [145] etc. and specifically for CO₂ capture. Amines (used as sorbents in the amination technique) as a nucleophile have strong affinity for CO₂ (electrophilic) and can interact through nucleophilic addition [146]. Aqueous amine scrubbing has proven to increase the CO₂ absorption rate [21]. However, the regeneration process is energy intensive because of the high specific heat of aqueous amines [21]. To overcome this drawback, CO₂ adsorption with solid sorbents is emerging as an efficient and economic technique because of the low heat capacity, high thermal stability and no corrosion problems of solids [147]. Moreover, the sorbents have tunable pore size and surface area and synthesized from readily available feedstock. Additionally, presence of effective oxygen functional groups facilitates the attachment of nitrogenous compounds (such as amines) to further improve the sorption capacity.

Apart from achieving optimized adsorption capacity, regeneration of the adsorbent is equally important from an economic point of view and for its long term use. The commonly available regeneration techniques are PSA, VSA, TSA and ESA [148]. In PSA, the pressure is reduced for the desorption since adsorption is done at high pressure, whereas in TSA, the temperature is raised to desorb the adsorbate gas since adsorption is an exothermic process, while desorption is endothermic [149]. VSA is the technique where vacuum or below atmospheric pressure is applied for regeneration. Within TSA technologies, the specific case in

which the solid is heated by the Joule effect is commonly referred to as ESA [148]. Each of the processes has its own importance and pitfalls as mentioned in the following section. PSA doesn't need elevated temperature, so energy requirement is low. But to effectively regenerate adsorbent it requires multiple stages which makes the process expensive [150]. Whereas, VSA requires a highly efficient vacuum pump to effectively desorb CO₂, which adds extra costs [151], [152]. TSA is very cost effective and easily operated since it does not need any pumping system, but it needs high volume purge gases to provide heat for regeneration [151], [153]. ESA has advantages of less heat requirement and fast kinetics, but its electrical energy consumption is very high [149]. Additionally, regeneration ability of the sorbent was studied in detail in our previous work [146]. TSA regeneration tests were conducted at the elevated temperature of 180 °C under He gas flow for 60 minutes. The test was conducted 15 times and the adsorbent was reused for CO₂ adsorption after each regeneration cycle. The results demonstrated that US0.5-EH1:1-T2.5 could maintain 56% of its initial adsorptive capacity after 15 cycles of adsorption-regeneration.

Additionally, key to enhanced adsorption capacity is effective nitrogenation that depends on the interactions between the functional group (such as amino group) and its support (carbonaceous materials). For instance, the reaction of carbonaceous compounds with ammonia leads to the formation of functional groups such as -NH₂, -CN, pyridine, quaternary nitrogen, imide and pyrrole-like structures [154], [155]. Another reaction, involving a mixture of nitric and sulfuric acids, creates nitro (-NO₂) groups through electrophilic aromatic substitution (Figure 1) followed by reduction to amino groups via NaHSO₃ [156].

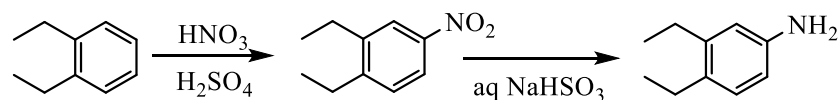


Figure 3.1. Nitration of carbonaceous compounds

Among different amination methods, EDC-HOBt coupling or KOH treatments are highly potent methods. EDC-HOBt reaction (Figure 3.2) is a one-pot method at room temperature with fast kinetics and ease of product separation. EDC as a coupling agent activates the -COOH group to form O-acyl-isourea followed by nucleophilic substitution by amino groups producing amide and releasing dialkyl-urea as a byproduct. However, it may lead to side reaction through cleaving off the activated ester intermediate (O-acylisourea) forming N-acyl urea [117]. This can be prevented by the addition of HOBt, which forms the intermediate (Figure 3.2) before the migration [117].

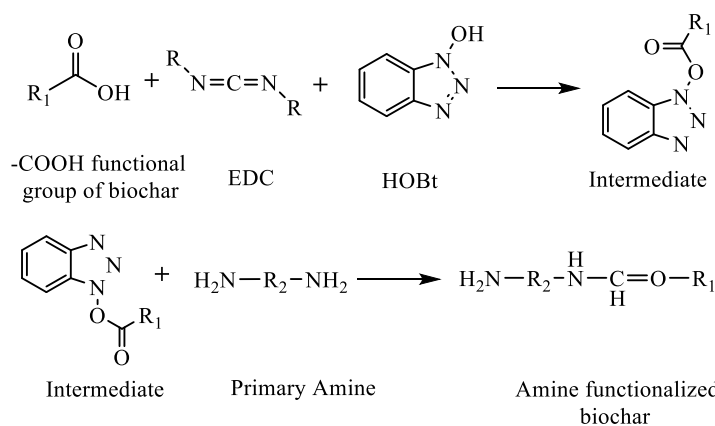


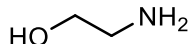
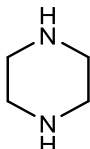
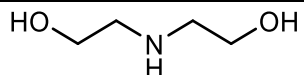
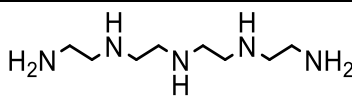
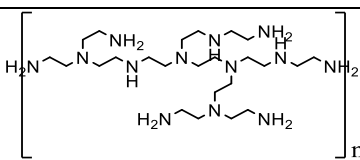
Figure 3.2. Amine treatment of carbonaceous compound

The alternate route of activation with KOH treatment (prior to amination) is used for metal ion adsorption [157]. The mechanism may be primarily physical, by causing changes in the porosity and surface area of the char [158]. Other studies have found evidence for chemical modification of the char, including an increase in oxygen content and a decrease in carbonyl groups [157]. Simple deprotonation of carboxyl groups by hydroxide would create carboxylates

that eventually protonated to carboxylic acids. Besides, opening of epoxides with hydroxide would add hydroxyl-group oxygen to the system that would allow for amine coordination through hydrogen bonding. KOH changes porosity and increase oxygen content of biochar under the extreme local temperatures generated during ultrasonication similar to the phenomenon observed under high temperature (850° C) treatments [159]. Alternatively, partial breakdown of the biochar carbon skeleton might be assisted by KOH, with air oxidation to more –COOH or –OH sites for interaction with amines.

A major goal of the amination is to achieve maximal amine loading that could be achieved through the amalgamation of two or more amines. Additionally, literature suggests that amine mixtures or blended amines can have higher reaction rates and sorption capacities, lower regeneration temperature than single amine systems [160].

Table 3.1. Structures and Properties of Different Amines

Amine	Structure	Empirical Formula	No. of amine groups	Molecular weight
MonoEthanolAmine		C ₂ H ₇ NO	1	61.08
PiperaZine		C ₄ H ₁₀ N ₂	2	86.14
DiEthanolAmine		C ₄ H ₁₁ NO ₂	1	105.14
TetraEthylenePentA mim		C ₈ H ₂₃ N ₅	5	189.30
PolyEthylenImine		(C ₂ H ₅ N) _n	1 (per repeating -CH ₂ CH ₂ NH - unit)	43.04 (per repeating -CH ₂ CH ₂ NH - unit)

1° and 2° amines can form ammonium bicarbonate salts (requiring only one amine per

CO₂) as well as zwitterion-carbamate products (requiring two amines), while 3° amines only form the salt. Therefore, 3° amines have a theoretically higher CO₂ adsorption capacity, but slow kinetics.

The present study explores the effect of five different amines: MEA, PZ, DEA, TEPA, and PEI, and binary-ternary mixtures: MEA-TEPA, DEA-TEPA, DEA-PEI, TEPA-PEI and DEA-TEPA-PEI, on ultrasonically activated biochar for enhanced CO₂ adsorption with their specifications reported in Table 3.1.

The main objective of a series of our previous studies [109, 146] is to develop an advanced method for activation of carbonaceous structures, which can be applied at very low temperature than conventional carbon activation. To reach this objective, the emphasis has been given on the integration of physico-chemical activation processes. The focus of the previous work was on investigating the effect of ultrasound intensity, amine concentration, adsorption temperature, and inlet CO₂ concentration on the adsorption capacity of the activated biochar. The current work investigates the interaction of blended amines in ultrasonic physical activation technique for its application in CO₂ capture. Ultrasound increases the porosity of the biochar, so a structure with the combination of micro and meso pores is generated. Such ultrasound assisted pore generation and surface destructions have wide arrays of applications in several fields, e.g. for water purification to break down pollutants [161], in medicine for the destruction of kidney stones [162], for targeted drug delivery through modification of the cell plasma membrane, [163] etc. The second reason is more related to the simplifying the chemical step by eliminating the pre-activation using EDC and HOBt and substituting it with KOH. So, based on our previous results [109, 146] and literature reports [160], the present study investigates the effects of different amines and their mixtures, with the aid of low frequency ultrasound energy, to achieve

enhanced adsorption capacity of biochar towards CO₂ capture.

3.3 Materials and Methods

3.3.1 Materials

Pine wood-based biochar, pyrolyzed between 550-600° C in an oxygen-deprived environment in a kiln reactor, was supplied by Biochar Now (Berthoud Colorado, U.S.A.). The reagents used in chemical functionalization, including methanol, EDC, HOBt, MEA, PZ, DEA, TEPA, PEI and KOH were obtained from Sigma-Aldrich. HCl acid (37%) and acetone were also supplied by Sigma-Aldrich. NaOH was obtained from Fisher Scientific. DI water was obtained from Milli-Q ultrapure water tap from Millipore Sigma. All chemicals used were of analytical grade.

3.3.2 Experimental Method

3.3.2.1 Functionalization with Ultrasound Treatment of Biochar

Prior to physico-chemical modification, raw biochar particles were resized in the range of 75-250 micron by crushing and screening. Physical modification of biochar was then accomplished by low frequency ultrasound (QSonica sonicator model no. Q700) with 3 g of biochar in 250 ml of water for 30 s. The duration was selected based on the optimum value obtained from a previous study [146]. Longer duration of sonication promotes intensified cavitation that could disarrange the orientation of the layered structure of biochar, consequently blocking the pores and reducing the adsorption capacity [164], [113]. The ultrasonically-modified biochar was then subjected to chemical modification with simple or blended amines, using either EDC-HOBt or KOH activation. The details of the chemical activation procedures are discussed in the following sections.

3.3.2.2 Amination of Ultrasonicated Biochar using EDC-HOBt Activation

First, the ultrasound treated biochar samples were subjected to the coupling agents EDC-HOBt (3.375 g of each coupling agent for 3 g of biochar) in water. EDC was selected as a coupling agent over other carbodiimides, such as DCC, that are sparingly soluble in any solvent, which makes separation very difficult to achieve. HOBt was used as an additive to prevent side reactions that would reduce the yield of products. An equal ratio of EDC and HOBt activates the maximum number of functional groups, as found from our previous study [146]. The mixture was stirred for 24 hours at 35°C, then filtered and dried under vacuum at 60°C overnight. In the next step, the dried samples were suspended in methanol (an organic solvent that makes the drying faster). Amines (MEA, PZ, DEA or PEI) with a weight ratio of 2.5, 5, or 10 times that of biochar were added to the suspension. The resultant mixtures were stirred for 24 hours with gentle heating as before. Finally, the suspension was filtered and washed in succession with 200 mL of 1N NaOH (3 times), 200 mL 1N HCl (3 times) and 200 mL of acetone (1 time) for each wash and dried as before. For activation with blended amines, the mixtures of MEA-TEPA, DEA-TEPA, DEA-PEI, TEPA-PEI and DEA-TEPA-PEI were added where the total weight of the mixture was 2.5 times to the weight of the biochar. To achieve this, the loadings of individual amine in binary and ternary mixtures were maintained at 1.25 and 0.83 times to the weight of the biochar respectively. Thus, the individual amine in the mixture was blended in equal weight ratio (1:1 and 1:1:1 for binary and ternary mixtures) to give the total weight 2.5 times to the weight of the biochar

3.3.2.3 Amination of Ultrasonicated Biochar using KOH Activation

Following sonication of the biochar-water mixture as before, KOH (1.5 times the biochar weight) was added to the mixture, which was stirred for 24 hours, filtered, and dried under

vacuum overnight. The sample was then suspended in methanol, and MEA, PZ, DEA, TEPA or PEI or their blended mixtures were added as before. All mixtures were kept under stirring for 24 hours, filtered, and washed with 1N NaOH, 1N HCl and acetone as before. The dried samples were kept in a desiccator for future CO₂ adsorption tests.

3.3.2.4 Characterizations of the Adsorbent

The surface morphology of both raw and activated biochars was examined using SEM (JSM-5600 Scanning Electron Microscope, JEOL USA Inc., Peabody, MS). The effects of ultrasound activation on the surface area and porosity were also investigated by a surface area analyzer (Nova 2000E series, Quantachrome). The elemental compositions of physico-chemically modified biochar samples were analyzed before and after modifications (Huffman Hazen Laboratory, Colorado, USA). The surface functional groups of the functionalized biochars were examined using Fourier Transform Infrared (FTIR, Cary 660 FTIR Agilent). The Raman spectroscopy (LabRam HR Evolution) of the activated samples was conducted for investigating the microstructure of biochar [165]. CO₂ adsorption studies were conducted with 2.5, 5 and 10 times amine loading. However, the adsorption capacities for 5 or 10 times loading were not enhanced substantially compared to the 2.5 times loading. So, the system was optimized with 2.5 times loading and the characterizations were performed only for the 2.5 times loading samples.

3.3.2.5 CO₂ Adsorption Studies

The CO₂ adsorption experiments were carried out in a tubular reactor made of alumina oxide. In a typical experiment (Appendix A- Figure A1 and A2), the functionalized biochar was placed into a temperature-controlled furnace inside the reactor. The biochar was degassed with helium gas (99.99%) at a flowrate of 500 cm³ min⁻¹ at 378 K for 1 hour, and then cooled to 333 K. The previous work showed that the optimum adsorption capacity was achieved when

experiment was conducted at 70°C temperature compared to 25, 50 and 90 °C. This is due to the chemical activation with amines resulting in chemisorption, which requires high activation energy, hence high temperature. However, the further reduction of adsorption capacity with increasing temperature was attributed to the exothermic nature of the process [125]. A similar phenomenon was observed by Heydari-Gorji and Jadhav et al. [125], [126]. Accordingly, the adsorption temperature of 70 °C was selected for the current study [146]. After setting the temperature at its desired value, the helium flow was switched to a CO₂-containing simulated flue gas of 10 vol.% (balanced with He) at a flow rate of 500 cm³ min⁻¹. The final concentration of CO₂ after adsorption was measured by a CO₂ analyzer, connected on-line via the adsorption column outlet. The adsorption capacity was calculated based on the difference between inlet and outlet CO₂ concentrations.

3.4 Results and Discussions

3.4.1 Physicochemical Properties of Raw and Modified Biochar Samples

3.4.1.1 SEM Analysis

Scanning electron microscopy (SEM) provides information about the surface morphology of any structure. SEM images of raw (both longitudinal and cross-sectional view), ultrasound treated, and EDC-HOBt-binary amine activated (US0.5-EH1:1-DT1:1) are shown in Figures 3.3a-d. The cross-sectional view (Figure 3.3a) shows the porous structure of biochar, whereas the longitudinal view (Figure 3.3b) shows that the raw biochar surface was rough and consisted of blocked pores as shown by the red oval shapes. The observed blockage on the surface can be ascribed to the formation of volatile compounds and ash (from the mineral matter) during the thermochemical decomposition of the cellular structure of the biomass in pyrolysis [166]. The resultant blockage made the surface inaccessible for subsequent chemical modification, lowering

adsorption capacity. However, upon sonication, the surface porosity was enhanced significantly as observed from Figure 3.3c because of the exfoliation of biochar's graphitic layers and leaching of ash from the pores [167].

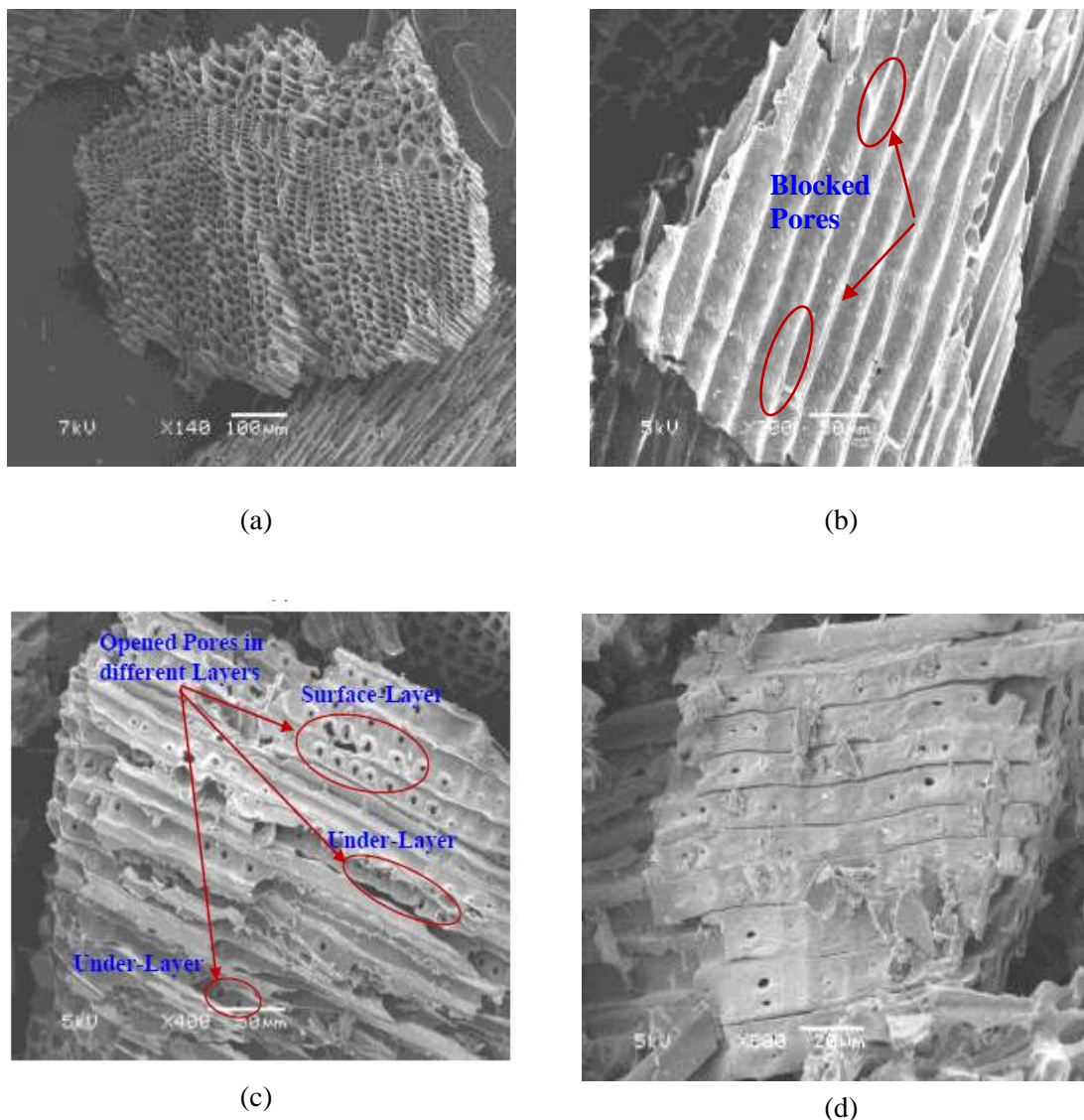


Figure 3.3. SEM images of (a) raw biochar (cross sectional view), (b) raw biochar (longitudinal view), (c) ultrasound activated biochar, (d) ultrasound-EDC-HOBt-binary amine (DEA-TEPA) activated biochar US0.5-EH1:1-DT1:1.

The figure also shows that the ultrasound cavitation was intense enough to create additional porosity not only to the layer adjacent to the surface but also penetrated to the interlayers, breaking the structure and generating pores. This substantially enhanced the surface

area of the biochar and facilitated the chemical activation of the underlayers' active sites. In Figure 3.3d the effect of amination (in presence of EDC-HOBt activating agents) is portrayed. This image further displays that the surface porous structure as well as the surface were partially covered with amine, which can be further explained as the formation of a coating on the biochar surface [168]. This observation is consistent with the surface analysis described in the next section.

3.4.1.2 BET Analysis

According to the IUPAC, adsorption pores can be classified into three groups: micropore (diameter < 2 nm), mesopore (2 nm < diameter < 50 nm) and macropore (diameter > 50 nm) [169]. The values of surface areas as summarized in Table 3.2.

Table 3.2. DR-CO₂ and BET-N₂ Surface Area of Raw and Physicochemically Activated Biochars

Sample Name	Micro-Porosity			Micro & Meso Porosity		
	Surface area (m ² /g)	Pore Volume (cm ³ /g)	Pore Radius [170]	Surface area (m ² /g)	Pore Volume (cm ³ /g)	Pore radius [170]
Raw Biochar	312.31	0.11	0.58	46.93	0.06	0.80
US0.5-EH0-A0	395.32	0.12	0.59	22.26	0.03	1.80
US0.5-EH1:1-M2.5	374.66	0.12	0.57	13.30	0.02	2.80
US0.5-EH1:1-PZ2.5	172.57	0.06	0.59	1.01	0.004	5.06
US0.5-EH1:1-D2.5	220.11	0.07	0.63	2.69	0.005	5.04
US0.5-EH1:1-P2.5	182.04	0.06	0.62	2.01	0.005	5.04
US0.5-EH1:1-MT1:1	375.12	0.12	0.58	18.16	0.02	2.10
US0.5-EH1:1-DT1:1	270.96	0.09	0.56	13.30	0.02	2.80
US0.5-EH1:1-DP1:1	233.46	0.08	0.62	3.41	0.005	4.94
US0.5-EH1:1-TP1:1	229.05	0.08	0.59	4.54	0.005	4.86
US0.5-EH1:1-DTP1:1:1	235.62	0.08	0.58	10.14	0.02	3.20
US0.5-K1.5-M2.5	308.22	0.09	0.55	14.30	0.02	2.92
US0.5-K1.5-T2.5	298.17	0.09	0.59	16.71	0.02	2.60
US0.5-K1.5-DT1:1	266.23	0.09	0.61	13.24	0.02	2.80

Note: US: Ultrasound; EH: EDC-HOBt; A: Amine; K: KOH; T: TEPA; P: PEI; D: DEA; M: MEA; PZ: Piperazine Number beside US denotes sonication time in minutes; Number beside EH denotes ratio of activating agents; Number beside K denotes loading of KOH (weight of KOH to the weight of biochar); Number beside A, T, P, D, M and PZ denotes amine loading, Numbers beside TD, TP, PD, TM and TPD denote weight ratio of amines.

As observed from the table that the biochar consists of mainly micropores (described by DR-CO₂) with a smaller quantity of mesopores (described by BET-N₂) (312.31 vs 46.93 m²/g, respectively). Under ultrasound irradiation physical effects such as microstreaming, shock waves, and especially microjets result in direct erosion of a particle's surface [159, 171]. Consequently, the microporous surface area for US0.5-EH0-A0 was enhanced as some new micropores were formed and some blocked pores were opened as observed in Table 3.2 and Figures 3.3c.

In this work, micro and meso porosities were studied through adsorption of CO₂ and N₂, respectively. However, it is worth noting that CO₂ can determine only microporous, while N₂ estimates both microporous and mesoporous surface area [172]. However, CO₂ and N₂ display certain differences when measuring microporous surface area since the CO₂ molecule (0.34 nm) is smaller than the N₂ molecule (0.36 nm). Besides, the analysis with CO₂ is conducted at 273 K whereas N₂ requires 77 K. Also, at 273 K the saturation pressure of CO₂ is 3.5 MPa, while at 77 K the saturation pressure of N₂ is 0.35 kPa [173]. Due to the extremely low saturation pressure, the number of N₂ molecules is significantly lower, and diffusion is also slower than with CO₂. This also lowers the relative pressure range (p/p_0) for CO₂ compared to N₂ (since p_0 for N₂ \ll p_0 for CO₂). Because of these reasons, N₂ only diffuses to the wide micro pores and meso pores of the material, but CO₂ diffuses into the narrow micro pores. Furthermore, the literature also suggests that the main source of heterogeneity for microporous solids like biochars is their complex porous structure which contains micropores of different dimension and shape such as wider micropores and narrower micropores [174]. The biochars used for the present study possess highly heterogeneous microporous structures with different shapes of micropores (wide and narrow). The CO₂-DR analysis determines the narrow micropores and the BET-N₂ analysis

estimates both wider micropores and mesopores (as tabulated in Table 3.2). This microporous behavior has been further described in the adsorption isotherm study.

Based on the porous nature of the biochars, the amines can be attached either through impregnation or through grafting. For impregnation, the amine molecules are dispersed inside the pores and over the internal and external surfaces of pores through weak van der Waals force [175]. For grafting, the amine molecules are chemically attached with the surface functional groups through strong covalent bonds. Primarily, the amines are attached to the functional groups and depending on the size, the amine molecules disperse into either of the pores (either micro or macro) [175]. Short amines like monoethanolamine preferably enter micropores. However, the highly branched PEI can't go inside micropores and so requires mesoporous support for attachment. TEPA can also be grafted onto the surface of the porous materials (mesopores) without destroying the intrinsic structure of the sorbent [176].

30 s of ultrasound irradiation was intense enough to produce maximum microporous surface area and adsorption capacity. Upon further increase of the sonication time, cavitation disarranged the orientation of the layered structure of biochar, consequently blocking the pores and reducing the adsorption capacity. Similar phenomena were observed by Verma et al. [164] and Hamdaoui et al. [113] Furthermore, it is observed from Table 3.2 that both surface area (based on CO₂ and N₂ analysis), and pore volume of biochar was decreased by amine functionalization, indicating that amines physically loaded on the solid support formed a layer that blocked some of the pores. Similar observations have also been reported by Yue et al. and Teng et al. where they used TEPA-grafted mesoporous silica and KOH-amine modified silica, respectively, for CO₂ adsorption [177, 178].

3.4.1.3 Elemental Analysis

The effects of different amine mixtures with EDC-HOBt or KOH activation on the C, H, N, O and ash content are presented in Table 3.3. Since the ash content varied widely, pure organic compositions were also calculated by omitting the contribution of ash (Table 3.4). As can be seen from the Table 3.3, amination of biochar increased the %N from 2 times to over 7 times its value in raw biochar. TEPA, with 5 amine groups, is very effective in increasing nitrogen content [146] since it has 37% N, followed by PZ, MEA and DEA with 32%, 23%, and 13% N, respectively.

Table 3.3. Elemental Analysis of Raw and Activated Biochars (Dry Basis)

Sample	C content (% wt.)	H content (% wt.)	N content (% wt.)	O content (% wt.)	Ash content (% wt.)
Raw biochar	65.36	1.97	0.18	11.22	23.95
US0.5-EH1:1-M2.5	64.42	2.43	1.17	13.66	20.50
US0.5-EH1:1-PZ2.5	57.57	2.33	0.38	15.26	27.28
US0.5-EH1:1-D2.5	65.66	2.30	0.58	13.16	21.03
US0.5-EH1:1-P2.5	61.84	2.25	0.46	13.99	23.95
US0.5-EH1:1-MT1:1	66.13	2.54	1.40	16.15	15.66
US0.5-EH1:1-DT1:1	64.70	2.34	0.78	12.76	23.22
US0.5-EH1:1-DP1:1	62.43	2.48	0.63	10.30	21.69
US0.5-EH1:1-TP1:1	57.75	2.32	0.64	22.81	20.10
US0.5-EH1:1-DTP1:1:1	66.02	2.41	0.68	14.91	17.82
US0.5-K1.5-M2.5	65.66	2.35	1.12	15.00	16.36
US0.5-K1.5-T2.5	57.47	2.33	0.79	15.04	26.14
US0.5-K1.5-DT1:1	60.66	2.31	0.76	13.00	24.75

Note: US: Ultrasound; EH: EDC-HOBt; K: KOH; T: TEPA; P: PEI; D: DEA; M: MEA; PZ: Piperazine
Number beside US denotes sonication time in minutes; Number beside EH and K denote ratio of activating agents and loading of KOH (weight of KOH to the weight of biochar); Number beside T, P, D, M and PZ denotes amine loading, Numbers beside TD, TP, PD, TM and TPD denote weight ratio of amines

Comparing Tables 3.3 and 3.4, the observed %N content increments follow the order TEPA-MEA > MEA > TEPA-DEA > TEPA-DEA-PEI > TEPA-PEI > PEI-DEA, with the other single-amine samples lower. Despite its high nitrogen content, PZ-activated samples showed only moderately enhanced nitrogenation; since PZ is somewhat volatile, its concentration tends to fall with time [179].

Table 3.4. Elemental Analysis of Biochars as Percentage of Organic Constituents, Omitting Ash Contribution (Dry Basis)

Sample	C content (% wt.)	H content (% wt.)	N content (% wt.)	O content (% wt.)	C/N	C/H
Raw biochar	83.02	2.50	0.23	14.25	421	5.53
US0.5-EH1:1-M2.5	78.87	2.97	1.43	16.72	64.4	4.42
US0.5-EH1:1-PZ2.5	76.21	3.08	0.50	20.20	178	4.12
US0.5-EH1:1-D2.5	80.37	2.82	0.71	16.11	132	4.75
US0.5-EH1:1-P2.5	78.74	2.86	0.59	17.81	156	4.59
US0.5-EH1:1-MT1:1	76.70	2.95	1.62	18.73	55.2	4.33
US0.5-EH1:1-DT1:1	80.29	2.90	0.97	15.84	96.6	4.61
US0.5-EH1:1-DP1:1	82.31	3.27	0.83	13.58	116	4.19
US0.5-EH1:1-TP1:1	69.14	2.78	0.77	27.31	105	4.14
US0.5-EH1:1-DTP1:1:1	78.58	2.87	0.81	17.75	113	4.56
US0.5-K1.5-M2.5	78.04	2.79	1.33	17.83	68.5	4.66
US0.5-K1.5-T2.5	75.99	3.08	1.04	19.89	85.2	4.11
US0.5-K1.5-DT1:1	79.05	3.01	1.00	16.94	92.2	4.37

This trend is consistent with the %N of the individual amines as discussed above. For example, a higher value of %N in MEA than DEA resulted in an elevated %N in biochar treated with the binary system TEPA-MEA compared with TEPA-DEA. In the biochar samples activated with DEA-PEI, TEPA-PEI, or DEA-TEPA-PEI, nitrogen attachment was lower than that in MEA-TEPA or DEA-TEPA. This could be due to agglomeration of PEI due to its high molecular weight and polymeric structure that would reduce the other amines (DEA and TEPA) accessibility to the biochar surface [21]. Additionally, it was observed comparing Tables 3.3-3.4 and Tables 3.6-3.7 that the %N content and the adsorption capacity followed the same trend with the maximum adsorption capacity for MEA activated sample that has highest nitrogen content.

Furthermore, the oxygen content of the treated samples was typically somewhat enhanced compared to raw biochar. This indicates the oxygenation of the biochar surface upon activation. During sonication, water undergoes dissociation into H• and •OH radicals. [180] Addition of •OH to biochar π bonds would oxidize it, thereby increasing its oxygen content. KOH activation could also enhance oxygenation, for example by saponifying ester groups or opening epoxides

[181]. Air oxidation of the carbon framework is also a possibility.

From Tables 3.3 and 3.4 it can be noted that the varying C, N and H content of the adsorbed amines caused variations in the C/N and C/H molar ratios of the aminated biochars (Table 3.4). For instance, raw biochar had C/N and C/H ratios of 421 and 5.53, respectively. Modification with MEA, which has lower values of C/N and C/H, significantly decreased the C/N and C/H molar ratios of US0.5-EH1:1-M2.5 to 64.4 and 4.42, respectively. Similar changes were observed for the rest of the amine functionalized samples. Similar explanations were provided by Zhou et al. [170] and Yue et al. [178] for the variation of elemental compositions of their amine activated adsorbents.

Physico-chemical activation of the samples usually led to reduction of the %ash, which is a key factor in increasing the adsorption efficiency and heating value of biochar (Table 3.4). A decrease in ash content represents the removal of minerals, as well as the enhancement of organic contents, upon activation or amination. The previous studies showed that ultrasound is very useful in leaching the minerals from the structure and making room for amines to attach [146]. Thus, the reduced ash content helped in incorporation of a greater number of amine groups in the structure, resulting in improved CO₂ adsorption efficiency of the prepared adsorbent. However, few samples showed enhancement of ash content after amination. KOH activation could be a reason for increased ash content (potassium as a mineral adds up to the ash) for the samples US0.5-K1.5-T2.5 and US0.5-K1.5-TD1:1. But for US0.5-EH1:1-PZ2.5 activated biochar ash content went up as well which require further investigation to determine the reason of increased ash content.

3.4.1.4 Raman Analysis

Raman spectroscopy is a common vibrational spectroscopy technique for investigating

the microstructure and mineralogy of carbonaceous compounds such as biochar [165]. Raman spectra of raw and singly-functionalized biochar with MEA, PZ, DEA and PEI are shown in Figure 3.4. Sonication duration, activating agents (EDC-HOBt) ratio, and amine concentration for all the samples were maintained at 30 seconds, 1:1, and 2.5 times weight, respectively. The G band for these spectra appeared at 1591, 1604, 1551, 1592, and 1600 cm^{-1} and the D band appeared at 1346, 1396, 1336, 1376, and 1359 cm^{-1} for raw biochar, US0.5-EH1:1-M2.5, US0.5-EH1:1-PZ2.5, US0.5-EH1:1-D2.5 and US0.5-EH1:1-P2.5, respectively. In addition to that, a strong peak (2D) was observed in the range of 2500-2800 cm^{-1} for the raw biochar sample. These are the signature peaks of graphitic sp^2 structure that confirm the structural similarity of biochar and graphene oxide [182].

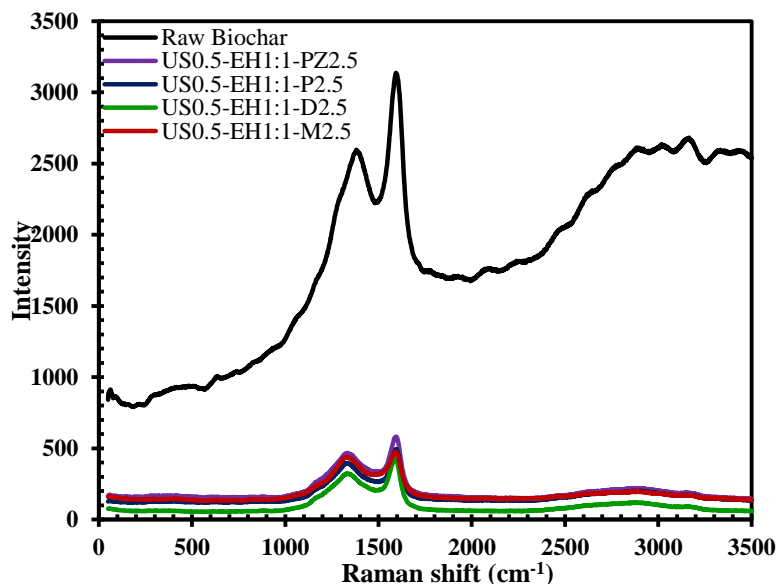


Figure 3.4. Raman spectra of raw biochar, US0.5-EH1:1-M2.5, US0.5-EH1:1-PZ2.5, US0.5-EH1:1-D2.5 and US0.5-EH1:1-P2.5

The G-band of the structure is attributed to the vibration of sp^2 carbon atoms found in graphitic materials, while the D-band is linked to the breathing modes of disordered graphite rings in the form of functionalities such as -OH, -C=O, -COOH [183]. The ratio between the

intensities of the D and G bands reflects disorder of the biochar structure due to the presence of oxygen functionalities [124]. The values of intensity ratios (I_D/I_G) of raw and activated biochar samples are summarized in Table 3.5. The activated biochars had higher values of I_D/I_G than raw biochar, reflecting the enhanced functionalities created by physico-chemical modification with sonication and amination. The I_D/I_G for raw biochar, US0.5-EH1:1-M2.5, US0.5-EH1:1-PZ2.5, US0.5-EH1:1-D2.5 and US0.5-EH1:1-P2.5 were 0.78, 0.93, 0.82, 0.88 and 0.87, respectively. The I_D/I_G was highest for the MEA-modified sample, followed by DEA, PEI and PZ for the single amine systems. The elemental analysis and the CO₂ adsorption results followed the same trend: elemental analysis (Table 3.3) showed the nitrogen content in MEA, DEA, PEI, and PZ-modified samples was 8, 3, 2.6, and 2 times higher than that in raw biochar, respectively. Correspondingly, the adsorption capacity was maximum for US0.5-EH1:1-M2.5 (Table 3.6), compared to other amine activated samples.

Table 3.5. Raman Intensity ratios I_D/I_G of raw biochar and physico-chemically activated biochars

Sample Name	Intensity Ratio
Raw Biochar	0.78
US0.5-EH1:1-M2.5	0.93
US0.5-EH1:1-PZ2.5	0.82
US0.5-EH1:1-D2.5	0.88
US0.5-EH1:1-P2.5	0.87
US0.5-EH1:1-MT1:1	0.95
US0.5-EH1:1-DT1:1	0.80
US0.5-EH1:1-DP1:1	0.85
US0.5-EH1:1-TP1:1	0.86
US0.5-EH1:1-DTP1:1:1	0.93
US0.5-K1.5-T2.5	0.86
US0.5-K1.5-M2.5	0.85
US0.5-K1.5-DT1:1	0.85

In Figure 3.5, the Raman spectra of binary and ternary amine mixtures are reported. Sonication duration and activating agent ratio (EDC-HOBt) for all the samples were maintained

at 30 seconds and 1:1, respectively. The intensity ratio I_D/I_G had the following values: 0.95, 0.80, 0.85, 0.86, and 0.93 for US0.5-EH1:1-MT1:1, US0.5-EH1:1-DT1:1, US0.5-EH1:1-DP1:1, US0.5-EH1:1-TP1:1, and US0.5-EH1:1-DTP1:1:1, respectively. The maximum departure of the I_D/I_G ratio was found for US0.5-EH1:1-MT1:1, suggesting that the maximum defects resulted from amination by the binary MEA-TEPA mixture. This is in accordance with the CO₂ sorption result (Table 6), showing that dual amination with MEA and TEPA using EDC-HOBt as activating agents provided a favorable combination for achieving improved adsorption capacity.

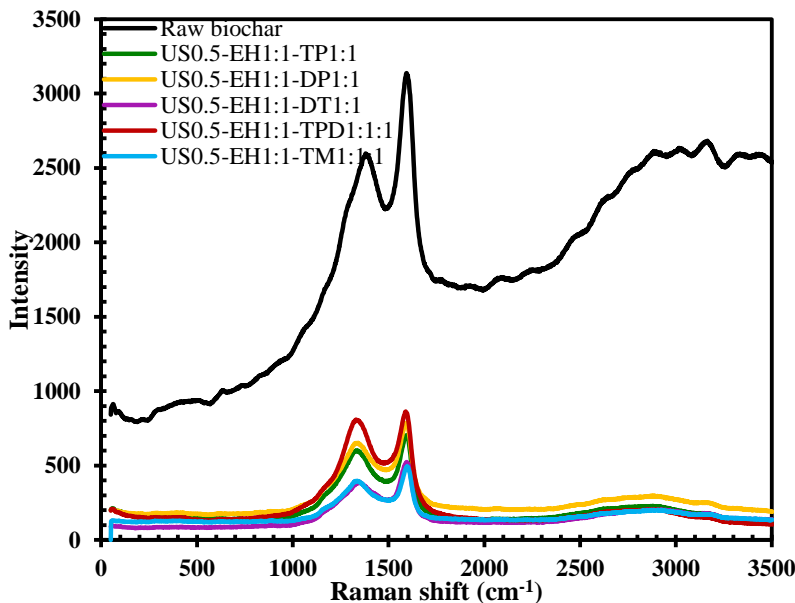


Figure 3.5. Raman spectra of raw biochar, US0.5-EH1:1-MT1:1, US0.5-EH1:1-DT1:1, US0.5-EH1:1-DP1:1, US0.5-EH1:1-TP1:1 and US0.5-EH1:1-DTP1:1:1

Finally, the Raman spectra of KOH-activated amine functionalized samples are presented in Figure 3.6. The increased values of the intensity ratios (0.85, 0.86, 0.85 respectively, from Table 3.5) compared to raw biochar are indicators of higher quantity of defects (functional groups) on the sorbents' surfaces due to activation [184]. This is consistent with the changes in adsorption capacity (Table 3.7).

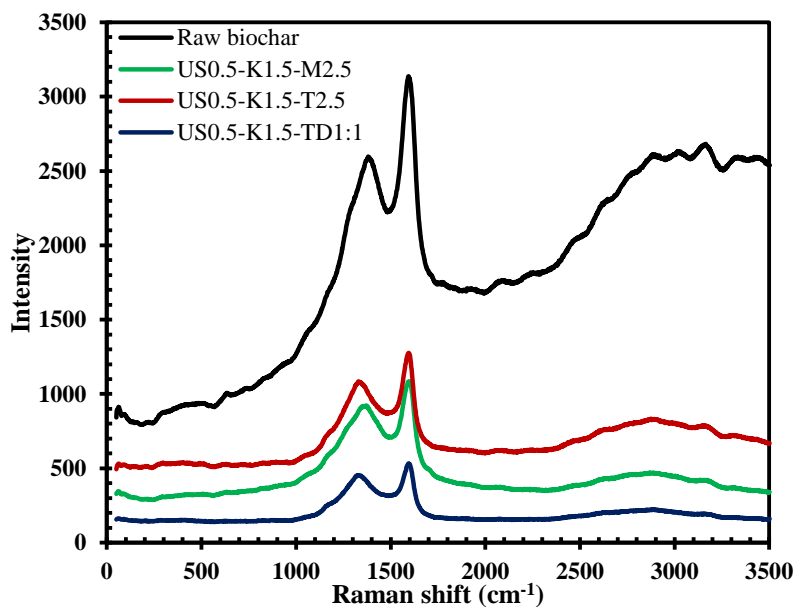


Figure 3.6. Raman spectra of raw biochar, US0.5-K1.5-M2.5, US0.5-K1.5-T2.5 and US0.5-K1.5-DT1:1

3.4.1.5 FTIR Analysis

The IR spectra of the biochar samples functionalized with EDC-HOBt and amines individually and their binary-ternary mixtures are shown in Figures 3.7 and 3.8, respectively.

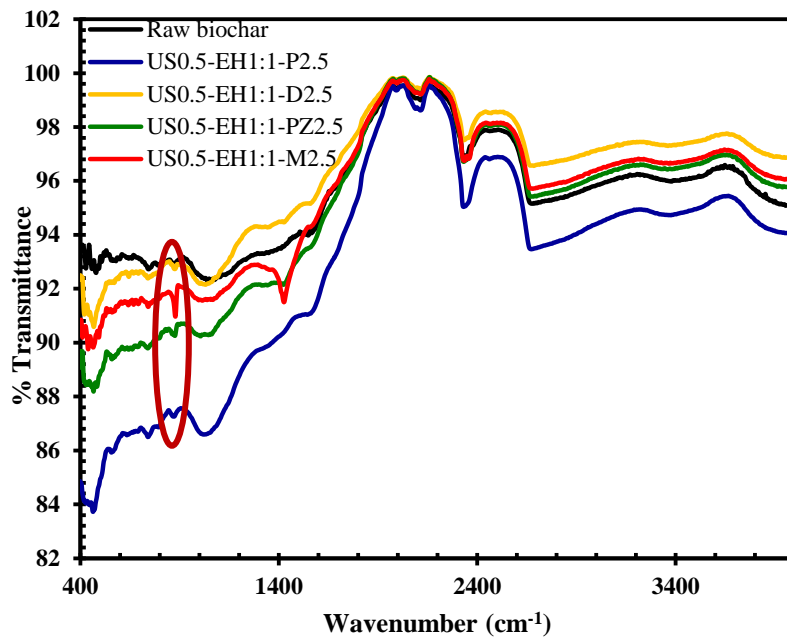


Figure 3.7. FTIR spectra of raw biochar, US0.5-EH1:1-M2.5, US0.5-EH1:1-PZ2.5, US0.5-EH1:1-D2.5 and US0.5-EH1:1-P2.5

The FTIR bands for the samples activated with KOH and amines (single: MEA, TEPA and binary: DEA-TEPA) are represented in Figure 3.9. The FTIR spectra had similar shapes for both raw and functionalized biochars. However, due to functionalization, some new peaks were generated. For instance, a new peak at 870 cm^{-1} was observed for all the activated samples that is attributed to the out of plane bending of N-H groups formed due to primary and secondary amines [128]. The band is most significant for the sample US0.5-EH1:1-M2.5 (Figure 3.7), demonstrating that MEA is more effective in grafting amino groups than the other amines. At $\sim 1430\text{ cm}^{-1}$ a peak was observed for the same sample US0.5-EH1:1-M2.5 (Figure 3.7), which could be attributed to C-H bending from sp^3 carbons, representing the methylene groups that are part of MEA. A peak in the region of $3300\text{-}3500\text{ cm}^{-1}$ was observed due to -OH (and -NH) stretching vibration and existed in all biochar samples [146].

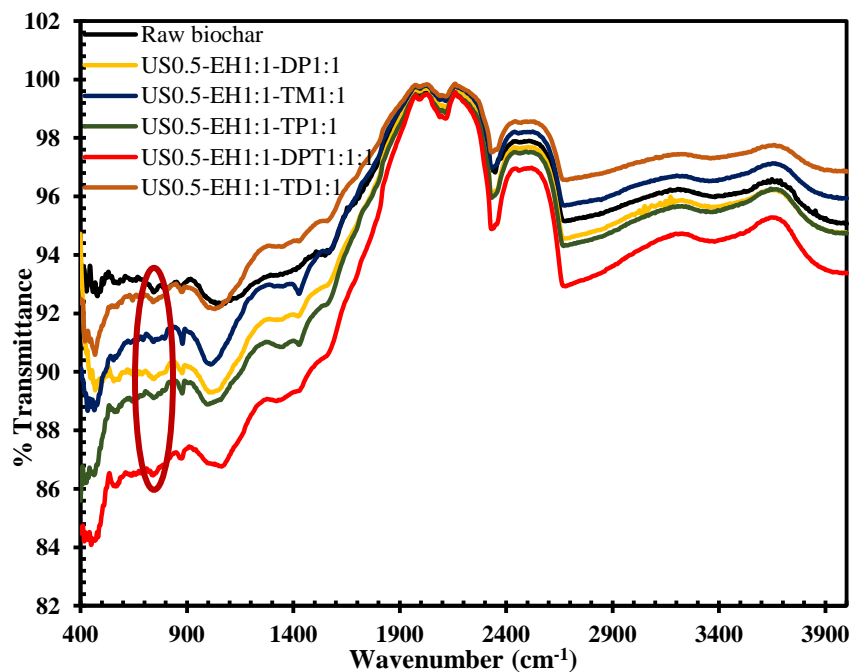


Figure 3.8. FTIR spectra of raw biochar, US0.5-EH1:1-MT1:1, US0.5-EH1:1-DT1:1, US0.5-EH1:1-DP1:1, EH1:1-TP1:1 and US0.5-EH1:1-DTP1:1:1

For KOH activated samples, shown in Figure 3.9, the band at 1097 cm^{-1} was intense, representing a high degree of oxygenation due to formation of C–O bonds. A more distinct carbonyl peak was observed for the KOH-amine activated samples at 1600 cm^{-1} in Figure 3.9, which could reflect additional carboxyl groups following saponification.

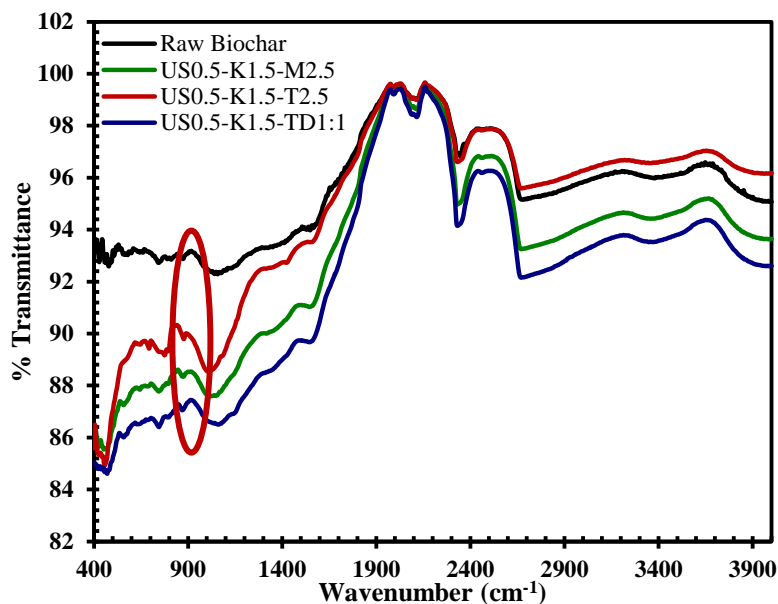


Figure 3.9. FTIR spectra of raw biochar, US0.5-K1:5-M2.5, US0.5-K1:5-T2.5 and US0.5-K1:5-DT1:1

3.4.2 CO₂ Adsorption Studies

3.4.2.1 CO₂ Adsorption with Amine Systems Activated by EDC-HOBt

The CO₂ adsorption capacities of biochar samples aminated with individual, binary, and ternary combinations of MEA, PZ, DEA, TEPA and PEI are summarized in Table 3.6. Two control tests were separately conducted which showed the effect of individual activation processes on CO₂ adsorption (see Table 3.6). In one test, biochar sample was chemically activated with TEPA (no ultrasonic irradiation), while the focus of the other test was only on physical activation under ultrasound irradiation (no TEPA). Comparison of the results of the two control tests with the integrated physico-chemical activation exhibited the following adsorption

range: physico-chemical activation (2.04 mmol/g) >> chemical activation (0.56 mmol/g) ~ physical activation (0.55 mmol/g). The result showed that the samples activated with either ultrasound or amine individually possess very limited adsorption capacity, while integrated activation strategies have had a significant effect on the CO₂ adsorption of biochar. This further demonstrates the effectiveness of the combined physical and chemical activation technique.

Table 3.6. CO₂ Adsorption Capacities (in mmol/g) of Biochars (raw and functionalized) at 70 °C and 10 vol.% CO₂ (effects of EDC-HOBt-activated amines and amine mixtures)

Sample	Amine	Amine loading (times mass of biochar)				CO ₂ conc (vol%)
		2.5	5	10	0	
Raw biochar	None	-	-	-	0.30	10
US3-EH0-T0	None	-	-	-	0.55	10
US0-EH1:1-T2.5	TEPA	0.56	-	-	-	10
US0.5-EH1:1-M2.5*	MEA	1.74 ± 0.04	1.81	1.84	-	10
US0.5-EH1:1-PZ2.5	PZ	1.02	1.12	1.13	-	10
US0.5-EH1:1-D2.5*	DEA	1.05 ± 0.05	1.14	1.16	-	10
US0.5-EH1:1-T2.5	TEPA	2.04 ^a	-	-	-	10
US0.5-EH1:1-P2.5*	PEI	1.02 ± 0.08	1.12	1.13	-	10
US0.5-EH1:1-MT1:1*	MEA-TEPA	1.91 ± 0.02	-	-	-	10
US0.5-EH1:1-DT1:1	DEA-TEPA	1.45	-	-	-	10
US0.5-EH1:1-DP1:1	DEA-PEI	1.08	-	-	-	10
US0.5-EH1:1-TP1:1	TEPA-PEI	1.20	-	-	-	10
US0.5-EH1:1-DTP1:1:1*	DEA-TEPA-PEI	1.20 ± 0.04	-	-	-	10
US0.5-EH1:1-T2.5	TEPA	2.93	-	-	-	100
US0.5-EH1:1-MT1:1	TEPA	2.21	-	-	-	100

*Values are averages of duplicate runs ± standard deviation

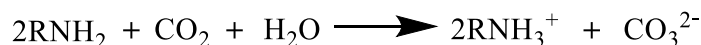
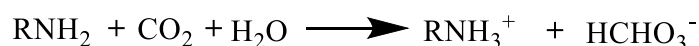
^aChatterjee et al. Fuel, 2018. **225**: p. 287-298

To study the effect of amine concentrations on CO₂ removal the amine loading was varied from 2.5-10 times the weight of the biochar. The results showed an increasing trend in adsorption capacity with amine loading. However, the increase in adsorption capacity was small after the initial increase of amine loading. Higher concentrations of impregnating amines during activation can supply more active sites but can also block the pores and result in lower adsorption values. This is in accordance to our previous research that demonstrated TEPA-activated biochar showed a maximal adsorption capacity (7 times higher than raw char) for CO₂

(2.04 mmol/g) with an optimal 2.5 times loading [146]. Therefore, in this study, sorbents were prepared with MEA, PZ, DEA, TEPA and PEI at the same 2.5 times total amine loading to investigate their effects on CO₂ adsorption capacity. The amine mixtures were set at a total 2.5 times loading to the weight of the biochar, with equal weight of the individual amines in the mixture.

Among the single amines, it can be observed from Table 3.6 that TEPA provided the maximum adsorption capacity (2.04 mmol/g), with MEA (1.74 mmol/g) notably stronger than the others. TEPA is aided by the five amino groups in its structure, and by its less viscous nature compared to PEI [185]. Among the blended mixtures, MEA-TEPA-activated biochar provided the maximum adsorption capacity (1.91 mmol/g), followed by DEA-TEPA, DEA-TEPA-PEI, TEPA-PEI and DEA-PEI.

Furthermore, the combinations MEA-TEPA and DEA-TEPA were aided by the presence of the hydroxyl groups in MEA and DEA. For example, hydroxyl groups are known to enhance CO₂ adsorption capacity on silica substrates as adsorbents [186]. To explain this effect, consider that the acid-base reaction of amines with carbonic acid O=C(OH)₂, formed by the addition of H₂O to CO₂, can sequester CO₂ in the form of either hydrogen carbonate or carbonate anions:



Alternatively, an amine can attack CO₂ covalently to form a carbamate anion, also balanced by an ammonium cation:



A possible role of alcohols in promoting these reactions is in offering hydrogen bonding

to stabilize the anionic product oxygens; O–H is a better hydrogen bond donor than N–H, so alcohols can perform this role better than amines. Another suggestion is that the alcohols aid in making the amine chains more flexible, making it easier for them to carry out the proton transfers required to attain the ionic products [186]. PZ may be hindered by the absence of hydroxyl groups as well as the lack of a 1° amine. Note that the balance of amino and hydroxyl groups matters: DEA had a low capacity in spite of two hydroxyls, since it has only a single 2° amine. The mixture of TEPA-PEI, without hydroxyl groups, had an adsorption capacity notably lower than the DEA-TEPA and MEA-TEPA mixtures. Another factor that affects sorption capacity is the low diffusion ability of the large PEI molecules, which could hinder their ability to effect proton transfers. Also, the more-viscous PEI (compared to the other amines) tends to form agglomerations on the surface of the sorbent, thus reducing active sites for adsorption (observed from Table 3.2). All of the PEI samples had low adsorption capacities.

Several of the runs were performed in duplicate and their standard deviations are included in Table 3.6. Standard deviations were in the range of 0.02-0.08, showing that the differences in adsorption capacity observed are significant.

3.4.2.2 CO₂ Adsorption with Amine Systems Activated by KOH

The adsorption capacities of KOH-amine activated samples are listed in Table 3.7. As shown in Table 3.3 (elemental analysis), pretreatment of biochar with KOH increased the %N in samples impregnated with amines, similar to the increase noted with EDC-HOBt activation. The CO₂ adsorption capacities were also much greater than that for raw biochar, although somewhat lower than for samples aminated with EDC-HOBt. This could be attributed to the destruction of some surface structure porosity due to application of the powerful base. This is also reflected in the surface area analysis (Table 3.2) where the surface area and pore volume were reduced for

KOH-aminated samples.

Table 3.7. Effect of KOH-Amine Mixture on CO₂ Adsorption Capacity at 70 °C and 10 vol% CO₂ Concentration

Sample Name	Adsorption capacity (mmol/g)	CO ₂ Concentration (vol%)
Raw Biochar	0.3	-
Effect of single and dual aminations		
US0.5-K1.5-M2.5	1.62	10
US0.5-K1.5-P2.5	1.00	10
US0.5-K1.5-D2.5	1.08	10
US0.5-K1.5-T2.5*	1.60 ± 0.05	10
US0.5-K1.5-DT1:1	1.38	10
US0.5-K1.5-TP1:1	1.12	10
US0.5-K1.5-M2.5	1.93	100
US0.5-K1.5-DT1:1	1.79	100

Note: * Value is the average of duplicate runs ± standard deviation

There remains the question of the extent of activation of KOH towards amination of the sonicated biochar. There is a report that solid NaOH can catalyze the alkylation of amines with alcohols via a hydride transfer from the corresponding alkoxide, forming an intermediate aldehyde [187]. However, this process requires high temperatures (> 180° C). It has also been reported that carbonyl groups in carbonaceous material are able to catalyze the same reaction through a “borrowing hydrogen” mechanism [188]. However, this process also requires a high temperature (> 130°). It may be that, through saponification of esters or alteration of the pore structure, the KOH provides more sites for hydrogen bonding of the impregnated amines and hydroxyamines with the biochar surface. Regardless, due to its simplicity, this technique may have wide application in sorbent synthesis. However, it will require further research and analysis to establish this procedure as a useful CO₂ capture technique.

Furthermore, as observed from the CO₂ adsorption result the adsorption capacity of the amine functionalized sorbent was enhanced in comparison with the pristine biochar at 70 ° C. This can be explained based on the differences of physical adsorption or physisorption, and chemical adsorption or chemisorption. Usually, physisorption is dominant at room temperature

over chemisorption. However, at elevated temperatures, chemisorption is more dominant than physisorption as a result of amine functionalization. Thus, even though the surface area and pore size reduced due to amine attachment, still improved capacity was attained at higher temperature, due to increase in the chemisorption process. The details discussion can be found in our previous study [146].

Additionally, in order to confirm the effectiveness of the developed activation technique, the adsorption capacity of the prepared adsorbent (present study) has been compared with the literature data as shown in Table 3.8.

Table 3.8. Comparison of Adsorption Capacity Obtained in Present Study with Literature

Support Material	Amine	Adsorption Capacity	References
Mesoporous Silica	TEPA	3.93	[189]
MCM-41	TEPA	5.39	[190]
Nanofibrillated Cellulose	N-(2-aminoethyl)3-aminopropylmethyldimethoxysilane	1.39	[191]
Saw dust biochar	MEA	1.02	[192]
Aminated graphene oxide	EDA, DETA, TETA	1.10	[120]
Palm Shell Activated Carbon	DEA	2.81	[193]
SBA-15	PEI	2.39	[194]
Nanocomposite sorbent	PEI	7.90	[185]
Mesoporous carbon	PEI-KOH	4.82	[24]
Pine-wood Biochar	TEPA	2.04	[146]
SBA-12 mesoporous silica	3-aminopropyl (AP)	1.04	[195]
Cotton stalk	Ammonia and CO ₂	2.25	[196]
Sawmill Residues	Aminopropyl triethoxysilane	3.70	[197]
Fly carbon	DETA, PEHA, PEI	1.56	[132]
Pine wood Biochar	TEPA	2.04	[146]
Pine wood Biochar	TEPA-MEA	1.91	This Study
Pine wood Biochar	MEA-KOH	1.61	This Study

It can be concluded from the table that the ultrasono-amine functionalized adsorbent material has comparatively higher adsorption capacity (2.04 mmol/g) than several adsorbents such as biochars, activated carbon, graphene oxide and SBA-12 [191], [195], [132]. However, the adsorption capacity of aminated biochar didn't show optimum adsorption capacity as found for mesoporous

silica functionalized with amines. This can be explained as a result of blocking the pores (primarily micropores) of carbon structure due to the introduction of nitrogen or other chemical functionalities [198]. This subsequently lowers the adsorption capacity. Whereas, for ordered mesoporous materials, because of ordered mesoporous structure with tunable pores, amines or other molecules can be easily accommodated without blocking the surface of the adsorbent owing to their higher adsorption capacity compared to microporous adsorbents[21].

3.5 Conclusions

The current study provides an analysis of the CO₂ adsorption potentials of biochar aminated with five different amines (MEA, PZ, DEA, TEPA, and PEI) and their binary (MEA-TEPA, DEA-TEPA, DEA-PEI, TEPA-PEI) and ternary (DEA-TEPA-PEI) mixtures coupled with ultrasonication and EDC-HOBt or (in 3 cases) KOH activation. Our previous study revealed that physical activation under ultrasound irradiation followed by chemical functionalization with TEPA leads to an elevated adsorption capacity (2.04 mmol/g at 0.10 atm. and 70 °C) compared to raw biochar (0.3 mmol/g at 0.10 atm. and 70 °C). This study investigates the effects of different amines that vary in the number of amine groups in their structure. The results showed that primary amine MEA with EDC-HOBt provided the highest adsorption capacity (1.74 mmol/g) after that of TEPA [146]. This is partly attributed to increased reaction rates for 1° amines such as MEA over 2° amines like PZ and DEA [199]. Functionalization with the MEA-TEPA mixture (with EDC-HOBt) led to 1.91 mmol/g of equilibrium sorption capacity. This indicated the synergetic effect between the hydroxyl in MEA and the amino groups present in TEPA to intensify CO₂ capture. For KOH activation, MEA-functionalized sorbent showed the highest equilibrium adsorption capacity of 1.62 mmol/g (5 times higher than raw char). However, the reaction with strong base resulted in the destruction of the surface structure for

functionalized sorbents, so the resulting char possessed lower sorption ability than EDC-HOBt-amine modified sorbents. Apart from the promising adsorption results, the sono-chemical technique is also very energy efficient since it is done at near room temperature. Hence, the developed ultrasono-amine functionalization technique provided a useful way for efficient functionalization of biochar to produce potential sorbents for CO₂ adsorption.

Author Contributions

Riya Chatterjee: Conducting the experiments, interpreting the results and writing the manuscript

Baharak Sajjadi: Idea of the work, interpreting the results and writing the manuscript

Wei-Yin Chen: Idea of the work and revise the manuscript

Daniell L Mattern: Interpreting the results and revise the manuscript

Nosa O. Egiebor: Revising the manuscript

Nathan Hammer: Conducting Raman Analysis

Vijayasankar Raman: Conducting SEM Analysis

CHAPTER IV

Impact of Biomass Sources on Acoustic Based Chemical Functionalization of Biochars for Improved CO₂ Adsorption

Riya Chatterjee, Baharak Sajjadi, Wei-Yin Chen, Daniell L. Mattern, Nathan Hammer, Vijayasankar Raman, Austin Dorris. Impact of Biomass Sources on Acoustic Based Chemical Functionalization of Biochars for Improved CO₂ Adsorption. Energy & Fuel (submitted)

4.1 Abstract

The present study investigates the impact of biomass origin on the properties of biochar and its interaction with different treatment conditions, CO₂ adsorption, and regeneration ability. The biochars were synthesized from eight biomasses- herbaceous (miscanthus and switchgrass), agro-industrial (corn stover and sugarcane bagasse) and crop residues (sorghum, wheat straw, rice straw and rice husk) and were subjected to three different treatment conditions: I. acoustic treatment using low frequency ultrasound, II. amination using the penta-amine and III. integrated sono-chemical activation. Adsorption studies revealed that sono-amination increased adsorption capacities up to 2-2.5 times that of physical or chemical activation techniques alone with the maximum improvements for herbaceous and agro-industrial residues over crop residues due to their large specific surface areas, high carbon and low ash content. Accordingly, miscanthus with increased nitrogen content after sono-amination (7.5 times that of raw miscanthus biochar) showed the highest adsorption capacity compared to any other biochar. The regeneration studies that were conducted on all the eight ultrasono-aminated samples showed 68% (crop residues) to 76% (herbaceous and agro industrials) retainment of the initial adsorption capacities after 15

cycles.

4.2 Introduction

Industrialization and fossil fuel combustion have increased the atmospheric CO₂ concentrations from pre-industrial levels of approximately 280 ppmv to the current level of approximately 390 ppmv [200]. The atmospheric CO₂ concentration is predicted to increase to 1000 ppmv and 2000 ppmv by the years 2100 and 2300, respectively, if the present energy utilization structure persists [201]. Such increases in CO₂ would lead to a reduction in pH and cause substantial chemical changes in seawater carbonate systems, including increases in HCO₃⁻ and increases in H⁺ and CO₃²⁻. Additionally, the increased level of CO₂ also resulted to increase global temperature that causes environmental degradation and climate change. So, it is of utmost important to reduce this green-house gas concentration to its earliest. Therefore, several remediation techniques [202] have been adopted including

- I. CO₂ capture from power plants and industries: This is primarily post combustion CO₂ capture and utilizes different amine-based solvents.
- II. CO₂ capture from air. This can be achieved with organics and metal carbonates and with the use of carbonaceous sorbents.

Among the described techniques CO₂ capture using solid carbonaceous adsorbents such as biochar (a form of char produced during biomass pyrolysis under anaerobic conditions) is gaining significant attention. Based on the origin or lignocellulosic constituents the biomass can be classified as herbaceous, agro-industrial, and crop based materials [203]. The further explanation on the classification has been described in the following section with its graphical representation and lignocellulosic compositional analysis in Figure 4.1 and Table 4.1 respectively.

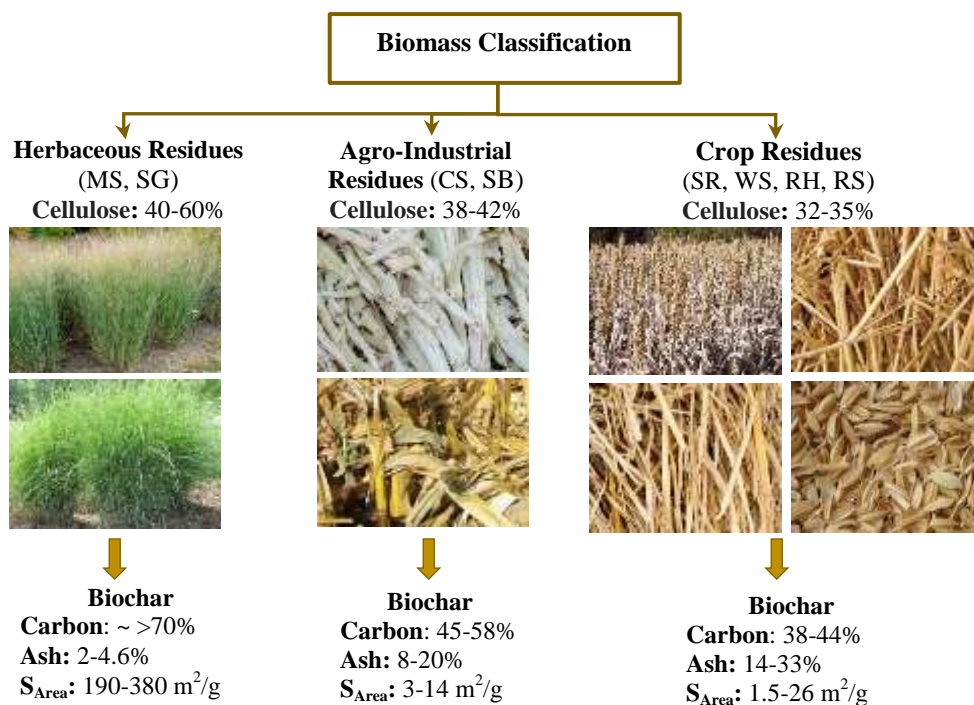


Figure 4.1. Schematic Representation of Biomass Classifications and the corresponding biochar

Table 4.1. Lignino-cellulosic Compositions of Different Biomasses

Biomass	Cellulose (wt.%)	Hemicellulose (wt.%)	Lignin (wt.%)	Ref
MS	40-60	20-40	10	[204]
SG	45	31.4	12	[205]
CS	38	26	19	[204, 206]
SB	42	25	20	[207]
SR	35.4	19.4	10.3	[206]
WS	38	29	15	[208]
RH	35	33	23	[209]
RS	32.1	24	18	[210]

- Agricultural Herbaceous Residue:* Miscanthus (MS) and switchgrass (SG) are high yielding, low cost materials that fall in this category. These biomasses are a rich source of cellulose (40-60%) that results in their natural enrichment in carbon content (>70%) [211]. Literature study revealed that miscanthus has low macronutrient concentrations (such as N, P and K) compared to switchgrass [212]. This leads to reduced values of %N and %ash content of

miscanthus biochars compared to switchgrass [212]. In addition, both these biochars possess low ash content (2-4.6%), high surface area, microporosity and micropore volume which make them highly suitable for adsorption of CO₂ [213-215].

- *Agro-Industrial Residues:* Both sugarcane bagasse and corn stover are agro-industrial residues and are inexpensive and readily available sources of lignocellulosic biomass. The biochars from SB and CS exhibit high microporosity and high chemical stability [216, 217]. As per literature study, it is evident that SB has higher %ash content and subsequently lower %carbon content than CS [218]. The macronutrient content (%N) for CS is higher than for SB [219, 220].
- *Crop Residues:* These are the remaining materials after crop is harvested and processed into usable resources and include sorghum (SR), wheat straw (WS), rice straw (RS) and rice husk (RH). Biochars derived from these residues have low carbon and high ash content (13-19%), indicating the presence of minerals such as alkali metals (Ca, Mg, K) [73] specifically for biochars derived from rice husk and rice straw show high amounts of silica [221]. As a result of that, these biochars exhibit high pH values [222-224].

As discussed above the characteristics of biochars change widely according to feedstock type that has been further emphasized in Table 4.2 that describes different physicochemical properties of biochars prepared from different origins.

Table 4.2. Physicochemical Properties of Different Biochars obtained from Literatures

Biochar	Pyrolysis T (°C)	C (%wt)	H (%wt)	O (%wt)	N (%wt)	S (%wt)	Ash (%wt)	Surface Area (m ² /g)	pH	Ref.
MS	600	46-90	2.3-5.9	6.7-48	0.31-0.33	0.09	2.3	381.5	10	[211, 214, 225, 226]
SG	600	82	2.4	14	1.2	0.30	4.6	188-260	9-11	[227-231]
CS	600	53-57	2.9	5.4	1.5	0.15	7.7-12	3.1	10	[215, 232-236]
SB	600	45-46	6.2	47.2	0.4	-	19	14.07	9	[62, 237-239]
SR	550	49	2.6	24.3	0.91	0.04	19	-	-	[240-242]
WS	575	49	2.3	37.7	0.97	-	22	20.2	10	[73, 243-245]
RH	650	42	5.3	30.6	0.38	0.17	33	1.5	5.6	[221, 243, 246, 247]
RS	600	39	6.1	10.7	1.3	-	14	25.6	6.5	[243]

As found from the literature, there are number of ways to activate biochar for the improvement of physical and chemical properties and CO₂ adsorption behavior such as by employing traditional physical activation technique [248]. Physical activation include partial oxidation in the presence of gaseous environments (air, CO₂, or steam) under very high temperature (>750 °C) making the process highly energy intensive [249]. In comparison to this, acoustic activation can be conducted at near room temperature within a very short duration of time, making the process efficient in terms of energy and time [250]. During acoustic irradiation the formation and collapse of vapor filled microbubbles during the alternate compression and rarefaction cycles of ultrasound leads to the exfoliation of the layered structure of graphitic clusters [251]. This phenomenon was first observed by Stankovich et al. where they found that a mild ultrasonic treatment ($f_c=78.6$ kHz, 150 W) of graphite oxide in water for 1 h exfoliates its layers and forms stable aqueous dispersions [252]. Based on this observation, the previous studies conducted by our group on sonolysis of biochars revealed that ultrasound promoted exfoliation of graphitic layers of biochars along with mineral leaching and carbon and hydrogen fixation (from CO₂ and water, respectively), resulting in significant increments in porosity,

surface area, and heating value of the biochar [109, 253]. Notably, the effectiveness of physical activation to improve the physical properties is found to be prominent for the biochar having high lignocellulosic contents. For instance, herbaceous and agro-industrial biochars have higher cellulose and hemicellulose contents than lignin so possess high carbon content and improved microporosity (both surface area and pore volume). But crop based biochars have increased lignin contents than cellulose-hemicellulose thus exhibit low surface properties and carbon contents. Thus, origin of feedstock plays a pivotal role on properties and subsequent activation technique. While aiming to maximize CO₂ capture capacity, the presence of nitrogenous compound (reflected by %N content) such as amine group plays an important role as a result of the acid-base interaction between CO₂ and amine which subsequently boosts the adsorption efficiency [254-256]. As found from Table 4.2, the nitrogen content also varies according to biomass feedstock origin and substrate type [257].

Hence, the present study applied acoustic based amination technique to improve physicochemical properties and adsorption capacities of biochars. In this regard at first, a low temperature (near ambient temperature) acoustic-amination process was developed followed by the optimization of process conditions such as ultrasound duration, activating agents ratio, effect of different amines (MEA, DEA, TEPA, PEI and PZ) etc. [146, 258]. The results obtained from these studies showed that ultrasono-MEA and TEPA functionalized pine wood derived biochars intensified their CO₂ adsorption capacities 5-7 times than that of raw char.

Next, it was aimed to study the importance of synergistic and antagonistic interaction of the developed method with biochar structure with particular focus on biomass origin since structural and chemical properties of biochars vary depending on the lignin, hemicellulose and cellulose contents which are governed by the feedstock sources. Thus, the main objectives of this study are

I. Determination of the importance of biochars' origin on CO₂ removal and II. Investigation of the response of each biochar to three different physicochemical activation processes, namely physical (ultrasonic irradiation), chemical (amine functionalization) and combined physico-chemical (ultrasono-amine) activation.

4.3 Materials and Methods

4.3.1 Materials

Eight different biomass feedstocks were obtained from the Idaho National Laboratory namely miscanthus, switchgrass, corn stover, sugarcane bagasse, sorghum, wheat straw, rice straw and rice husk. The chemicals utilized in functionalization were methanol, EDC, HOBt, and TEPA. All chemicals were obtained from Sigma-Aldrich. Hydrochloric acid-37% (Sigma-Aldrich), acetone (Sigma-Aldrich) and sodium hydroxide (Fisher Scientific) were used during the filtrations of the functionalized biochars. DI water used in the experimentation was obtained from Milli-Q ultrapure water tap (Millipore Sigma). All chemicals used were of analytical grade.

4.3.2 Experimental Method

4.3.2.1 Pyrolysis of Biochar

At first, the as-received biomasses were ground using an IKA MF10 basic continuous feed grinder and sieved using a Gilson SS 15D 8-in sieve shaker to particles of size range 75–250 μm. The sieved biomasses were dried under vacuum overnight at 60 °C prior to pyrolysis. Nickel-chromium-iron alloy Inconel crucibles were used for the pyrolysis. The crucibles were filled with biomasses, covered with lids and placed inside a muffle furnace (in triplicate) for pyrolysis. The covered crucibles were heated up to 600 °C with a 20 °C/min heating ramp under nitrogen flow. The temperature was held at 600 °C for 2 hrs. and then allowed to cool to room temperature under nitrogen flow.

4.3.2.2 Physical Activation of Biochar under Acoustic Treatment

For physical activation, 3 g of biochar was subjected to low frequency ultrasonic irradiation (QSonica sonicator model no. Q700) in 250 ml of water for 30 s. Our previous study demonstrated that 30 s of acoustic irradiation was enough to induce surface area enhancement [146]. In contrast, prolonged sonication diminished the effect of ultrasound on surface area enhancement, most likely through disarranging the orientation of the layered structures and blocking pores [146]. This observation is in accordance with the literature [113, 258]. The ultrasonicated biochar-water mixtures were subjected to the following chemical activation steps without further treatment.

4.3.2.3 Chemical Functionalization of Biochar with TEPA

Raw or physically activated biochar-water mixtures were treated with the coupling agents EDC-HOBt (3.375 g of each coupling agent for 3 g of biochar) [146]. EDC is highly soluble in water compared to the other coupling agents (such as dicyclohexylcarbodiimide – DCC) which makes its separation very easy. The additive HOBt was used to prevent an undesired side reaction that could reduce the yield of the product where the ratio of EDC: HOBt kept at 1:1 ratio. The EDC-HOBt-biochar mixture was kept under stirring for 24 hours at 35°C, then filtered and dried under vacuum at 60°C overnight. Next, the dried samples were suspended in methanol, and TEPA (2.5 times weight to the weight of biochar) was added to the suspension. The resultant mixture was stirred for 24 hours with gentle heating as before. Finally, the resultant mixture was filtered and washed in succession with 200 mL of 1N NaOH (3 times), 200 mL of 1N HCl (3 times) and 200 mL of acetone (1 time) and dried.

4.3.2.4 Characterizations of the Adsorbent

The following characterization techniques were applied to both raw and functionalized

chars. First, the surface morphology was determined using scanning electron microscopy (JSM-7200 FLV by JEOL). Textural properties such as specific surface area and pore volume were examined using BET sorptometry (Micromeritics TriStar II 3020, Malaysia). The adsorption isotherm study was conducted under liquid nitrogen environment at 77 K and the technique measures volume adsorbed by the sample as the relative pressure is gradually increased from 0 to 1. Then, the mesopore area and pore volume were calculated by the BET (Brunauer, Emmett and Teller) equation:

$$\frac{1}{v\left[\left(\frac{p}{p_0}\right)-1\right]} = \frac{c-1}{v_m c} \left(\frac{p}{p_0}\right) + \frac{1}{v_m c} \quad (4.1)$$

Where p , p_0 , v , v_m , c respectively represent equilibrium pressure of adsorbate at the temperature of adsorption, saturation pressure of adsorbate at the temperature of adsorption, adsorbed gas quantity, monolayer adsorbed gas quantity and BET constant.

The t-plot based on the de-Boer equation was also used to calculate micropore surface area and pore volume.

$$p = K_2 \frac{\frac{v}{v_m}}{1 - \frac{v}{v_m}} \exp\left[\frac{\frac{v}{v_m}}{1 - \frac{v}{v_m}} - K_1 \frac{v}{v_m}\right] \quad (4.2)$$

Where p , v , v_m , K_2 , K_1 respectively represent equilibrium pressure of adsorbate at the temperature of adsorption, adsorbed gas quantity, monolayer adsorbed gas quantity, parameter related to the gas-solid interaction which is function of temperature and the properties of the adsorbate.

Mesopore area is calculated by subtracting t-plot area from the BET surface area. In the similar way t-plot micropore volume is subtracted from total pore volume to get meso pore volume. Elemental compositions were determined through C, H, N, S, O, ash analysis (Huffman Hazen Laboratory, Colorado, USA). The changes of the chemical functional groups and the

chemical structure before and after activation were assessed using Fourier Transform Infrared (FTIR, Cary 660 FTIR Agilent) and Raman (LabRam HR Evolution) spectroscopies.

4.3.2.5 CO₂ Adsorption Studies

The CO₂ adsorption tests were conducted in a tubular reactor made of alumina oxide, which was placed inside a temperature-controlled furnace. The details experimental set up has been represented in Figures A1-A2 with the descriptions of each part and their functions. For each run, 2 g of biochar sample was placed inside the reactor, degassed using helium (99.99%) at a flow rate of 500 cm³ min⁻¹ at 378 K for 1 hour, and then cooled to 333 K. This temperature was kept constant throughout the course of the reaction. In the next step, the helium gas was switched to a CO₂-containing simulated flue gas of 10 vol.% CO₂ balanced with He at the same flow rate, and was allowed to interact with the adsorbent. The CO₂ concentrations before and after adsorption were measured by a CO₂ analyzer connected to the adsorption column. The detection limit for the CO₂ concentration is up to 20 vol.% with repeatability of 0.5% of full scale. The adsorption capacity of CO₂ after a certain time was then calculated using the following equation:

$$q_a = \frac{1}{M} \times \left[\int_0^t Q \times (C_0 - C) dt \right] \times \frac{1}{V_m} \quad (4.3)$$

where, q_a is the adsorption capacity for CO₂, mmol g⁻¹; M is the mass of adsorbent, g; Q is the gas flow rate, cm³ min⁻¹; C_0 and C are influent and effluent CO₂ concentrations, vol.%; t denotes the time, min; and V_m is 22.4 mL mmol⁻¹.

4.3.2.6 Regeneration Study

Thermal swing adsorption-desorption experiments have been conducted to determine the stability or the regeneration capacity of the adsorbents. To study this, ultrasono-amine functionalized adsorbents (prepared from all the eight different biomasses) have been used. Regeneration experiments were conducted by heating the adsorbent at the elevated temperature of 453 K under helium gas flow for 60 minutes followed by adsorption experiment at 333 K. For each adsorbent, 15 adsorption-regeneration cycles have been carried out.

4.4 Results and Discussions

4.4.1 Surface Area Analysis

Effect of Feedstock Origin: Surface area is one of those factors that significantly affects the adsorption capacity of solid sorbents. Table 4.3 represents the surface area and pore volume of raw, ultrasonically activated, aminated, and sono-chemically activated chars which are reported with the symbols R, US, Am, and US-Am, respectively. In terms of origins, micro and mesopore surface areas and volumes the order is as follows: herbaceous biochars (MS, SG) > agro-industrial residues (CS, SB) > crop residues (SR, WS, RH, RS).

This is consistent with the elemental compositions of the synthesized biochars that demonstrate a roughly increasing trend of %ash contents following the same order (Table 4.4). The ash generated during pyrolysis remains trapped inside the pores of the biochar, thus lowering the surface area [259]. The surface area trend can be further explained based on the inherent physical and chemical properties of different lignocellulosic biomasses. Lignocellulosic biomasses contain hemicellulose (40–50%), cellulose (20–40%) and lignin (10–40%) [260]. Decomposition of hemicellulose takes place mainly at 250–350°C, followed by cellulose at 325–400°C and lignin at 300–550°C [260]. The biochars that are primarily composed of cellulose and hemicelluloses, with lesser lignin contents, decompose easier and possess higher

surface areas [261].

Table 4.3. Surface Area Analysis of Different Biochar Samples (Raw, Ultrasonically, Chemically and Sono-Chemically Activated Biochars)

Sample Name	Micro ^a -Porosity		Meso ^b Porosity	
	Surface area (m ² /g)	Pore Volume (cm ³ /g)	Surface area (m ² /g)	Pore Volume (cm ³ /g)
Raw Biochars				
R-MS ^c	340	0.12	64	0.05
R-SG	324	0.11	61	0.05
R-CS	266	0.10	58	0.04
R-SB	220	0.10	40	0.03
R-SR	203	0.09	41	0.03
R-WS	179	0.07	39	0.03
R-RH	173	0.07	35	0.03
R-RS	152	0.06	33	0.03
Ultrasonically Treated Chars				
US-MS ^d	520	0.17	61	0.04
US-SG	486	0.14	58	0.04
US-CS	399	0.14	55	0.04
US-SB	341	0.12	37	0.03
US-SR	320	0.11	36	0.03
US-WS	307	0.10	32	0.03
US-RH	281	0.10	30	0.03
US-RS	242	0.08	22	0.02
Aminated Chars				
Am-MS ^e	170	0.07	50	0.04
Am-SG	169	0.07	42	0.03
Am-CS	158	0.06	40	0.03
Am-SB	109	0.04	28	0.03
Am-SR	112	0.04	28	0.03
Am-WS	111	0.04	25	0.02
Am-RH	92	0.02	27	0.02
Am-RS	90	0.02	22	0.02
Sono-Chemically Treated Chars				
US-Am-MS	207	0.09	39	0.03
US-Am-SG	210	0.09	43	0.03
US-Am-CS	170	0.07	42	0.03
US-Am-SB	150	0.06	26	0.03
US-Am-SR	138	0.06	28	0.03
US-Am-WS	116	0.04	29	0.03
US-Am-RH	107	0.04	23	0.02
US-Am-RS	106	0.04	23	0.02

^a micropores: d<2 nm and ^b mesopores: 2nm<d<50 nm; ^cR-raw; ^dUS-ultrasound; ^eAm- amine

As found in Table 4.2, herbaceous (MS, SG) and agro industrial residues (CS, SB) tend to have elevated cellulose and hemicellulose contents, indicating higher surface areas over crop residues (SR, WS, RS RH) that possess higher lignin and lower cellulose-hemicellulose contents.

Effect of ultrasound: Ultrasound activation significantly increased the surface area and pore volume of micropores in all biochars, without any exception. Ultrasound cavitation and its implications result in the exfoliation of the graphitic cluster of the biochar structure, leaching of mineral matters and opening of the pores (which otherwise remains blocked) and lead to enhancement of microporous surface area [109, 252, 253, 262, 263]. Sonication resulted in increased microporosity by up to 50-71% and the extent of increase followed this trend: crop residues: WS (71%) > RH (63%) > RS (60%) > SR (57%); agricultural residues: SB (55%) > CS (50%) and herbaceous residues: MS (53%) > SG (50%). This trend suggests that acoustic activation has a higher effect on biochar containing more mineral matter or ash (referring to Table 4.4). However, the overall trends for US-treated chars were the same as for raw chars; that is, the maximum and minimum surface areas were observed for miscanthus ($520 \text{ m}^2/\text{g}$) and rice straw ($242 \text{ m}^2/\text{g}$), respectively.

Unlike microporosity, mesoporous surface area was slightly reduced upon sonication due to the formation of small aggregates (that form micropores) and partial destruction of mesopores under ultrasonic irradiation [264]. As found in Table 4.3, MS possessed the maximum ($61 \text{ m}^2/\text{g}$) and RS the minimum ($22 \text{ m}^2/\text{g}$) mesoporous surface area. Biochar samples with highest and lowest surface areas (both microporous and mesoporous) also had the maximum and minimum pore volumes. For instance, US-MS had the highest microporous surface area ($520 \text{ m}^2/\text{g}$) and pore volume ($0.17 \text{ cm}^3/\text{g}$), whereas US-RS had the lowest surface area ($242 \text{ m}^2/\text{g}$) and pore volume ($0.08 \text{ cm}^3/\text{g}$). Similar trends were obtained for mesopore volume.

Effect of amination: Amines can be attached to the porous structure of biochar either through impregnation or through grafting. During impregnation, amine molecules are dispersed into the pores over internal and external surfaces through weak van der Waals forces [175].

The following decreasing trend for microporous and mesoporous surface areas and pore volumes can be obtained (Table 4.3) - herbaceous residues: MS > SG; agricultural residues: CS > SB; and crop residues: SR > WS > RH > RS (micropores) and SR > RH > WS > RS (mesopores). Reduction in surface area corresponds to quantity of amines attached and consequently to improved adsorption capacity.

Effect of sono amination (compared to raw and aminated biochar): Sono-aminated biochars showed lower surface areas than raw chars, but the values were notably higher than aminated chars (without acoustic treatment). Generally, the sono-aminated biochars had 4-38% higher surface areas than aminated BC's (without acoustic treatment). This is because of the acoustic treatment which greatly enhanced microporous surface area, before it was lowered by amination. Consistent with the previous trend, MS exhibited the maximum (207 m²/g) and RS the minimum (106 m²/g) surface area with reductions of 39% and 30% with respect to raw char, but increases of 22% and 18% compared with aminated chars. On the other hand, mesoporous surface area showed a different trend because of its reduced value after sonication, which would lead to further lowering of the surface area after amine grafting, with reductions of 28-39% with respect to raw and 2-22% with respect to aminated chars.

Hence, surface area analysis along with the adsorption isotherms revealed that herbaceous biochars provided the maximum surface area and porosity than agro-industrial and crop based chars.

4.4.2. SEM Analysis

Surface morphology of the raw biochars (prepared from different biomass sources) and ultrasound activated biochars are presented in Figures 4.2-4.4. Herbaceous biomasses such as raw MS and SG both exhibited (Figures 4.2a and 4.2c) structural similarity, having smooth and

non-porous surfaces. As observed from their surface morphology, these samples possessed a comparatively thicker tubular structure (see arrows in Figure 4.2a; ca. 100 μm) than agro industrial and crop based biochars (for example, see arrows in Figure 4.4b, ca. 10 μm). When exposed under ultrasound irradiation, the induced microjets penetrate the structure, resulting in significant increment of surface porosity as observed in Figures 4.2b and 4.2d.

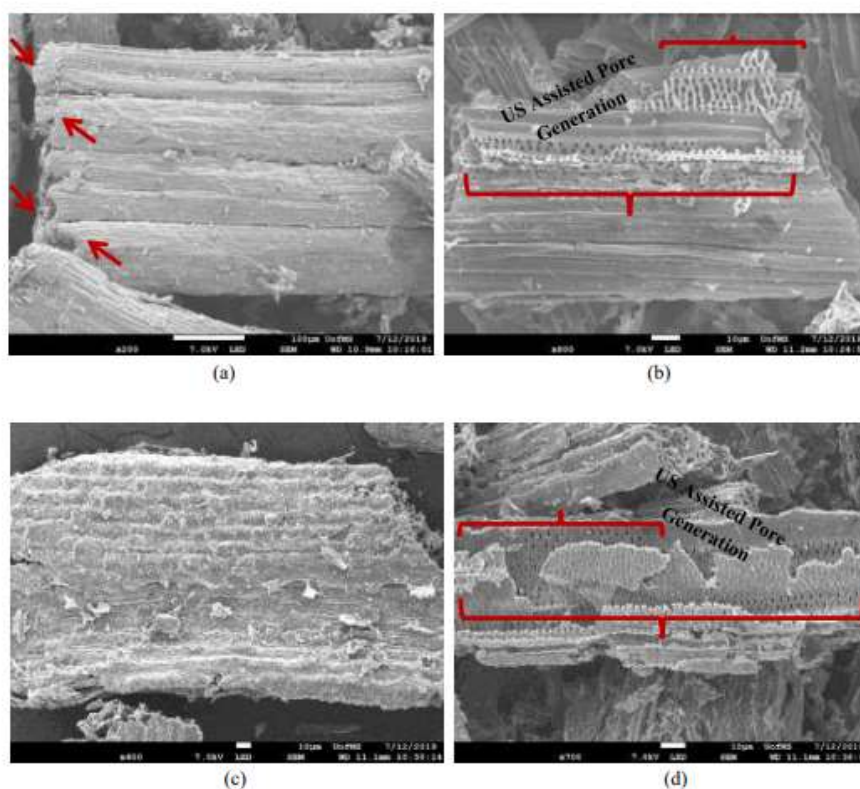


Figure 4.2. SEM images of Herbaceous Biochars (a) R-MS; (b) US-MS; (c) R-SG and (d) US-SG. Note: US- Ultrasound

Alteration and disarrangement of the layer was less pronounced for these chars; thus a uniform pore formation and opening of porous structure was observed for MS and SG (shown by the arrows in Figures 4.2b and 4.2d). This is consistent with the surface area analysis (Table 4.3) that demonstrated MS and SG possessed the highest microporous surface area and pore volume upon ultrasonication. These properties favor CO_2 adsorption capacity; thus MS and SG

possessed maximum adsorption capacities compared to other biochars.

Figures 4.3a and 4.3c describe SEM images of raw CS and SB biochars. The surface layers of these biochars are thinner than those of MS and SG. As a result of this the ultrasound waves disarrange the biochar structure significantly than the herbaceous residues, as seen in Figures 4.3b and 4.3d (pores are highlighted using red arrows).

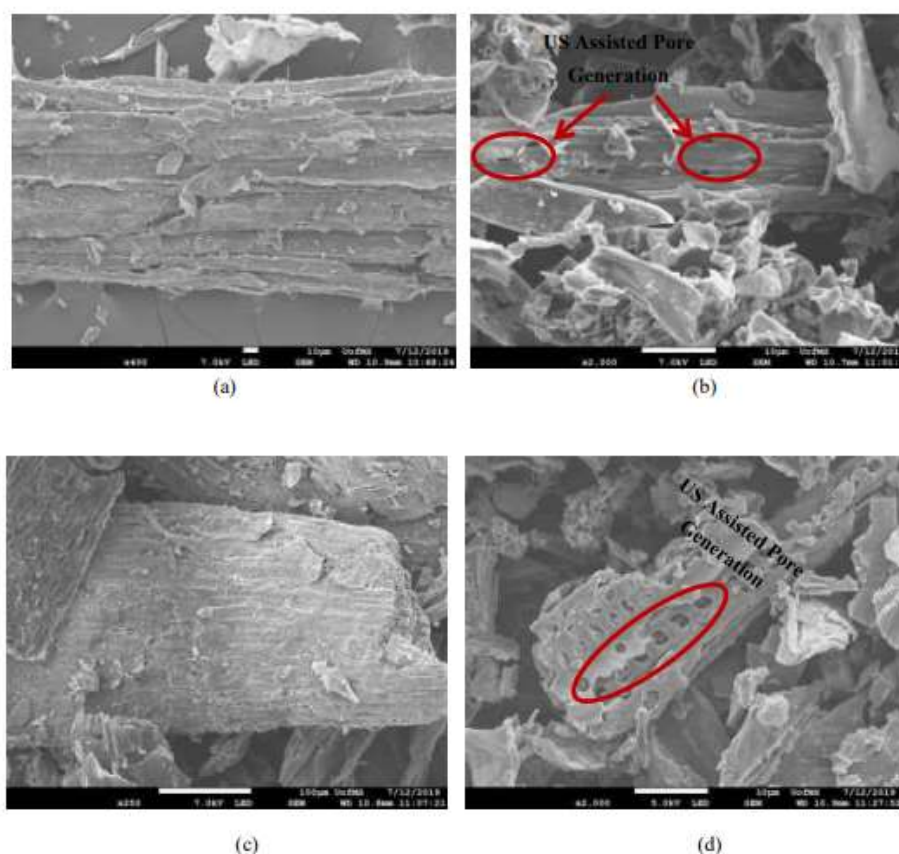


Figure 4.3. SEM images of Agro-Industrial Biochars (a) R-CS; (b) US-CS; (c) R-SB and (d) US-SB
As found from the Figures 4.3b and 4.3d, CS and SB showed low porosity along with the severe structural deformation under sonication. Notably, for SB, the pores that formed got disrupted (Figure 4.3d), resulting in low microporous surface areas and pore volumes (Table 4.3) and significant ash reduction (Table 4.4). As a result, the biochars of this category showed intermediate CO₂ adsorption capacities.

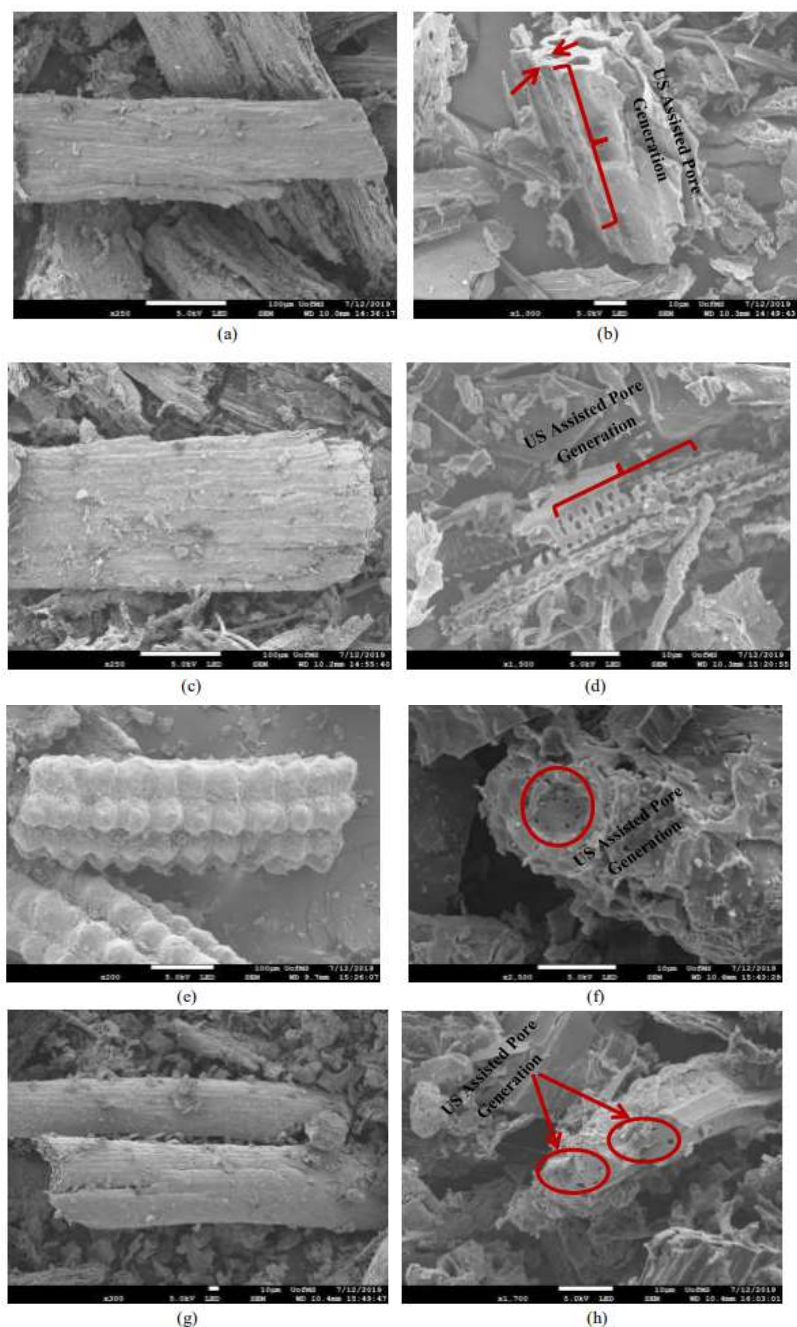


Figure 4.4. SEM images of Crop Biochars (a) R-SR; (b) US-SR; (c) R-WS; (d) US-WS; (e) R-RH; (f) US-RH; (g) R-RS; (h) US-RS

Figures 4.4a, 4.4c, 4.4e, and 4.4g portray surface morphologies for raw SR, WS, RH and RS samples. As per the figures, SR, WS and RS showed similarity in structure. Notably, RH had

swollen surfaces attributed to its high silica content. Similar to agro-industrial residues, these chars also possessed relatively weak structures. Thus the raw chars underwent significant disarrangement when exposed to acoustic field (Figures 4.4b, 4.4d, 4.4f, 4.4h), resulting in small fragments and destruction of porosity (Figure 4.4d) with significant reduction in ash contents. As a result, the obtained surface area was very low, consistent with their limited adsorption capacity. Thus, the SEM images revealed that herbaceous biochars have more rigid structure compared to agro-industrial and crop based chars that promote uniform pore generation under acoustic field and enhanced CO₂ adsorption capacities.

4.4.3 Elemental Analysis

Effect of Feedstock Origin: Elemental compositions of raw biochars and biochars activated under different conditions (ultrasonically, chemically, or ultrasono-chemically), as well as their organic-only compositions omitting ash, are presented in Tables 4.4 and 4.5, respectively. The results (Table 4.4) show that raw herbaceous biochars (MS and SG) had a higher %C content (77-82%) and lower %ash content (4.35-12.78%) compared to the most of the other chars (except CS for %ash). The %C followed a similar trend for organic-only composition (Table 4.5). Intense carbon concentration of MS and SG can be ascribed to their rich cellulose content (Table 4.2). For both chars, %O and %H content was found to be between 9.68-11.2% and 2.04-2.32%, respectively. The %N content of MS-biochar was about half that of SG-biochar because of the lower macronutrient concentrations (such as N, Ca, K) of MS in comparison to SG [212]. This higher carbon and lower nitrogen content of MS results in its high C/N value (343) relative to SG (158) as found from Table 4.5. The low macronutrient concentration of MS further leads to its low %ash content and pH value (8.77) compared to other chars (> 9.48). These results are consistent and comparable with the literature [213, 265].

Agro-industrial residues (raw CS and SB) had %C contents between 68.10-74.47% (Table 4.4). However, bagasse showed higher %ash content (19.78%) than corn stover (12.00%) despite the higher pH for CS (11.56) compared to SB (9.48). These observations are in accordance with the literature as discussed in Table 4.1. Mineral content of CS primarily consists of Ca, Mg and K whereas SB mostly consists of Zn, Fe and K [220, 265]. The presence of minerals such as Ca and Mg can significantly increase the pH of biochars, which has been observed for CS despite its low ash content [266]. Both of these biochars had considerably high carbon content (though lower than that in herbaceous biochars) with comparable oxygen and hydrogen content. The %N content of CS was higher than SB as a result of the higher macro element content (%N) of CS biomass [219, 220]. This resulted in a higher C/N ratio for SB (162) than for CS (107).

Crop residues tend to have comparatively lower %C and higher %ash contents than the two preceding biochar categories. Biomass combustion research has shown that feedstocks containing more silica have relatively high slagging tendencies and relatively high ash content [267]. Silica content (RH > RS > WS) and alkaline elements (Na, K, Ca, Mg) contribute to high ash and pH values [268, 269]. Thus, WS, RH and RS exhibited higher ash contents than SB and accordingly lower carbon contents, with pH in the range of 9.9-11.54. In crop residue-based biochars, RH (with the highest silica content) represented the lowest pH value, though it contained the maximum ash. In contrast, SR, with the lowest ash percentage, had the highest pH (11.72), since it is a rich source of minerals like Ca, Mg, K [266, 270]. A similar trend was also observed for CS, which showed low ash (12%) but high pH (11.56) [17]. On the other hand, elemental nitrogen contents of this group showed more elevated values than herbaceous and agricultural based biochars, except for RH. As a result, RH exhibited the highest C/N ratio in this

group, followed by SR, WS and RS.

Effect of ultrasound: As already stated, the cavitation phenomenon exfoliates biochar structure and leaches out mineral matters, thus lowering ash content and increasing carbon content [271]. As might be expected, biochars with comparatively higher ash contents, such as WS, RH and RS (crop residues), showed significantly greater ash loss (losing from 14 to 19 %ash) under ultrasound irradiation in comparison to herbaceous (MS, SG) and agro-industrial (CS, SB) biochars, along with SR (the crop residue having the lowest ash content), that lost between 0.4 and 3.3 %ash. The substantial ash removal caused significant increases of %C and reductions of %O content in most biochars. Oxygen reduction could be attributed to removal of inorganic oxygen of mineral compounds. Similar results were also found in our previous studies [109, 253, 263]. However, CS and RS showed %O increments (Table 4.5). The reason for oxygen increase may be related to increased oxygen functionality as a result of exfoliation of biochar structure [253]. Increases in %O content of CS and RS subsequently reduced its percentage of C (Table 4.5). In addition, the physically activated biochars showed slight increments of %N content, compared to raw biochars, in herbaceous residues MS and SG, and agro-industrial biochar CS (Table 4.5). On the other hand, reduction in nitrogen content was observed in crop residue biochars (Table 4.5). Because of their slight enhancements in %N content, MS, SG, and CS biochar samples showed reduced C/N ratios, while the opposite trend was observed in SB, SR, WS, RH and RS chars.

Effect of amination: TEPA-aminated biochar samples without sonication showed mineral (ash) leaching and subsequent variations in %C content. Removal of some ash from the biochar structure could be attributed to the washing away of mineral contents of the biochars during aqueous modification procedures [170]. As expected, the %N content of TEPA-functionalized

samples increased in the range of 1.4 - 4 times compared to raw chars (Table 4.5). Therefore, the C/N ratio of TEPA-treated samples showed a notable reduction compared to raw char as a result of incorporation of TEPA (C/N = 1.37). Following amination, the %N was lowest for the herbaceous residues (1.2-1.4%), higher for the agro-industrial biochars (1.4-1.6%), and, except for RH (1.4%), highest for the crop residues biochars (2.1-3.5%) with the order of (Table 4.5): RS>WS>SR>SB>RH=CS=SG>MS.

Effect of sono amination (compared to raw biochar): Sono-amination resulted in increased ash contents for three of the samples (MS, SG, WS) with respect to raw chars, exceptionally so for MS and WS. The increased ash contents for these chars are associated with a significant reduction of %C. For the other sono-chemically treated biochars, a reduction of ash content and an accompanying increase in %C were observed, exceptionally so for SB, SR, and RH. As a result of amalgamated sono-chemical treatments, most activated samples showed somewhat increased values of %H compared to raw chars, excluding RH (Table 4.5). TEPA functionalization resulted in increased nitrogen content for all the biochar samples. Sono-aminated RH, WS and MS showed the highest gains in %N content and SR showed no change with the following overall order and %increment of nitrogen content for the samples, based on Table 4.5: RH (1.7) > WS (1.6) > MS (1.5) > RS (1.2) > SG (0.9) > CS (0.6) = SB (0.6) > SR (0). In addition, for CS, SB, RH and RS, amine grafting slightly lowered %O content (compared to raw BCs) because TEPA has no oxygen (Table 4.4). Also, for SR and RH the significant reduction in %ash content resulted in overall increases of %C, %H, %O and %N (Table 4.4).

Effect of sono amination (compared to aminated biochar): The %C content of sono-aminated chars showed some fluctuations compared to aminated ones; however, organic analysis (omitting ash content, Table 4.5) suggested that sono-amination did not significantly change the

%C content of biochar compared to aminated chars (without US). Similarly, oxygen and hydrogen contents of sono-aminated samples did not change significantly compared to the aminated ones.

Table 4.4. Elemental compositions (dry basis) of Different Biochar Samples (Raw, Ultrasonically, Chemically and Sono-Chemically Activated Biochars)

Sample	C content (% wt.)	H content (% wt.)	N content (% wt.)	O content (% wt.)	S content (% wt.)	Ash content (% wt.)	pH
Raw Biochars							
R-MS	82.35	2.32	0.28	11.22	0.03	4.35	8.77
R-SG	77.00	2.04	0.57	9.68	0.03	12.78	10.56
R-CS	74.47	2.24	0.81	11.82	0.09	12.00	11.56
R-SB	68.10	1.90	0.49	10.08	0.03	19.78	9.48
R-SR	67.76	1.87	1.09	10.51	0.09	18.84	11.72
R-WS	66.18	1.60	1.27	9.92	0.13	23.16	11.54
R-RH	49.30	1.67	0.32	10.10	0.02	40.15	9.91
R-RS	50.17	1.49	1.41	9.57	0.23	38.68	11.06
Ultrasonically Treated Chars							
US-MS	86.91↑↑	1.99↓	0.55↑	6.65↓↓	0.03	3.73↓	
US-SG	79.67↑	0.87↓	0.64~	5.74↓	0.08	12.42↓	
US-CS	72.28↓	2.64↑	0.90~	14.51↑	0.09	10.88↓	
US-SB	73.39↑↑	1.75↓	0.50~	7.19↓	0.05	18.57↓	
US-SR	74.31↑↑	1.87~	1.04~	7.47↓↓	0.04	15.52↓↓	
US-WS	81.35↑↑	1.73↑	1.27~	6.53↓↓	0.08	9.09↓↓	
US-RH	65.36↑↑	1.97↑	0.18↓	11.22↑	0.05	23.95↓↓	
US-RS	57.75↑↑	2.32↑	0.64↓	22.81↑↑	0.01	20.10↓↓	
Aminated Chars							
Am-MS	82.44~	2.49↑	1.12↑	11.02↓	0.03	3.31↓	
Am-SG	78.00↑	2.16↑	1.30↑	9.74~	0.06	7.84↓↓	
Am-CS	72.81↓	2.06↓	1.16↑	9.57↓	0.02	9.10↓	
Am-SB	68.87↑	1.93~	1.31↑	9.74↓	0.03	18.82↓	
Am-SR	71.78↑↑	2.10↑	1.83↑	10.71↑	0.06	15.60↓↓	
Am-WS	67.85↑	1.77↑	1.89↑	10.53↑	0.08	19.29↓↓	
Am-RH	51.18↑	1.62~	0.89↑	9.61↓	0.01	38.55↓	
Am-RS	52.15↑	1.71↑	2.31↑	9.85↑	0.08	35.69↓	
Sono-Chemically Treated Chars							
US-Am-MS	70.16↓↓↓↓	2.13↓	1.5↑↑	10.09↓↓	0.03	17.47↑↑↑↑	
US-Am-SG	69.71↓↓↓↓	2.06~↓	1.25↑~	10.37↑↑	0.09	17.38↑↑↑↑	
US-Am-CS	77.00↑↑↑	2.57↑↑	1.41↑↑	10.92↓↑	0.06	7.90↓↓↓	
US-Am-SB	78.11↑↑↑↑	2.24↑↑	1.12↑↓	10.15~↑	0.03	8.91↓↓↓↓	
US-Am-SR	81.12↑↑↑↑	2.60↑↑	1.25↑↓	12.80↑↑	0.02	3.17↓↓↓↓	
US-Am-WS	53.58↓↓↓↓	1.81↑~	2.10↑↑	8.48↓↓	0.10	36.00↑↑↑↑	
US-Am-RH	71.45↑↑↑↑	2.27↑↑	1.96↑↑	11.52↑↑	0.09	15.64↓↓↓↓	
US-Am-RS	52.09↑~	1.75↑~	2.25↑~	9.22↓↓	0.10	37.34↓↓	

Note: ↑ increase (0.1-3%); ↓ decrease (0.1-3%); doubled arrows, significant change (> 3%), ~ not significant change (<0.1%), ■ compared to raw BC, ■ compared to aminated BC.

The slight increase or reduction of O content is mainly observed due to ash changes in the

carbonaceous structure of the biochars. %N contents of physico-chemical activated chars showed increases compared to aminated biochars in most cases because sono activation further aided in attaching more amine moieties by increasing surface area.

Table 4.5. Organic compositions (dry ash free basis) of Different Biochar Samples (Raw, Ultrasonically, Chemically and Sono-Chemically Activated Biochars)

Sample	C content (% wt.)	H content (% wt.)	N content (% wt.)	O content (% wt.)	S content (% wt.)	C/N
Raw Biochars						
R-MS	85.6	2.4	0.3	11.7	0.03	343
R-SG	86.2	2.3	0.6	10.8	0.03	158
R-CS	83.3	2.5	0.9	13.2	0.10	107
R-SB	84.5	2.4	0.6	12.5	0.04	162
R-SR	83.3	2.3	1.3	12.9	0.11	73
R-WS	83.7	2.0	1.6	12.5	0.16	61
R-RH	80.3	2.7	0.5	16.4	0.03	180
R-RS	79.8	2.4	2.2	15.2	0.37	42
Ultrasonically Treated Chars						
US-MS	90.4↑↑	2.1↓	0.6↑	6.9↓↓	0.03	184
US-SG	91.6↑↑	1.0↓	0.7↑	6.6↓↓	0.09	145
US-CS	79.9↓↓	2.9↑	1.0↑	16.1↑	0.10	94
US-SB	88.5↑↑	2.1↓	0.6~	8.7↓↓	0.06	171
US-SR	87.7↑↑	2.2↓	1.2↓	8.8↓↓	0.05	83
US-WS	89.4↑↑	1.9↓	1.4↓	7.2↓↓	0.09	75
US-RH	83.0↑	2.5↓	0.2↓	14.2↓	0.06	424
US-RS	69.1↓↓	2.8↑	0.8↓	27.3↑↑	0.01	105
Aminated Chars						
Am-MS	84.9↓	2.6↑	1.2↑	11.3↓	0.03	86
Am-SG	85.5↓	2.4↑	1.4↑	10.7↓	0.07	70
Am-CS	85.0↑	2.4↓	1.4↑	11.2↓	0.02	73
Am-SB	84.1↓	2.4~	1.6↑	11.9↓	0.04	61
Am-SR	83.0↓	2.4↑	2.1↑	12.4↓	0.07	46
Am-WS	82.6↓	2.2↑	2.3↑	12.8↑	0.10	42
Am-RH	80.8↑	2.6↓	1.4↑	15.2↓	0.02	67
Am-RS	78.9↓	2.6↑	3.5↑	14.9↓	0.12	26
Sono-Chemically Treated Chars						
US-Am-MS	83.6↓↓	2.5↑↑	1.8↑↑	12.0↑↑	0.04	55
US- Am-SG	83.5↓↓	2.5↑↑	1.5↑↑	12.4↑↑	0.11	65
US-Am-CS	83.7↑↓	2.8↑↑	1.5↑↑	11.9↓↑	0.07	64
US-Am-SB	85.2↑↑	2.4~ ~	1.2↓	11.1↓↓	0.03	81
US-Am-SR	83.0↓~	2.7↑↑	1.3~↓	13.1↑↑	0.02	76
US-Am-WS	81.1↓↓	2.7↑↑	3.2↑↑	12.8↑~	0.15	30
US-Am-RH	81.9↑↑	2.6↓~	2.2↑↑	13.2↓↓↓	0.10	43
US-Am-RS	79.6↓↑	2.7↑↑	3.4↑↓	14.1↓↓	0.15	27

Note: ↑ increase (0.1-3%); ↓ decrease (0.1-3%); doubled arrows, significant change (> 3%), ~ not significant change (<0.1%), ■ compared to raw BC, ■ compared to aminated BC

The only significant reductions of amine grafting compared with amination alone were observed in sono-aminated SB and SR (Table 4.5).

Comparing the results of elemental analysis from both Tables 4.4 and 4.5, it can be inferred that the combined acoustic-amine activation approach was effective in terms of increasing the nitrogen content of biochars owing to their modified textural properties under ultrasound irradiation, which subsequently improved the functionalization efficiency.

4.4.4. FTIR Analysis

Effect of Feedstock Origin: FTIR spectroscopy is an analytical technique that can identify the changes in surface functional groups of biochar. FTIR spectra of raw, ultrasonically activated, amine activated and sono-chemically activated samples are presented in Figures 4.5-4.8. To have a correct comparison of the intensity of the peaks, the baselines of the graphs were revised in Origin lab (Version 2019b). The origin plots are shown in Appendix G, Figures G1-G4. Thermal destruction of cellulose and lignin during pyrolysis results in the exposure of aliphatic $-\text{CH}_2-$, hydroxyl $-\text{OH}$, and $\text{C}=\text{O}$ functional groups in biochars [272]. As a result of that, all raw biochars showed O-H stretching vibrations of hydrogen bonded hydroxyl groups at $3300\text{-}3600\text{ cm}^{-1}$. The source of the unusual asymmetric peak around 2600 cm^{-1} is unclear. A peak at 2300 cm^{-1} is attributed to CO_2 absorption [273]. A peak around 2100 cm^{-1} is likely an overtone of the C-O peak near 1050 cm^{-1} . A peak at 1600 cm^{-1} is ascribed to carboxylate ($\text{COO}-$), 1° amine N-H bending, or aromatic C=C stretch [274], and alkyl CH bending can appear around 1400 cm^{-1} [275]. The peak in the region of 1026 cm^{-1} is typical of C-O stretching vibrations (which suggests the pyranose C-O structures from cellulose were preserved to some extent after pyrolysis) and/or the CNH_2 stretch of an aliphatic primary amine [276]. Aromatic C-H deformation in the region $465\text{-}832\text{ cm}^{-1}$ indicates the presence of aromatic hydrogen and a

greater degree of aromaticity of the sample [225, 277-280].

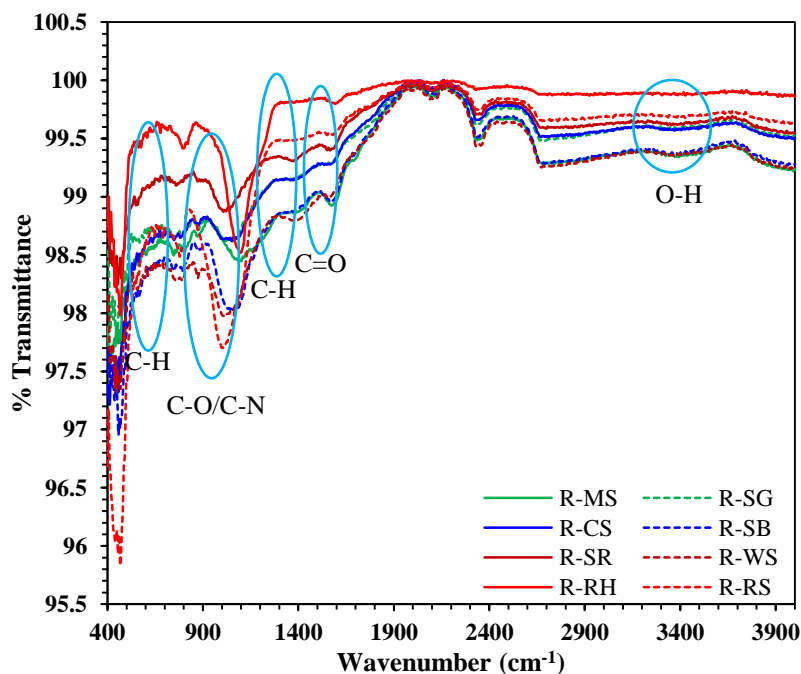


Figure 4.5. FTIR Spectra of Raw Biochar Samples The transmittance of all raw biochar samples is reported in 400-4000 cm^{-1} range. Strong peaks at 1100, 1600 cm^{-1} and 3300-3600 cm^{-1} are ascribed to C-O, C=O and -OH stretching

Raw biochar samples showed strong C-O stretching vibrations in the region 1000-1200 cm^{-1} with the following order: RS>RH>SB>WS>MS>SR>CS>SG (Figure G1). With the exception of RS, RH, and SG, this roughly follows the trend of ligninocellulosic compositions given in Table 4.2. The strong peak for RH in the region 1000-1100 cm^{-1} is partly due to the presence of a high amount of silica that overlaps the C-O peak [276, 281]. The same region for RS may be partly attributed to 1° amine C-N stretch, which correlates to its elemental composition that shows very high %N (highest among all raw chars) [276]. In addition, the COO^- (carboxylate) peak at 1600 cm^{-1} is strong for the MS sample, which is consistent with the high O content of this biochar (Table 4.4).

Effect of ultrasound: The spectra of physically activated biochar samples (Figs 4.6 and

G2) showed lowered % transmittance compared to raw samples which can be explained because of the reduced particle size upon sonication [282]. Moreover, sonication resulted in the peaks becoming more distinct and intense. For instance, the peaks between 1500-1700 cm^{-1} (C=O) and 3300-3600 cm^{-1} (O-H group) became more intense, as did the CO_2 signal at 2300 cm^{-1} and the peaks for C-H (at 832 cm^{-1}) and C-H (at 1400 cm^{-1}). As per the figure, C-H deformation at 800 cm^{-1} is more prominent in crop based biochars than agro-industrial and herbaceous based biochars. These results are consistent with the textural property analysis (Table 4.3) of ultrasonically treated biochars that showed the following trend for % enhancement of microporous surface area and its corresponding pore volume: crop residues: (WS>RH>RS>SR) > agricultural residues: (SB>CS) > herbaceous residues: (MS >SG).

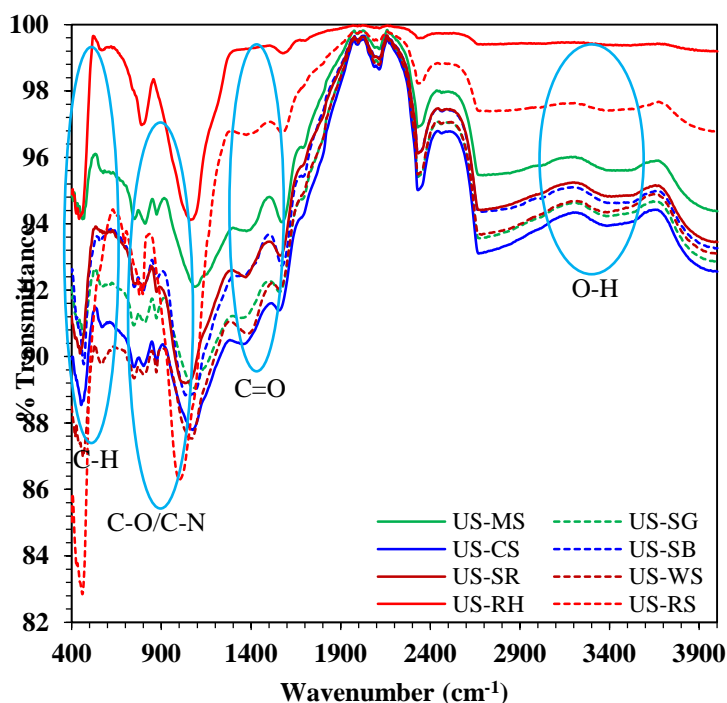


Figure 4.6. FTIR Spectra of Physically Activated Biochar Samples. The spectra show similar peaks as observed for raw biochars samples. However, acoustic treatment made the peaks more intense and distinct. For instance, peaks at ~ 800 and 1000 cm^{-1} (attributed as aromatic C-H deformation and -COOH group) became stronger and visible upon sonication. Similar behavior has been observed for peak at $3300\text{-}3600 \text{ cm}^{-1}$ (-OH stretching) that further demonstrate the importance of sonication, exfoliating biochar structure and making oxygen functionalities

available

Effect of amination: Effect of amination (no ultrasonication) on surface functional groups can be observed from Figures 4.7 and G3. The peak in region $\sim 1600-1700\text{ cm}^{-1}$ was intensified, indicating possible incorporation of NH_2 groups (Figure G3). A similar trend was observed for IR peaks for agro-industrial based chars CS and SB. In addition, the strong peak at $1000-1100\text{ cm}^{-1}$, which is partly attributed to the attachment of aliphatic amine, is intense for all aminated biochar samples, except for aminated MS and RS that didn't show any significant change in peak intensity. On the other hand, increased nitrogen content of aminated MS, SB and RH compared to raw samples is consistent with their strong IR peaks observed at 1600 cm^{-1} (NH_2) and 1100 cm^{-1} (C-N).

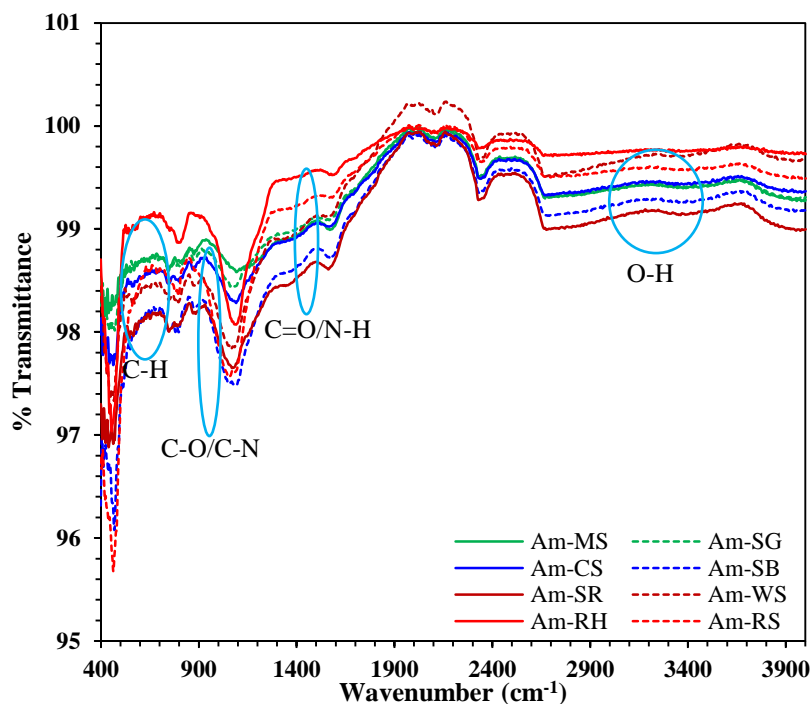


Figure 4.7. FTIR Spectra of Chemically Activated (no US) Biochar Samples. The treatments were done in the presence of amine only. These tests were intended to determine the effect of amine alone on the surface functionalities of biochars. The treatments resulted to the changes in the IR peaks primarily for hydroxyl group in region of $3300-3600\text{ cm}^{-1}$, carbonyl at 1605 cm^{-1} and formation of new bonds at $1000-1200$ and $1500-1600\text{ cm}^{-1}$.

Effect of sono amination (compared to raw biochar): The spectra of sono-aminated chars are depicted in Figures 4.8 and G4. As discussed earlier, the intensified peak around $\sim 1100\text{ cm}^{-1}$ (C-N bond) is because of attachment of aliphatic amine. This peak follows the trend of RS>WS>CS>SG>MS>SR>SB>RH, with prominent changes for SG and CS. A sharp peak around 1600 cm^{-1} is observed due to contributions from COO^- and NH_2 groups for MS and CS. Comparing these trends with elemental analysis it can be suggested that MS and CS showed significant improvement in nitrogen content.

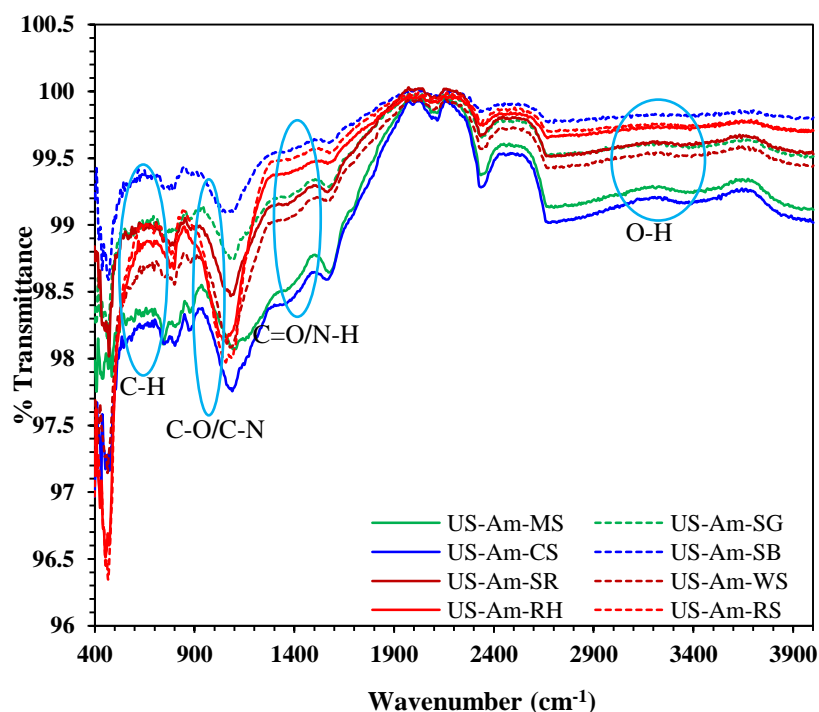


Figure 4.8. FTIR Spectra of Sono-Chemically Activated Biochar Samples. The activation was done physico-chemically i.e. first physical activation in presence of acoustic field followed by chemical functionalization using amine. The peaks do not have significant changes compared to the aminated samples. The only observed difference is the formation of new bonds for C-N and N-H.

Effect of sono amination (compared to aminated biochar): Mostly, the spectra of sono-aminated samples have similar trends as those observed for aminated samples. The observed differences can be attributed to the variation in intensity of the peaks as a result of the attachment

of higher number of amine moieties following activation. Strong C-N stretch attributed to aliphatic amine has been observed in region $1100\text{-}1200\text{ cm}^{-1}$ for most of the sono-aminated samples, except that SB and SR show weaker peaks than aminated-only chars (Figure G4). Peaks at 1600 cm^{-1} may be stronger for ultrasono-aminated samples than for aminated chars. Accordingly, this reflects the incorporation of NH_2 groups, with emphasis on MS and CS. Comparing the IR spectra of sono-aminated chars with their %N content leads to the conclusion that MS, CS, WS and RS showed intensified nitrogenation.

Thus, the FTIR spectrum also corroborate sono-amination resulted to attach more amines than amination alone that subsequently improve adsorption capacities of the activated chars.

4.4.5 Raman Analysis

The Raman spectra of raw and activated biochars under the different treatment conditions (ultrasonically activated, amine activated and sono-chemically activated) are demonstrated in Figures 4.9-4.12. Raman spectroscopy has been widely used to evaluate the microstructure of carbon materials, particularly the distribution and state of sp^2 -bonded (aromatic) carbon, which is embedded in a disordered and amorphous matrix of both sp^3 and sp^2 carbon [165]. Overall, the Raman spectra reveal the presence of an amorphous phase along with highly disordered graphitic-like crystallites in all char samples. The figures exhibit two prominent peaks around 1400 and 1600 cm^{-1} which are assigned to the D-band and the G-band respectively. The D-band is attributed to in-plane vibrations of sp^2 bonded carbon (intramolecular C–C vibration of aromatic carbon layers) within structural defects [283]. The G-band arises from the in-plane vibrations of the sp^2 -bonded crystallite carbon (intermolecular shear vibration between individual C-layers) [284]. In addition, another band around 2800 cm^{-1} can be observed which indicates the multilayer graphene-phase structure [285]. The ratio of the D to G bands (I_D/I_G), termed the

intensity ratio, describes the graphitization degree of carbonaceous materials and is tabulated in Table 4.6 for all the samples [285]. The lower the I_D/I_G ratio, the higher the graphitization of a carbonaceous structure.

Table 4.6. Raman Intensity Ratios of Biochars Samples (Raw and Activated under Different Conditions)

Sample Name	Raw	Physical Activation	Chemical Activation	Sono-chemical Activation
MS	0.71	0.81	0.83	0.84
SG	0.74	0.79	0.81	0.83
CS	0.74	0.79	0.81	0.82
SB	0.75	0.78	0.81	0.81
SR	0.75	0.77	0.79	0.79
WS	0.78	0.77	0.78	0.78
RH	0.78	0.73	0.75	0.75
RS	0.79	0.68	0.69	0.74

Effect of Feedstock Origin: As observed in Table 4.6, intensity ratios of the raw samples ranged between 0.71-0.79 where rice straw had the highest (0.79) and miscanthus had the lowest value (0.71), with the following order for intensity ratios: crop residue (RS>RH>WS>SR) > agro industrial residue (SB>CS) > herbaceous residue (SG>MS). This can be explained in the following way: during formation of char, the biomass undergoes a first stage decomposition where a 3D network of benzene rings is formed with separate or bicyclic aromatic rings having functional groups such as methyl, methylene, oxygen etc. attached [286]. In the second stage, cleavage reactions occur (involving -OH, -COOH and -CO groups) that lead to increases in the number of fused aromatic rings, resulting in more-extended 2D structures [286]. The char formation finally ends up with the formation of microcrystalline structures consisting of greater than six fused aromatic rings [286]. This crystalline structure (with high carbon content) results in less disorder in biochars like herbaceous (MS, SG) and agro-industrial residues (CS, SB) that have higher %C content compared to crop residues, and accordingly they exhibit low intensity ratios. Additionally, literature suggests that the biochars with high cellulose and hemicellulose

content and low lignin content like MS, SG, CS and SB possesses less disorder [287] and have lower intensity ratios (or higher graphitic structure) than biochars that possess high lignin content, like SR, WS, RH and RS.

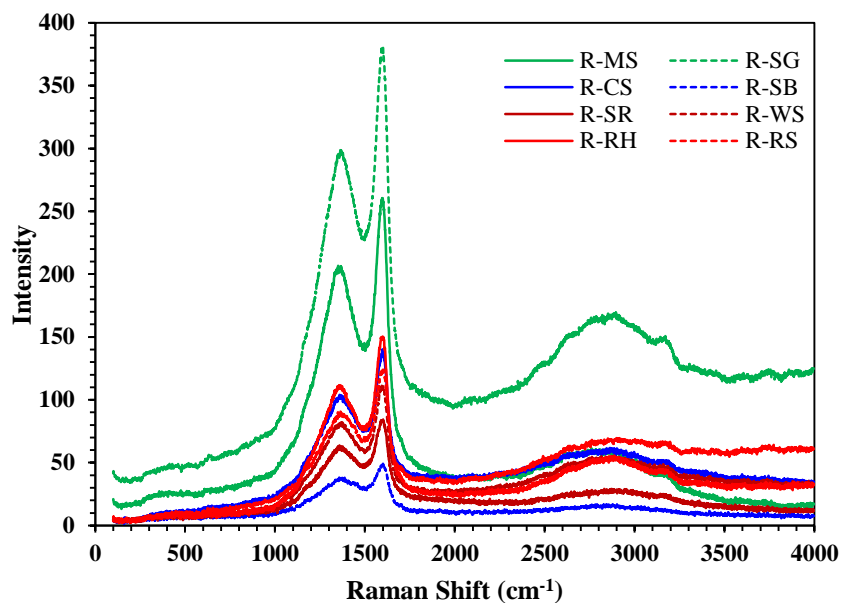


Figure 4.9. Raman Spectra of Raw Biochar Samples. Raw samples show very less intensities indicating their low intensity ratios as described in the results and discussion section

Effect of ultrasound: According to the Table 4.6, the I_D/I_G ratios of the five raw biochars with the lowest intensity ratios increased upon sonication, implying the presence of more sp^3 bonds and more defects and disorders in sonicated samples. Physical activation led to a maximum enhancement of I_D/I_G ratio to 0.81 for MS, and the intensity ratios exhibited the following order: $MS > SG = CS > SB > SR = WS > RH > RS$. The surface areas of these chars followed the same trend, as ultrasonic cavitation exfoliated the biochar structures, followed by removal of mineral matter (ash) and enhancement of surface area and pore volume. This resulted in the addition of disorder to the structure and therefore increased the I_D/I_G ratio. However, RH and RS showed reduced values of I_D/I_G ratio after sonication and WS has almost no change in intensity ratio. A reduction of intensity ratio can indicate an increase in aromaticity in biochars [288]. This

can be further supported based on the elemental analysis result (Table 4.4) of these chars that show acoustic cavitation resulted in reduction of %N content for RH and RS whereas WS showed no change. This supports the observed trend for the I_D/I_G ratio of WS, RH and RS. Henceforth, based on the above discussion, it can be concluded that ultrasound resulted in a reduced degree of graphitization for herbaceous (MS, SG) and agro industrial (CS, SB) based chars as reflected in their higher intensity ratios, whereas crop residue chars showed higher graphitization degrees by their reduced intensity ratios.

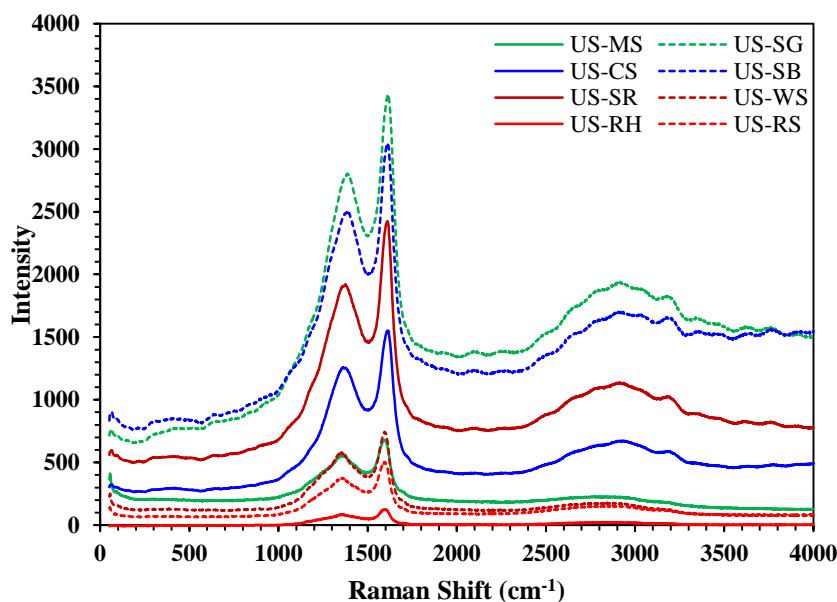


Figure 4.10. Raman Spectra of Physically Activated (no amine) Biochar Samples. The treatment was done in the presence of ultrasound only. These tests were intended to determine the effect of physical activation alone on the graphitic structure of biochars. The treatments didn't show any significant change for intensity ratio measurement compared to chemically and sono-chemically modified biochars

Effect of amination: The five raw biochars with the lowest intensity ratios showed increment upon amination; two chars had decreased ratios and one didn't show any change. The intensity ratios for chemically modified samples ranged between 0.69 and 0.83; these were 0.87-1.2 times those of the raw chars with the following trend: herbaceous residue: MS>SG; agro

industrial residue: CS=SB; crop residues: SR>WS>RH>RS. This suggests that this is the trend of the extent of amination, since amination should cause defects. In addition to that, the extent of decrease in surface area (Table 4.3) upon amine functionalization also follows the same trend, as increased amination fills pores.

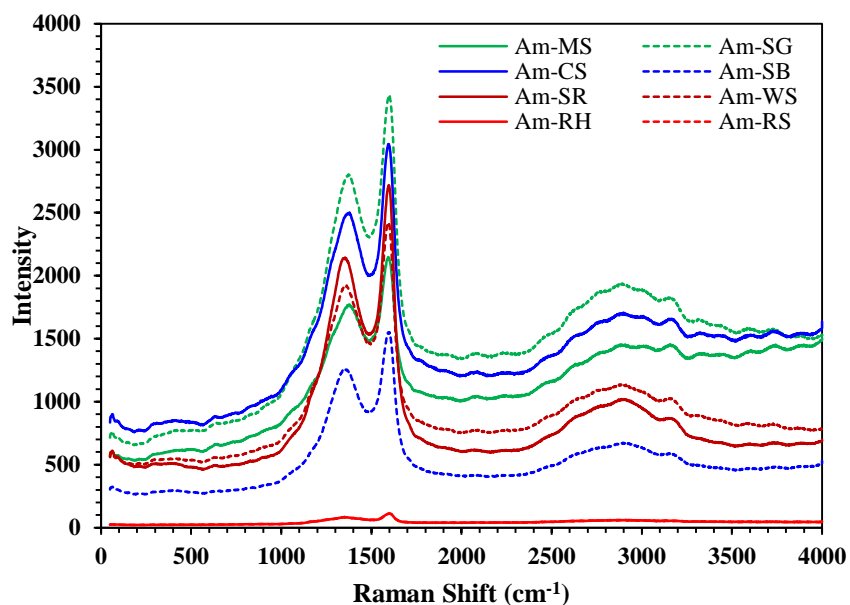


Figure 4.11. Raman Spectra of Chemically Activated (no US) Biochar Samples. The treatment was done in the presence of amine only. These tests were intended to determine the effect of amine functionalization alone on the graphitic structure of biochars. The treatments show comparable differences specifically for herbaceous (MS, SG) and agro-industrial (CS, SB) based biochars.

Effect of sono amination (compared to raw biochar): As observed, sono-chemical activation created more defects (in terms of intensity ratio) than raw samples had for 5 of the chars, and fewer defects for 2 of them. US-Am intensity ratios were 0.94-1.2 times those of raw chars, with the following trend: herbaceous residues > agro-industrial residues > crop residues, with the maximum and minimum ratios for MS (0.84) and RS (0.74), respectively. Moreover, the observed trend further matched the textural analysis (Table 4.3) that showed sono-amination resulted in lower surface areas than raw chars as a result of amine grafting. Thus, the above

discussion elucidates that MS, with increased %N content and lower surface area had additional defects in its structure and an increased intensity ratio, where RS, with low %N, showed a low intensity ratio.

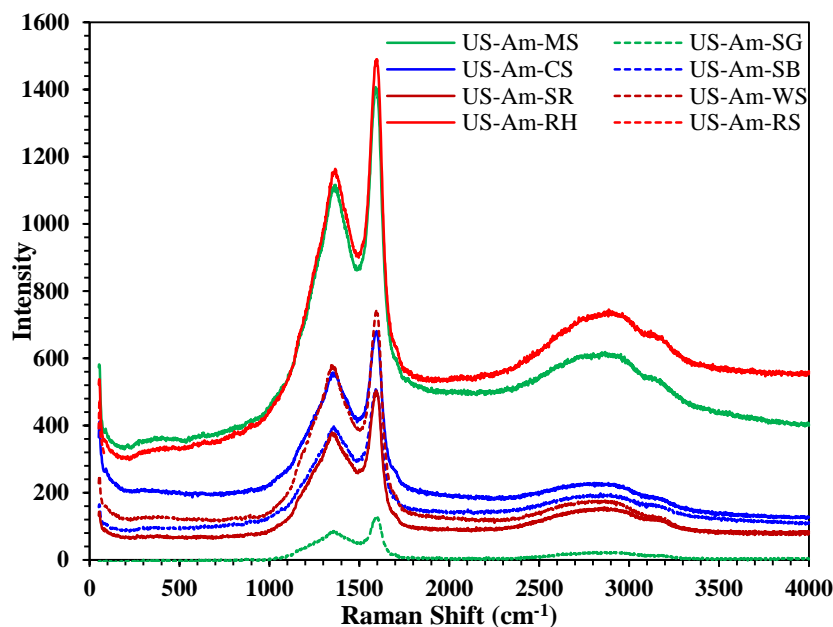


Figure 4.12. Raman Spectra of Sono-Chemically Activated Biochar Samples. The activation was done physico-chemically i.e. first physical activation in presence of acoustic field followed by chemical functionalization using amine. The treatments resulted to the changes in intensity ratio with the highest possible intensity ratio for miscanthus and lowest possible for rice straw

Effect of sono amination (compared to aminated biochar): In comparison to aminated chars, increases in intensity ratios of sono-aminated chars followed the trend of: RS>SG>CS~MS (1.01-1.07 times aminated-only values) while SB, SR, WS and RH didn't show any change in their I_D/I_G ratio. As found in Table 4.4, MS showed increased %N content, suggesting modification of the biochar structure that would be associated with an increased intensity ratio; however, WS and RH significantly increased their %N without a concomitant change in intensity ratio. SB and SR had reduced %N content and so did not show an increase in intensity ratio. In spite of sono-aminated biochars having lower surface areas than aminated chars, the acoustic energy transferred during sono-chemical activation resulted in higher disorder

in the biochars (through exfoliation and ash removal) and contributed to more defects. In accord, the FTIR spectra (Figures G3 and G4) showed that intensity of peaks at 1100-1200 cm^{-1} (C-N) are strong for all sono-aminated chars, especially MS and CS, but are less intense for SB and SR, consistent with the high and low intensity ratios of these chars, respectively.

Hence, the above discussion reveals that sono-chemical activation played a more promising role for herbaceous (MS, SG) and agro industrial residues than for crop residues (SR, WS and RH) in terms of increasing I_D/I_G intensity ratios, which may imply improve subsequent CO_2 removal capacity.

4.4.6 Adsorption Study

Effect of Feedstock Origin: Figure 4.13 presents adsorption capacities of different biochars under different activation conditions, and their corresponding breakthrough plots have been reported in supplementary documents Figures H1-H4. As observed, raw biochar samples have adsorption capacities in the range of 0.49-0.82 mmol/g with the following order: herbaceous (MS and SG) > agro-industrial (CS and SB) > crop residues (SR, WS, RH and RS). This trend can be correlated to their ligninocellulosic compositions that exhibit high cellulose and low lignin for MS and SG chars, which accordingly possess high %C and surface area, since cellulose degrades preferentially over lignin. Despite high %N and comparable %C content of SG with respect to MS, SG has a lower adsorption capacity because of its higher ash content. Among agro-industrial residues, CS is found to have a higher adsorption capacity than SB. Although the carbon contents of these two biochars are comparable (Table 4.5), CS has higher %N and lower %ash content and also a larger surface area than SB. Crop residues have notably the lowest adsorption capacity of the biochar categories. SR and WS have very similar %C contents (Table 4.5), along with very close %ash and %N values. These observations are also in

accordance with the surface area analyses and thus SR and WS exhibit similar adsorption capacity values. On the other hand, RH and RS showed very low values for adsorption capacity, consistent with their high ash content, low %C and low surface area.

The breakthrough plots (Figure H1) describe the effluent adsorptive concentration at the outlet of the adsorption bed. The concentration wave moves through the bed as the adsorption proceeds and so most of the mass transfer at any one time occurs in a fairly small region. The mass transfer zone moves down the bed until it “breaks through” at the point where the adsorbent no longer will be solely adsorbed to the biochar (adsorbate) and starts to appear in the effluent. For herbaceous biochars MS and SG, the breakthrough curves shift to the right compared to the other plots. This signifies that more adsorbate was adsorbed by the adsorbent and hence the adsorption capacity increased.

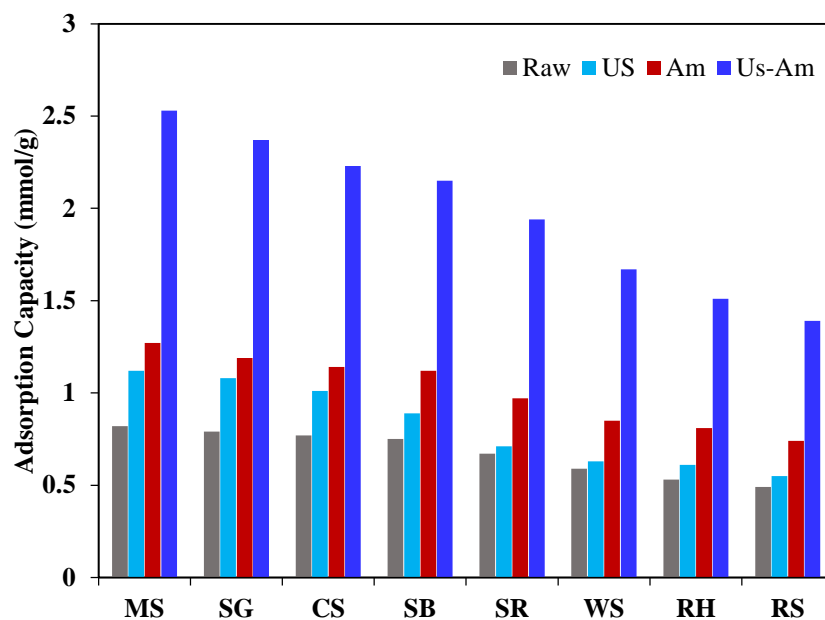


Figure 4.13. Adsorption capacities of different biochars at 70 °C and 10 vol% CO₂ inlet concentration. ■ Raw biochars, ■ Acoustic activated biochar ■ chemically activated biochar, ■ sono-chemically activated biochar. **herbaceous residues** (MS:miscanthus and SG: switchgrass), **agro-industrial residues** (CS: corn stover, SB: sugarcane bagasse and), **crop residues** (SR: sorghum, WS: wheat straw, RH: rice husk, RS: rice straw).

Moving on to next category, agro-industrial chars have smaller shifts from the origin and so they have lesser adsorption capacities than herbaceous biochars, and similarly for crop residues.

Effect of Physical Activation on CO₂ Adsorption: Physical activation employing ultrasonication had a noticeable effect in improving adsorption capacities, in the range of 1.1-1.4 times the capacities of raw chars. The trend followed the pattern of the raw biochars, with MS exhibiting the highest and RS the lowest adsorption capacities. As Table 4.4 shows, sonicated MS and SG have relatively high %C and low %ash, and MS has a significant increment in nitrogen content; these properties support their highest adsorption behavior. Agro-industrial biochars also have improvement in %N, whereas crop residues (specifically RS) showed reduction (0.55 times) in %N, in accord with its smaller adsorption capacity. The change in the %N content of the biochars following ultrasonication, compared to raw chars, is in the same order as the adsorption ability: MS (0.3), SG (0.1), CS (0.1), SB (0.0), SR (-0.1), WS (-0.2), RH (-0.3), and RS (-1.4). This suggests that the nitrogen content that is increased or decreased by ultrasonication can assist in the adsorption of CO₂. This shows the importance of nitrogen content for improving adsorption ability although why ultrasound should alter that type of nitrogen preferentially is not clear. Thus, based on the above discussion, it can be highlighted that ultrasonication resulted in improved %N content for MS, but showed negative affect for RH and RS, accounting for their high and low adsorption capacities respectively. Although sonication of SG, CS, SB, SR and WS didn't significantly change their %N contents, their adsorption capacities were higher than the corresponding raw chars; the capacities were higher than RH and RS but lower than MS.

Additionally, the breakthrough plots (Figure H2) reveal that herbaceous chars (MS, SG)

and agro-industrial CS char had increased mass transfer zones with longer breakthrough times than the other sonicated chars, suggesting their superior adsorption capacities. The other agro-industrial and crop based biochars (SR, WS, RH, RS) had short breakthrough times, representing diminished adsorption capacity.

Effect of Amination on CO₂ Adsorption: Amine treated biochars exhibited 1.51-1.54 times higher adsorption capacities than raw biochar samples. The trend followed the pattern of the raw biochars. MS and RS showed the highest (1.27 mmol/g) and lowest (0.74 mmol/g) adsorption capacities, which is consistent with their micro and mesoporous surface areas and pore volumes. Amine functionalization resulted in increased %N of biochars in the range of 1.4 - 4 times. The %N content of the aminated chars had a negative correlation with their adsorption ability (except for RH). The order of %N contents (from Table 4.5) were: RS > WS > SR > SB > RH = CS = SG > MS. It may be that substantial portions of the %N of the poorly-adsorbing biochars are in groups, such as within aromatic rings, that do not interact well with CO₂, or are sequestered in inaccessible locations. Breakthrough plots (Figure H3) further verified the above observed result of adsorption capacity of various aminated samples. MS, SG and CS had more prominent mass transfer zones, with more gradually sloping curves shifted towards the right, signifying increased adsorbate retention ability. SB, SR, WS, RH and RS had steep curves and short retention times, in concert with their lesser adsorption capacities.

Effect of Sono-Amination on CO₂ Adsorption: The integrated sono-chemical treatments resulted in increased adsorption capacities in the range of 2.8-3.1 times those of raw chars, with the trend following the pattern of the raw biochars. The effect of the applied physical activation during sono-amination can be observed in both micro and nano scale. Since biochar contains graphene cluster so ultrasound induced microjets and shock waves expected to exfoliate the

graphene cluster [252]. This effect can be corroborated by the Raman Spectroscopy that showed reduction trend of graphiticity and enhancement of distortion for the sonicated samples (Table 4.6). These structural alteration provides active sites for subsequent chemical modification using amine [251]. In addition to that the effect of acoustic treatment is also obvious in micro scale. Ultrasound cavitation and its consequences (shock waves and microjets) resulted to the generation of new pores/opening of blocked pores of the biochar which can be observed by SEM images (Figures 4.3-4.5) and further substantiated by the textural analysis (Table 4.3) that showed increased value of surface area and pore volume after sonication. Increased surface area and porosity can boost the physical adsorption of biochar while they may open channels to the under-layers. On the other hand, exfoliation of the graphitic structure of biochar exposes a greater number of potential groups to the amine functionalization. Thus, CO₂ capture capacity of biochar is not only determined by the enhanced surface area and pore volume but also by the basic amine functionalities which are the active sites for CO₂ adsorption [289, 290]. Indeed, the higher CO₂ uptake obtained for sono-aminated samples that have lower surface areas and pore volumes than the raw chars highlight the importance of the nitrogen functionalities on the surface of the modified adsorbents which can be further verified from elemental analysis that exhibit increased %N contents for ultrasonic-TEPA activated biochars. The similar findings were also reported in the literature [291]. As observed from tables (4.4-4.5) the treated chars had significant nitrogen increases (0.5-1.3 %N) compared to raw chars, although not necessarily with respect to amination-only chars. MS, with the most increased %N content, showed the most promising adsorption capacity. After MS, it can be observed that SG, CS and SB have a decreasing trend in surface area and pore volume followed by SR, WS and RS.

Despite good correlations of adsorption capacity to surface area, elemental analysis and

Raman intensity ratios, correlations are poor when all treatment sets are considered together. This again suggests that a complex interplay of factors are involved in determining adsorption capacity. Furthermore, different factors may be in play for different biomass sources.

The sono-chemically treated chars had 1.8-2 times higher adsorption capacity than aminated-only chars. The breakthrough curves for MS, SG, and CS had increased mass transfer zones, followed by SB, SR, WS, RH and RS. Therefore, it can be concluded that sono-amination employing ultrasound and TEPA together can significantly improve the CO₂ adsorption capacities of biochar samples compared to either treatment alone. The dependence of adsorption capacity on biomass source followed the trend of herbaceous > agro-industrial > crop based biochars, with MS char having almost twice the adsorption capacity of RS char.

4.4.7 Mechanism of Physicochemical Activation of Char and Interactions with CO₂

The interaction of char with acoustic cavitation and amine functionalization is represented in Figure 4.14. As observed from during the first step of the activation, the applied ultrasound waves promote cavitation that generates bubbles which result in high-speed liquid jets and shockwaves. This eventually drives into the surface of the biochar and increases the interlayer spacing among the layers. The ultrasound also causes vibration which passes through the biochar structure and gradually peels off the stacked graphene layers exposing the individual graphene sheets and the oxygen functional groups (-COOH, -OH and C=O). These functional groups helped to attach amine during chemical functionalization. However, -COOH group needs additional pre-activation using EDC-HOBt prior to amination. As found from the figure, EDC activates -COOH group to form O-acylisourea [292]. However, the reaction tends to produce N-acyl urea as undesired side product and reducing the yield of the product by O-N migration of the activated carboxyl functional group which is prevented by adding additives such as HOBt

that displaces EDC and forms the intermediate as shown in the Figure 15 [292]. In the final step, the nucleophilic attack by the amino group of TEPA resulted to form amide ($-\text{CONH}$) bond followed by release of HOBT as by-product which can be easily removed through simple filtration.

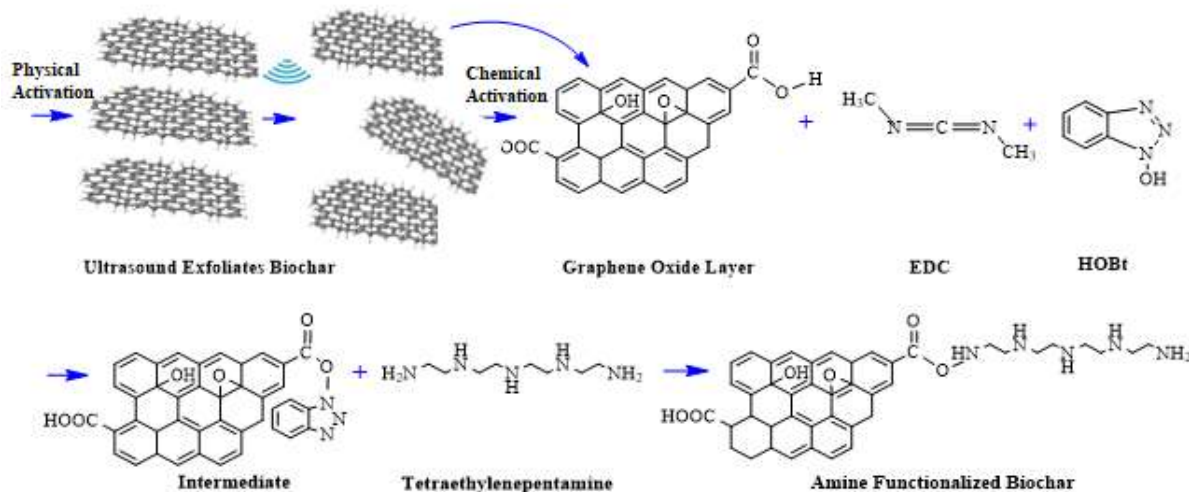
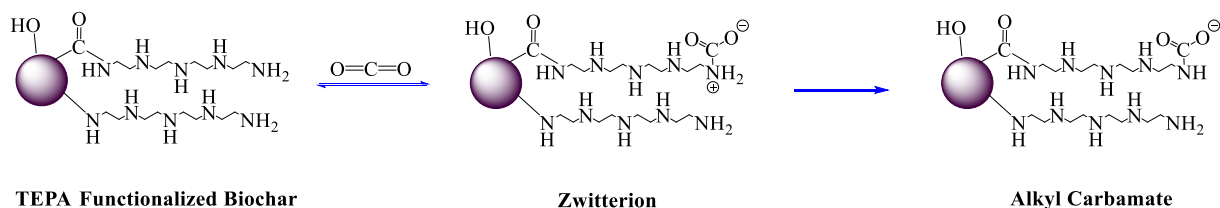
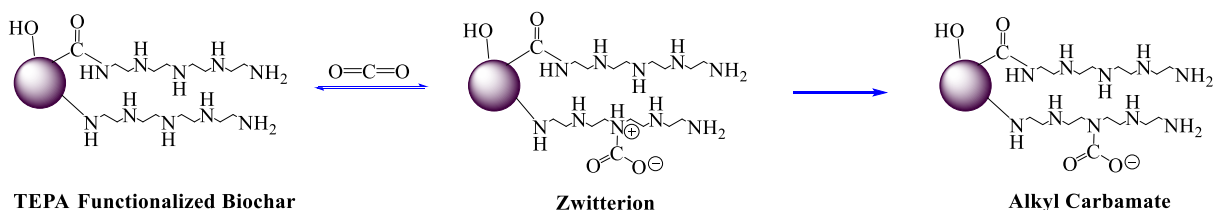


Figure 4.14. Postulated Mechanism of Char Formation under Different Activation Conditions

The major pathway that contributes to amine-based CO_2 capture includes the formations of carbamate anions for gas-solid reactions. During the reaction (Figure 4.15) at first amine molecules react with CO_2 molecule to form a carbamate ion and a protonated amine. This has been proposed to occur via two-step zwitterion mechanism. In the first step zwitterion is formed as intermediate through the interaction between terminal amino group and CO_2 followed by deprotonation in the second step by a base to produce a carbamate that resulted to the attachment of CO_2 with the aminated biochar structure (Scheme 1). Few literature reports that zwitterion is unstable to further proceed for CO_2 capture [293, 294]. However, more recently, ab initio molecular dynamics (AIMD) simulations based on density functional theory (DFT) demonstrates that reaction between CO_2 and amine occurs through two-step zwitterion mechanism [295].



Scheme 1: For Terminal Amino Group



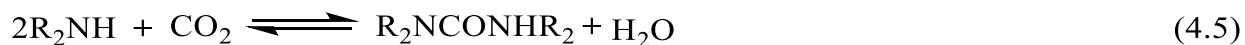
Scheme 2: For Intermediate Amino Group

Figure 4.15. Mechanism of Zwitterion and Alkyl Carbamate formation during the Interaction between Biochar Chemical Structure (C and N) with CO₂

Likewise, the terminal amino group, the reaction for intermediate amino group proceeds by nucleophilic addition of 1 mol of amine to the carbons of 1 mol of CO₂ forming 1 mol of ammonium-carbamate zwitterion intermediates as shown in Scheme 2. The zwitterions are then deprotonated by 1 mol of free amine groups, producing 1 mol of ammonium-carbamate ion pairs [296].

4.4.8 Regeneration Study

Stability analysis of the adsorbent is important from an economic point of view as well as for long term use. Figure 4.16 shows the cyclic adsorption-desorption behavior of different sonchemically treated samples. As observed, after 15 cycles the adsorptive capacities were reduced in the range of 24-32% than the original adsorption capacities. The maximum and minimum reductions were observed for crop and herbaceous based biochars respectively. As found from the figure, herbaceous and agro-industrial biochars have comparable regeneration ability as these



biochars retained 74-76% of their actual adsorption capacities after 15 cycles. Whereas, the significant reduction in adsorption capacities (30-32%) were observed for crop residues. The greater the cyclic adsorption capacity, the lesser the replacement of the adsorbent and potentially more efficient the adsorbent will be. Thus, based on this point of view it is suggested that herbaceous and agro-industrial based biochars are more promising than crop residue based biochars in terms of both adsorption and regeneration behaviors.

The probable reason for the reduction of adsorption capacities could be the volatilization or loss of reactive amino functional groups from the aminated adsorbents [297]. Literature also shows that the interaction between CO₂ and amine above 403 K resulted in the formation of urea linkage followed by the loss of water [297]. This may occur either from the secondary reaction of the carbamate ion formed (4.4) or direct reaction of CO₂ and the amine group (4.5) [297]. Thus, formation and deposition of stable urea compounds on the surface of the adsorbent during thermal reactions tend to reduce the interaction between CO₂ and the amino functional groups that leads to the reduction of adsorption capacity [298]. Usually, the regeneration is carried out at very high temperatures, ranging from 200 to 500°C [138, 139]. However, the present study was conducted under much lower temperature range of 453 K (180°C) to make the process less energy intensive and more economic.

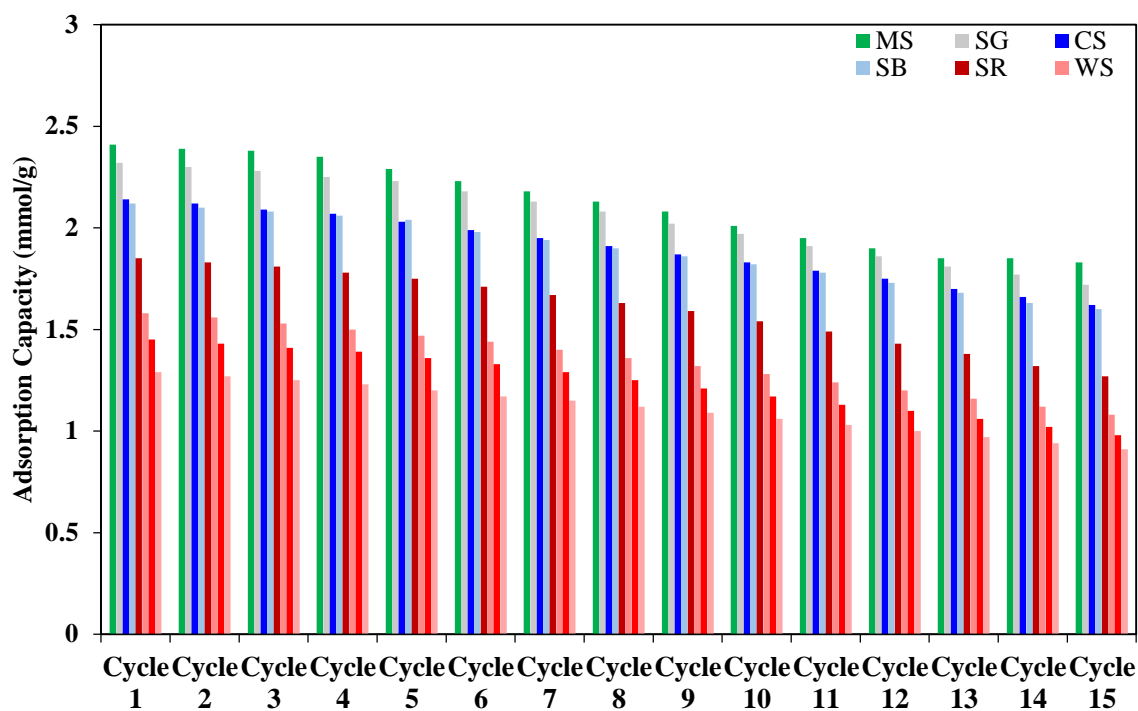


Figure 4.16: Cyclic adsorption-desorption behavior of ultrasono-aminated Herbaceous residue based chars (MS, SG), Agro-industrial based biochars (CS and SB) and Crop residue based biochars (SR, WS, RH and RS)

4.5 Conclusions

The current study investigated the effect of biomass origin on the carbonaceous structure (including its physical and chemical properties), activation conditions and CO₂ adsorption capacities of biochars that were prepared from eight different biomasses of three different categories: herbaceous, agro-industrial and crop residues. The biochars were subjected to acoustic-based physical activation, chemical functionalization, and integrated physicochemical activation techniques. The biochar production is affected by the following factors-moisture, volatiles and mineral matter contents which are further controlled by biomass feedstock sources primarily cellulose, hemicellulose and lignin contents. Biochars produced from high cellulose and low lignin contents biomass have higher %C and reduced %ash contents as observed for herbaceous and agro industrial chars than crop based chars. Additionally, chars with the highest

%C and lowest %ash contents interact very effectively with ultrasound with further enhancement of their carbon and ash contents. The advantages of the induced interactions between ultrasound and carbonaceous structure include enhancement of microporous surface area and microporosity. Micropores have higher surface area than meso or macropores because of the lowest pore size thus induced microporosity increases specific surface area of the char and making it effective for the subsequent amination and CO₂ adsorption. The results showed that the highest improvements of adsorption capacities were attained for the combined ultrasono-amine functionalization technique that increased adsorption between 184-200% over raw char. Among the different categories the herbaceous based biochars MS and SG have the highest adsorption capacities of 2.53 and 2.37 mmol/g respectively at 0.10 atm. and 70 °C. This is primarily attributed to the high %C content (77-82%), low %ash content (4.35-12.78) and improved textural properties (324-340 m²/g) which promoted enhanced nitrogenation during amination and facilitated CO₂ adsorption. Additionally, the entire sono-chemical activation is conducted at room temperature, while utilization of easily-available biomass makes it highly economic, providing an efficient way for synthesizing adsorbent for effective CO₂ adsorption.

Author Contributions

Riya Chatterjee: Conducting the experiments, interpreting the results and writing the manuscript

Baharak Sajjadi: Idea of the work, interpreting the results and writing the manuscript

Wei-Yin Chen: Idea of the work and revise the manuscript

Daniell L Mattern: Interpreting the results and revise the manuscript

Nathan Hammer: Conducting Raman Analysis

Austin Dorris: Conducting Raman Analysis

Vijayshankar Ramna: SEM Analysis

CHAPTER V

Determination the Impact of Pyrolysis Temperature on PhysicoChemical Properties and Ultrasound-Promoted Amination of Biochar for CO₂ Capture

Riya Chatterjee, Baharak Sajjadi, Wei-Yin Chen, Daniell L. Mattern, Nathan Hammer, Vijayasankar Raman, Austin Dorris. Effect of Pyrolysis Temperature on PhysicoChemical Properties and Acoustic-Based Amination of Biochar for Efficient CO₂ Adsorption. *Frontiers in Energy Research, Bioenergy and Biofuels*, (accepted with revision)

5.1 Abstract

The present study examined the effect of pyrolysis temperature on the physicochemical properties of biochar, activation process and carbon capture. Two different categories of biochars were synthesized from herbaceous (miscanthus and switchgrass) and agro-industrial (corn stover and sugarcane bagasse) feedstock under four different pyrolysis temperatures- 500, 600, 700 and 800 °C. The synthesized biochars underwent sono-amination activation comprising low-frequency acoustic treatment followed by amine functionalization to prepare adsorbents for CO₂ capture. The CO₂ capture capacity of sono-aminated biochars synthesized at 600 and 700 °C were almost 200% greater than that of raw biochars. There were 127-159% and 115-151% increases in adsorption capacity of biochars synthesized at 800 and 500 °C upon ultrasono-amine functionalization. The improvement of adsorption capacity can be explained based on the elemental and textural analysis results. The elevated pyrolysis temperature resulted in increased %C and %ash contents and reduced %N contents of biochar. Additionally, 3-times enhancement of micro surface area and pore volume were observed up to 700 °C, with a reduction at 800 °C

temperature. Accordingly, Miscanthus biochar synthesized at 700 °C and treated sonochemically demonstrated the highest adsorption ability of 2.89 mmol/g at 70 °C and 0.10 atm partial pressure, which is 211% higher than its pristine condition. The superior adsorption capacity of miscanthus (at 700 °C) can be attributed to its large surface area (324.35 m²/g), high carbon content (84%), and low ash content (4.9%), as well as its %N content after sonamination that was twice that of raw char.

5.2 Introduction

Pyrolysis is a thermo-chemical decomposition of organic material (such as biomass) under oxygen-deprived environment at elevated temperature [299-302]. The solid carbon-rich product of this process is known as biochar or char, and the volatile fraction of pyrolysis is partly condensed to a liquid fraction called tar or bio-oil along with the formation of a mixture of non-condensable and volatile condensable organic products into low-molecular-weight gases, secondary tar and char via secondary reactions of the primary pyrolysis products [303, 304]. Depending on the conditions, pyrolysis processes can be classified into three main categories: slow pyrolysis (slow heating rates for a long time, temperatures less than 300 °C), moderate pyrolysis (temperatures of 300-500 °C) and fast pyrolysis (fast heat transfer rates over a short time, temperatures greater than 500 °C) [300]. Literature shows that, during biomass pyrolysis, primary cracking and secondary decomposition along with the formation of oxygen functional groups start around 400-500 °C [305-307]. Thus, 500 °C is considered to be a suitable temperature for the initiation of pyrolysis and production of char [306].

Pyrolysis temperature affects the structural and physicochemical properties of biochar such as surface area, pore structures, surface functional groups and elemental compositions [307]. The effect of pyrolysis temperature on such properties can be ascribed to the release of

volatiles at high temperature [62]. The higher temperature results in higher carbon content while losing nitrogen, hydrogen and oxygen contents of biochar structure [308]. Particularly, biochar produced at high temperature has high aromatic content, which is recalcitrant to decomposition [309]. In contrast, biochar produced at low temperature has a less-condensed carbon structure [73]. However, a very high temperature (>800 °C) leads to the destruction of oxygen functional groups and surface porosity leading to a decrease in the surface area [249]. In addition, increasing the temperature can lead to an increase in the ash content and a reduction of volatile materials [225, 228, 305, 310, 311]. Thus, the selection of suitable pyrolysis temperature is a compromise between the surface and chemical properties as described. Generally, 500-800 °C is considered as the optimum range for pyrolysis temperature in the endeavor of producing biochars.

Table 5.1: Literature Data on Physico-Chemical Properties of Biochars Synthesized at Different Pyrolysis Temperatures

Biochar	Synthesis T(°C)	Surface Area (m ² /g)	Ash (wt. %)	C (wt. %)	H (wt. %)	N (wt. %)	O (wt.%)	pH	Ref
MS	400	2.41	7.85-12	81.20	4.09	0.42	14.29	8.7	[225, 305, 311]
	500	181	10.06-13.5	86.66	3.20	0.40	9.74	9.5	
	600	382	9.4-13.8	90.71	2.26	0.33	6.70	10	
SG	400	1.1	14.40	-	-	-	-	6.7	[228, 229, 312-315]
	500	9.3-50	18.40	39.4	1.30	0.7	16	6.6	
	600	15	3-26.3	68.2	2.21	1.9	14-25	7.4-9.8	
CS	500	4.58	12.70	71.1	3	0.07	12.50	-	[234, 316-318]
	600	18-40	12.80	75.2	2.20	0.06	9.21	-	
	700	107	18.70	72.8	0.09	0.10	6.10	9.1	
	800	-	14	76.7	0.11	0.07	7.61	-	
SB	500	-	11.5	-	-	-	-	9.2	[239, 319, 320]
	600	-	12.4-19	50.90	3.49	0.004	45.5	9.6	
	750	-	21.01	86.30	1.16	-	24.7	9.7	

Note: MS- Miscanthus; SG- Switchgrass; CS- Corn stover; SB: Sugarcane bagasse

Table 5.1 summarizes the impact of pyrolysis temperature on various physicochemical properties of biochars. These characteristics cumulatively drive the sorption ability of biochar. Adsorption is primarily a surface phenomenon and greatly depends on the surface area and surface functional groups of biochar [309]. Thus, attempts have been made on improving the textural properties and chemical functionality through physical and chemical modifications [100]. Physical modification of biochar is aimed at improving surface properties whereas chemical activation with heteroatoms facilitates the addition of functionality [100, 250]. Ultrasonic treatment has recently been introduced as a physical activation technique which is an alternative to high-temperature steam or air oxidation [249]. Ultrasound irradiation results in the formation and collapse of vapor filled microbubbles during the alternate compression and rarefaction cycles of ultrasound, which leads to the exfoliation of the layered structure of graphitic clusters [250]. The interaction of ultrasound waves with graphitic structure was first demonstrated by Stankovich et al. where they found that a mild ultrasonic treatment ($f_c=78.6$ kHz, 150 W) of graphite oxides in water for 1 h exfoliates its layers and forms stable aqueous dispersions [252]. In addition to exfoliation of graphitic structure, ultrasound treatment opens up the clogged pores, cleans the surface, and facilitates the leaching of ash content of biochar, resulting in increased surface area and porosity [251]. The similar phenomena were also observed by our research group while studying the sonolysis of biochars under aqueous environment with CO₂ bubbling which showed attachment of carbon and increment of heating value of biochar [109, 253]. The above mentioned structural alterations promote chemical activation by providing active sites that can be effectively tuned by chemical modification; e.g. amination that introduces the amino group to the biochar [251]. Most importantly, acoustic activation through ultrasonic treatment is conducted at near room temperature within a very short

duration of time that could significantly reduce energy consumption [250] and has advantages over traditional physical activation conducted at very high temperatures (>750 °C) [251]. In addition, the chemical functionalization can be conducted with easy separation of the product from unreacted reagents. Thus, the applied ultrasonic-amination technique provided an energy-efficient and easy route to prepare effective CO₂ adsorbent.

In continuation of our pioneering works [109, 253] the subsequent work revealed that acoustic treatment followed by amine modification using tetraethylenepentamine could intensify the CO₂ adsorption capacity of pine wood-based commercial biochar up to 7 times compared to raw char [146]. To establish the mechanism, the next work studied the role of sonochemical activation incorporating different 1°, 2° and 3° amines (MEA, DEA, TEPA, PEI and PZ), with focus on determining the key role of each parameter, particularly the activation of carboxyl groups as the potential sites for amination to drive the correct mechanism of the activation process [258]. In the next step, the impact of the carbonaceous structure of biochar on sono-amination and CO₂ adsorption was assessed. Thus, eight different biochars were synthesized from three different classes of biomasses, namely herbaceous residue (MS, SG); agro-industrial residue (CS, SB) and crop residue (SR, WS, RH and RS). The study indicated that biochars with high carbon contents, low ash contents and high surface areas can be tuned effectively through the combined sono-amination technique and had significant improvement in adsorption capacity with the following trend: herbaceous residue (MS>SG) > agro-industrial residue (CS>SB) > crop residue (SR>WS>RH>RS) (Chatterjee et al. Energy and Fuels).

The last step of this series of our project is dedicated to investigating the synergistic and antagonistic impact of pyrolysis temperature on ultrasound activation and the subsequent adsorption capacity of biochar. To our best knowledge, there is hardly any literature that

integrates pyrolysis conditions and CO₂ capture together. Accordingly, the four biochars which have already shown the maximum CO₂ adsorption potential in our previous project (i.e., MS, SG, CS, SB) were selected for this work to obtain: I. the effect of different pyrolysis conditions (500, 600, 700 and 800 °C) on physicochemical properties of the raw biochars, II. the interaction between the pyrolysis temperature and the sonochemical activation, and III. the key role of the pyrolysis temperature on the CO₂ adsorption ability of the activated biochars.

5.3 Materials and Methods

5.3.1 Materials

Four common agro-based biomasses from the Idaho National Laboratory were chosen for the study, namely miscanthus, switchgrass, corn stover and sugarcane bagasse. The following reagents for chemical functionalization were purchased from Sigma Aldrich: EDC, HOBt, TEPA, HCl (37%), and acetone. NaOH was purchased from Fisher Scientific and deionized water was obtained from Milli-Q ultrapure water tap (Millipore Sigma). All chemicals used in this work were of analytical grade.

5.3.2 Experimental Method

5.3.2.1 Pyrolysis of Biochar under Different Temperature Ranges

The initial grinding and drying procedure has been described in our previous work (Chatterjee et al. Green House Gas Control). The biomass samples were ground and sieved in the size range 75–250 µm and were dried under vacuum at 60 °C overnight prior to pyrolysis. Then the dried biomasses were filled into crucibles (made of Nickel-Chromium-Iron Alloy), covered with lids and placed in the muffle furnace with 3 crucibles of the same biomass at a time to avoid any non-homogeneous behavior during pyrolysis. To produce biochar, the furnace was heated up to the desired temperature (with 20 °C/min heating ramp) under continuous nitrogen gas flow

and was held there for 2 hr. Then the furnace was switched off and the crucibles were allowed to cool to room temperature before taking them out under continuous nitrogen gas flow. The process was repeated for each pyrolysis temperature (500, 600, 700 and 800 °C). Upon cooling to room temperature, the biochars were transferred into glass vials and sealed with parafilm and stored for further treatments and characterizations.

5.3.2.2 Physical Activation of Biochar under Acoustic Treatment

The synthesized biochars underwent a two-step activation technique—physical activation using low-frequency ultrasound and then chemical activation in the presence of TEPA. The physical activation was carried out with 3 g of biochar in 250 ml of water for 30 s using an ultrasound sonicator equipped with controller and horn (QSonica model no. Q700). Our previous study elucidated that 30 s of sonication provided optimum adsorption capacity that was further justified based on the literature [113, 164]. However, increasing the duration beyond that leads to the disarrangement of the layered graphene clusters of biochars and tends to block the porous structure. This negatively affects the textural properties and adsorption capacity of biochar. After physical activation, the biochar was subjected to the following chemical activation steps.

5.3.2.3 Chemical Functionalization of Biochar with TEPA

Chemical activation followed two steps. At first, the ultrasonicated biochar-water suspension was mixed with the activating agents EDC and HOBt (3.375 g of each reagent with 3 g of biochar) followed by stirring for 24 hours with slight heating (at 35°C) [146]. The mixture was then filtered and dried at 60°C under vacuum overnight. In the next step, the dried sample was suspended in methanol and TEPA was added to the solution with a 2.5 times weight ratio with respect to dried biochar sample. The mixture was subjected to stirring with heating at 35°C for 24 hours, filtered and washed with 200 mL of 1N NaOH, 200 mL 1N HCl and 200 mL of

acetone and dried as before. EDC is preferred over other carbodiimides such as DCC because it is soluble in water which results in the easy separation of the product and unreacted reagent. HOBt is usually applied as an additive to prevent undesirable side reactions which may reduce the yield of the product. Further explanations and detailed mechanism of the activation process have been demonstrated in our previous works [146, 258].

5.3.2.4 Characterizations of the Adsorbent

The biochars, both raw and functionalized, were characterized using Scanning Electron Microscopy for the determination of surface morphology using JEOL JSM-7200 FLV SEM instrument. Surface area and porosity (textural properties) were measured using Micromeritics 3-Flex Surface Area Analyzer. Elemental constituents were determined using Perkin Elmer Series II CHNS/O Analyzer. The spectroscopic studies were conducted using Agilent Cary 660 Fourier Transform Infrared (FTIR) instrument to evaluate the change of surface functional groups, and degree of graphitization and defects were measured using LabRam HR Evolution Raman Spectroscopy technique. The thermal stability evaluation of the biochars was performed by thermogravimetric analysis (TGA Q500, V20.13 Build 39, TA Instrument). Approximately 7-8 mg of raw and ultrasound-amine functionalized miscanthus biochars synthesized at 500, 600, 700 and 800 °C were weighed into platinum crucible and was subjected to thermogravimetric analysis in a nitrogen flow (gas flow of 60 mL·min⁻¹) at a heating rate of 5 °C min⁻¹, from 21°C to 700 °C. The surface crystallinity of the biochar samples were determined from the XRD analysis in a Rigaku powder diffractometer (Rigaku, Japan) with Cu K α radiation ($\lambda=0.15406\text{nm}$). The tube voltage was 45 kV, and the current was 40 mA. The XRD diffraction patterns were taken in the 2θ range of 10–80° for raw and ultrasound amine activated of miscanthus biochars synthesized at 500, 600, 700 and 800 °C.

5.3.2.5 CO₂ Adsorption Experiments

The experimental set-up and detailed procedures of the tests are presented in Appendix A (Figures A1-A2). In brief, adsorption experiments were conducted in a temperature-controlled tubular reactor (alumina oxide, Al₂O₃). For each experimental run, a biochar sample of 2 g was put inside the tube and heated under helium (99.99%) gas flow (500 cm³ min⁻¹) at 378 K for 1 hour to remove moistures from the adsorbent. Then, the reactor was cooled to 333 K and the helium gas was switched to a simulated flue gas consisting of 10 vol. % CO₂ balanced with He. A CO-CO₂ analyzer connected to the set-up was used to detect the concentration of CO₂ before and after the experiment. The calculation of adsorption capacity was based on the change in concentration of CO₂ after adsorption.

5.4 Results and Discussions

5.4.1 Surface Morphology Analysis

Effect of pyrolysis temperature on surface morphology of raw chars: The SEM images of raw and activated biochars, pyrolyzed at 700 °C temperature are presented in Figs 5.1-5.4.

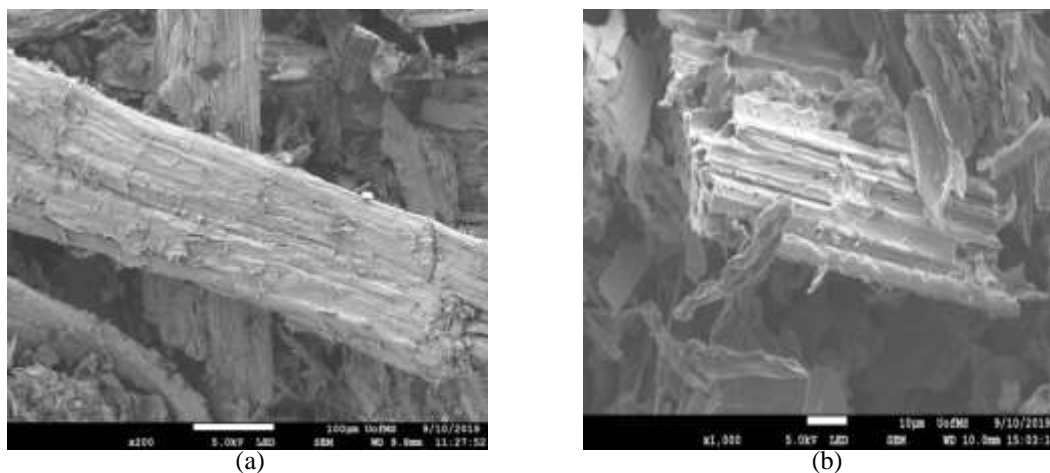


Figure 5.1. SEM images of (a) R-MS 700; (b) US-MS 700

As observed, the char particles show different sizes and shapes that may be attributed to

the sample preparation such as grinding, sieving and treatment. The raw samples show overall similarity in their surface morphology, having rough and non-porous structure. Images obtained revealed two main morphological features for all biochar samples: fiber structures and pith. The fibrous surface is formed by parallel stripes and is partially covered with residual material, and pith is a more fragile and fragmented structure which is primarily cracks that connect neighboring cells on the surface of the walls. As observed from Fig 5.1a, raw MS sample is characterized by jagged particles of varying size with vascular elements packed in bundles and possess a relatively flat surface which is also consistent to the literature [321, 322]. SEM micrographs of raw SG samples (Fig 5.2a) exhibit rough surface with long ridges, resembling a series of parallel lines. Similar structural features are also observed for CS (Fig 5.3a) and SB (Fig 5.4a), which exhibit rough, irregular and bundle like shapes. In addition to that, all samples exhibit fracture and cracks attributed to release of volatile matters during pyrolysis. These morphological observations were further substantiated based on the surface area analysis data using BET technique as described in the subsequent section.

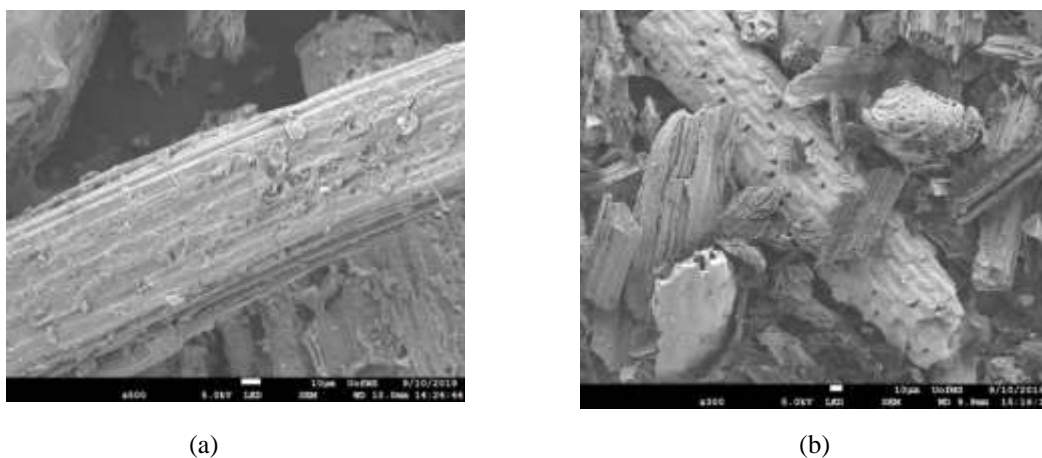


Figure 5.2. SEM images of (a) R-SG 700; (b) US-SG 700

Effect of pyrolysis temperature on surface morphology of ultrasound activated chars:

Pyrolysis temperature has a prominent role in promoting the ultrasound effect. Macroscopically,

the samples become very fine powders under ultrasound irradiation and microscopically, acoustic activation causes a structural degradation by opening/creation of new micro-pores as observed from the Figures 5.1b, 5.2b, 5.3b, 5.4b.

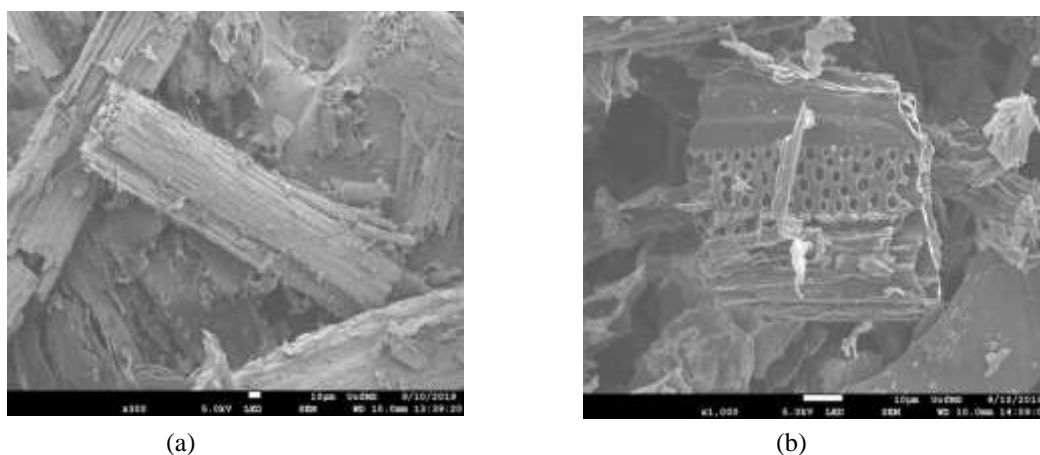
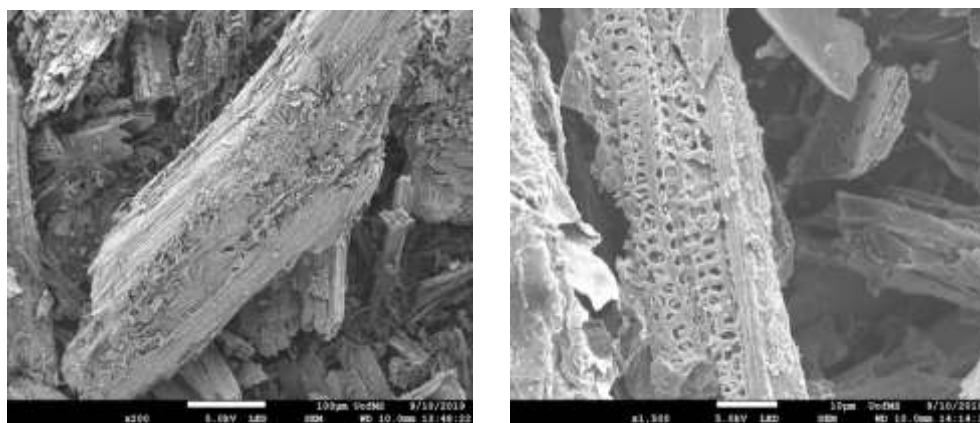


Figure 5.3. SEM images of (a) R-CS 700 and (b) US- CS 700

The maximum pore generation was observed for 700 °C, accordingly SEM images of sonicated chars pyrolyzed at 700 °C have been presented. As observed from the figures the effect of sonication is more observable for agro-industrial (CS, SB) chars than herbaceous biochars (MS, SG). For example, US-MS 700 sample (Figure 5.1b) shows the least alteration to their structure. Similarly, For US-SG 700, SEM image (Figure 5.2b) depicts that acoustic treatment slightly affected the structures. In contrast to herbaceous biochars, US-CS 700 (Figure 5.3b) and US-SB 700 (Figure 5.4b) show significant increased porosity and greater structural deformations upon sonication.

This structural deformation can be explained because of the thinner walls of CS and SB than MS and SG. This leads to the generation of porosity more in the agro-industrial residues (CS and SB) than herbaceous residues (MS and SG).



(a) (b)
Figure 5.4. SEM images of (a) R-SB 700 and (b) US- SB 700

Note: MS- Miscanthus; SG- Switchgrass; CS- Corn stover; SB: Sugarcane bagasse. R- Raw; US- Ultrasound Activated

5.4.2 Surface Area Analysis

Effect of pyrolysis temperature on surface area of raw chars: The surface area and pore volume (both micro and micro-meso porosity) of raw and ultrasound activated samples pyrolyzed under different temperatures are reported in Table 5.2. As observed, maximum surface area values for both the microporosity (R-SG-700 with surface area 325 m²/g) and micro-mesoporosity (R-SG-800 with surface area 351 m²/g) are observed for herbaceous residues, whereas the minimum values for the microporosity (R-SB-500 with surface area 83 m²/g) and micro-mesoporosity (R-SB-500 with surface area 138 m²/g) are observed for agro-industrial based chars. This shows that surface area is significantly affected by the biochar feedstock and pyrolysis temperature.

Surface area and pore volume for herbaceous chars (MS and SG) are higher than agro-industrial chars (CS and SB). Accordingly, the microsurface area and pore volumes for MS and SG ranged between 115-325 m²/g and 0.06-0.16 cc/g over the temperature of 500-800 °C. The increase of pyrolysis temperature from 500 to 600 °C resulted in a significant and sudden jump in the surface area (from 119 to 303 m²/g for MS and from 115 to 290 m²/g for SG) and the pore

volume of 0.06-0.14 cc/g for both the herbaceous biochars. This trend is similar to what is reported in the literature for MS [305, 323] and SG [324-326]. The enhancement of surface area and pore volumes was caused by the degradation of the organic materials (hemicelluloses, cellulose, and lignin) and the formation of vascular bundles or channel structures during pyrolysis [225, 327]. Lee et al. reported that cellulose and hemicellulose in the MS decompose at 500 °C [328]. When the applied pyrolysis temperature is increased beyond 500°C, the rupture of the hemicellulose along with other organic compounds generates more micropores within biochar [329]. The decomposition of lignin and the quick releases of H₂ and CH₄ contribute to a sharp increase of the surface area and pore volumes from 500 to 600 °C. Further increase of the temperature to 700 °C magnifies surface area and pore volume, especially for the micropores. This is mostly attributed to the further degradation of lignin and the reaction of aromatic condensation [330], which increases the release of volatile matter and creates more pores. However, increasing the pyrolysis temperature beyond 700 °C, (up to 800 °C) resulted in decreased surface area and pore volume. This can be described as a result of elevated temperatures that cause structural ordering and merging of pores, thus reducing the char surface area [331]. Although surface areas for agro-industrial chars are lower than herbaceous ones, they follow a similar trend. For instance, CS and SB exhibited a significant increase in surface area (96-284 and 83-221 m²/g for CS and SB respectively) and pore volumes (0.05-0.14 and 0.05-0.11 cc/g) upon increasing the temperature from 500 to 600°C. Higher pyrolysis temperature caused higher devolatilization, resulting in more pore volume in the samples and, in turn, a greater surface area up to 700 °C [324, 332]. However, the temperature increase to 800 °C resulted in reduced micro surface area for CS. The reactivity of the biochar samples is strongly affected by the surface area [332].

Table 5.2. Surface Area Analysis of Raw and Sono-Chemically Activated Biochars Samples Synthesized at Different Pyrolysis Temperatures

Samples	Microporosity		Micro-Mesoporosity	
	Surface Area (m ² /g)	Pore Volume (cc/g)	Surface Area (m ² /g)	Pore Volume (cc/g)
R-MS 500	119	0.06	168	0.08
R-MS 600	303	0.14	345	0.18
R-MS 700	324	0.15	368	0.18
R-MS 800	316	0.14	390	0.20
R-SG 500	115	0.06	162	0.08
R-SG 600	290	0.14	325	0.15
R-SG 700	325	0.15	344	0.18
R-SG 800	311	0.14	351	0.18
R-CS 500	96	0.05	149	0.08
R-CS 600	284	0.14	293	0.14
R-CS 700	298	0.14	308	0.14
R-CS 800	288	0.14	357	0.18
R-SB 500	83	0.05	138	0.08
R-SB 600	221	0.11	273	0.14
R-SB 700	236	0.12	289	0.14
R-SB 800	240	0.12	290	0.14
US-MS 500	323	0.15	388	0.20
US-MS 600	520	0.21	581	0.21
US-MS 700	532	0.21	588	0.21
US-MS 800	526	0.21	576	0.21
US-SG 500	309	0.14	374	0.20
US-SG 600	486	0.17	544	0.21
US-SG 700	520	0.21	570	0.21
US-SG 800	503	0.21	550	0.21
US-CS 500	215	0.11	279	0.14
US-CS 600	399	0.20	454	0.20
US-CS 700	423	0.20	473	0.21
US-CS 800	407	0.20	452	0.20
US-SB 500	192	0.11	250	0.13
US-SB 600	332	0.15	382	0.20
US-SB 700	352	0.18	400	0.20
US-SB 800	358	0.18	403	0.20

The observations can be further explained based on surface morphology as depicted in Figures 5.1-5.4. As can be seen from the figures that elevated pyrolysis temperature created more cracks and irregularities on the biochar surface as a result of rupture of lignocellulosic structure of biomasses and release of volatiles gases that resulted to increase surface area and pore volume. Thus, biochar samples produced within the temperature range of 500-700 °C showed

better reactivity and adsorption behavior than biochar samples produced at 800 °C.

Effect of pyrolysis temperature on surface area of ultrasound activated chars: As found from Table 5.2, upon sonication the microporous surface area and pore volumes for all the biochars increased. Additionally, as for raw chars, ultrasonicated herbaceous biochars possessed higher surface areas and pore volumes than agro-industrial chars. The sonicated samples also showed significant increases in surface area (323 to 520 m²/g for MS, from 309 to 486 m²/g for SG, from 215 to 399 m²/g for CS, and 192 to 332 m²/g for SB) with increasing the pyrolysis temperature from 500 to 600 °C. Further elevation of temperature to 700 °C exhibited enhancement in surface areas followed by reduction at 800 °C for all the US-treated samples except SB which showed slight increment from 352-358 m²/g. US-MS 700 showed the maximum surface areas with the values of 532 and 588 m²/g for micro and micro-meso porosity respectively, whereas US-SB 500 showed minimum values for the micro and micro-mesoporous surface areas (192 and 250 m²/g). Biochars pyrolyzed at 700 °C demonstrated the highest surface areas, indicating the most effective interaction with ultrasound waves. It is worth noting that the micro surface area of all biochars increased by almost 200 m²/g (on average) with a pyrolysis temperature increase of 500 to 700 °C. However, the same increment was observed by 30 sec of ultrasound activation at ambient conditions. Ultrasound cavitation results in the exfoliation of the graphitic clusters of the biochar structure, removal of mineral matter, and opening of the pores, thereby increasing microporous surface area. Similar observations are found in the literature and in our previous studies [109, 252, 253, 262, 263]. Similar to the surface areas, the pore volumes also exhibit a trend where maximum and minimum pore volumes can be obtained for US-MS 700 and US-SB 500 with the values of 0.21 and 0.11 cc/g respectively. The surface area data can be also verified using the SEM analysis results as observed from Figures 5.1-5.4. For instance,

among the ultrasound treated samples, US-SG 700 and US-MS 800 showed improved pore generation that corresponds to their high micropore surface areas ($520 \text{ m}^2/\text{g}$) and pore volume (0.21 cc/g) values. Hence, based on the surface area analysis results it can be emphasized that miscanthus biomass pyrolyzed at $700 \text{ }^\circ\text{C}$ and sonicated had the highest possible microporous surface area that would provide more active sites for amine activation to improve the CO_2 adsorption capacity.

5.4.3 Elemental Analysis

Carbon (C), nitrogen (N) and hydrogen (H), oxygen (O), sulfur (S), and the ash content of raw and activated biochars synthesized under different temperatures are summarized in Table 5.3 and the corresponding organic analysis on a dry ash-free basis are reported in Table 5.4. Oxygen (O) content was calculated by difference ($100\% - \%C + \%H + \%N + \%S + \%ash$).

Effect of pyrolysis temperature on the elemental composition of raw chars: Increasing pyrolysis temperature had a significant effect on the elemental constituents and H/C (the degree of aromaticity) [333] and O/C (the degree of polarity) ratios [334] of raw biochars. The following notable changes are observed for MS in the temperature range $500\text{-}600 \text{ }^\circ\text{C}$: %C increment from 75% to 82%; reduction in H/C and O/C ratios from 0.27 to 0.17 and 0.18 to 0.07, respectively, and %N content reduced by half. SG behaved in a similar manner: %C content showed significant increase from 68% to 77% with lowering of H/C and O/C ratios in the range of 0.29 to 0.16 and 0.18 to 0.09, respectively, and the increment of ash from 10.8% to 12.8%. Further increases in pyrolysis temperature exhibited small changes in %C and ash content (although there was wider variation in ash content for SG) and almost no changes in both H/C and O/C ratios (although there was wider variation in O/C for SG). The increase in carbon

content at higher temperature reflects the increasing degree of carbonization [170] and the decrease in H and O contents is likely due to dehydration reactions, the decomposition of the oxygenated bonds, and the release of low molecular weight byproducts containing H and O. In terms of structural transformation, the higher extent of carbonization indicates a more aromatic structure [333], and loss of O and H functional groups (such as hydroxyl, carboxyl, etc.) indicates a more hydrophobic structure [276]. Reduction in %N and %S contents can be attributed to the volatilization of nutrients at a high temperature which were resistant at low temperature and not easily volatilized. The observation is consistent with the literature, too [170, 335]. The results of the present study also generally exhibited enhancement of ash content with pyrolysis temperature, mainly due to the increase in the concentration of minerals (such as Na, Mg, Ca, K, etc.) in biochar samples with temperature since these elements are not lost by volatilization [170]. The two agro-industrial-based biochars (CS and SB) showed similar trends. For instance, CS follows an increasing trend of %C content up to 700 °C with a gradual rise of ash content and reduction of H/C and O/C ratios and %N contents. But a further increase in pyrolysis temperature (to 800 °C) resulted in a reduction in %C content and similarly follows a reverse trend for other elemental constituents. Similar to herbaceous chars, the trend for elemental analysis of agro-industrials is similar to the trend for surface area analysis data (Table 5.2) that showed a substantial change in surface area and pore volumes up to 700 °C with a reduction at 800 °C. Although %N content was maximum at 500 °C, maximum %C content was achieved at 700 °C. In comparison to other biochars, SB has comparatively lower %C content that ranged between 65 to 74% in the temperature interval of 500-800 °C which is also reflected in Table 5.2 that showed the lowest values of surface area for SB than any other raw biochar samples.

Table 5.3. Elemental Compositions (dry basis) of Raw and Activated Biochar Samples Synthesized at Different Pyrolysis Temperatures

Effect of Temperature on Raw Char Composition								
Sample Name	%C (wt. %)	%H (wt. %)	%N (wt. %)	%O (wt. %)	%S (wt. %)	%Ash (wt. %)	H/C ratio	O/C ratio
R-MS-500	74.60	3.38	0.45	17.42	0.74	3.41	0.27	0.18
R-MS-600	82.35	2.32	0.28	11.22	0.03	4.35	0.17	0.10
R-MS-700	83.69	2.4	0.39	8.20	0.45	4.87	0.17	0.07
R-MS-800	84.47	2.28	0.30	7.61	0.32	5.02	0.16	0.07
R-SG-500	67.83	3.28	1.01	16.32	0.8	10.76	0.29	0.18
R-SG-600	77.00	2.04	0.57	9.68	0.03	12.78	0.16	0.09
R-SG-700	76.98	2.25	0.91	11.00	0.47	8.39	0.18	0.11
R-SG-800	78.64	1.46	0.79	4.88	0.29	13.94	0.11	0.05
R-CS-500	71.47	3.28	0.85	13.44	0.76	10.20	0.28	0.14
R-CS-600	74.47	2.24	0.81	11.82	0.09	12.00	0.18	0.12
R-CS-700	76.23	1.92	0.68	5.83	0.34	15.00	0.15	0.06
R-CS-800	73.50	2.12	0.69	10.92	0.47	12.30	0.17	0.11
R-SB-500	65.12	2.13	0.62	15.80	0.59	15.74	0.20	0.18
R-SB-600	68.10	1.90	0.49	10.08	0.03	19.78	0.17	0.11
R-SB-700	73.58	2.40	0.61	3.09	0.52	19.80	0.20	0.03
R-SB-800	72.73	1.66	0.49	4.67	0.33	20.12	0.14	0.20
Effect of Temperature on Activated Char Composition								
A-MS-500	75.26	3.33	1.45	15.35	0.63	3.98	0.27	0.15
A-MS-600	70.16	2.13	1.50	10.09	0.03	17.47	0.18	0.11
A-MS-700	84.16	2.47	0.73	7.25	0.39	5.00	0.18	0.06
A-MS-800	85.79	1.79	1.31	6.05	0.26	4.8	0.13	0.05
A-SG-500	71.47	3.44	2.41	14.44	0.70	7.54	0.29	0.15
A-SG-600	69.71	2.06	1.25	10.37	0.09	17.38	0.18	0.11
A-SG-700	79.78	2.22	1.44	7.01	0.41	9.16	0.17	0.07
A-SG-800	80.12	1.49	2.19	7.59	0.31	8.3	0.11	0.07
A-CS-500	73.62	3.29	2.02	13.5	0.62	6.95	0.27	0.14
A-CS-600	77.00	2.57	1.41	10.92	0.06	7.90	0.20	0.11
A-CS-700	78.62	2.22	1.62	8.40	0.44	8.70	0.17	0.08
A-CS-800	77.51	2.26	1.36	9.35	0.42	9.10	0.17	0.09
A-SB-500	64.49	3.24	1.74	16.8	0.66	13.07	0.30	0.20
A-SB-600	78.11	2.24	1.12	10.15	0.03	8.91	0.17	0.09
A-SB-700	71.74	2.38	1.12	9.64	0.42	14.7	0.20	0.10
A-SB-800	77.48	1.75	1.37	3.50	0.30	15.6	0.14	0.03

Similar to CS, it generally showed increased %C and ash content, and reduced H/C-O/C ratios and %N content, for the temperature range of 500-800 °C, although values at 700 °C were

often the most extreme. Based on the above discussion it can be suggested that herbaceous biochars showed greater variations in elemental compositions compared to agro-industrial chars for the pyrolysis temperature range of 500-800 °C.

Effect of pyrolysis temperature on elemental composition of ultrasound amine activated chars: As per our previous studies, amination usually caused a reduction in ash content. Removal of ash from the biochar structure could be attributed to the washing away of mineral contents of the biochars during aqueous modifications [225]. On the other hand, ash content increases with temperature, as organic components are volatilized. These two contradictory effects caused some irregular alterations in ash content of biochars (particularly in herbaceous chars). However, an increasing trend was observed in the ash content of agro-industrial-based biochars with temperature, indicating the domination of temperature effect over amination impact. In order to prevent misinterpretation concerning organic content, elemental analysis of aminated samples is discussed by eliminating the impact of ash alteration. Table 5.4 (organic analysis) depicts gradual increment in %C contents of aminated MS samples with temperature, which is consistent to what was obtained for raw chars. Similar to MS, pyrolysis temperature caused increment of (ash-excluded) %C contents from 76-91% in raw SG chars to 77-88% in activated chars. Consistent with these observations, the C content of agro-industrial-based biochars (CS and SB) increased with temperature and also with respect to the %C content of their corresponding raw chars. As a general trend and by eliminating some minor fluctuations, %O contents for aminated samples were reduced with temperature, and were lower than the corresponding raw chars, since TEPA has no oxygen. The activated samples did not show any significant change in H/C and O/C ratios compared to the raw samples, despite substantial differences for C or O (Table 5.3) in sono-aminated vs. raw chars for some samples (MS600, SG600, SB600 and SB800 for %C;

SB700 for % O).

Table 5.4. Organic Compositions (dry ash-free basis) of Raw and Activated Biochars Synthesized at Different Pyrolysis Temperatures

Effect of Temperature on Raw Char Composition					
Sample Name	%C (wt. %)	%H (wt. %)	%N (wt. %)	%O (wt. %)	%S (wt. %)
R-MS-500	77.23	3.50	0.47	18.03	0.77
R-MS-600	85.60	2.41	0.29	11.66	0.03
R-MS-700	87.97	2.52	0.41	8.62	0.47
R-MS-800	88.93	2.40	0.32	8.01	0.34
R-SG-500	76.01	3.68	1.13	18.29	0.90
R- SG-600	86.21	2.28	0.64	10.84	0.03
R- SG-700	84.03	2.46	0.99	12.01	0.51
R- SG-800	91.38	1.70	0.92	5.67	0.34
R-CS-500	79.59	3.65	0.95	14.97	0.85
R-CS-600	83.27	2.50	0.91	13.22	0.10
R-CS-700	89.68	2.26	0.80	6.86	0.40
R-CS-800	83.81	2.42	0.79	12.45	0.54
R-SB-500	77.28	2.53	0.74	18.75	0.70
R-SB-600	84.49	2.36	0.61	12.51	0.04
R-SB-700	91.75	2.99	0.76	3.85	0.65
R-SB-800	76.54	1.75	0.52	20.85	0.35
Effect of Temperature on Activated Char Composition					
A-MS-500	78.38	3.47	1.51	15.98	0.66
A-MS-600	83.61	2.54	1.79	12.02	0.04
A-MS-700	88.59	2.60	0.77	7.63	0.41
A-MS-800	90.12	1.88	1.38	6.36	0.27
A-SG-500	77.30	3.72	2.61	15.62	0.76
A-SG-600	83.51	2.47	1.50	12.42	0.11
A-SG-700	87.81	2.44	1.58	7.72	0.45
A-SG-800	87.37	1.62	2.39	8.28	0.34
A-CS-500	79.12	3.54	2.17	14.51	0.67
A-CS-600	83.73	2.79	1.53	11.87	0.07
A-CS-700	86.11	2.43	1.77	9.20	0.48
A-CS-800	85.27	2.49	1.50	10.29	0.46
A-SB-500	74.19	3.72	2.00	19.33	0.76
A-SB-600	85.23	2.44	1.22	11.07	0.03
A-SB-700	84.10	2.79	1.31	11.30	0.49
A-SB-800	91.80	2.07	1.62	4.15	0.35

This can be explained as a result of changes of both numerator and denominator for H/C and O/C ratios, making the entire ratio almost equal.

As expected, the %N content of the activated biochar significantly increased, in the range of 2 - 6 times in MS and 1.6 - 2.6 times in SG samples, compared to the corresponding raw chars, since the aminated chars incorporated N-containing TEPA. In terms of temperature effects, the maximum of N content was observed in the lower temperatures (600 °C for MS and 500 °C for SG), the N content was reduced for middle-ranged temperatures (600 or 700 °C) and enhanced by further increase of temperature (to 800 °C). Similar behavior was observed in the two agro-industrial-based biochars (CS and SB). It can be concluded that elevated pyrolysis temperature showed overall reduction in elemental %N contents of both raw and aminated chars (Table 5.4), though a sudden jump in N content of almost all samples was observed at 800 °C.

5.4.4 FTIR Analysis

FTIR spectra of the raw and aminated biochars derived under different temperatures are depicted in Figures 5.5a-d. The baselines of the graphs were revised in Origin lab (Version 2019b) to allow a correct comparison of the intensity of the peaks and represented in Appendix I, Figures Ia-d. As found from the figures, the spectra include O-H stretching vibrations of hydrogen bonded hydroxyl groups at 3300-3600 cm^{-1} , and CO_2 absorption peak at 2300 cm^{-1} . The peak at 1600 cm^{-1} is ascribed to carboxylate (COO^-) and 1° amine N-H bending, [277] and aromatic C=C stretch is $\sim 1400 \text{ cm}^{-1}$ [305]. The peak around 1026 cm^{-1} is attributed to C-O stretching vibrations or the C-N stretch of an aliphatic primary amine [278]. Pyridine ring vibration and aromatic C-H deformation in the region 465-832 cm^{-1} indicate the presence of aromatic hydrogens [279, 283-285, 336].

Effect of pyrolysis temperature on surface functional groups of raw chars: As observed from the Figures 5.5a-d biochars began to increase aromatic deformation at higher pyrolysis temperature particularly at 800 °C. Most of the biochars showed intensified peak at 1400 cm⁻¹ attributed to aromatic C=C stretching except for MS. This result is likely due to the degradation and depolymerization of lignocellulosic structure. This further indicates the decrease of aliphatic

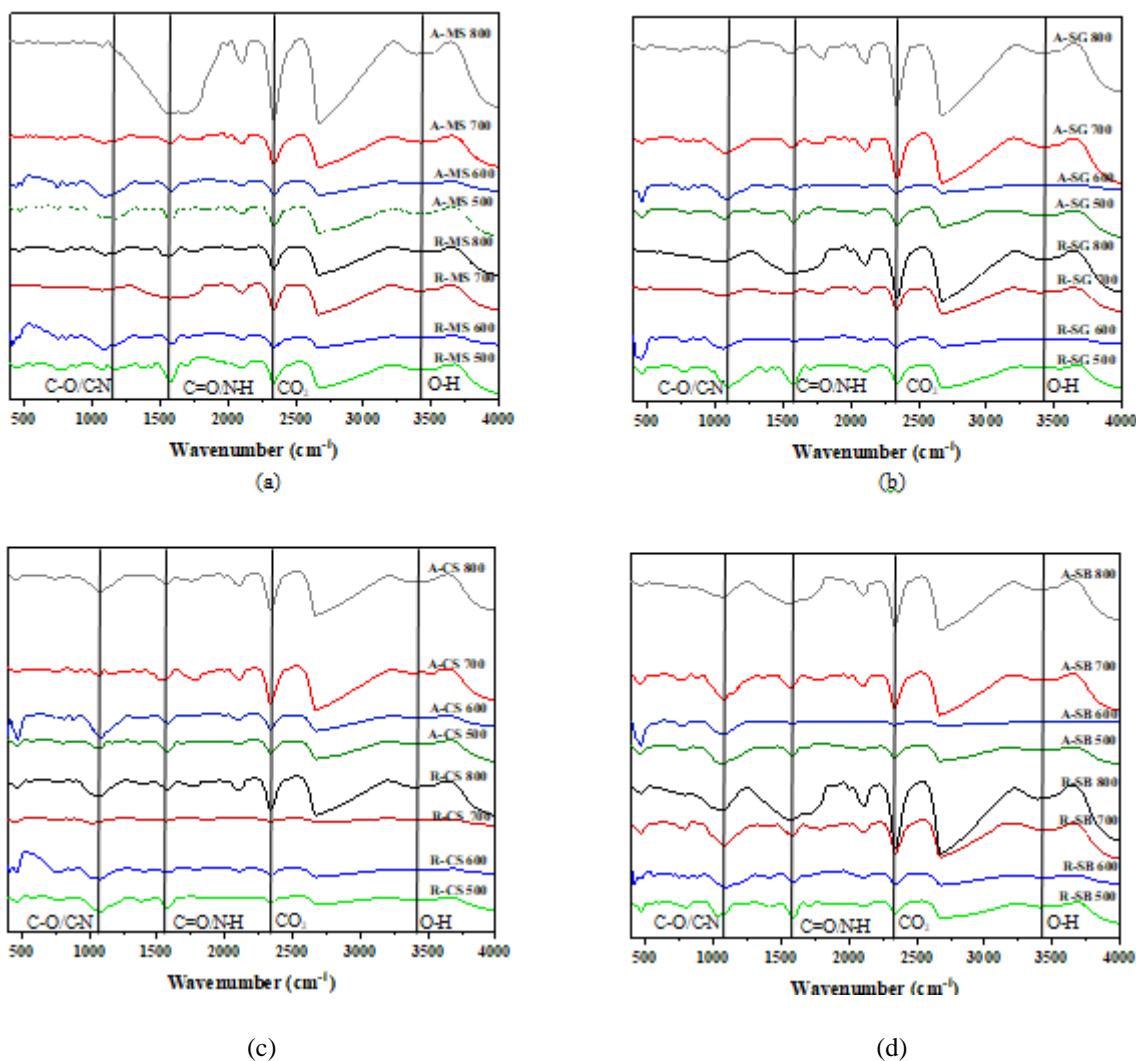


Figure 5.5. FTIR Spectra of Raw and Activated Samples (a) Miscanthus, (b) Switchgrass, (c) Corn Stover and (d) Sugarcane Bagasse Synthesized at Different Pyrolysis Temperatures

Effect of pyrolysis temperature on surface functional groups of ultrasound amine activated chars: The ultrasonic-amine functionalized spectra show shifts in peaks due to

interaction between surface functional groups and amino groups and the subsequent amine attachment. Ultrasonic treatment resulted in cleaning the surface which was also observed in the SEM images Figs 5.1-5.4. The FTIR results for aminated samples showed amino or nitrogen containing functionality such as C-N at $1000-1100\text{ cm}^{-1}$, which is attributed to the attachment of aliphatic amine. For instance, aminated MS samples showed strong C-N peak at $600\text{ }^{\circ}\text{C}$ compared to raw char which is also in accordance with %N content of A-MS-600 (-0.38) exhibiting 5 times increased value than R-MS-600 (-0.34) along with intense amine peak for A-MS-500 (-0.3) and A-MS-700 (-0.16) over the R-MS 500 (-0.13) and R-MS 700 (-0.12). Similarly, A-SG 600 (-0.39) and A-SG-700 (-0.39) showed improved amination than R-SG 600 (-0.29) and R-SG 700 (-0.20). A-CS 600 (-0.60), A-CS-700 (-0.16), A-CS 800 (-0.45) exhibited stronger C-N peak over R-CS 600 (-0.28), R-CS 700 (-0.10) and R-CS 800 (-0.42). Also aminated SB samples such as A-SB 500 (-0.45) and A-SB 700 (-0.68) have enhanced C-N peak than R-SB 500 (-0.34) and R-SB 700 (-0.61).

5.4.5 Raman Analysis

Raman spectroscopy combines a prominent surface selectivity and an exceptional sensitivity to the degree of structural order [312]. It is considered to be one of the most informative methods for investigation of the structural perfection of carbonaceous material (such as biochar). Figures 5.6 a-d show the Raman spectra of all raw and activated biochar samples synthesized under different temperature ranges- 500, 600, 700 and 800 $^{\circ}\text{C}$. The spectra exhibit two prominent peaks at 1400 and 1600 cm^{-1} designated as D and G peaks. The D-band is attributed to in-plane vibrations of sp^2 bonded carbon (intramolecular C-C vibration of aromatic carbon layers) within structural defects [337]. The G-band arises from the in-plane vibrations of the sp^2 -bonded crystallite carbon (intermolecular shear vibration between individual C-layers)

[229]. The ratio of the disorder-induced band (D band) to the Raman-allowed band (G band) is termed the intensity ratio (I_D/I_G). This describes the amount of disorganized material present [314]. The lower the I_D/I_G ratio, the higher the degree of graphitization of the carbonaceous structure. The intensity ratio values of all the samples have been reported in Table 5.5.

Table 5.5. Raman Intensity Ratios of Biochars Samples (Raw and Ultrasound Amine Activated Samples Synthesized at Different Pyrolysis Temperatures)

Sample Name	Intensity Ratio	Sample Name	Intensity Ratio
R-MS-500	0.65	A-MS-500	0.78
R-MS-600	0.73	A-MS-600	0.84
R-MS-700	0.76	A-MS-700	0.92
R-MS-800	0.88	A-MS-800	0.96
R-SG-500	0.70	A-SG-500	0.75
R-SG-600	0.82	A-SG-600	0.77
R-SG-700	0.86	A-SG-700	0.85
R-SG-800	0.88	A-SG-800	0.93
R-CS-500	0.58	A-CS-500	0.76
R-CS-600	0.73	A-CS-600	0.81
R-CS-700	0.80	A-CS-700	0.87
R-CS-800	0.83	A-CS-800	0.89
R-SB-500	0.59	A-SB-500	0.81
R-SB-600	0.82	A-SB-600	0.82
R-SB-700	0.90	A-SB-700	0.81
R-SB-800	1.01	A-SB-800	0.89

Effect of pyrolysis temperature on graphitic structure of raw chars: The I_D/I_G ratio for this category falls in the following range- 0.65 to 0.88 for MS, 0.70 to 0.88 for SG, 0.58 to 0.83 for CS and 0.59 to 1.01 for SB. For all of the biochar samples, an increment in the I_D/I_G ratio was observed with increasing pyrolysis temperature, indicating that the structure of the biochar becomes more and more disordered. A similar observation has been reported by Major and Jones et al. where the authors explained this increasing trend of the disorder as the evolvement of gas species including CH_4 , CO_2 , CO and H_2O forming throughout pyrolysis [317, 338]. These gasses emanate throughout the structure, promoting disorder until > 1000 °C. In addition, the most notable change in the I_D/I_G intensity ratio of both herbaceous and agro-industrial chars was observed when the temperature was raised from 500 to 600 °C followed by a slight increment

from 600 to 800 °C. This trend can be correlated to Table 5.2 and Table 5.3 that showed significant changes in surface areas and elemental compositions, respectively, when pyrolysis temperature was increased from 500 to 600 °C, irrespective of the biochar type.

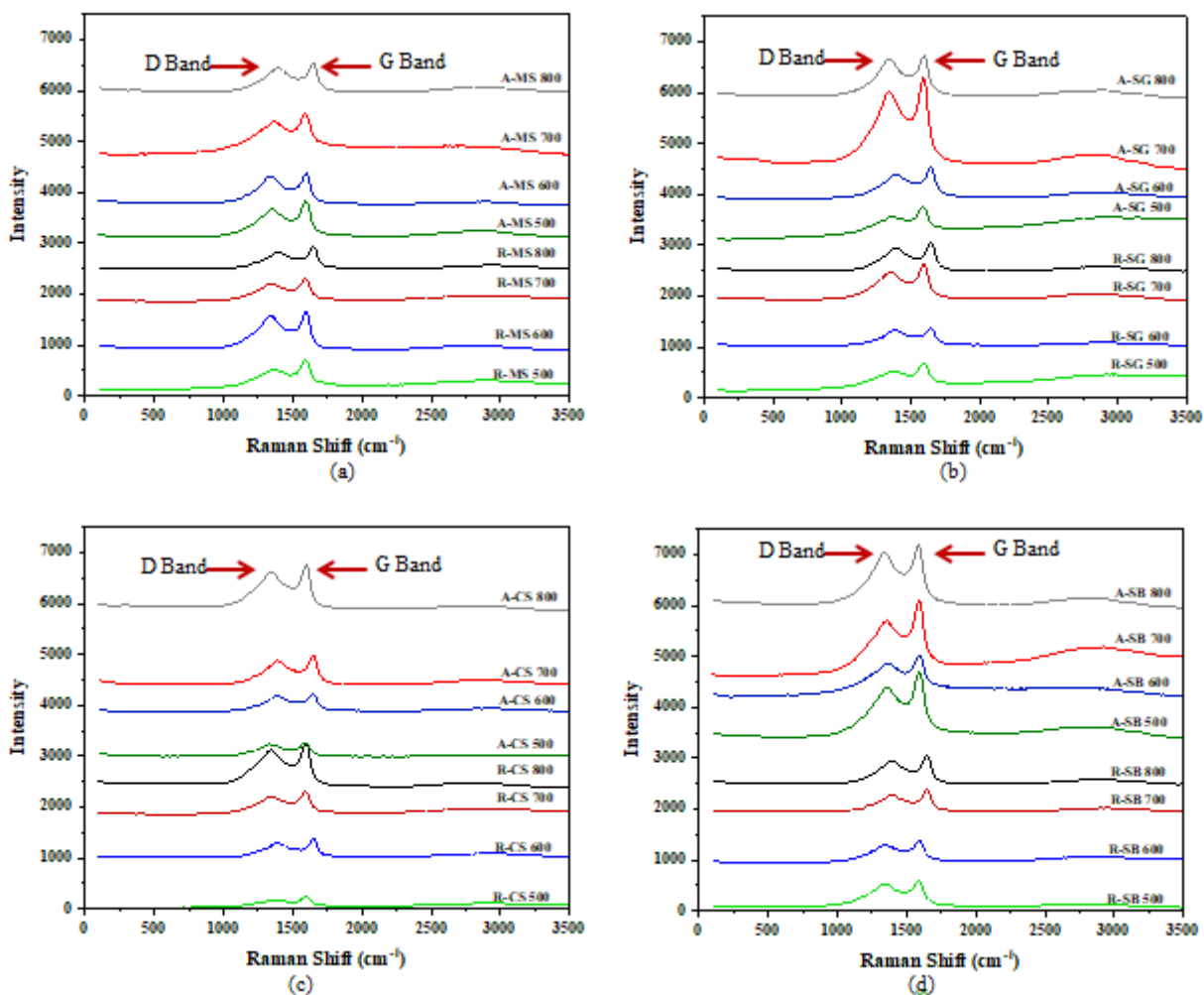


Figure 5.6. Raman Spectra of Raw and Activated Samples (a) Miscanthus, (b) Switchgrass, (c) Corn Stover and (d) Sugarcane Bagasse Synthesized at Different Pyrolysis Temperatures

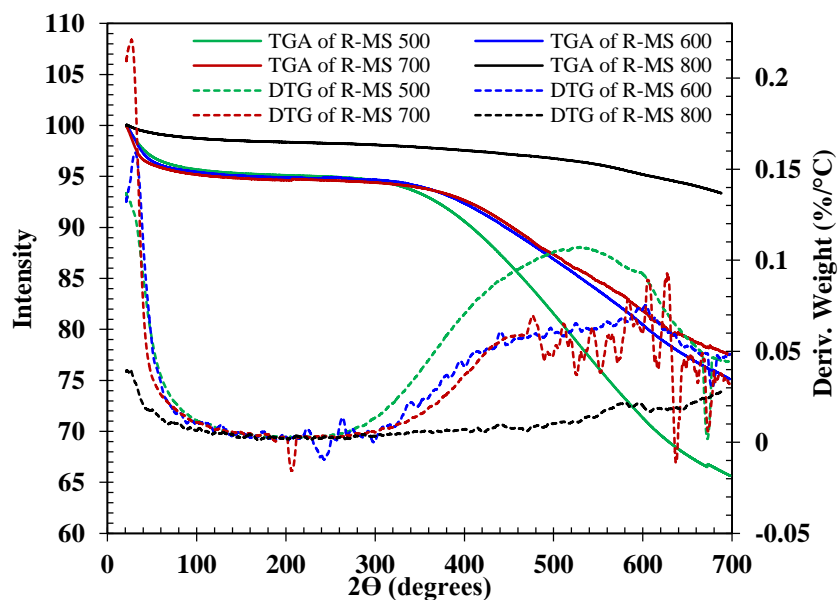
Effect of pyrolysis temperature on graphitic structure of ultrasound amine activated

chars: As a result of the addition of disordered functional groups, the I_D/I_G intensity ratio is expected to be greater for sono-aminated chars compared with raw samples. Consistent with this, almost all activated biochars (except A-SG-600/700 and A-SB-700/800) demonstrated a

significant increase in the I_D/I_G ratio compared with their pristine condition (Table 5.5). The maximum values were observed for MS, ranging from 0.78 to 0.96 for 500 to 800°C, respectively, consistent with their surface area data (Table 5.2). SG and CS showed similar behavior in terms of intensity ratio, but exhibited slightly lower values than MS. Compared to other activated biochar samples, SB showed the least I_D/I_G changes for 500, 600 and 700 °C, though the value increased to 0.89 by a further increase of temperature to 800 °C.

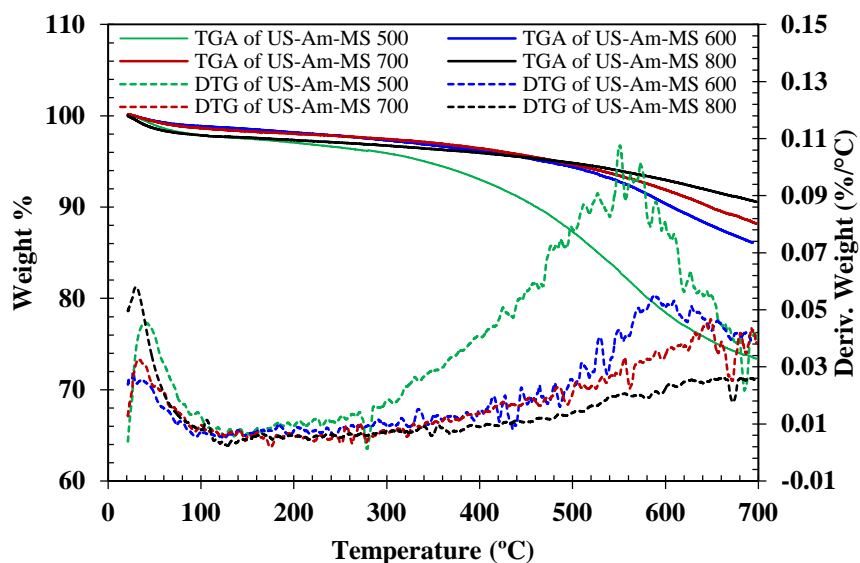
5.4.6 Thermal Stability Analysis

Thermogravimetric analysis and differential thermogravimetry curves for all the biochars are presented in Figures 5.7a-b. The mass loss occurred slowly around 60-70 °C, which is associated with the loss of the initial moisture of the raw sample observed in Figure 5.7a [339]. Beyond this, the main mass losses started at around 310-320 °C for R-MS-500 and 350-390 °C for R-MS-600 and R-MS-700 respectively and followed the trend as observed in the literature [305]. For MS-800 the curve is mostly flat indicating the negligible loss due to its high synthesis temperature. The above mentioned weight loss can be attributed to the degradation and decomposition of organic materials [62]. Above 600°C, decomposition for all the biochars completed and the curves became stable. It was interesting to note that the total weight losses resulting from thermal degradation were 34.3%, 24.9%, 22.3% and 6.6% for MS-500, MS-600, MS-700 and MS-800, respectively. This furthermore proves that the lower temperature derived biochars were less thermally stable than the higher temperature derived ones, probably because they were not fully carbonized [62, 305].



(a)

The TGA curve for aminated samples (5.7b) have similar trend as observed for raw samples where the samples showed reduction in mass around 60-70 °C attributed to the desorption of moisture.



(b)

Figure 5.7. TGA-DTG curves of (a) Raw and (b) Activated Miscanthus Samples Synthesized at 500, 600, 700 and 800 °C

The mass loss around 450-460 °C (TGA curve of Figure 5.7b) corresponds to the decomposition of the immobilized amine groups [340]. This higher decomposition temperatures of the amine activated samples (in comparison to the raw samples) revealed that the amine groups were effectively stabilized on the biochar [340]. The total weight loss for these samples can be listed as 26.7%, 13.9%, 11.8% and 9.5% respectively for US-Am-MS 500, US-Am-MS 600, US-Am-MS 700 and US-Am-MS 800 respectively. This indicates the stability of the aminated samples.

5.4.7 XRD Analysis

The X-ray diffraction plots of raw and aminated samples are shown in Figures 5.8a-b.

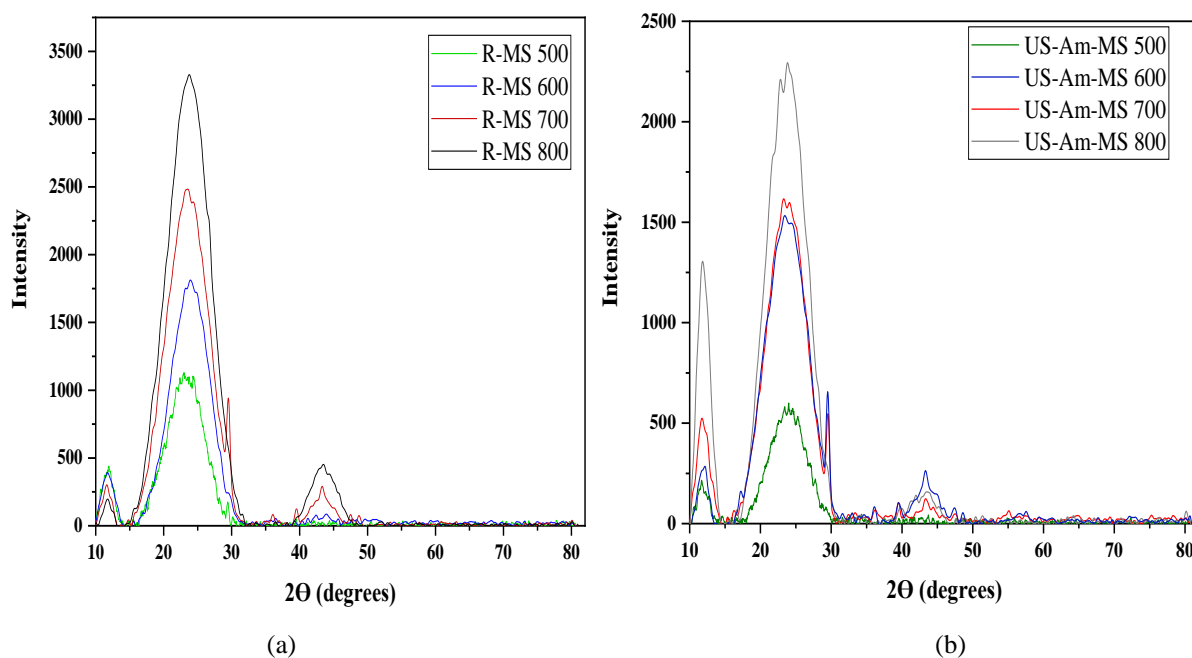


Figure 5.8. XRD plots of (a) Raw and (b) Activated Miscanthus Samples Synthesized at 500, 600, 700 and 800 °C

The presence of cellulose or other similar organic compounds is highlighted by the increase of the background level and by a large hump between 11° and 13° [341]. The sharp peak at the 2θ values around 23° associated with the crystalline cellulose for amorphous regions

(Figure 8a) [342, 343]. Notably, higher pyrolysis temperatures gave rise to the peak at 23° consistent to the literature [344]. A narrow peak at around 30° was found and identified as amorphous carbon [345, 346]. A new peak at 43° appeared for samples pyrolyzed at 600 and 700 °C that indicated the development of atomic order in the increasingly carbonized material [347]. This peak comes from the formation and successive ordering of aromatic carbon [283] indicating crystallization [348]. The formation of aromatic structures began after the complete decomposition of the wood nanocomposite structure during the charring process [283].

Interestingly, the peak at 11-13° for aminated samples (Figure 5.8b) showed relative intensity higher than the raw char. This is due to largely exposed facets of the crystal lattice that show a few peaks with high relative intensity [349]. However, the peaks around 23°, 30° and 43° showed reduction in intensity indicates the loss of crystallinity due to TEPA treatment.

5.4.8 CO₂ Adsorption Study

Effect of pyrolysis temperature on adsorption capacities of raw chars: Adsorption capacities of raw and sono-aminated biochars synthesized under different temperature conditions are presented in Figure 5.9. As observed, raw MS shows maximum adsorption capacities in comparison to all other raw chars (MS>SG>CS>SB) under all temperature ranges, although the differences are small. All raw biochars exhibited a gradual increase in adsorption capacity in the range of 67-88% while increasing the temperature from 500 to 600 °C. Although %N content decreased with temperature, the carbon content increased significantly, thus facilitating the increase in adsorption capacities. This is consistent with Raman and textural analysis that showed substantial increment in intensity ratio and surface area values, respectively, upon increasing the temperature from 500 to 600 °C. All the raw samples demonstrated a slight increase (4-13%) in CO₂ capture capacity at 700 °C compared with 600 °C, which can be

substantiated as per the elemental analysis data (C and N contents) (Table 5.3).

Effect of pyrolysis temperature on adsorption capacities of ultrasound amine activated chars: Although the pyrolysis temperature showed a slight effect on adsorption capacity of the raw biochars, it demonstrated a significant interaction with the acoustic-based amination process and the subsequent adsorption capacity of activated biochars. Based on Figure 5.9, adsorption capacities for activated chars can be categorized as: 0.86-1.23, 2.15-2.53, 2.22-2.89 and 1.34-1.74 mmol/g for the temperature ranges of 500, 600, 700 and 800 °C, respectively. These values are 215-251, 287-309, 285-310 and 227-259% higher compared to those of the raw biochar at the temperatures of 500, 600, 700 and 800 °C respectively. Similar to raw biochars, sono-chemically functionalized samples exhibited an increasing trend of adsorption capacities with temperature up to 700 °C, followed by a reduction at 800 °C; optimum adsorption capacities were obtained for temperatures 600-700 °C, which is in accordance to the Table 5.3 that showed notable differences (>3% change) in %C contents of MS, SG and SB at 600 °C temperature.

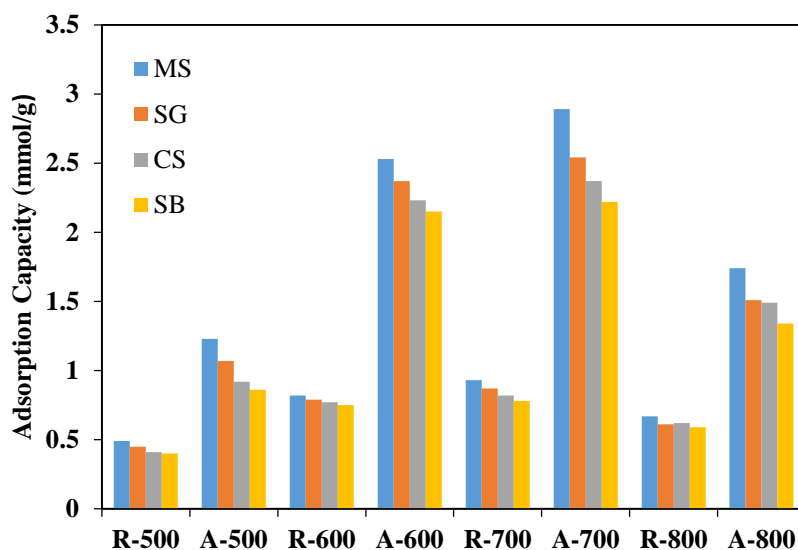


Figure 5.9. CO₂ Adsorption Capacities of both Raw and Sono-Chemically Activated Biochar Samples Synthesized at Different Pyrolysis Temperatures

As observed from Fig 5.9, the sono-aminated chars have much higher adsorption

capacities (almost 3 times) those of raw chars. The effect of ultrasound activation can be observed from the surface morphology analysis (Figs 5.1-5.4) where the activated char particles exhibited generation/opening of pores that resulted in increases of their surface area and porosity leading them to achieve higher amine loading. Among different sono-aminated samples, herbaceous biochars (MS and SG) showed greater adsorption capacity than agro-based chars (CS and SB). The results suggest that both surface area and functional groups play key roles in CO₂ capture. For example, on one hand, aminated MS contained the least N content compared to the other biochars, but on the other hand, MS structure involved the maximum porosity and surface area. Yet, the aminated MS, particularly at 600 and 700 °C, represented the maximum CO₂ adsorption. This trend is also corroborated based on Raman analysis. Increasing temperature showed increasing trend of intensity ratios and more defects in forms of functionality which is also observed in IR spectra of aminated samples for A-MS-500, A-MS-600 and A-MS-700. SG also exhibit similar behavior where %C content showed gradual increment and %N content showed gradual reducing trend with temperature but C-N peak from IR showed improved intensity for aminated samples at 600 and 700 °C than raw SG under same temperatures. Generally, the minimum CO₂ capture was observed in agro-industrial category, particularly SB biochar. Aminated SB had the lowest carbon and highest ash contents that resulted in low adsorption capacity. As observed, the ash content even increased with temperature. Accordingly, like other aminated biochars, A-SB-700 and A-SB-600 demonstrated a much greater adsorption compared with A-SB-500 and A-SB-800.

In general the biochars synthesized at 600-700 °C and sono-chemically modified showed improved adsorption capacities than 500 and 800 °C. This trend is further verified from the following physicochemical characterizations data. For instance, elemental analysis results (Table

5.3) expressed intense %N contents for aminated biochars at 600 °C. In addition to that the strong C-N peak for the TEPA activated samples (as observed from FTIR plots, Figures 5.5) for the temperature range of 600-700 °C also matches the adsorption capacity results. The intensity ratio values as observed from Table 5.4 exhibited the highest increment for 600-700 °C corresponding to their maximum adsorption capacity.

5.5 Conclusions

The present study investigated the importance of pyrolysis temperature on biochar properties, acoustic-based amination of biochar, and CO₂ adsorption. Herbaceous (MS and SG) and agro-industrial based biochars (CS and SB) were used for synthesizing biochars at four different pyrolysis temperatures that ranged from 500 to 800 °C. The biochars underwent two-step sonochemical activation: low-frequency low-temperature ultrasound activation followed by TEPA functionalization. The effectiveness of the prepared sorbents was assessed based on characterizations and CO₂ adsorption results. The increasing of pyrolysis temperature resulted in high %C and %ash contents with a reduction of %H, %O and %N contents for most of the samples with most prominent changes observed in the temperature range of 500-700 °C. Additionally, surface area and pore volumes were also enhanced at elevated temperatures up to 700 °C. All of these factors played a cumulative role in increasing adsorption capacity. Pyrolysis temperature had a lesser impact on enhancing CO₂ capture capacity of raw chars. Notable changes were observed in the structural and chemical properties of activated chars with pyrolysis temperature. The maximum adsorption capacities and the highest level of adsorption increment upon acoustic-based amination were both observed at 600-700 °C, which were 2.8-3.1 times greater than the adsorption capacity of the corresponding raw biochars. These intermediate temperatures are clearly the pyrolysis temperatures of choice for maximizing adsorption

capacity. The highest CO₂ capture was achieved for R-MS-700 among the raw chars, and A-MS-700 among the activated chars, with adsorption capacities of 0.93 and 2.89 mmol/g, respectively, at 70 °C and 0.10 atm CO₂ partial pressure. It must also be highlighted that the activating treatments of the biochars were conducted near room temperature, making the sonication and amination activation processes notably energy efficient, compared to thermal activation.

Author Contributions

Riya Chatterjee: Conducting the experiments, interpreting the results and writing the manuscript

Baharak Sajjadi: Idea of the work, interpreting the results and writing the manuscript

Wei-Yin Chen: Idea of the work and revise the manuscript

Daniell L Mattern: Interpreting the results and revise the manuscript

Nathan Hammer: Conducting Raman Analysis

Austin Dorris: Conducting Raman Analysis

Vijayshankar Raman: SEM Analysis

CHAPTER VI

Acoustic Treatment of Coal Gasification Residue for Extraction of Selenium

Baharak Sajjadi, Wei-Yin Chen, **Riya Chatterjee**. Acoustic Treatment of Coal Gasification Residue for Extraction of Selenium. *Energy & Fuels*, 2019. **33**(5): p. 4676-4680.

6.1 Abstract

The present study demonstrates that acoustic treatment of coal gasification residue in water with dissolved CO₂ is an effective route for extracting Se. It was recently revealed that the acoustic treatment can enhance the extraction of a series of metals, Na, K, Ca, Si, from the carbonaceous structures, e.g., biochar, due to the cavitation-induced phenomena including generation of micro-jets, shock-waves and hot-spots. US irradiation of graphitic carbonaceous structures in water/CO₂ partially exfoliates the graphitic clusters, creates new and opens the blocked pores, and increases the internal surface area, carbon content and hydrogen content through a group of sonolysis reactions of CO₂ and H₂O [109],[253]. The present study utilized ultrasound treatment with different amplitudes and total US energy consumption or irradiation durations under CO₂ blanket in the headspace of the solution to determine the extraction of a series of heavy metals, including selenium, from a coal gasification residue. The experimental results (not yet optimized) showed a significant reduction in selenium content (71%) in treated samples at 2000 J - 50% ultrasound (US) amplitude. A thorough study of this approach is certainly warranted.

6.2 Introduction

The coal combustion and gasification residues typically contain toxic heavy metals including arsenic, lead, mercury, cadmium, chromium, selenium etc. causing cancer, pulmonary disorder, cognitive defects, developmental delays, and behavioral problems [232]. Coal gasification residue is a major waste stream from the power plants, which is often stored in landfills as a long-term disposal means [211]. A typical concern regarding the landfills involves the risk of catastrophic failure (such as impoundment of ponds containing coal ash slurry), groundwater contamination, and their hazardous nonreversible effects on the local environment, especially with selenium [232]. The major environmental implication of selenium is its propensity to accumulate in aquatic food chains endangering human lives [350]. No satisfactory chemical, physical or biological treatment exists to remove selenium because the existing treatments can only work on small scale and are inefficient and expensive for large scale [351]. Acoustic treatment of biochar has been considered a new route for the production of advanced sorbents for CO₂ capture [146] and adsorption of heavy metals in wastewater [285].

6.3 Materials and Methods

The residue used in the current study was obtained from a coal gasifier in China. It was derived from lignite and has unusually low carbon content, 20.6%, representing a significant fraction of unused energy. The company is currently storing the residue in a landfill. In the current study, the acoustic energy was applied to the mixture of 7.5 g residual powders in 125 ml of water saturated with CO₂ [253]. The US treatment was conducted with a QSonica - Q700 sonicator of 20 kHz and 700 W in presence of 7% CO₂ in head-space. In order to control CO₂ concentration at 7%, a mixture of CO₂ (50 ml/min) balanced with helium (664 ml/min) was injected to the head space of the system. The following US amplitude and energy were chosen to

evaluate their effects on mineral leaching: 5% US amplitude and 2000 J energy (US-A5%-E2000J), 50% US amplitude and 2000 J energy (US-A50%-E2000J) and 50% US amplitude and 4000 J energy (US-A50%-E4000J). In order to explain ultrasound amplitude it can be expressed as a measurement of the excursion of the tip of the probe. The change of electrical energy into mechanical energy in ultrasound transducer causes the tip to move up and down. The displacement of ultrasound tip is called its amplitude and this is adjustable. In this work, an ultrasound tip with the amplitude of 120 microns was used (amplitude of 100%). Therefore, at settings of 50% and 5% amplitude, the probe will achieve the amplitudes of approximately 60 and 6 μm respectively. QSonica - Q700 sonicator is equipped with a monitor which shows the amplitude and the total amount of electrical energy. Additionally, 1800 s of ultrasonication was employed at 50% amplitude to assess the effect of prolonged acoustic treatment. To illuminate the impact of US irradiation, the leaching of metal was studied with water washing for 167 and 1800 s without irradiation. The durations were selected based on the experiments with 5% amplitude-2000 J energy, and 50% amplitude-1800 s, respectively. After each treatment, the mixture was filtered, and the residue was dried at 60 °C overnight under vacuum and analyzed for mineral and organics changes as well as elemental compositions and metal removal.

6.4 Results and Discussions

6.4.1 Effects of Ultrasound Amplitude, Energy and Irradiation Duration

Table 6.1 depicts the role of acoustic treatment in the extraction of heavy metals. Leaching of selenium, sodium, and potassium was accelerated when the US amplitude was increased from 5% to 50% (at constant ultrasound energy of 2000 J). Se removal increased from 33% for US-A5%-E2000J to 71% for US-A50%-E2000J. This behavior can be explained as a function of acoustic cavitation intensity, which increased significantly at high amplitude

accelerating the mass transfer. This facilitates the leaching of minerals which have strong bonding with the carbonaceous support. Meanwhile, the removal of cadmium and chromium was reduced with ultrasound amplitude.

Table 6.1. Changes in elemental metal concentration of the residue upon treatment (weight-based calculation*). Maximum possible selenium removal was achieved at 50% US amplitude and 2000 J US energy consumption within 41 s. 80% of arsenic was soluble in water for 1800 s implying the risk of leaching of metals in water

Sample Description	Na (µg/g)	Cd (µg/g)	Se (µg/g)	K (µg/g)	Ca (µg/g)	As (µg/g)	Hg (µg/g)	Cr (µg/g)	Pb (µg/g)
Raw	10,900	0.66	2.6	13,400	43,000	7.7	<0.02	98	80
US0-A0-W167s (Water Washed)	11,000	0.80	2.5	14,400	43,900	3.0	<0.02	97	80
Change during treatment, %	-26	-11	-29	-74	-21	-71	-	-27	-26
US0-A0-W1800s (Water Washed)	10,800	0.80	2.5	14,100	42,500	2.0	<0.02	95.8	85.6
Change during treatment, %	-26	-9.2	-28	-21	-26	-80	-	-27	-27
US-A5%-E2000J	10,650	0.64	2.25	13,350	41,950	7.7	<0.02	96	79.5
Change during treatment, %	-26	-25	-33	-23	-26	-24	-	-25	-24
US-A50%-E2000J	10,200	0.60	1.0	13,300	43,000	8.4	<0.02	105	79.3
Change during treatment, %	-30	-17	-71	-25	-25	-18	-	-19	-25
US-A50%-E4000J	10,400	0.60	1.3	13,400	43,800	8.7	<0.02	110	83.9
Change during treatment, %	-29	-32	-63	-26	24	-16	-	-17	22
US-A50%-E62977J-	11,000	0.8	2.4	14,400	44,400	3.0	<0.02	96	84.7
Change during treatment, %	-24	-9	-30	-19	-22	-71	-	-26	-20

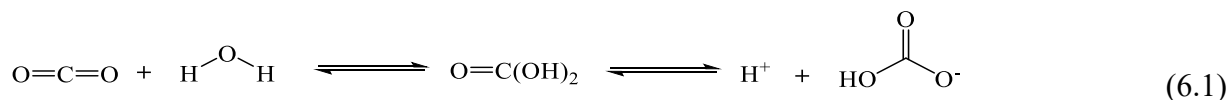
*Change in metal concentration was calculated taking weight change into consideration during treatment

This may be due to the formation of agglomeration of metal due to fusion at high temperature as a result of intensified sonication [352]. Similar behavior was observed when greater acoustic energy (4000 J) was applied at the same amplitude (50%). The results showed 12% reduction in Se and 2% in Cr removals, when the energy increased from 2000 to 4000 J. On the contrary, Cd removal was almost doubled with increasing acoustic energy. These results suggest that a combination of different acoustic amplitudes, while keeping the total energy consumption constant, can warrant significant removal of a wide range of heavy metals. This necessitates a

thorough analysis of the interaction between the kinetics of leaching of different minerals with acoustic intensity. In the next step, the effect of ultrasonication duration was investigated by treating the residue sample for a longer duration (1800 sec) at 50% amplitude. Data in Table 6.1 suggest that longer duration does not enhance the leaching of heavy metals, which could be attributed to aggregation during the long treatment time [353].

6.4.2 Effect of Dissolved CO₂

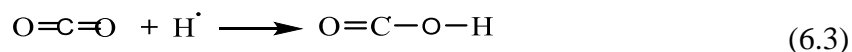
Dissolved CO₂ is the main source of water acidity in the system of interest. CO₂ keeps entering water through its interface with the atmosphere. Water reacts with aqueous CO₂ (aq), forming carbonic acid; $H_2O + CO_2(aq) \rightleftharpoons H_2CO_3(aq)$. Dissolved CO₂ in the form of carbonic acid may lose protons to form bicarbonate (6.1, $K=2.00 \times 10^{-4}$) and carbonate ($K=4.69 \times 10^{-11}$) [253].



The generated H⁺ ions interact with the metallic ions present in residue sample through ion exchange and remove them from the structure. This phenomenon contributes in hydrogen uptake as well. Moreover, sonolysis of CO₂ in water yields acidic organics including formaldehyde and formic acid in the following way. Our previous work revealed that ultrasound played a pivotal role in the complex 3-phase biochar/H₂O/CO₂ system that can be described with the following two reaction schemes: sonolysis of CO₂ followed by reactions between the sonolysis products and biochar [253]. Several studies showed the sonolysis of CO₂ in aqueous solution [180], [354] [355]. Henglein et al. revealed that CO₂ plays two major roles: scavenging hydrogen radicals and decomposition to CO [355]. It is known that ultrasound splits water to form hydrogen and hydroxyl radicals (6.2).



Scavenges $\cdot\text{H}$ from the sonolysis of water to form $\cdot\text{COOH}$ (6.3).



Small amounts of formic acid (HCOOH) are also observed, which could be explained by radical recombination (6.4).



These compounds could react with graphitic carbonaceous structures containing Lewis base and the π electrons. The basic nature of residue in water increased alkalinity that helped to trap a higher amount of CO_2 and organic acids during CO_2 bubbling and treatment thus enhanced the removal of basic cations through ion exchange and acid/base reactions.

6.4.3 Effect of Water Washing

The heavy metals are partially soluble in water. Hence, the water washing tests were conducted to illuminate the impact of ultrasound treatment. As observed, 29% of Se was leached out of the residue by simple washing. The value increased to 71% by using a short-term of ultrasound irradiation under CO_2 blanket. Therefore, enhanced removal of selenium through acoustic cavitation serves as a viable treatment technique for overcoming the challenges of handling coal fired residues. However, the dissolved selenium (selenite or selenate) can be further removed from the wastewater through either biological or chemical/physical processes. In the former, the dissolved selenium can be biologically reduced by bacteria under anoxic conditions to elemental selenium [356]. The later technologies include: oxidation/reduction, iron co-precipitation [357, 358], ion exchange (IX), and adsorption [359]. On the other hand, arsenic exhibited easy percolation during water washing. As observed, 80% of arsenic that was removed

from the residue was water leachable as reported earlier [360]. Therefore, integration and optimization of water and ultrasonic washing can effectively remove a wide range of metals, particularly As and Se, which can induce plant toxicity and subsequent effects on animals and humans [360].

6.4.4 Implications of mineral and organics change during treatment

The various parameters involving in the acoustic treatment process and their changes along with the elemental compositions are reported in Tables 6.2-6.3.

Table 6.2. Treatment of residue: treatment conditions, changes in biochar weight, pH, mineral content and organics; %weight change, %ash content and %mineral change is proportionate to the US energy consumed

Parameters	Raw	US0- W167s ^b	US0- W1800s ^b	US- A5%- E2000J ^a	US- A50%- E2000J ^b	US- A50%- E4000J ^b	US- A50%- E62977J ^b
Mass of residue (res) used in the sonication, g	-	7.5	7.5	7.5	7.5	7.5	7.5
pH of water	-	6.92	6.91	6.34	6.85	6.92	6.95
Water volume used, mL	-	125	125	125	125	125	125
pH of H ₂ O+ res	-	7.83	7.80	8.12	7.77	7.81	7.83
pH of H ₂ O+ res +CO ₂	-	4.90	4.94	4.98	4.92	5.07	4.84
Amplitude of sonication, %	-	-	-	5	50	50	50
CO ₂ in headspace, %	-	-	-	7	7	7	7
U.S. energy consumed, kJ/g	-	-	-	0.25	0.25	0.55	8.4
U.S. energy consumed, kcal/g	-	-	-	0.06	0.06	0.13	2
Maximum temperature, °C	-	-	-	26	25	28	32*
Treatment time, s	-	167	1800	167	41	80	1800
pH of filtrate	-	5.79	5.81	6.88	6.51	6.71	7.14
Weight change, %	-	-23.43	-22.18	-22.40	-22.78	-23.55	-21.75
Ash content, %	80.30	77.17	77.28	78.90	78.36	77.96	77.50
Mineral change, %	-	-26.41	-25.11	-23.75	-24.65	-25.03	-24.48
Organics, %	19.70	22.83	22.72	21.10	21.64	22.04	22.5
Organics change during treatment	-	-0.44	-0.39	-0.66	-0.59	-0.56	-0.41

^a done with de-ionized water; ^b done with distilled water; US: ultrasound; A= Ultrasound Amplitude ; E: Ultrasound Energy Supplied ; W= Water Washed ; number besides A denoted % of ultrasound amplitude; number besides W denotes time of water washing in sec; number besides E denotes ultrasound energy in Joule, *Temperature was controlled using ice bath

Note: the source of de-ionized water gave fluctuating pH values after the initial experiments were done and so, subsequent experiments were conducted using distilled water which demonstrated a more stable pH values

Weight change (in Table 6.2) represents a combination of mineral leaching, organics leaching as well as fixation of organics and minerals on the graphitic carbonaceous structure (herein residue) during the treatment. All weight changes show negative values, indicating the acoustic treatment induced a weight loss through the removal of inorganics or minerals and a small amount of change in organic compounds. The weight loss was more pronounced with increasing the ultrasonic amplitude and energy. This trend was also observed in our previous studies [109, 253]. In addition, the observed trend of weight loss is consistent with the % ash reduction and mineral leaching (Table 6.1). As a result, an increase in sonication amplitude (from 5% to 50% at constant energy consumption 0.06 kcal/g) and energy (0.06 kcal/g to 0.13 kcal/g) enhanced the mineral loss from 23.75 to 25.03%.

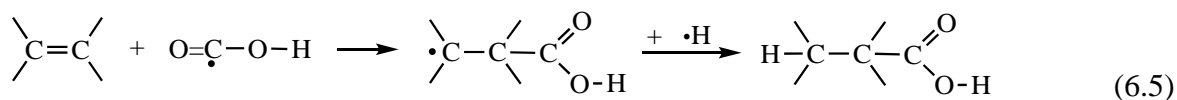
Organic content is a measure of the combustible (i.e., the gasified) fraction of the residue such as %C, %H, %O, %N and %S content. Change in organic composition during the treatments has been calculated and reported in Table 6.3. The highest hydrogen fixation was observed in water washed samples, while a slight H increase was obtained in ultrasonic-treated samples. This attributes to the different types of minerals removed and the kinetic of removal. The gain in hydrogen content of water-treated samples suggested the attachment of H^+ ion through ion exchange, $\overline{M}^+ + H^+ \rightleftharpoons \overline{H}^+ + M^+$; however, removal of mineral compounds under ultrasound irradiation is most likely due to cavitation and its implications. On the other hand, the reduction in O and C contents of samples treated with ultrasound is significantly lower compared with water washed residue. Since the weight loss is a combination of mineral leaching, organics leaching and fixation of organics, and given the fact that the values of ash loss in both ultrasound and water treated residues are very close, data in Table 6.3 imply significant losses of both organic content (C and O) during water washing.

Table 6.3. Elemental compositions of the raw and treated residues (dry basis)

Sample	C (% wt.)	H (% wt.)	N (% wt.)	O* (% wt.)	S (% wt.)	Ash (% wt.)
Raw	20.60	0.17	0.11	7.00	0.69	78.54
US0-A0-W167s	20.64	0.33	0.11	4.45	0.57	78.28
Change during treatment, %	-23	49	-23	-51	-37	-23
US0-A0-W1800s	20.62	0.33	0.12	3.71	0.60	78.49
Change during treatment, %	-22	51	-22	-59	-32	-22
US-A5%-E2000J	21.52	0.17	0.11	6.42	0.70	78.39
Change during treatment, %	-19	-22	-22	-29	-22	-22
US-A50%-E2000J	20.65	0.19	0.08	6.22	0.62	78.63
Change during treatment, %	-22.4	-14	-44	-32	-31	-23
US-A50%-E4000J	19.90	0.18	0.08	5.99	0.62	78.14
Change during treatment, %	-26	-19	-44	-26	-31	-24
US-A50%-E62977J	20.37	0.35	0.11	3.31	0.69	78.63
Change during treatment, %	-22	61	-22	-63	-31	-21

Oxygen content was calculated by "direct method".

Nevertheless, ultrasound appears to reduce these losses and possibly induces C and O fixation. Generally, nineteen complicated reactions occur in sonolysis of pure water alone, generating a series of highly reactive species and radicals including \dot{H} , $\dot{O}H$, H_2 , $\dot{H}O_2$, O_2 , H_2O_2 , \dot{O} [361, 362]. On the other hand, CO_2 and H_2O are the only sources for C, O and H fixation on the residue. Since an initial sonochemical reaction is the addition of $H\cdot$ to CO_2 to form a carbon-centered $\cdot COOH$ radical, it is possible that the radical adds to a π bond, and the resulting radical combines with another radical, giving a carboxylic acid (6.5).



Sonolysis of dissolved CO_2 can also directly split CO_2 to form highly reactive $\cdot O\cdot$. Diradical oxygen initiates a chain of reactions to form \dot{O}_2 , carbon atom and CO. Formic acid and formaldehyde may also be fixed on the residue that cause increases in C. We remain interested in the possible fixation of carbon from CO_2 to the graphitic carbonaceous structure [253].

6.5 Conclusions

This study introduced a fast and economically feasible method for removal of selenium from coal combustion and gasification residues in water/CO₂ system under ultrasound irradiation. The process was applied at room temperature and effectively removed 71% Se within 41 seconds. Additionally, the study revealed that simple water washing dissolved with CO₂ can remove significant amount of arsenic (80%) from the residue samples. The results suggested that integration and optimization of ultrasonic treatment of different acoustic amplitudes (5 to 50%) with simple water washing can maximize the removal of a wide range of residual's heavy metals. The results were obtained at early stage of our study thus it needs further thorough investigation to optimize the process aiming at maximum removal of all the heavy metals.

Author Contributions

Baharak Sajjadi: Idea of the work, interpreting the results and writing the manuscript

Wei-Yin Chen: Idea of the work and revise the manuscript

Riya Chatterjee: Conducting the experiments, interpreting the results and writing the manuscript

CHAPTER VII

CONCLUSIONS AND RECOMMENDATIONS

7.1 Conclusions

The current study aimed at introducing a fast, economically feasible and efficient physical chemical method for the modification of biochar. In this process, biochar was first treated under ultrasonic irradiation with an optimum exposure time of only 30 s, followed by chemical amination at room temperature. From the characterization of activated biochar, it became clear that ultrasound exfoliated the graphene clusters of biochar, cleaned and opened blocked micro-pores, and increased its surface area. All these factors intensified the chemical functionalization of biochar with TEPA. In continuation to that the study further provides an analysis of the CO₂ adsorption potentials of biochar aminated with five different amines (MEA, PZ, DEA, TEPA, and PEI) and their binary (MEA-TEPA, DEA-TEPA, DEA-PEI, TEPA-PEI) and ternary (DEA-TEPA-PEI) mixtures coupled with ultrasonication and EDC-HOBt or (in 3 cases) KOH activation. Functionalization with the TEPA and MEA-TEPA mixture (with EDC-HOBt) led to 2.04 and 1.91 mmol/g of equilibrium sorption capacity.

Thus, the further approach with different biomasses were followed where the biochars were further subjected to acoustic-based physical activation, chemical functionalization employing TEPA amine and integrated physico-chemical activation techniques. The results indicated that physical activation and chemical modification separately enhanced adsorption capacity in the range of 12-37% and 51-55% (compared to raw char) respectively. However, maximum improvement was attained for the combined ultrasono-amine functionalization

technique that falls between 184-200% over raw char. Moreover, it has been also observed that herbaceous category based biochars such as MS and SG have the highest adsorption capacities (2.53 and 2.37 mmol/g respectively at 0.10 atm. and 70 °C) over the other two categories under the integrated sono-chemical activation route. This is primarily attributed to the high %C content (77-82%), low %ash contents (4.35-12.78) and improved textural properties (324-340 m²/g) for raw MS and SG that when modified employing sono-chemical pathway provided maximum nitrogenation (2.2-5.35 times than raw char) and corresponding optimum adsorption capacities. Additionally, the entire sono-chemical activation is conducted at room temperature that makes it very energy efficient and utilization of biomass makes it highly economic providing an efficient way for synthesizing adsorbent for effective CO₂ adsorption.

7.2 Recommendations for Future Work

7.2.1. Plasma Activation of Biochar

Non-thermal plasma produces energetic electrons, ions and active radicals that improve the pore structure of sorbent and increase the active functional groups on the surface of sorbent. Plasma caused the biochar surface to become porous and promoted the thermal stability of the biochar. Thus, the surface become highly accessible for further modification through chemical treatment that would lead to increased CO₂ adsorption capacity. In this regard the following works can be performed-

- Applications of different gases such as NH₃, O₂, Cl₂ gases to determine the effectiveness of each one for CO₂ adsorption

- Amalgamating plasma and chemical modification to further improve carbon capture properties of biochar
- Comparing the effectiveness of both ultrasound-chemical and plasma-chemical modifications in terms of increasing CO₂ capture capacity

7.2.2 Simultaneous Pyrolysis and Activation

Additionally, pyrolysis of biomass can be conducted in presence of reactive gases such as CO₂ or steam to identify their importance to increase CO₂ adsorption behavior.

BIBLIOGRAPHY

BIBLIOGRAPHY

1. Bose, B.K., *Global warming: Energy, environmental pollution, and the impact of power electronics*. IEEE Industrial Electronics Magazine, 2010. **4**(1): p. 6-17.
2. Lee, S.-Y. and S.-J. Park, *A review on solid adsorbents for carbon dioxide capture*. Journal of Industrial and Engineering Chemistry, 2015. **23**: p. 1-11.
3. Prices, E.C., *CO₂ Emissions from Fuel Combustion International Energy Agency*.
4. Truth, A.I., *directed by Davis Guggenheim*. Performed by Al Gore, 2006.
5. James, R., et al., *The power to reduce CO₂ emissions: The full portfolio*. Electric Power Research Institute: Palo Alto, CA, 2007.
6. Houghton, J.T., et al., *Climate change 2001: the scientific basis*. 2001: The Press Syndicate of the University of Cambridge.
7. ; Available from: www.ipcc.ch/.
8. Freibauer, A., et al., *Carbon sequestration in the agricultural soils of Europe*. Geoderma, 2004. **122**(1): p. 1-23.
9. Zeman, F., *Energy and material balance of CO₂ capture from ambient air*. Environmental science & technology, 2007. **41**(21): p. 7558-7563.
10. Creamer, A.E. and B. Gao, *Carbon-Based Adsorbents for Postcombustion CO₂ Capture: A Critical Review*. Environmental Science & Technology, 2016. **50**(14): p. 7276-7289.
11. Bui, M., et al., *Dynamic modelling and optimisation of flexible operation in post-combustion CO₂ capture plants—A review*. Computers & Chemical Engineering, 2014. **61**: p. 245-265.
12. Goto, K., K. Yogo, and T. Higashii, *A review of efficiency penalty in a coal-fired power plant with post-combustion CO₂ capture*. Applied Energy, 2013. **111**: p. 710-720.
13. Cotton, A., K. Patchigolla, and J.E. Oakey, *Minor and trace element emissions from post-combustion CO₂ capture from coal: Experimental and equilibrium calculations*. Fuel, 2014. **117**: p. 391-407.
14. Lockwood, T., *A comparative review of next-generation carbon capture technologies for coal-fired power plant*. Energy procedia, 2017. **114**: p. 2658-2670.
15. Jansen, D., et al., *Pre-combustion CO₂ capture*. International Journal of Greenhouse Gas Control, 2015. **40**: p. 167-187.
16. TEC, R., *Carbon Dioxide Capture Technology Sheets*.
17. Lockwood, T., *Developments in oxyfuel combustion of coal*. Report of IEA Clean Coal Centre, 2014.
18. da Costa, J., et al., *State of art (SOTA) report on dense ceramic membranes for oxygen separation from air*. 2013.
19. Suzuki, T., et al., *Regio-and stereoselective ring opening of epoxy alcohols with organoaluminium compounds leading to 1, 2-diols*. Tetrahedron Letters, 1982. **23**(35): p. 3597-3600.
20. Choi, S., J.H. Drese, and C.W. Jones, *Adsorbent materials for carbon dioxide capture from large anthropogenic point sources*. ChemSusChem: Chemistry & Sustainability

Energy & Materials, 2009. **2**(9): p. 796-854.

21. Yu, C.-H., C.-H. Huang, and C.-S. Tan, *A review of CO₂ capture by absorption and adsorption*. Aerosol Air Qual. Res, 2012. **12**(5): p. 745-769.
22. Keskes, E., C.S. Adjiman, and A. Galindo, *A Physical Absorption Process for The Capture of CO₂ From CO₂-Rich Natural Gas Streams*. 2006.
23. Spigarelli, B.P. and S.K. Kawatra, *Opportunities and challenges in carbon dioxide capture*. Journal of CO₂ Utilization, 2013. **1**: p. 69-87.
24. Hinkov, I., et al., *Carbon Dioxide Capture by Adsorption*. Journal of Chemical Technology & Metallurgy, 2016. **51**(6).
25. Creamer, A.E., B. Gao, and M. Zhang, *Carbon dioxide capture using biochar produced from sugarcane bagasse and hickory wood*. Chemical Engineering Journal, 2014. **249**: p. 174-179.
26. Ghosh, A., et al., *Uptake of H₂ and CO₂ by graphene*. The Journal of Physical Chemistry C, 2008. **112**(40): p. 15704-15707.
27. Saha, D. and S. Deng, *Adsorption equilibrium and kinetics of CO₂, CH₄, N₂O, and NH₃ on ordered mesoporous carbon*. Journal of colloid and interface science, 2010. **345**(2): p. 402-409.
28. Younas, M., et al., *Feasibility of CO₂ adsorption by solid adsorbents: a review on low-temperature systems*. International journal of environmental science and technology, 2016. **13**(7): p. 1839-1860.
29. Seema, H., et al., *Highly selective CO₂ capture by S-doped microporous carbon materials*. Carbon, 2014. **66**: p. 320-326.
30. Bai, B.C., et al., *Effects of aminated carbon molecular sieves on breakthrough curve behavior in CO₂/CH₄ separation*. Journal of Industrial and Engineering Chemistry, 2013. **19**(3): p. 776-783.
31. Yu, J., et al., *One-pot synthesis of highly ordered nitrogen-containing mesoporous carbon with resorcinol-urea-formaldehyde resin for CO₂ capture*. Carbon, 2014. **69**: p. 502-514.
32. Himeno, S., T. Komatsu, and S. Fujita, *High-Pressure Adsorption Equilibria of Methane and Carbon Dioxide on Several Activated Carbons*. Journal of Chemical & Engineering Data, 2005. **50**(2): p. 369-376.
33. Sevilla, M. and A.B. Fuertes, *CO₂ adsorption by activated templated carbons*. Journal of Colloid and Interface Science, 2012. **366**(1): p. 147-154.
34. Wang, J. and S. Kaskel, *KOH activation of carbon-based materials for energy storage*. Journal of Materials Chemistry, 2012. **22**(45): p. 23710-23725.
35. Park, S.-J., et al., *Studies on pore structures and surface functional groups of pitch-based activated carbon fibers*. Journal of Colloid and Interface Science, 2003. **260**(2): p. 259-264.
36. Zhao, Y., et al., *Superior Capture of CO₂ Achieved by Introducing Extra-framework Cations into N-doped Microporous Carbon*. Chemistry of Materials, 2012. **24**(24): p. 4725-4734.
37. Sevilla, M. and A.B. Fuertes, *Sustainable porous carbons with a superior performance for CO₂ capture*. Energy & Environmental Science, 2011. **4**(5): p. 1765-1771.
38. Meng, L.-Y. and S.-J. Park, *One-pot synthetic method to prepare highly N-doped nanoporous carbons for CO₂ adsorption*. Materials Chemistry and Physics, 2014. **143**(3): p. 1158-1163.

39. Meng, L.-Y. and S.-J. Park, *Effect of exfoliation temperature on carbon dioxide capture of graphene nanoplates*. Journal of colloid and interface science, 2012. **386**(1): p. 285-290.
40. Jang, D.-I. and S.-J. Park, *Influence of nickel oxide on carbon dioxide adsorption behaviors of activated carbons*. Fuel, 2012. **102**: p. 439-444.
41. Lee, J., J. Kim, and T. Hyeon, *Recent Progress in the Synthesis of Porous Carbon Materials*. Advanced Materials, 2006. **18**(16): p. 2073-2094.
42. Yuan, B., et al., *Adsorption of CO₂, CH₄, and N₂ on Ordered Mesoporous Carbon: Approach for Greenhouse Gases Capture and Biogas Upgrading*. Environmental Science & Technology, 2013. **47**(10): p. 5474-5480.
43. Pevida, C., T.C. Drage, and C.E. Snape, *Silica-templated melamine-formaldehyde resin derived adsorbents for CO₂ capture*. Carbon, 2008. **46**(11): p. 1464-1474.
44. Ma, X., M. Cao, and C. Hu, *Bifunctional HNO₃ catalytic synthesis of N-doped porous carbons for CO₂ capture*. Journal of Materials Chemistry A, 2013. **1**(3): p. 913-918.
45. Mahurin, S.M., et al., *Enhanced CO₂/N₂ selectivity in amidoxime-modified porous carbon*. Carbon, 2014. **67**: p. 457-464.
46. Yoo, H.-M., S.-Y. Lee, and S.-J. Park, *Ordered nanoporous carbon for increasing CO₂ capture*. Journal of Solid State Chemistry, 2013. **197**: p. 361-365.
47. Suzuki, M., *Activated carbon fiber: Fundamentals and applications*. Carbon, 1994. **32**(4): p. 577-586.
48. Yoon, S.-H., et al., *KOH activation of carbon nanofibers*. Carbon, 2004. **42**(8): p. 1723-1729.
49. Lee, S.-Y. and S.-J. Park, *Carbon dioxide adsorption performance of ultramicroporous carbon derived from poly(vinylidene fluoride)*. Journal of Analytical and Applied Pyrolysis, 2014. **106**: p. 147-151.
50. Álvarez-Gutiérrez, N., et al., *Adsorption Performance Indicator to Screen Carbon Adsorbents for Post-combustion CO₂ Capture*. Energy Procedia, 2017. **114**: p. 2362-2371.
51. Chua, C.K. and M. Pumera, *Chemical reduction of graphene oxide: a synthetic chemistry viewpoint*. Chemical Society Reviews, 2014. **43**(1): p. 291-312.
52. Zhao, Y., H. Ding, and Q. Zhong, *Synthesis and characterization of MOF-aminated graphite oxide composites for CO₂ capture*. Applied Surface Science, 2013. **284**: p. 138-144.
53. Lee, S.-Y. and S.-J. Park, *Isothermal exfoliation of graphene oxide by a new carbon dioxide pressure swing method*. Carbon, 2014. **68**: p. 112-117.
54. Han, K.K., et al., *Efficient MgO-based mesoporous CO₂ trapper and its performance at high temperature*. Journal of Hazardous Materials, 2012. **203-204**: p. 341-347.
55. Bhagiyalakshmi, M., et al., *A direct synthesis of mesoporous carbon supported MgO sorbent for CO₂ capture*. Fuel, 2011. **90**: p. 1662-1667.
56. Pierre-Louis, A.-M., et al., *Adsorption of carbon dioxide on Al/Fe oxyhydroxide*. Journal of colloid and interface science, 2013. **400**.
57. Liu, W.-J., et al., *Mesoporous Carbon Stabilized MgO Nanoparticles Synthesized by Pyrolysis of MgCl₂ Preloaded Waste Biomass for Highly Efficient CO₂ Capture*. Environmental Science & Technology, 2013. **47**(16): p. 9397-9403.
58. Lu, A.-H., G.-P. Hao, and X.-Q. Zhang, *Porous Carbons for Carbon Dioxide Capture*. 2014. p. 15-77.

59. Alhwaige, A.A., et al., *Biobased chitosan hybrid aerogels with superior adsorption: Role of graphene oxide in CO₂ capture*. RSC Advances, 2013. **3**(36): p. 16011-16020.
60. Dissanayake, P.D., et al., *Biochar-based adsorbents for carbon dioxide capture: A critical review*. Renewable and Sustainable Energy Reviews, 2019: p. 109582.
61. Liu, Y., et al., *Impact of biochar amendment in agricultural soils on the sorption, desorption, and degradation of pesticides: a review*. Science of the Total Environment, 2018. **645**: p. 60-70.
62. Sun, Y., et al., *Effects of feedstock type, production method, and pyrolysis temperature on biochar and hydrochar properties*. Chemical Engineering Journal, 2014. **240**: p. 574-578.
63. Mulabagal, V., et al., *Biochar from biomass: a strategy for carbon dioxide sequestration, soil amendment, power generation, and CO₂ utilization*. Handbook of Climate Change Mitigation and Adaptation, 2015: p. 1937-1974.
64. Dikin, D.A., et al., *Preparation and characterization of graphene oxide paper*. Nature, 2007. **448**(7152): p. 457-460.
65. Loh, K.P., et al., *Graphene oxide as a chemically tunable platform for optical applications*. Nature chemistry, 2010. **2**(12): p. 1015.
66. Novoselov, K.S., et al., *Electric field effect in atomically thin carbon films*. science, 2004. **306**(5696): p. 666-669.
67. Stolyarova, E., et al., *High-resolution scanning tunneling microscopy imaging of mesoscopic graphene sheets on an insulating surface*. Proceedings of the National Academy of Sciences, 2007. **104**(22): p. 9209-9212.
68. Xiao, X., et al., *Sugar cane-converted graphene-like material for the superhigh adsorption of organic pollutants from water via coassembly mechanisms*. Environmental science & technology, 2017. **51**(21): p. 12644-12652.
69. Mkhoyan, K.A., et al., *Atomic and Electronic Structure of Graphene-Oxide*. Nano Letters, 2009. **9**(3): p. 1058-1063.
70. Cheng, F. and X. Li, *Preparation and application of biochar-based catalysts for biofuel production*. Catalysts, 2018. **8**(9): p. 346.
71. Zhang, X., et al., *Nitrogen enriched biochar modified by high temperature CO₂-ammonia treatment: Characterization and adsorption of CO₂*. Chemical Engineering Journal, 2014. **257**: p. 20-27.
72. You, S., et al., *A critical review on sustainable biochar system through gasification: energy and environmental applications*. Bioresource technology, 2017. **246**: p. 242-253.
73. Xu, X., et al., *Chemical transformation of CO₂ during its capture by waste biomass derived biochars*. Environmental pollution, 2016. **213**: p. 533-540.
74. Palansooriya, K.N., et al., *Response of microbial communities to biochar-amended soils: a critical review*. Biochar, 2019. **1**(1): p. 3-22.
75. Hansen, V., et al., *Gasification biochar as a valuable by-product for carbon sequestration and soil amendment*. Biomass and Bioenergy, 2015. **72**: p. 300-308.
76. Gai, X., et al., *Effects of feedstock and pyrolysis temperature on biochar adsorption of ammonium and nitrate*. PloS one, 2014. **9**(12).
77. Ahmad, M., et al., *Biochar as a sorbent for contaminant management in soil and water: a review*. Chemosphere, 2014. **99**: p. 19-33.
78. Pacioni, T.R., et al., *Bio-syngas production from agro-industrial biomass residues by steam gasification*. Waste management, 2016. **58**: p. 221-229.
79. Zhang, Z., et al., *Critical role of small micropores in high CO₂ uptake*. Physical

- Chemistry Chemical Physics, 2013. **15**(7): p. 2523-2529.
80. Angin, D., *Effect of pyrolysis temperature and heating rate on biochar obtained from pyrolysis of safflower seed press cake*. Bioresource technology, 2013. **128**: p. 593-597.
 81. Lahijani, P., M. Mohammadi, and A.R. Mohamed, *Metal incorporated biochar as a potential adsorbent for high capacity CO₂ capture at ambient condition*. Journal of CO₂ Utilization, 2018. **26**: p. 281-293.
 82. Sajjadi, B., W.-Y. Chen, and N. Egiebor, *A comprehensive review on physical activation of biochar for energy and environmental applications*. Reviews in Chemical Engineering, 2018. **35**.
 83. Hulicova-Jurcakova, D., et al., *Combined effect of nitrogen-and oxygen-containing functional groups of microporous activated carbon on its electrochemical performance in supercapacitors*. Advanced functional materials, 2009. **19**(3): p. 438-447.
 84. Xing, W., et al., *Oxygen-containing functional group-facilitated CO₂ capture by carbide-derived carbons*. Nanoscale research letters, 2014. **9**(1): p. 1-8.
 85. Liu, Y. and J. Wilcox, *Effects of surface heterogeneity on the adsorption of CO₂ in microporous carbons*. Environmental science & technology, 2012. **46**(3): p. 1940-1947.
 86. Shafeeyan, M.S., et al., *A review on surface modification of activated carbon for carbon dioxide adsorption*. Journal of Analytical and Applied Pyrolysis, 2010. **89**(2): p. 143-151.
 87. Guo, T., et al., *Characteristics of CO₂ adsorption on biochar derived from biomass pyrolysis in molten salt*. The Canadian Journal of Chemical Engineering, 2018. **96**(11): p. 2352-2360.
 88. Shen, W. and W. Fan, *Nitrogen-containing porous carbons: synthesis and application*. Journal of Materials Chemistry A, 2013. **1**(4): p. 999-1013.
 89. Nugent, P., et al., *Porous materials with optimal adsorption thermodynamics and kinetics for CO₂ separation*. Nature, 2013. **495**(7439): p. 80-84.
 90. Gao, F., et al., *Dynamic hydrophobic hindrance effect of zeolite@ zeolitic imidazolate framework composites for CO₂ capture in the presence of water*. Journal of Materials Chemistry A, 2015. **3**(15): p. 8091-8097.
 91. Igalavithana, A.D., et al., *Advances and future directions of biochar characterization methods and applications*. Critical reviews in environmental science and technology, 2017. **47**(23): p. 2275-2330.
 92. Rajapaksha, A.U., et al., *Engineered/designer biochar for contaminant removal/immobilization from soil and water: potential and implication of biochar modification*. Chemosphere, 2016. **148**: p. 276-291.
 93. Zhang, Y.-N., et al., *Antenna-predominant and male-biased CSP19 of Sesamia inferens is able to bind the female sex pheromones and host plant volatiles*. Gene, 2014. **536**(2): p. 279-286.
 94. Antolini, E., *Nitrogen-doped carbons by sustainable N- and C-containing natural resources as nonprecious catalysts and catalyst supports for low temperature fuel cells*. Renewable and Sustainable Energy Reviews, 2016. **58**: p. 34-51.
 95. Guizani, C., et al., *Biomass char gasification by H₂O, CO₂ and their mixture: Evolution of chemical, textural and structural properties of the chars*. Energy, 2016. **112**: p. 133-145.
 96. Sevilla, M. and R. Mokaya, *Energy storage applications of activated carbons: supercapacitors and hydrogen storage*. Energy & Environmental Science, 2014. **7**(4): p. 1250-1280.

97. Zhang, X., et al., *Nitrogen enriched biochar modified by high temperature CO₂-ammonia treatment: Characterization and adsorption of CO₂*. Chemical Engineering Journal, 2014. **257**: p. 20–27.
98. Rajapaksha, A.U., et al., *Engineered/designer biochar for contaminant removal/immobilization from soil and water: Potential and implication of biochar modification*. Chemosphere, 2016. **148**: p. 276-291.
99. Shahkarami, S., et al., *Breakthrough CO₂ adsorption in bio-based activated carbons*. Journal of Environmental Sciences, 2015. **34**: p. 68-76.
100. Sajjadi, B., et al., *Chemical activation of biochar for energy and environmental applications: a comprehensive review*. Reviews in Chemical Engineering, 2019. **35**(7): p. 777-815.
101. El-Hendawy, A.-N.A., *An insight into the KOH activation mechanism through the production of microporous activated carbon for the removal of Pb²⁺ cations*. Applied Surface Science, 2009. **255**(6): p. 3723-3730.
102. Chen, Y., et al., *The structure evolution of biochar from biomass pyrolysis and its correlation with gas pollutant adsorption performance*. Bioresource technology, 2017. **246**: p. 101-109.
103. Chen, J.P. and S. Wu, *Acid/base-treated activated carbons: characterization of functional groups and metal adsorptive properties*. Langmuir, 2004. **20**(6): p. 2233-2242.
104. Tong, Y., B.K. Mayer, and P.J. McNamara, *Triclosan adsorption using wastewater biosolids-derived biochar*. Environmental Science: Water Research & Technology, 2016. **2**(4): p. 761-768.
105. Basta, A., et al., *2-Steps KOH activation of rice straw: an efficient method for preparing high-performance activated carbons*. Bioresource technology, 2009. **100**(17): p. 3941-3947.
106. Bhatnagar, A., et al., *An overview of the modification methods of activated carbon for its water treatment applications*. Chemical Engineering Journal, 2013. **219**: p. 499-511.
107. Igalavithana, A.D., et al., *Gasification biochar from biowaste (food waste and wood waste) for effective CO₂ adsorption*. Journal of Hazardous Materials, 2019: p. 121147.
108. Adelodun, A.A., et al., *A review on the effect of amination pretreatment for the selective separation of CO₂*. Applied energy, 2015. **158**: p. 631-642.
109. Chen, W.Y., et al., *Photochemical and acoustic interactions of biochar with CO₂ and H₂O: applications in power generation and CO₂ capture*. AIChE Journal, 2014. **60**(3): p. 1054-1065.
110. Chateaneuf, J.E., et al., *Photochemical fixation of supercritical carbon dioxide: the production of a carboxylic acid from a polyaromatic hydrocarbon*. Advances in Environmental Research, 2002. **6**(4): p. 487-493.
111. Park, S., et al., *Colloidal suspensions of highly reduced graphene oxide in a wide variety of organic solvents*. Nano letters, 2009. **9**(4): p. 1593-1597.
112. Verma, Y.L., M.P. Singh, and R.K. Singh, *Effect of ultrasonic irradiation on preparation and properties of ionogels*. Journal of Nanomaterials, 2012. **2012**.
113. Hamdaoui, O., et al., *Effects of ultrasound on adsorption-desorption of p-chlorophenol on granular activated carbon*. Ultrasonics Sonochemistry, 2003. **10**(2): p. 109-114.
114. Levêque, J.-M., et al., *Ultrasonic treatment of glassy carbon for nanoparticle preparation*. Ultrasonics Sonochemistry, 2017. **35**: p. 615-622.
115. Stankovich, S., et al., *Graphene-based composite materials*. nature, 2006. **442**(7100): p.

- 282-286.
116. Lin, Z., et al., *Simple Technique of Exfoliation and Dispersion of Multilayer Graphene from Natural Graphite by Ozone-Assisted Sonication*. *Nanomaterials*, 2017. **7**(6): p. 125.
 117. Al-Warhi, T.I., H.M. Al-Hazimi, and A. El-Faham, *Recent development in peptide coupling reagents*. *Journal of Saudi Chemical Society*, 2012. **16**(2): p. 97-116.
 118. Koenig, W. and R. Geiger, *A new method for synthesis of peptides: activation of the carboxyl group with dicyclohexylcarbodiimide using 1-hydroxybenzotriazoles as additives*. *Chemische Berichte*, 1970. **103**(3): p. 788.
 119. Montalbetti, C.A. and V. Falque, *Amide bond formation and peptide coupling*. *Tetrahedron*, 2005. **61**(46): p. 10827-10852.
 120. Zhao, Y., H. Ding, and Q. Zhong, *Preparation and characterization of aminated graphite oxide for CO₂ capture*. *Applied Surface Science*, 2012. **258**(10): p. 4301-4307.
 121. Saleh, M.A., et al., *The ultra-sonication of minerals in swine feed*. *Journal of animal science and biotechnology*, 2015. **6**(1): p. 32.
 122. Biswal, D. and R. Singh, *Characterisation of carboxymethyl cellulose and polyacrylamide graft copolymer*. *Carbohydrate polymers*, 2004. **57**(4): p. 379-387.
 123. Ferrari, A.C., *Raman spectroscopy of graphene and graphite: disorder, electron-phonon coupling, doping and nonadiabatic effects*. *Solid state communications*, 2007. **143**(1-2): p. 47-57.
 124. Perumbilavil, S., et al., *White light Z-scan measurements of ultrafast optical nonlinearity in reduced graphene oxide nanosheets in the 400–700 nm region*. *Applied Physics Letters*, 2015. **107**(5): p. 051104.
 125. Heydari-Gorji, A., Y. Belmabkhout, and A. Sayari, *Polyethylenimine-impregnated mesoporous silica: effect of amine loading and surface alkyl chains on CO₂ adsorption*. *Langmuir*, 2011. **27**(20): p. 12411-12416.
 126. Jadhav, P., et al., *Monoethanol amine modified zeolite 13X for CO₂ adsorption at different temperatures*. *Energy & Fuels*, 2007. **21**(6): p. 3555-3559.
 127. Plasynski, S.I. and Z.-Y. Chen. *Review of CO₂ capture technologies and some improvement opportunities*. in *Abstracts of Papers of The American Chemical Society*. 2000. Amer Chemical Soc 1155 16th St, Nw, Washington, DC 20036 USA.
 128. Songolzadeh, M., et al., *Carbon dioxide separation from flue gases: a technological review emphasizing reduction in greenhouse gas emissions*. *The Scientific World Journal*, 2014. **2014**.
 129. Shiue, A., et al., *Adsorption kinetics and breakthrough of carbon dioxide for the chemical modified activated carbon filter used in the building*. *Sustainability*, 2017. **9**(9): p. 1533.
 130. Xu, X., et al., *Chemical transformation of CO₂ during its capture by waste biomass derived biochars*. *Environmental Pollution*, 2016. **213**(Supplement C): p. 533-540.
 131. Ghani, W.A.W.A.K., et al., *Biochar production from waste rubber-wood-sawdust and its potential use in C sequestration: chemical and physical characterization*. *Industrial Crops and Products*, 2013. **44**: p. 18-24.
 132. Plaza, M., et al., *CO₂ capture by adsorption with nitrogen enriched carbons*. *Fuel*, 2007. **86**(14): p. 2204-2212.
 133. Sreńscek-Nazzal, J., et al., *The Increase of the Micoporosity and CO₂ Adsorption Capacity of the Commercial Activated Carbon CWZ-22 by KOH Treatment*, in *Microporous and Mesoporous Materials*, R.S. Dariani, Editor. 2016, InTech: Rijeka. p. Ch. 01.

134. Anuwattana, R., C. Patkool, and P. Chawakitchareon, *Carbon Dioxide Adsorption Using Activated Carbon via Chemical Vapor Deposition Process*. Engineering Journal, 2016. **20**(4).
135. Gargiulo, V., et al., *Assessing the potential of biochars prepared by steam-assisted slow pyrolysis for CO₂ adsorption and separation*. Energy & fuels, 2018. **32**(10): p. 10218-10227.
136. Nguyen, M.-V. and B.-K. Lee, *A novel removal of CO₂ using nitrogen doped biochar beads as a green adsorbent*. Process Safety and Environmental Protection, 2016. **104**: p. 490-498.
137. D'Alessandro, D.M., B. Smit, and J.R. Long, *Carbon dioxide capture: prospects for new materials*. Angewandte Chemie International Edition, 2010. **49**(35): p. 6058-6082.
138. Song, X., et al., *Regeneration performance and mechanism of modified walnut shell biochar catalyst for low temperature catalytic hydrolysis of organic sulfur*. Chemical Engineering Journal, 2017. **330**: p. 727-735.
139. Lashaki, M.J., et al., *Effect of adsorption and regeneration temperature on irreversible adsorption of organic vapors on beaded activated carbon*. Environmental science & technology, 2012. **46**(7): p. 4083-4090.
140. Martín, C.F., et al., *On the limits of CO₂ capture capacity of carbons*. Separation and Purification Technology, 2010. **74**(2): p. 225-229.
141. Calvo-Muñoz, E.M., et al., *Biomass waste carbon materials as adsorbents for CO₂ capture under post-combustion conditions*. Frontiers in Materials, 2016. **3**: p. 23.
142. Diaf, A., J.L. Garcia, and E.J. Beckman, *Thermally reversible polymeric sorbents for acid gases: CO₂, SO₂, and NO_x*. Journal of applied polymer science, 1994. **53**(7): p. 857-875.
143. Rezaei, F., et al., *SO_x/NO_x removal from flue gas streams by solid adsorbents: a review of current challenges and future directions*. Energy & fuels, 2015. **29**(9): p. 5467-5486.
144. Dong, Y., et al., *Polyamine-functionalized carbon quantum dots for chemical sensing*. Carbon, 2012. **50**(8): p. 2810-2815.
145. Slowing, I.I., et al., *Mesoporous silica nanoparticles for drug delivery and biosensing applications*. Advanced Functional Materials, 2007. **17**(8): p. 1225-1236.
146. Chatterjee, R., et al., *Ultrasound cavitation intensified amine functionalization: A feasible strategy for enhancing CO₂ capture capacity of biochar*. Fuel, 2018. **225**: p. 287-298.
147. Samanta, A., et al., *Post-combustion CO₂ capture using solid sorbents: a review*. Industrial & Engineering Chemistry Research, 2011. **51**(4): p. 1438-1463.
148. Dillon, D., et al. *Oxy-combustion processes for CO₂ capture from advanced supercritical PF and NGCC power plant*. in *7 th International Conference on Greenhouse Gas Technologies, Vancouver, Canada*. 2004.
149. Raganati, F., P. Ammendola, and R. Chirone, *On improving the CO₂ recovery efficiency of a conventional TSA process in a sound assisted fluidized bed by separating heating and purging*. Separation and Purification Technology, 2016. **167**: p. 24-31.
150. Riboldi, L. and O. Bolland, *Evaluating Pressure Swing Adsorption as a CO₂ separation technique in coal-fired power plants*. International Journal of Greenhouse Gas Control, 2015. **39**: p. 1-16.
151. Plaza, M.G., et al., *Post-combustion CO₂ capture with a commercial activated carbon: comparison of different regeneration strategies*. Chemical Engineering Journal, 2010. **163**(1-2): p. 41-47.

152. Li, G., et al., *Capture of CO₂ from high humidity flue gas by vacuum swing adsorption with zeolite 13X*. Adsorption, 2008. **14**(2-3): p. 415-422.
153. Mason, J.A., et al., *Evaluating metal–organic frameworks for post-combustion carbon dioxide capture via temperature swing adsorption*. Energy & Environmental Science, 2011. **4**(8): p. 3030-3040.
154. Laheäär, A., et al., *Ammonia treatment of activated carbon powders for supercapacitor electrode application*. Journal of The Electrochemical Society, 2014. **161**(4): p. A568-A575.
155. Przepiórski, J., M. Skrodzewicz, and A. Morawski, *High temperature ammonia treatment of activated carbon for enhancement of CO₂ adsorption*. Applied Surface Science, 2004. **225**(1-4): p. 235-242.
156. Shafeeyan, M.S., et al., *Modification of activated carbon using nitration followed by reduction for carbon dioxide capture*. Bulletin of the Korean Chemical Society, 2015. **36**(2): p. 533-538.
157. Lalhruaitluanga, H., et al., *Lead (II) adsorption from aqueous solutions by raw and activated charcoals of Melocanna baccifera Roxburgh (bamboo)—a comparative study*. Journal of Hazardous Materials, 2010. **175**(1-3): p. 311-318.
158. Regmi, P., et al., *Removal of copper and cadmium from aqueous solution using switchgrass biochar produced via hydrothermal carbonization process*. Journal of environmental management, 2012. **109**: p. 61-69.
159. Wu, T.Y., et al., *Advances in ultrasound technology for environmental remediation*. 2012: Springer Science & Business Media.
160. Zhu, D., et al., *Selection of blended solvents for CO₂ absorption from coal-fired flue gas. Part 1: Monoethanolamine (MEA)-based solvents*. Energy & Fuels, 2011. **26**(1): p. 147-153.
161. Navarro, N.M., et al., *Effect of ultrasonic frequency on the mechanism of formic acid sonolysis*. The Journal of Physical Chemistry B, 2011. **115**(9): p. 2024-2029.
162. Ganz, S. and E. Gutierrez, *Cavitation: Causes, Effects, Mitigation and Application*. 2012, Rensselaer Polytechnic Institute: Hartford, CT, USA.
163. Qin, J., T.-Y. Wang, and J.K. Willmann, *Sonoporation: applications for cancer therapy, in Therapeutic Ultrasound*. 2016, Springer. p. 263-291.
164. Verma, Y.L., M.P. Singh, and R.K. Singh, *Effect of ultrasonic irradiation on preparation and properties of ionogels*. Journal of Nanomaterials, 2012. **2012**: p. 6.
165. Zhao, L., et al., *Heterogeneity of biochar properties as a function of feedstock sources and production temperatures*. Journal of hazardous materials, 2013. **256**: p. 1-9.
166. Mukherjee, A. and R. Lal, *Biochar impacts on soil physical properties and greenhouse gas emissions*. Agronomy, 2013. **3**(2): p. 313-339.
167. Stankovich, S., et al., *Graphene-based composite materials*. nature, 2006. **442**(7100): p. 282.
168. Ohs, B., M. Krödel, and M. Wessling, *Adsorption of carbon dioxide on solid amine-functionalized sorbents: A dual kinetic model*. Separation and Purification Technology, 2018. **204**: p. 13-20.
169. Juan, Y. and Q. Ke-Qiang, *Preparation of activated carbon by chemical activation under vacuum*. Environmental science & technology, 2009. **43**(9): p. 3385-3390.
170. Zhou, Y., et al., *Sorption of heavy metals on chitosan-modified biochars and its biological effects*. Chemical Engineering Journal, 2013. **231**: p. 512-518.

171. Mahvi, A., *Application of ultrasonic technology for water and wastewater treatment*. Iranian Journal of Public Health, 2009. **38**(2): p. 1-17.
172. Garrido, J., et al., *Use of nitrogen vs. carbon dioxide in the characterization of activated carbons*. Langmuir, 1987. **3**(1): p. 76-81.
173. Thommes, M., et al., *Physisorption of gases, with special reference to the evaluation of surface area and pore size distribution (IUPAC Technical Report)*. Pure and Applied Chemistry, 2015. **87**(9-10): p. 1051-1069.
174. Dabrowski, A., *Adsorption from theory to practice* Advances in Colloid and Interface Science, 2001. **93**: p. 135-224.
175. Houshmand, A., W.M.A. Wan Daud, and M.S. Shafeeyan, *Exploring Potential Methods for Anchoring Amine Groups on the Surface of Activated Carbon for CO₂ Adsorption*. Separation Science and Technology, 2011. **46**(7): p. 1098-1112.
176. Huang, Z.-H., et al., *Relation between the charge efficiency of activated carbon fiber and its desalination performance*. Langmuir, 2012. **28**(11): p. 5079-5084.
177. Teng, Y., et al., *Promoting Effect of Inorganic Alkali on Carbon Dioxide Adsorption in Amine-Modified MCM-41*. Energies, 2016. **9**(9): p. 667.
178. Yue, M.B., et al., *Efficient CO₂ capturer derived from as synthesized MCM 41 modified with amine*. Chemistry—A European Journal, 2008. **14**(11): p. 3442-3451.
179. Alvis, R.S., N.A. Hatcher, and R.H. Weiland, *CO₂ removal from syngas using piperazine-activated MDEA and potassium dimethyl glycinate*. Nitrogen+ Syngas, 2012: p. 20-23.
180. Shah, Y.T., A. Pandit, and V. Moholkar, *Cavitation reaction engineering*. 2012: Springer Science & Business Media.
181. Sun, K., et al., *Characterization of potassium hydroxide (KOH) modified hydrochars from different feedstocks for enhanced removal of heavy metals from water*. Environmental Science and Pollution Research, 2015. **22**(21): p. 16640-16651.
182. Ferrari, A.C., *Raman spectroscopy of graphene and graphite: disorder, electron–phonon coupling, doping and nonadiabatic effects*. Solid state communications, 2007. **143**(1): p. 47-57.
183. McDonald-Wharry, J., et al. *Studying carbonisation with raman spectroscopy in New Zealand 2013 Biochar Workshop—The Final Answer?* 2013.
184. Theodore, M., et al., *Influence of functionalization on properties of MWCNT–epoxy nanocomposites*. Materials Science and Engineering: A, 2011. **528**(3): p. 1192-1200.
185. Qi, G., et al., *High efficiency nanocomposite sorbents for CO₂ capture based on amine-functionalized mesoporous capsules*. Energy & Environmental Science, 2011. **4**(2): p. 444-452.
186. Dao, D.S., H. Yamada, and K. Yogo, *Large-pore mesostructured silica impregnated with blended amines for CO₂ capture*. Industrial & Engineering Chemistry Research, 2013. **52**(38): p. 13810-13817.
187. Lu, X.-H., et al., *Solid base catalyzed highly efficient N-alkylation of amines with alcohols in a solvent-free system*. Catalysis Communications, 2014. **55**: p. 78-82.
188. Yang, H., et al., *Carbon-catalysed reductive hydrogen atom transfer reactions*. Nature communications, 2015. **6**: p. 6478.
189. Yue, M.B., et al., *CO₂ capture by as-prepared SBA-15 with an occluded organic template*. Advanced Functional Materials, 2006. **16**(13): p. 1717-1722.
190. Yue, M.B., et al., *Efficient CO₂ capturer derived from as-synthesized MCM-41 modified*

- with amine*. Chemistry—A European Journal, 2008. **14**(11): p. 3442-3451.
191. Gebald, C., et al., *Amine-Based Nanofibrillated Cellulose As Adsorbent for CO₂ Capture from Air*. Environmental Science & Technology, 2011. **45**(20): p. 9101-9108.
 192. Madzaki, H. and W.A.W.A. KarimGhani, *Carbon dioxide adsorption on sawdust biochar*. Procedia engineering, 2016. **148**: p. 718-725.
 193. Kongnoo, A., et al., *Diethanolamine impregnated palm shell activated carbon for CO₂ adsorption at elevated temperatures*. Journal of Environmental Chemical Engineering, 2016. **4**(1): p. 73-81.
 194. Yan, X., et al., *Amine-Modified SBA-15: Effect of Pore Structure on the Performance for CO₂ Capture*. Industrial & Engineering Chemistry Research, 2011. **50**(6): p. 3220-3226.
 195. Zelenak, V., et al., *Amine-modified SBA-12 mesoporous silica for carbon dioxide capture: Effect of amine basicity on sorption properties*. Microporous and Mesoporous Materials, 2008. **116**(1): p. 358-364.
 196. Xiong, Z., et al., *Influence of NH₃/CO₂ modification on the characteristic of biochar and the CO₂ capture*. BioEnergy Research, 2013. **6**(4): p. 1147-1153.
 197. Bamdad, H., K. Hawboldt, and S. MacQuarrie, *Nitrogen Functionalized Biochar as a Renewable Adsorbent for Efficient CO₂ Removal*. Energy & Fuels, 2018. **32**(11): p. 11742-11748.
 198. Wang, Q., et al., *CO₂ capture by solid adsorbents and their applications: current status and new trends*. Energy & Environmental Science, 2011. **4**(1): p. 42-55.
 199. Versteeg, G. and W.P.M. van Swaaij, *On the kinetics between CO₂ and alkanolamines both in aqueous and non-aqueous solutions—I. Primary and secondary amines*. Chemical engineering science, 1988. **43**(3): p. 573-585.
 200. Stiasny, M.H., et al., *Ocean acidification effects on Atlantic cod larval survival and recruitment to the fished population*. PLoS One, 2016. **11**(8): p. e0155448.
 201. Hu, S., et al., *Effect of CO₂-induced seawater acidification on growth, photosynthesis and inorganic carbon acquisition of the harmful bloom-forming marine microalga, Karenia mikimotoi*. PloS one, 2017. **12**(8): p. e0183289.
 202. Koytsoumpa, E.I., C. Bergins, and E. Kakaras, *The CO₂ economy: Review of CO₂ capture and reuse technologies*. The Journal of Supercritical Fluids, 2018. **132**: p. 3-16.
 203. Cai, J., et al., *Review of physicochemical properties and analytical characterization of lignocellulosic biomass*. Renewable and Sustainable Energy Reviews, 2017. **76**: p. 309-322.
 204. Brosse, N., et al., *Miscanthus: a fast-growing crop for biofuels and chemicals production*. Biofuels, Bioproducts and Biorefining, 2012. **6**(5): p. 580-598.
 205. Bajpai, P., *Structure of Lignocellulosic Biomass*. SpringerBriefs in Molecular Science. 2016, Singapore: Springer.
 206. Saeed, H.A., et al., *Evaluation of Sudanese Sorghum and Bagasse as a Pulp and Paper Feedstock*. BioResources, 2017. **12**(3): p. 5212-5222.
 207. Anwar, Z., M. Gulfranz, and M. Irshad, *Agro-industrial lignocellulosic biomass a key to unlock the future bio-energy: a brief review*. Journal of radiation research and applied sciences, 2014. **7**(2): p. 163-173.
 208. Burhenne, L., et al., *The effect of the biomass components lignin, cellulose and hemicellulose on TGA and fixed bed pyrolysis*. Journal of Analytical and Applied Pyrolysis, 2013. **101**: p. 177-184.
 209. Johar, N., I. Ahmad, and A. Dufresne, *Extraction, preparation and characterization of*

- cellulose fibres and nanocrystals from rice husk*. Industrial Crops and Products, 2012. **37**(1): p. 93-99.
210. Nasri-Nasrabadi, B., T. Behzad, and R. Bagheri, *Extraction and characterization of rice straw cellulose nanofibers by an optimized chemomechanical method*. Journal of Applied Polymer Science, 2014. **131**(7).
 211. Mimmo, T., et al., *Effect of pyrolysis temperature on miscanthus (Miscanthus × giganteus) biochar physical, chemical and functional properties*. Biomass and Bioenergy, 2014. **62**: p. 149-157.
 212. Oliveira, J.A., et al., *Comparison of Miscanthus and Switchgrass Cultivars for Biomass Yield, Soil Nutrients, and Nutrient Removal in Northwest Spain*. Agronomy Journal, 2017. **109**: p. 122-130.
 213. Sadaka, S., et al., *Characterization of biochar from switchgrass carbonization*. Energies, 2014. **7**(2): p. 548-567.
 214. Janus, A., et al., *Elaboration, characteristics and advantages of biochars for the management of contaminated soils with a specific overview on Miscanthus biochars*. Journal of environmental management, 2015. **162**: p. 275-289.
 215. Shen, Y., et al., *Producing pipeline-quality biomethane via anaerobic digestion of sludge amended with corn stover biochar with in-situ CO₂ removal*. Applied energy, 2015. **158**: p. 300-309.
 216. Wang, Y., et al., *Porous carbonaceous materials from hydrothermal carbonization and KOH activation of corn stover for highly efficient CO₂ capture* AU - Shen, Feng. Chemical Engineering Communications, 2018. **205**(4): p. 423-431.
 217. Luo, S., et al., *Preparation and characterization of amine-functionalized sugarcane bagasse for CO₂ capture*. Vol. 168. 2015. 142-148.
 218. Sriprasod, R., N. Patikarnmonthon, and K. Kamwilaisak, *Comparison study of sugarcane leaves and corn stover as a potential energy source in pyrolysis process*. Energy procedia, 2016. **100**: p. 26-29.
 219. Janke, L., et al., *Biogas production from sugarcane waste: assessment on kinetic challenges for process designing*. International journal of molecular sciences, 2015. **16**(9): p. 20685-20703.
 220. Mourtzinis, S., et al., *Carbohydrate and nutrient composition of corn stover from three southeastern USA locations*. Biomass and Bioenergy, 2016. **85**: p. 153-158.
 221. Zhang, X., et al., *Effects of hydrofluoric acid pre-deashing of rice husk on physicochemical properties and CO₂ adsorption performance of nitrogen-enriched biochar*. Energy, 2015. **91**: p. 903-910.
 222. Chuah, T.G., et al., *Rice husk as a potentially low-cost biosorbent for heavy metal and dye removal: an overview*. Desalination, 2005. **175**(3): p. 305-316.
 223. Uzunova, S., et al., *Preparation of low-ash-content porous carbonaceous material from rice husks*. Bulg. Chem. Commun, 2010. **42**(2): p. 130-137.
 224. Manna, S. and N. Singh, *Effect of wheat and rice straw biochars on pyrazosulfuron-ethyl sorption and persistence in a sandy loam soil*. Journal of Environmental Science and Health, Part B, 2015. **50**(7): p. 463-472.
 225. Kim, W.-K., et al., *Characterization of cadmium removal from aqueous solution by biochar produced from a giant Miscanthus at different pyrolytic temperatures*. Bioresource technology, 2013. **138**: p. 266-270.
 226. Wilk, M. and A. Magdziarz, *Hydrothermal carbonization, torrefaction and slow*

- pyrolysis of Miscanthus giganteus*. Energy, 2017. **140**: p. 1292-1304.
227. Peterson, S.C., et al., *Comparing corn stover and switchgrass biochar: characterization and sorption properties*. Journal of agricultural science, 2012. **5**(1): p. 1.
 228. Imam, T. and S. Capareda, *Characterization of bio-oil, syn-gas and bio-char from switchgrass pyrolysis at various temperatures*. Journal of Analytical and Applied Pyrolysis, 2012. **93**: p. 170-177.
 229. Sadaka, S., et al., *Characterization of biochar from switchgrass carbonization*. Energies, 2014. **7**(2): p. 548-567.
 230. Hu, Z., et al., *Chemical profiles of switchgrass*. Bioresource technology, 2010. **101**(9): p. 3253-3257.
 231. Clay, S.A., et al., *Maize, switchgrass, and ponderosa pine biochar added to soil increased herbicide sorption and decreased herbicide efficacy*. Journal of Environmental Science and Health, Part B, 2016. **51**(8): p. 497-507.
 232. Mullen, C.A., et al., *Bio-oil and bio-char production from corn cobs and stover by fast pyrolysis*. Biomass and bioenergy, 2010. **34**(1): p. 67-74.
 233. Carpenter, D.L., et al., *Pilot-scale gasification of corn stover, switchgrass, wheat straw, and wood: 1. Parametric study and comparison with literature*. Industrial & Engineering Chemistry Research, 2010. **49**(4): p. 1859-1871.
 234. Rafiq, M.K., et al., *Influence of pyrolysis temperature on physico-chemical properties of corn stover (Zea mays L.) biochar and feasibility for carbon capture and energy balance*. PloS one, 2016. **11**(6): p. e0156894.
 235. Lizotte, P.-L., P. Savoie, and A. De Champlain, *Ash content and calorific energy of corn stover components in Eastern Canada*. Energies, 2015. **8**(6): p. 4827-4838.
 236. jutakridsada, P., et al., *Comparison Study of Sugarcane Leaves and Corn Stover as a Potential Energy Source in Pyrolysis Process*. Energy Procedia, 2016. **100**: p. 26-29.
 237. Guimarães, J., et al., *Characterization of banana, sugarcane bagasse and sponge gourd fibers of Brazil*. Industrial Crops and Products, 2009. **30**(3): p. 407-415.
 238. Inyang, M., et al., *Biochar from anaerobically digested sugarcane bagasse*. Bioresource Technology, 2010. **101**(22): p. 8868-8872.
 239. Peng, Y. and S. Wu, *Fast pyrolysis characteristics of sugarcane bagasse hemicellulose*. Cellulose chemistry and technology, 2011. **45**(9): p. 605.
 240. Naik, D.K., et al., *Pyrolysis of sorghum bagasse biomass into bio-char and bio-oil products*. Journal of Thermal Analysis and Calorimetry, 2017. **127**(2): p. 1277-1289.
 241. Yin, R., et al., *Characterization of bio-oil and bio-char obtained from sweet sorghum bagasse fast pyrolysis with fractional condensers*. Fuel, 2013. **112**: p. 96-104.
 242. Santos, B.S. and S.C. Capareda, *Energy sorghum pyrolysis using a pressurized batch reactor*. Biomass Conversion and Biorefinery, 2016. **6**(3): p. 325-334.
 243. Liu, Z., et al., *Effect of the Carbonization Temperature on the Properties of Biochar Produced from the Pyrolysis of Crop Residues*. BioResources, 2018. **13**(2): p. 3429-3446.
 244. Ibrahim, N., et al., *Influence of reaction temperature and water content on wheat straw pyrolysis*. World Academy of Science, Engineering and Technology, International Journal of Chemical, Molecular, Nuclear, Materials and Metallurgical Engineering, 2012. **6**(10): p. 919-925.
 245. Bruun, E.W., et al., *Effects of slow and fast pyrolysis biochar on soil C and N turnover dynamics*. Soil Biology and Biochemistry, 2012. **46**: p. 73-79.
 246. Leng, L., et al., *Surface characterization of rice husk bio-char produced by liquefaction*

- and application for cationic dye (Malachite green) adsorption.* Fuel, 2015. **155**: p. 77-85.
247. Ahiduzzaman, M. and A.K.M. Sadrul Islam, *Preparation of porous bio-char and activated carbon from rice husk by leaching ash and chemical activation.* SpringerPlus, 2016. **5**(1): p. 1248-1248.
 248. Sajjadi, B., W.-Y. Chen, and N.O. Egiebor, *A comprehensive review on physical activation of biochar for energy and environmental applications.* Reviews in Chemical Engineering, 2019. **35**(6): p. 735-776.
 249. Hagemann, N., et al., *Activated carbon, biochar and charcoal: linkages and synergies across pyrogenic carbon's ABCs.* Water, 2018. **10**(2): p. 182.
 250. Sajjadi, B., W.-Y. Chen, and O. Egiebor Nosa, *A comprehensive review on physical activation of biochar for energy and environmental applications,* in *Reviews in Chemical Engineering.* 2018.
 251. Guittonneau, F., et al., *The effect of high power ultrasound on an aqueous suspension of graphite.* Ultrasonics Sonochemistry, 2010. **17**(2): p. 391-398.
 252. Stankovich, S., et al., *Graphene-based composite materials.* Nature, 2006. **442**: p. 282.
 253. Sajjadi, B., et al., *Variables governing the initial stages of the synergisms of ultrasonic treatment of biochar in water with dissolved CO₂.* Fuel, 2019. **235**: p. 1131-1145.
 254. Munoz, D.M., et al., *New liquid absorbents for the removal of CO₂ from gas mixtures.* Energy & Environmental Science, 2009. **2**(8): p. 883-891.
 255. Dondini, M., et al., *The potential of Miscanthus to sequester carbon in soils: comparing field measurements in Carlow, Ireland to model predictions.* Gcb Bioenergy, 2009. **1**(6): p. 413-425.
 256. Oliveira, J.A., et al., *Comparison of miscanthus and switchgrass cultivars for biomass yield, soil nutrients, and nutrient removal in northwest spain.* Agronomy Journal, 2017. **109**(1): p. 122-130.
 257. Xiaofeng, B., et al., *Properties and applications of biochars derived from different biomass feedstock sources.* International Journal of Agricultural and Biological Engineering, 2017. **10**(2): p. 242-250.
 258. Chatterjee, R., et al., *Low Frequency Ultrasound Enhanced Dual Amination of Biochar: A Nitrogen-Enriched Sorbent for CO₂ Capture.* Energy & fuels, 2019. **33**(3): p. 2366-2380.
 259. Sellaperumal, P., *Evaluation of thermochemical decomposition of various lignocellulosic biomasses for biochar production.* 2012: McGill University (Canada).
 260. Chemerys, V. and E. Baltrėnaitė, *A review of lignocellulosic biochar modification towards enhanced biochar selectivity and adsorption capacity of potentially toxic elements.* Ukrainian Journal of Ecology, 2018. **8**(1): p. 21-32.
 261. Li, J., et al., *A comparison of biochars from lignin, cellulose and wood as the sorbent to an aromatic pollutant.* Journal of hazardous materials, 2014. **280**: p. 450-457.
 262. Chatterjee, R., et al., *Ultrasound cavitation intensified amine functionalization: A feasible strategy for enhancing CO₂ capture capacity of biochar.* Fuel, 2018. **225**: p. 287-298.
 263. Chatterjee, R., et al., *Low Frequency Ultrasound Enhanced Dual Amination of Biochar: A Nitrogen-Enriched Sorbent for CO₂ Capture.* Energy & Fuels, 2019.
 264. Zhou, M., J. Yu, and B. Cheng, *Effects of Fe-doping on the photocatalytic activity of mesoporous TiO₂ powders prepared by an ultrasonic method.* Journal of Hazardous Materials, 2006. **137**(3): p. 1838-1847.
 265. PatriciaOrdonez, S., C.H. Garcıa, and J. Larrahondo, *Fruit Waste and Sugarcane Bagasse*

- as Potential Natural Resources of Mineral and Lipophilic Substances.*
266. Xu, G., et al., *What is more important for enhancing nutrient bioavailability with biochar application into a sandy soil: Direct or indirect mechanism?* Ecological engineering, 2013. **52**: p. 119-124.
 267. Brewer, C.E., et al., *Characterization of biochar from fast pyrolysis and gasification systems.* Environmental Progress & Sustainable Energy: An Official Publication of the American Institute of Chemical Engineers, 2009. **28**(3): p. 386-396.
 268. Wu, W., et al., *Chemical characterization of rice straw-derived biochar for soil amendment.* Biomass and bioenergy, 2012. **47**: p. 268-276.
 269. Singh, B., B.P. Singh, and A.L. Cowie, *Characterisation and evaluation of biochars for their application as a soil amendment.* Soil Research, 2010. **48**(7): p. 516-525.
 270. Paiva, C.L., et al., *Mineral content of sorghum genotypes and the influence of water stress.* Food Chemistry, 2017. **214**: p. 400-405.
 271. Sajjadi, B., W.-Y. Chen, and N.O. Egiebor, *A comprehensive review on physical activation of biochar for energy and environmental applications.* Reviews in Chemical Engineering, 2018.
 272. Chen, B., D. Zhou, and L. Zhu, *Transitional adsorption and partition of nonpolar and polar aromatic contaminants by biochars of pine needles with different pyrolytic temperatures.* Environmental science & technology, 2008. **42**(14): p. 5137-5143.
 273. Krukowski, E.G., et al., *FT-IR study of CO₂ interaction with Na⁺ exchanged montmorillonite.* Applied Clay Science, 2015. **114**: p. 61-68.
 274. Xu, S., et al., *Alkali-assisted hydrothermal route to control submicron-sized nanoporous carbon spheres with uniform distribution.* Colloids and Surfaces A: Physicochemical and Engineering Aspects, 2017. **515**: p. 1-11.
 275. Das, O., A.K. Sarmah, and D. Bhattacharyya, *A novel approach in organic waste utilization through biochar addition in wood/polypropylene composites.* Waste Management, 2015. **38**: p. 132-140.
 276. Peterson, S.C., et al., *Comparing corn stover and switchgrass biochar: characterization and sorption properties.* Journal of agricultural science, 2013. **5**(1): p. 1.
 277. Liu, Y., Z. He, and M. Uchimiya, *Comparison of biochar formation from various agricultural by-products using FTIR spectroscopy.* Modern Applied Science, 2015. **9**(4): p. 246.
 278. Coates, J., *Interpretation of infrared spectra, a practical approach.* Encyclopedia of analytical chemistry: applications, theory and instrumentation, 2006.
 279. Vaughn, S.F., et al., *Comparison of biochars derived from wood pellets and pelletized wheat straw as replacements for peat in potting substrates.* Industrial crops and products, 2013. **51**: p. 437-443.
 280. Fuertes, A., et al., *Chemical and structural properties of carbonaceous products obtained by pyrolysis and hydrothermal carbonisation of corn stover.* Soil Research, 2010. **48**(7): p. 618-626.
 281. Lee, T., R. Othman, and F.-Y. Yeoh, *Development of photoluminescent glass derived from rice husk.* 2013.
 282. Udvardi, B., et al., *Effects of particle size on the attenuated total reflection spectrum of minerals.* Applied spectroscopy, 2017. **71**(6): p. 1157-1168.
 283. Paris, O., C. Zollfrank, and G.A. Zickler, *Decomposition and carbonisation of wood biopolymers—a microstructural study of softwood pyrolysis.* Carbon, 2005. **43**(1): p. 53-

- 66.
284. Lespade, P., R. Al-Jishi, and M. Dresselhaus, *Model for Raman scattering from incompletely graphitized carbons*. Carbon, 1982. **20**(5): p. 427-431.
285. Sajjadi, B., et al., *Urea functionalization of ultrasound-treated biochar: A feasible strategy for enhancing heavy metal adsorption capacity*. Ultrasonics Sonochemistry, 2019. **51**: p. 20-30.
286. Yang, H., et al., *Biomass-based pyrolytic polygeneration system for bamboo industry waste: evolution of the char structure and the pyrolysis mechanism*. Energy & Fuels, 2016. **30**(8): p. 6430-6439.
287. Tsaneva, V., et al., *Assessment of the structural evolution of carbons from microwave plasma natural gas reforming and biomass pyrolysis using Raman spectroscopy*. Carbon, 2014. **80**: p. 617-628.
288. Mohanty, P., et al., *Evaluation of the physiochemical development of biochars obtained from pyrolysis of wheat straw, timothy grass and pinewood: effects of heating rate*. Journal of analytical and applied pyrolysis, 2013. **104**: p. 485-493.
289. Drage, T.C., et al., *Preparation of carbon dioxide adsorbents from the chemical activation of urea-formaldehyde and melamine-formaldehyde resins*. Fuel, 2007. **86**(1-2): p. 22-31.
290. Shafeeyan, M.S., et al., *Ammonia modification of activated carbon to enhance carbon dioxide adsorption: effect of pre-oxidation*. Applied Surface Science, 2011. **257**(9): p. 3936-3942.
291. Zhang, C., et al., *CO₂ capture with activated carbon grafted by nitrogenous functional groups*. Energy & fuels, 2013. **27**(8): p. 4818-4823.
292. Valeur, E. and M. Bradley, *Amide bond formation: beyond the myth of coupling reagents*. Chemical Society Reviews, 2009. **38**(2): p. 606-631.
293. Da Silva, E.F. and H.F. Svendsen, *Ab initio study of the reaction of carbamate formation from CO₂ and alkanolamines*. Industrial & engineering chemistry research, 2004. **43**(13): p. 3413-3418.
294. Da Silva, E.F. and H.F. Svendsen, *Computational chemistry study of reactions, equilibrium and kinetics of chemical CO₂ absorption*. International Journal of Greenhouse Gas Control, 2007. **1**(2): p. 151-157.
295. Stowe, H.M. and G.S. Hwang, *Fundamental Understanding of CO₂ Capture and Regeneration in Aqueous Amines from First-Principles Studies: Recent Progress and Remaining Challenges*. Industrial & Engineering Chemistry Research, 2017. **56**(24): p. 6887-6899.
296. Wilfong, W.C., C.S. Srikanth, and S.S. Chuang, *In situ ATR and DRIFTS studies of the nature of adsorbed CO₂ on tetraethylenepentamine films*. ACS applied materials & interfaces, 2014. **6**(16): p. 13617-13626.
297. Drage, T.C., et al., *Thermal stability of polyethylenimine based carbon dioxide adsorbents and its influence on selection of regeneration strategies*. Microporous and Mesoporous Materials, 2008. **116**(1): p. 504-512.
298. Ezeh, C.I., et al., *Sonochemical surface functionalization of exfoliated LDH: Effect on textural properties, CO₂ adsorption, cyclic regeneration capacities and subsequent gas uptake for simultaneous methanol synthesis*. Ultrasonics Sonochemistry, 2017. **39**: p. 330-343.
299. Antonakou, E., et al., *Evaluation of various types of Al-MCM-41 materials as catalysts in*

- biomass pyrolysis for the production of bio-fuels and chemicals*. Fuel, 2006. **85**(14-15): p. 2202-2212.
300. Dhyani, V. and T. Bhaskar, *A comprehensive review on the pyrolysis of lignocellulosic biomass*. Renewable Energy, 2018. **129**: p. 695-716.
 301. Amini, E., et al., *Characterization of pyrolysis products from slow pyrolysis of live and dead vegetation native to the southern United States*. Fuel, 2019. **235**: p. 1475-1491.
 302. Lewis, A.D. and T.H. Fletcher, *Prediction of sawdust pyrolysis yields from a flat-flame burner using the CPD model*. Energy & Fuels, 2013. **27**(2): p. 942-953.
 303. Vizzini, G., et al., *Prediction of rapid biomass devolatilization yields with an upgraded version of the Bio-CPD model*. Combustion Institute Italian section, 2008.
 304. Patwardhan, P.R., et al., *Distinguishing primary and secondary reactions of cellulose pyrolysis*. Bioresource technology, 2011. **102**(8): p. 5265-5269.
 305. Zhao, S.-X., N. Ta, and X.-D. Wang, *Effect of temperature on the structural and physicochemical properties of biochar with apple tree branches as feedstock material*. Energies, 2017. **10**(9): p. 1293.
 306. Liang, C., et al., *Biochar from pruning residues as a soil amendment: effects of pyrolysis temperature and particle size*. Soil and Tillage Research, 2016. **164**: p. 3-10.
 307. Tag, A.T., et al., *Effects of feedstock type and pyrolysis temperature on potential applications of biochar*. Journal of analytical and applied pyrolysis, 2016. **120**: p. 200-206.
 308. Brassard, P., et al., *The production of engineered biochars in a vertical auger pyrolysis reactor for carbon sequestration*. Energies, 2017. **10**(3): p. 288.
 309. Li, H., et al., *Mechanisms of metal sorption by biochars: biochar characteristics and modifications*. Chemosphere, 2017. **178**: p. 466-478.
 310. Zambon, I., et al., *An innovative agro-forestry supply chain for residual biomass: Physicochemical characterisation of biochar from olive and hazelnut pellets*. Energies, 2016. **9**(7): p. 526.
 311. Budai, A., et al., *Surface Properties and Chemical Composition of Corn cob and Miscanthus Biochars: Effects of Production Temperature and Method*. Journal of Agricultural and Food Chemistry, 2014. **62**(17): p. 3791-3799.
 312. Ashworth, A.J., et al., *Influence of pyrolysis temperature and production conditions on switchgrass biochar for use as a soil amendment*. BioResources, 2014. **9**(4): p. 7622-7635.
 313. Pilon, G. and J.-M. Lavoie, *Pyrolysis of Switchgrass (*Panicum virgatum* L.) at Low Temperatures within N₂ and CO₂ Environments: Product Yield Study*. ACS Sustainable Chemistry & Engineering, 2013. **1**(1): p. 198-204.
 314. Wang, S., et al., *Physicochemical and sorptive properties of biochars derived from woody and herbaceous biomass*. Chemosphere, 2015. **134**: p. 257-262.
 315. Kim, P., et al., *Effect of pH on surface characteristics of switchgrass-derived biochars produced by fast pyrolysis*. Chemosphere, 2013. **90**(10): p. 2623-2630.
 316. Brewer, C. and R. Brown, *E.(2012) Biochar characterization and engineering*. Graduate Teses and Dissertations. **12284**.
 317. Vyas, A., T. Chellappa, and J.L. Goldfarb, *Porosity development and reactivity changes of coal–biomass blends during co-pyrolysis at various temperatures*. Journal of analytical and applied pyrolysis, 2017. **124**: p. 79-88.
 318. Gai, X., et al., *Effects of feedstock and pyrolysis temperature on biochar adsorption of*

- ammonium and nitrate*. PloS one, 2014. **9**(12): p. e113888.
319. Nwajiaku, I.M., et al., *Change in nutrient composition of biochar from rice husk and sugarcane bagasse at varying pyrolytic temperatures*. International Journal of Recycling of Organic Waste in Agriculture, 2018. **7**(4): p. 269-276.
 320. Domingues, R.R., et al., *Properties of biochar derived from wood and high-nutrient biomasses with the aim of agronomic and environmental benefits*. PloS one, 2017. **12**(5): p. e0176884.
 321. Wang, X., et al., *Characteristics of maize biochar with different pyrolysis temperatures and its effects on organic carbon, nitrogen and enzymatic activities after addition to fluvo-aquic soil*. Science of the Total Environment, 2015. **538**: p. 137-144.
 322. Zhang, J., et al., *Humification characterization of biochar and its potential as a composting amendment*. Journal of Environmental Sciences, 2014. **26**(2): p. 390-397.
 323. Suliman, W., et al., *Influence of feedstock source and pyrolysis temperature on biochar bulk and surface properties*. Biomass and Bioenergy, 2016. **84**: p. 37-48.
 324. Zanzi, R., K. Sjöström, and E. Björnbom, *Rapid pyrolysis of agricultural residues at high temperature*. Biomass and Bioenergy, 2002. **23**(5): p. 357-366.
 325. Guerrero, M., et al., *Pyrolysis of eucalyptus at different heating rates: studies of char characterization and oxidative reactivity*. Journal of Analytical and Applied Pyrolysis, 2005. **74**(1-2): p. 307-314.
 326. Cetin, E., R. Gupta, and B. Moghtaderi, *Effect of pyrolysis pressure and heating rate on radiata pine char structure and apparent gasification reactivity*. Fuel, 2005. **84**(10): p. 1328-1334.
 327. Li, M., et al., *Cu (II) removal from aqueous solution by *Spartina alterniflora* derived biochar*. Bioresource technology, 2013. **141**: p. 83-88.
 328. Lee, Y., et al., *Comparison of biochar properties from biomass residues produced by slow pyrolysis at 500°C*. Bioresource Technology, 2013. **148**: p. 196-201.
 329. Jeong, C.Y., S.K. Dodla, and J.J. Wang, *Fundamental and molecular composition characteristics of biochars produced from sugarcane and rice crop residues and by-products*. Chemosphere, 2016. **142**: p. 4-13.
 330. Chen, Y., et al., *Biomass-based pyrolytic polygeneration system on cotton stalk pyrolysis: influence of temperature*. Bioresource technology, 2012. **107**: p. 411-418.
 331. Kumar, U., et al., *Cleaner production of iron by using waste macadamia biomass as a carbon resource*. Journal of cleaner production, 2017. **158**: p. 218-224.
 332. Onay, O., *Influence of pyrolysis temperature and heating rate on the production of bio-oil and char from safflower seed by pyrolysis, using a well-swept fixed-bed reactor*. Fuel Processing Technology, 2007. **88**(5): p. 523-531.
 333. Al-Wabel, M.I., et al., *Pyrolysis temperature induced changes in characteristics and chemical composition of biochar produced from *conocarpus* wastes*. Bioresource technology, 2013. **131**: p. 374-379.
 334. Mimmo, T., et al., *Effect of pyrolysis temperature on miscanthus (*Miscanthus × giganteus*) biochar physical, chemical and functional properties*. Biomass and Bioenergy, 2014. **62**: p. 149-157.
 335. Yuan, H., et al., *Influence of pyrolysis temperature and holding time on properties of biochar derived from medicinal herb (*radix isatidis*) residue and its effect on soil CO₂ emission*. Journal of analytical and applied pyrolysis, 2014. **110**: p. 277-284.
 336. Liu, F., et al., *Effect of microstructure on the mechanical properties of PAN-based*

- carbon fibers during high-temperature graphitization.* Journal of Materials Science, 2008. **43**(12): p. 4316-4322.
337. Pilon, G. and J.-M. Lavoie, *Pyrolysis of switchgrass (Panicum virgatum L.) at low temperatures within N₂ and CO₂ environments: Product yield study.* ACS Sustainable Chemistry & Engineering, 2012. **1**(1): p. 198-204.
338. Brewer, C.E., *Biochar characterization and engineering.* 2012.
339. Santos, L.B., et al., *Characterization of biochar of pine pellet.* Journal of Thermal Analysis and Calorimetry, 2015. **122**(1): p. 21-32.
340. Plaza, M., et al., *Application of thermogravimetric analysis to the evaluation of aminated solid sorbents for CO₂ capture.* Journal of Thermal Analysis and Calorimetry, 2008. **92**(2): p. 601-606.
341. Fancello, D., et al., *XRD-thermal combined analyses: An approach to evaluate the potential of phytoremediation, phytomining, and biochar production.* International journal of environmental research and public health, 2019. **16**(11): p. 1976.
342. Jiang, Z.-H., et al., *Rapid prediction of wood crystallinity in Pinus elliotii plantation wood by near-infrared spectroscopy.* Journal of wood science, 2007. **53**(5): p. 449-453.
343. Osman, A.I., et al., *Physicochemical characterization of miscanthus and its application in heavy metals removal from wastewaters.* Environmental Progress & Sustainable Energy, 2018. **37**(3): p. 1058-1067.
344. Kim, K.H., et al., *Influence of pyrolysis temperature on physicochemical properties of biochar obtained from the fast pyrolysis of pitch pine (Pinus rigida).* Bioresource technology, 2012. **118**: p. 158-162.
345. Fu, R., et al., *Adsorptive removal of Pb (II) by magnetic activated carbon incorporated with amino groups from aqueous solutions.* Journal of the Taiwan Institute of Chemical Engineers, 2016. **62**: p. 247-258.
346. Zhao, Y., et al., *Green preparation of magnetic biochar for the effective accumulation of Pb(II): Performance and mechanism.* Chemical Engineering Journal, 2019. **375**: p. 122011.
347. Keiluweit, M., et al., *Dynamic molecular structure of plant biomass-derived black carbon (biochar).* Environmental science & technology, 2010. **44**(4): p. 1247-1253.
348. Tushar, M.S.H.K., et al., *Production, characterization and reactivity studies of chars produced by the isothermal pyrolysis of flax straw.* Biomass and bioenergy, 2012. **37**: p. 97-105.
349. Zhang, L., A.A. Gonçalves, and M. Jaroniec, *Identification of preferentially exposed crystal facets by X-ray diffraction.* RSC Advances, 2020. **10**(10): p. 5585-5589.
350. Lemly, A.D., *Environmental implications of excessive selenium: a review.* Biomed Environ Sci, 1997. **10**(4): p. 415-35.
351. Presser, T.S. and S.N. Luoma, *Forecasting selenium discharges to the San Francisco Bay-Delta Estuary: ecological effects of a proposed San Luis Drain extension.* 2006: Geological Survey (US).
352. Vyas, S. and Y.-P. Ting, *A review of the application of ultrasound in bioleaching and insights from sonication in (bio) chemical processes.* Resources, 2018. **7**(1): p. 3.
353. Ali, F., et al., *Effect of sonication conditions: solvent, time, temperature and reactor type on the preparation of micron sized vermiculite particles.* Ultrasonics sonochemistry, 2014. **21**(3): p. 1002-1009.
354. Rooze, J., *Cavitation in gas-saturated liquids.* Eindhoven: Technische Universiteit

- Eindhoven–2012.–120 pp. DOI, 2012. **10**.
355. Henglein, A., *Sonolysis of carbon dioxide, nitrous oxide and methane in aqueous solution*. Zeitschrift für Naturforschung B, 1985. **40**(1): p. 100-107.
356. Hageman, S.P.W., et al., *Microbial selenium sulfide reduction for selenium recovery from wastewater*. Journal of Hazardous Materials, 2017. **329**: p. 110-119.
357. Li, Y., et al., *Selenite removal from groundwater by zero-valent iron (ZVI) in combination with oxidants*. Chemical Engineering Journal, 2018. **345**: p. 432-440.
358. Liu, J., J.C. Taylor, and S.A. Baldwin, *Removal of selenate from brine using anaerobic bacteria and zero valent iron*. Journal of Environmental Management, 2018. **222**: p. 348-358.
359. He, Y., et al., *Selenium contamination, consequences and remediation techniques in water and soils: A review*. Environmental Research, 2018. **164**: p. 288-301.
360. Dellantonio, A., et al., *Disposal of coal combustion residues in terrestrial systems: contamination and risk management*. Journal of environmental quality, 2010. **39**(3): p. 761-775.
361. Adewuyi, Y.G., *Sonochemistry: Environmental Science and Engineering Applications*. Industrial & Engineering Chemistry Research, 2001. **40**(22): p. 4681-4715.
362. Gong, C. and D.P. Hart, *Ultrasound induced cavitation and sonochemical yields*. The Journal of the Acoustical Society of America, 1998. **104**(5): p. 2675-2682.

LIST OF APENDICES

Appendix A: Experimental Set Up and Schematic Diagram

A1. Experimental Set-Up



(a)



(b)

Figure A1. (a) Front Panel of the Unit and (b) Back Panel of the Unit

A2. Schematic of Experimental Set-Up

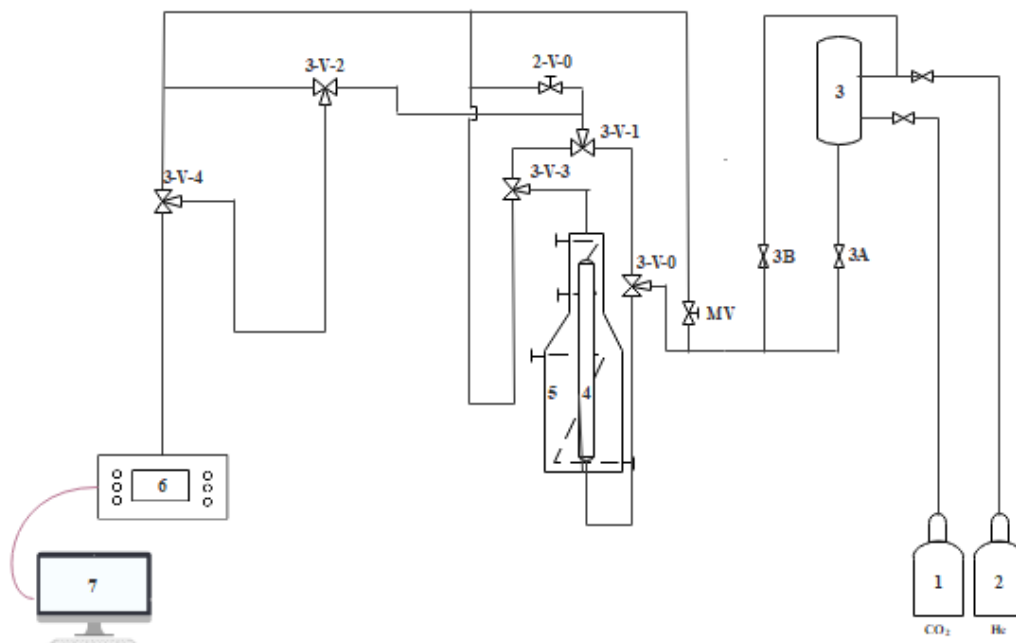


Figure A2. Schematic Representation of the Experimental Set-Up

1. CO₂ gas cylinder; 2. He gas cylinder; 3. Mixing Column; 4. Reactor Tube; 5. Furnace; 6. CO-CO₂ analyzer; 7. Computer; MV: Metering Valve

A3. Functions of Valves

Valve 3A: Let the gas pass to the analyzer; **Valve 3B:** Let the helium gas flow to the column

Valve 2-V-0: Controls flow of analyzer; **Valve 3-V-0:** Switch the gas flow between column and analyzer;

Valve 3-V-1: Switch between inlet gas and outlet gas during adsorption; **Valve 3-V-2:**

Direct the sample gas towards analyzer; **Valve 3-V-3:** When turned towards the bypass it

bypasses excess gas from the analyzer and when turned towards the analyzer it directs the

sample gas towards the analyzer; **Valve 3-V-4:** Directing the gas to the analyzer.

Appendix B: Details of Experimental Procedure

B1. CO₂ Adsorption Experimental Procedure

1. Sample Preparation and Degassing

- a. The biochar sample is put inside the stainless steel cloth and placed inside the tube furnace
- b. The Helium cylinder is turned on and a flow rate of 500 cc/min was maintained.
- c. The temperature controller of the the furnace is switched on followed by gradual temperature rise at an interval of 5 °C till 105 °C
- d. The temperature is hold for 60 minutes to degas the adsorbent
- e. After 60 minutes the temperature is reduced to 60 °C like previously
- f. The CO₂ cylinder is turned on and the flow rate is maintained at 50 cc/min with a total flow rate at 500 cc/min (rest with helium gas)

2. Analysis of Inlet CO₂ Concentration

- a. The 3-V-0 is turned to 3-V-1
- b. The 3-V-1 is turned to in gas
- c. The 3-V-2 is turned to analyzer
- d. The 3-V-4 is turned to bypass
- e. The 3A valve is opened
- f. After a while when the flow meters reading reached stable values, the 3-V-4 is turned to analyzer

3. Adsorption

- a. The 3-V-3 is turned to 3-V-1
- b. The 3-V-1 is turned to out gas
- c. The 3-V-0 is turned to column quickly and the CO₂ concentration is started to analyze
- d. The adsorption is carried out for sufficient time until the outlet concentration further reaches inlet concentration

4. Desorption

- a. The valve 3A is closed and the valve 3V is opened
- b. The CO₂ cylinder is shut off
- c. Then the temperature is increased gradually to 180 °C
- d. For the desorption, temperature at 180 °C is kept for 60 minutes
- e. Then the temperature is reduced to below 40 °C and the furnace is shut off

Appendix C: Maintenance and Calibration Procedures of the Experimental Set Up

C1. Instrument Maintenance and Calibration

1. Maintenance

The Analyzer is sensitive towards dust and moisture. To make sure normal and accurate operation, the following checks needs to be carried out periodically

I. Moisture

Source of moisture is primarily the gases used to carry out the experiment. So at first instance, it needs to be taken care that the gas passing into the analyzer should be moisture free.

To absorb the moisture desiccant can be used in the following way-

- i. Installation of desiccant tube adjacent to both the cylinder for carrier gas (Helium) and reacting gas (CO₂) so that the gas which are routed to the analyzer will be moisture free
- ii. Check and replacement of the desiccant periodically. The desiccant needs to be regenerated periodically and to be replaced with the freshly regenerated one.

II. Particles

The analyzer is equipped with gas filter to trap the dust particles that may enter with the gas sources. The filter needs to be maintained otherwise the output may drift and data will be erroneous since the dust may accumulate inside. The dust can also affect the sample cell inside the analyzer so the following maintenance needs to be done-

i. Cleaning of Sample Cell:

- a. At first using soft brush for wiping the dust
- b. Using Kim wipes to thoroughly clean the cell for any remaining small size dust or particles
- c. For thick dust layer cleaning, Kim Wipes soaked into alcohol or acetone may be used

ii. Maintenance of Filter: When contamination is very severe, mere cleaning of samples cell may not be useful. In that case the filter needs to be replaced with new filter.

1. Calibration

I. Zero Calibration: This is required when the analyzer shows a drift in a way that it deviates from the lower end value (also called zero) and couldn't reach the possible lower range for either of the component. The steps for "Zero Calibration" are

- i. Press "Zero" Key until it starts to blink
- ii. Turn on the "Zero Gas" (usually N₂ at flow rate of 0.5-1 l/min)
- iii. Select Range (high or low)
- iv. After the displayed concentration value reaches final value "CAL" button needs to be pressed
- v. When the calibration will start light for "CAL" key button will lit and light for "ZERO" key button will be in continuous mode from blinking mode
- vi. After the calibration is successful, both "ZERO" and "CAL" key light are turned off and the mode is returned to "Measuring Mode"

- vii. If the calibration needs to be stopped at any point in between, then pressing “ZERO” key will stop the calibration and the mode will be returned to “Measuring Mode”

II. **Span Calibration:** This is required when the instrument drift in a way that the output is either amplified or reduced from actual output. Thus, the span or range of the instrument changes that leads to erroneous result. Usually done with the gas CO and CO₂. The steps for “Span Calibration” are-

- i. At first, range of span gas needs to be selected
- ii. Press “FUNC” key until light for “SPAN” starts to blink
- iii. The display will show current Span Value. If it is okay then pressing “FUNC” will take to next step
- iv. If the value is not right then pressing “>” or “^” will let to select the correct value of concentration
- v. If span calibration needs to be done for both ranges, then the range button needs to be pressed to change between the ranges
- vi. After the new value is selected, press “ENT”
- vii. Similarly, for both of the component gases (CO and CO₂) span calibration can be done.
- viii. To do this press “COMP” key to change between component gases
- ix. Afterwards, press “SPAN” and the light will start to blink indicating analyzer is in SPAN Calibration mode
- x. Turn of gas for which the calibration is intended

- xii. Then the component is selected for which calibration is done by pressing “COMP” key
- xiii. Select Range for the component gas
- xiv. After displayed concentration reaches final value press “CAL” key and the light will lit to indicate calibration is going on
- xv. Accordingly, Span Key light will be in continuous mode
- xvi. After the calibration is successful, both “SPAN” and “CAL” key light are turned off and the mode is returned to “Measuring Mode”
- xvii. If the calibration needs to be stopped at any point in between, then pressing “SPAN” key will stop the calibration and the mode will be returned to “Measuring Mode”

Appendix D: Data Acquisition and Analysis

D1. Data Acquisition

- The data is collected using Tracer DAQ 1208FS input and output data acquisition device.
- The device is connected through USB to the computer and the data is acquired using MCC DAQ Software.
- Once the data are collected, it is saved with .txt format in the computer which is then exported as .csv format for analysis.

D2. Data Analysis using LabView 2018

1. Import the data from .csv file to LabView

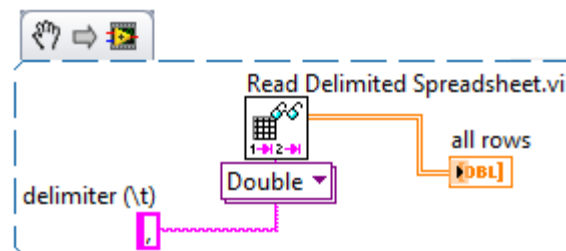
- I. In LabView, the Functions Palette is opened and then the following option is selected

File I/O » Read Delimited Spreadsheet.vi

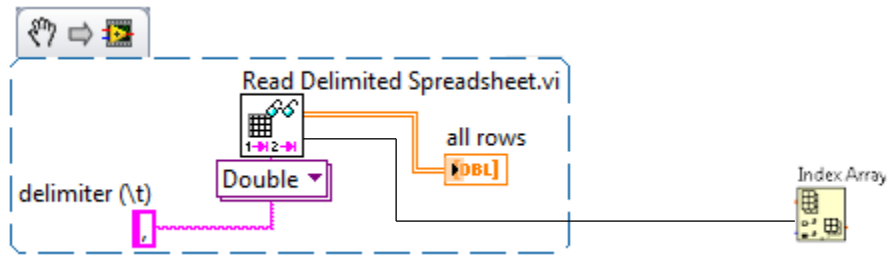
- II. Right-click on the delimiter (\t) and the following option is selected

Create » Constant

- III. The default value for this input is a single tab character (\t).

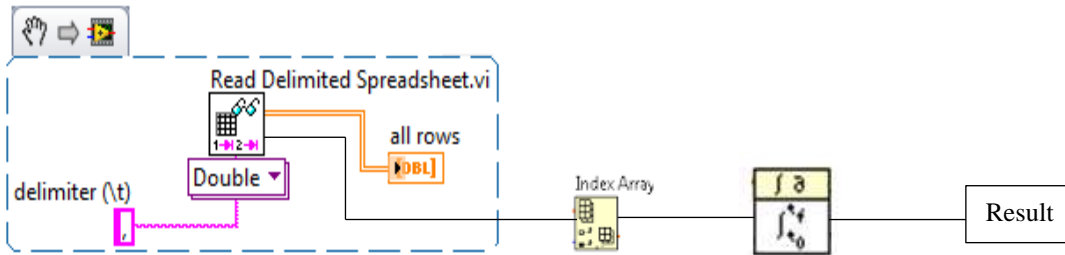
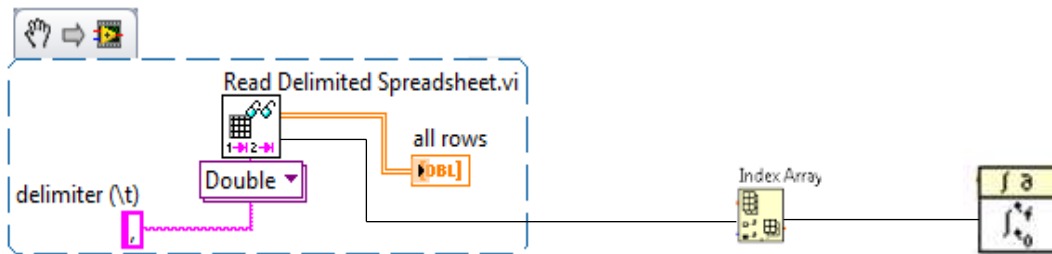


2. Read the Data using indexing array



3. Data Integration

Function \longrightarrow Mathematics \longrightarrow Numerical Integration



Appendix E: Sample Preparation and Parameters Settings for Characterization Techniques

- 1. SEM:** The samples were mounted on aluminum stubs using glued carbon tapes and then coated with gold using a Hummer 6.2 sputter coater (Anatech USA, Union City, CA, USA). The sputter coater chamber was supplied with argon gas during the coating process. Photomicrographs of the samples were prepared using a JSM-5600 SEM (JEOL Ltd., Tokyo, Japan) where all the samples were dried at 60 °C under vacuum (overnight).
- 2. Sorptometry:** Surface area analysis using sorptometry technique involves two steps- degassing and analysis. For degassing, at first the empty sample tube was weighed. Then around 0.2 g of samples were taken and transferred to empty sample tube which was weighed again. Sample tube was placed in the degassing section and degassed overnight at 350 °C under vacuum to drive off debris such as water that clogs up pore space. After degassing the samples were cooled down to room temperature and then weighed again. For analysis, the sample tube (including the sample) was transferred to the analysis section inside the liquid nitrogen bath. The following parameters were set for analysis- liquid nitrogen does at 5 mmHg for relative pressure range of 0 to 1 where the volume adsorbed (amount of N₂ adsorbate by the sample) was recorded versus relative pressure.
- 3. Elemental Analysis:** At first, unweighed sulfamic acid (sulfur conditioner) was run to prepare the combustion chamber for CHNS mode. Then empty tin capsules were run as blank to create baseline for the desired elements such as nitrogen, carbon, sulfur, and hydrogen. The blanks are run multiple times to get consistent detector reading. After the system is calibrated, the K factors (cysteine) were run that is used as conversion factor to convert

detector readings into %C, %H, %N, %S. Several duplicates of the K factors were run at the beginning of the run sequence, spaced by blanks to get consistent response. After K factor, unknown samples were run. Prior to analysis all samples were dried at 60 °C under vacuum (overnight). Each sample was placed in a tared tin capsule and precisely weighed (2 ± 0.5 mg) and run several times to get consistent composition after analysis.

- 4. Fourier Transform Infrared Spectroscopy:** For the FTIR analysis, ATR-FTIR instrumentation was used. The samples were dried at 60 °C under vacuum before analysis. At first the data acquisition parameters such as scan rate and wavenumber ranges were set for the analysis which remained same for both background and sample. Then background was run without adding the sample and the data was recorded. After background, the sample (1-2 mg) was run followed by the data acquisition.
- 5. Raman Spectroscopy:** For Raman spectroscopy the cover glass was put on a powder sample taken on a slide glass or the like, and the measurement was done as it is or after gently removing the mounted cover glass under the incident laser beam.

Appendix F: Elemental Compositions of Raw and Activated Samples with Mineral Free and Dry Basis

Table F1. Elemental Analysis of Biochars as Percentage of Organic Constituents, omitting Ash Contribution

Entry	Sample	Ultrasound power	Ultrasound duration (min)	EDC:HOBt:TEPA wt:wt:wt	C (% w/w)	H (% w/w)	N (% w/w)	O (% w/w)	S (% w/w)
1	R-BC	—	—	—	82.97	2.50	0.23	14.24	0.06
2	US0-EH1:1-T2.5	—	—	1 : 1 : 2.5	77.08	2.86	1.15	18.88	0.02
3	US3-EH0-T0	low	3	—	77.54	2.87	0.30	19.27	0.02
4	US0.5-EH1:1-T2.5	low	0.5	1 : 1 : 2.5	81.67	3.06	1.91	13.33	0.02
5	US1-EH1:1-T2.5	low	1	1 : 1 : 2.5	78.62	2.92	0.94	17.49	0.02
6	US3-EH1:1-T2.5	low	3	1 : 1 : 2.5	78.19	2.72	0.97	18.09	0.02
7	US0.5-EH1:1-T2.5	high	0.5	1 : 1 : 2.5	73.77	2.88	0.58	22.75	0.02
8	US1-EH1:1-T2.5	high	1	1 : 1 : 2.5	74.18	2.74	0.72	22.34	0.02
9	US3-EH1:1-T2.5	high	3	1 : 1 : 2.5	69.14	2.78	0.77	27.31	0.01
10	US3-EH1:0.75-T10	low	3	1 : 0.75 : 10	78.74	2.80	0.93	17.50	0.02
11	US3-EH1:1-T10	low	3	1 : 1 : 10	74.91	2.90	0.89	21.28	0.01
12	US3-EH0.75:1-T10	low	3	0.75 : 1 : 10	79.32	2.70	1.03	16.94	0.01
13	US3-EH1:1-T15	low	3	1 : 1 : 15	79.41	2.66	1.18	16.72	0.02

Table F2. Elemental Analysis of biochars as percentage of Organic Constituents, omitting Contributions from Ash and from Assumed Absorbed CO₂

Entry	Sample	Ultrasound power	Ultrasound duration (min)	EDC:HOBt:TEPA wt:wt:wt	assumed absorbed CO ₂ (% w/w)	C (% w/w)	H (% w/w)	N (% w/w)	O (% w/w)	S (% w/w)
1	R-BC	—	—	—	0.00	82.97	2.50	0.23	14.2	0.06
2	US0-EH1:1-T2.5	—	—	1 : 1 : 2.5	7.78	81.49	3.09	1.25	14.1	0.03
3	US3-EH0-T0	Low	3	—	8.60	82.27	3.14	0.33	14.2	0.03
4	US0.5-EH1:1-T2.5	Low	0.5	1 : 1 : 2.5	-1.56*	81.67	3.06	1.91	13.3	0.02
5	US1-EH1:1-T2.5	Low	1	1 : 1 : 2.5	5.56	81.64	3.09	1.00	14.2	0.03
6	US3-EH1:1-T2.5	Low	3	1 : 1 : 2.5	6.58	81.78	2.91	1.04	14.2	0.03
7	US0.5-EH1:1-T2.5	High	0.5	1 : 1 : 2.5	14.55	81.69	3.37	0.68	14.2	0.03
8	US1-EH1:1-T2.5	High	1	1 : 1 : 2.5	13.85	81.72	3.18	0.84	14.2	0.03
9	US3-EH1:1-T2.5	High	3	1 : 1 : 2.5	22.35	81.19	3.58	0.99	14.2	0.02
10	US3-EH1:0.75-T10	Low	3	1 : 0.75 : 10	5.57	81.78	2.97	0.98	14.2	0.03
11	US3-EH1:1-T10	Low	3	1 : 1 : 10	12.04	81.43	3.30	1.01	14.2	0.01
12	US3-EH0.75:1-T10	Low	3	0.75 : 1 : 10	4.62	81.84	2.83	1.08	14.2	0.01
13	US3-EH1:1-T15	Low	3	1 : 1 : 15	4.24	81.71	2.78	1.24	14.2	0.02

*The small negative value suggests no CO₂ absorption for this sample, so analysis values are those from Table 2.2

Appendix G: FTIR Spectrums of Raw and Activated Samples after Baseline Correction in Origin

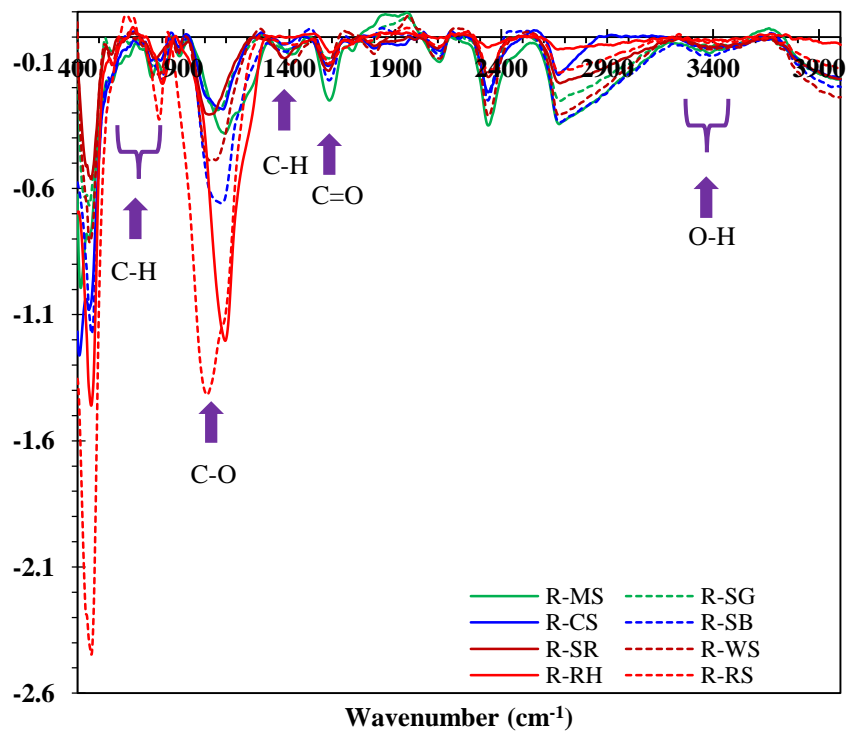


Figure G1. FTIR spectra of raw biochar samples after baseline correction. Strong peaks at 1000-1100, 1600-1700, 2300 and 3300-3600 cm^{-1} are ascribed to C-O, C=O, CO_2 and -OH stretching.

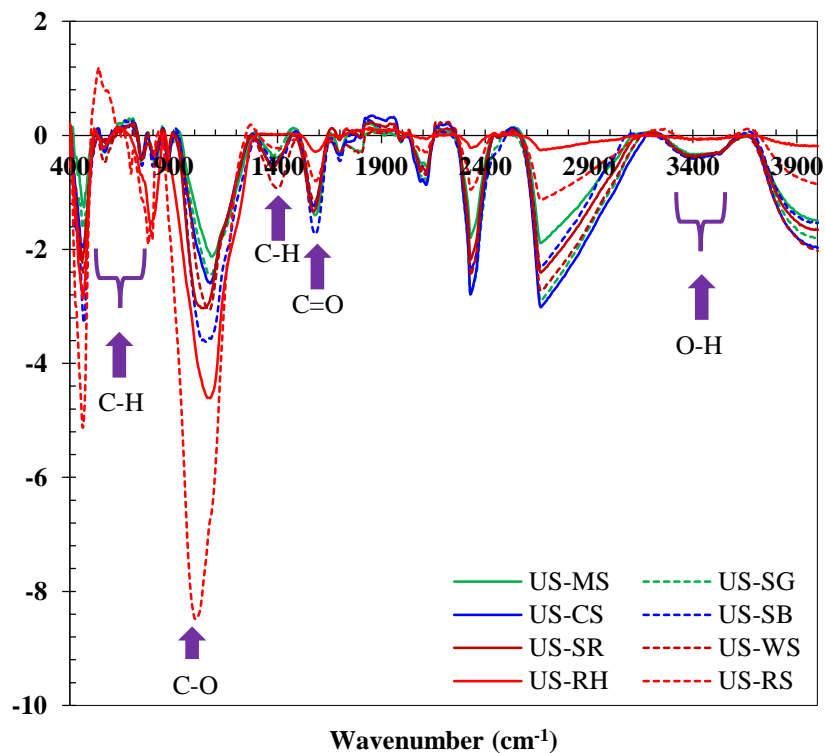


Figure G2. FTIR spectra of ultrasound activated biochar samples after baseline correction. Physical activation made the peaks more intense and distinct specifically at 1100 (C-O), 1600 (C=O), and 3300-3600 cm^{-1} (-OH) that further demonstrate the importance of sonication in exfoliating biochar structure and making oxygen functionalities available.

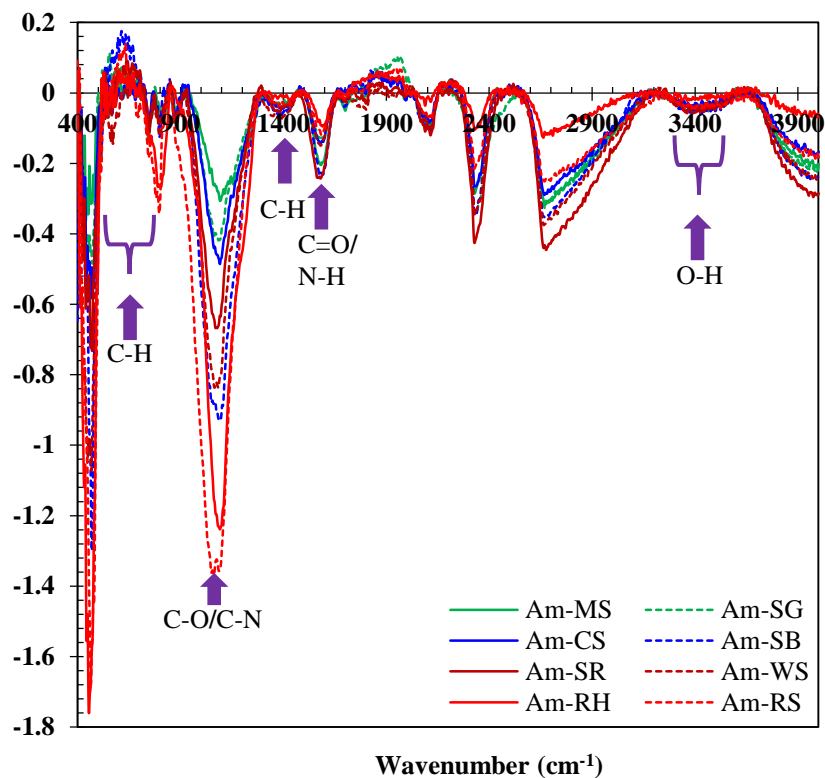


Figure G3. FTIR spectra of aminated biochar samples after baseline correction. Two new peaks appear at 1000-1200 and 1600 cm^{-1} for C-N and N-H and overlap with C-O and C=O peaks thus show intense peaks

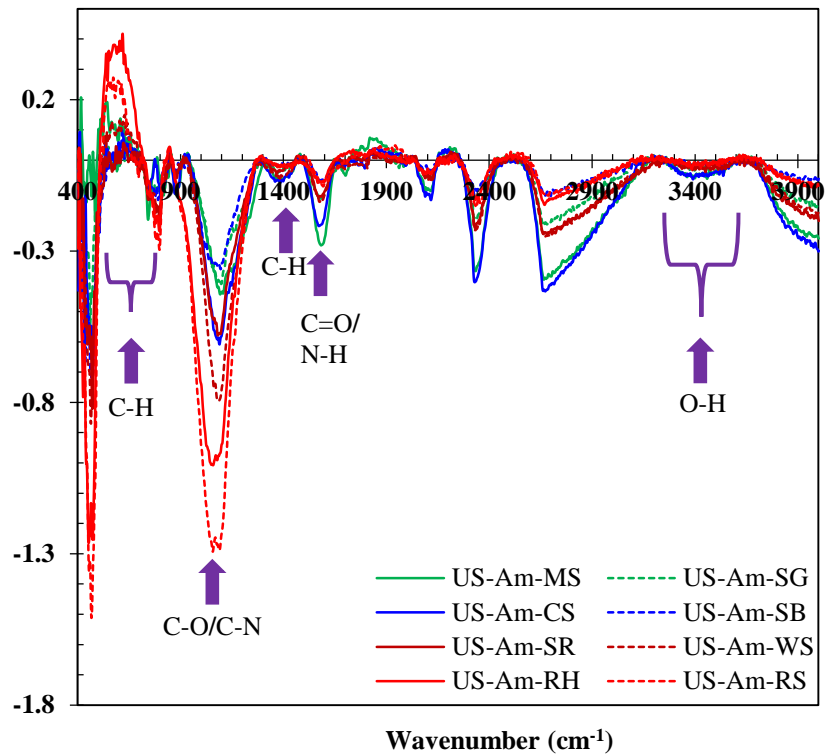


Figure G4. FTIR spectra of ultrasonicated-aminated biochar samples after baseline correction. Two new peaks appear at 1000-1200 and 1600 cm^{-1} for C-N and N-H similar to aminated samples.

Appendix H: Breakthrough Plots of Raw and Activated Samples

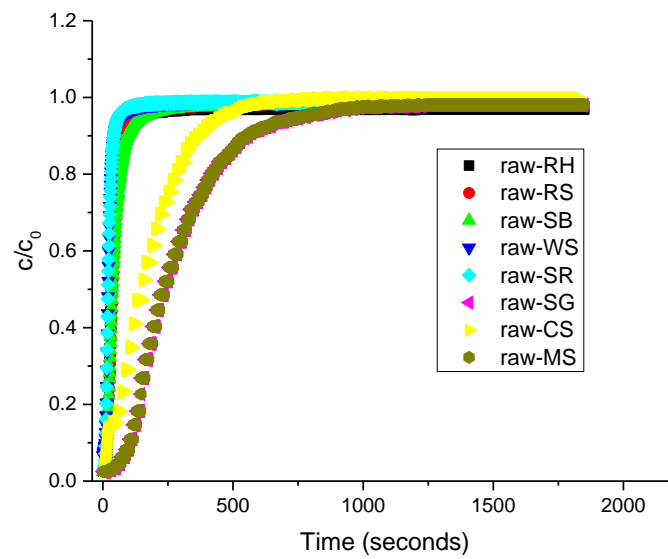


Figure H1. Adsorption Breakthrough Curves for Raw Biochar Samples

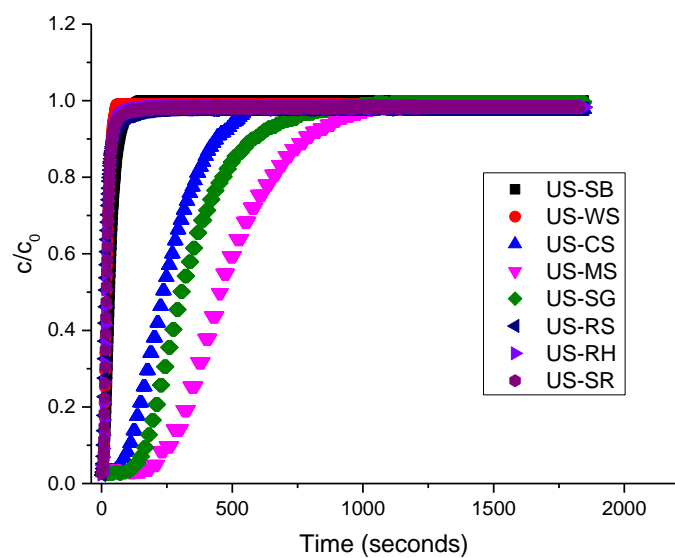


Figure H2. Adsorption Breakthrough Curves for Physically Activated (Ultrasound Treated) Biochar Samples

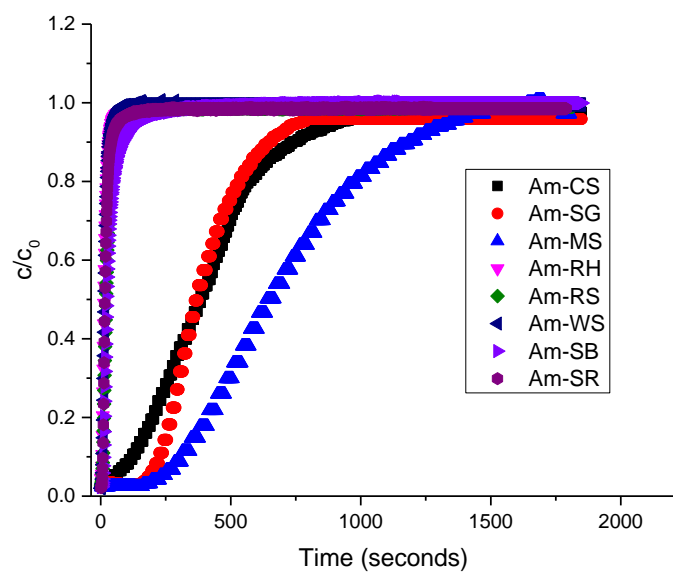


Figure H3. Adsorption Breakthrough Curves for Chemically Activated (Amine Only) Biochar Samples

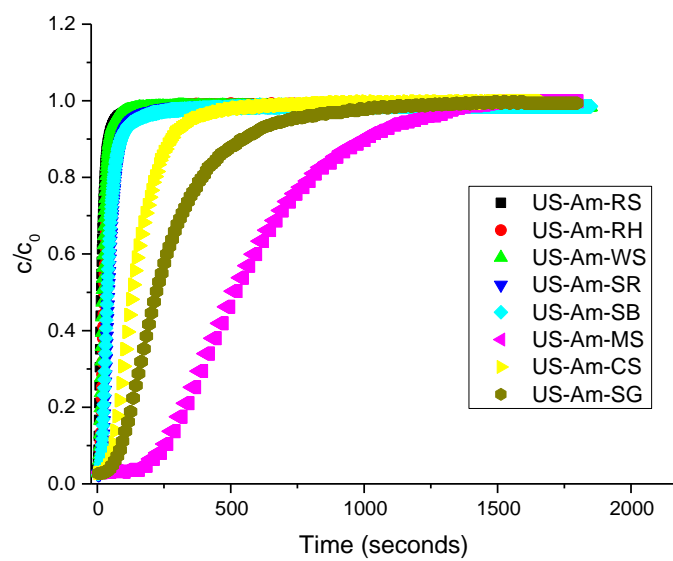


Figure H4. Adsorption Breakthrough Curves for Sono-Chemically Activated (Ultrasound and Amine) Biochar Samples

Appendix I: FTIR Spectrums of Raw and Activated Samples after Baseline Correction in Origin

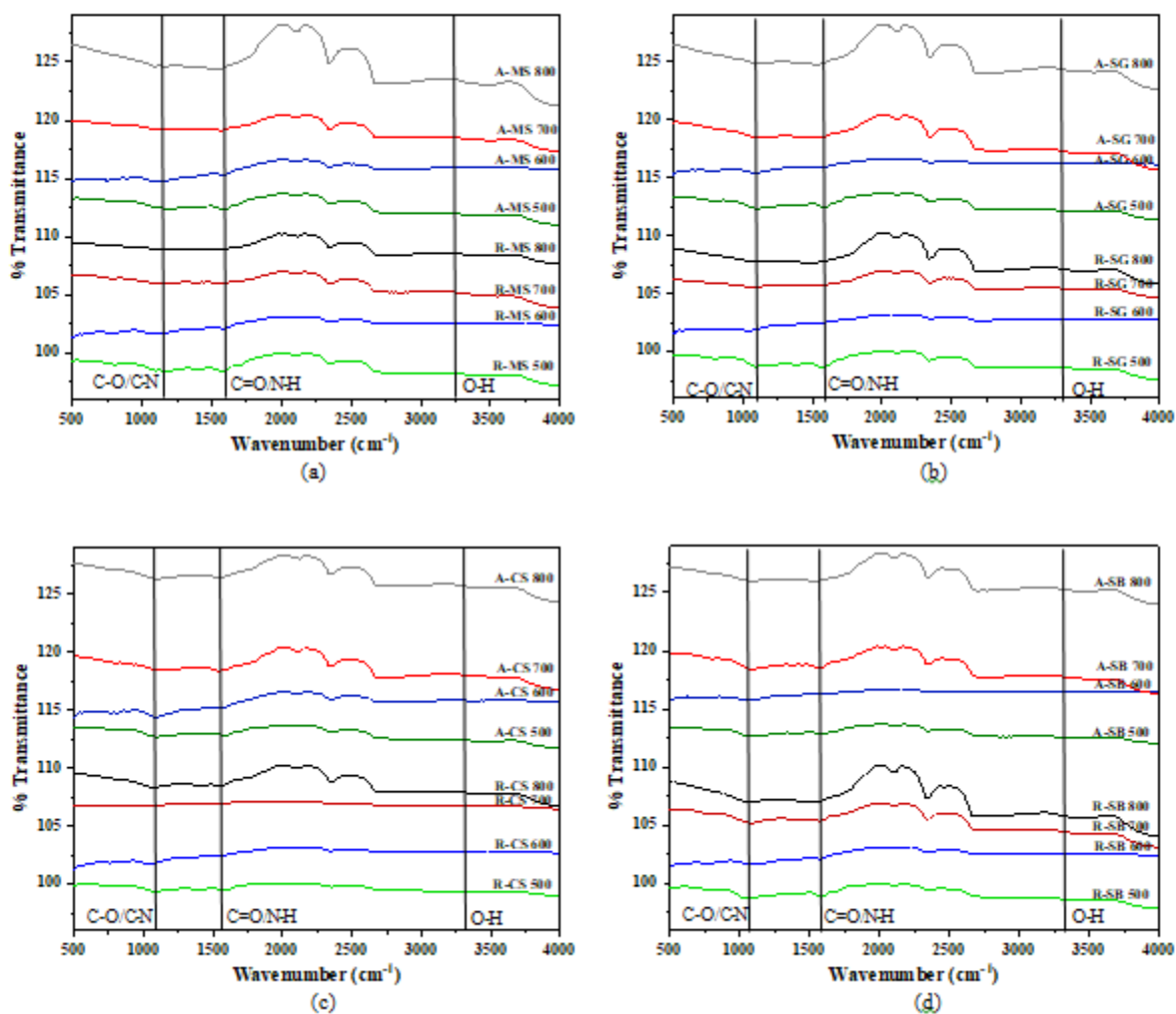


Figure I. FTIR Spectra of Raw and Activated Samples (a) Miscanthus, (b) Switchgrass, (c) Corn Stover and (d) Sugarcane Bagasse Synthesized at Different Pyrolysis Temperatures

VITA

RIYA CHATTERJEE

Born in Kolkata, one of the big cities in India, I enjoyed my stay and living there. I had completed my elementary, middle and high school from Kolkata and moved to a nearby city for my undergrad study. After completing my undergrad, I came back to Kolkata for my MS and started my research career there. Then, my research interest grew further, so I decided to pursue my research career in USA as a PhD student and thereafter, joined The University of Mississippi.

EDUCATION

2016-2020	Ph.D.	Acoustic and Chemical Modifications to Biochar for Pollution Abatement
	Thesis Title:	Physico-Chemical Activation of Biochar Using Acoustic Treatment and Amine Functionalization for Efficient CO ₂ Adsorption
2014-2016	MS	University of Calcutta, Department of Chemical Engineering, India
	Thesis Title:	Adsorptive Removal of Fluoride from Aqueous Solution using Rice Husk
2008-2012	BS	West Bengal University of Technology, Department of Chemical Engineering, India
	Thesis Title:	Hydrodynamic Study of Fluid Flow through Flexible Tubes

PROFESSIONAL ACTIVITIES

1. Member of The American Institute of Chemical Engineers
2. Member of American Chemical Society
3. Nationwide (India) test, Graduate Aptitude Test for Engineering, (GATE)

SCHOLARSHIPS AND AWARDS

1. Recipient of Technical Education Quality Improvement Programme Scholarship (University of Calcutta)

2. Receptient of Gold Medal for MS study (University of Calcutta)
3. Receptient of Dean of the Graduate School Dissertation Fellowship (University of Mississippi)

JOURNAL PUBLICATIONS

1. Yamin Liu, Baharak Sajjadi, Wei-Yin Chen, **Riya Chatterjee**. Ultrasound-Assisted Amine Functionalized Graphene Oxide for Enhanced CO₂ Adsorption; Fuel 247 (2019) 10-18.
2. Baharak Sajjadi, Wei-Yin Chen, **Riya Chatterjee**. Acoustic Treatment of a Coal Gasification Residue for Extraction of Selenium; Energy & Fuels (2019) 33, 5, 4676-4680.
3. **Riya Chatterjee**, Baharak Sajjadi, Wei-Yin Chen, Daniell L Mattern, Nosa O Egiebor, Nathan Hammer, Vijayasankar Raman. Low Frequency Ultrasound Enhanced Dual Amination of Biochar: A Nitrogen-Enriched Sorbent for CO₂ Capture; Energy & Fuels (2019) 33, 3, 2366-2380.
4. **Riya Chatterjee**, Baharak Sajjadi, Daniell L Mattern, Wei-Yin Chen, Tetiana Zubatiuk, Danuta Leszczynska, Jerzy Leszczynski, Nosa O Egiebor, Nathan Hammer. Ultrasound cavitation intensified amine functionalization: A feasible strategy for enhancing CO₂ capture capacity of biochar; Fuel 225 (2018) 287–298.
5. **Riya Chatterjee**, Baharak Sajjadi, Wei-Yin Chen, Daniell L. Mattern, Nathan Hammer, Vijayasankar Raman, Austin Dorris. Effects of Biomass Origin on CO₂ Capture by Ultrasound-Promoted, Amine-Functionalized Biochar. Journal of Green House Gas and Control (under review).
6. **Riya Chatterjee**, Baharak Sajjadi, Wei-Yin Chen, Daniell L. Mattern, Nathan Hammer, Vijayasankar Raman, Austin Dorris. Effect of Pyrolysis Temperature on PhysicoChemical Properties and Acoustic-Based Amination of Biochar for Efficient CO₂ Adsorption. Journal of Frontiers Energy Research (accepted with revisions).
7. Baharak Sajjadi, Wei-Yin Chen, Daniell L. Mattern, **Riya Chatterjee**. Mechanistic Implications of the Effects of Acoustic Power, Amplitude and CO₂ Concentration on the Biochar Properties. Journal of Fuel (under review).
8. Bijoyaditya Mondal, **Riya Chatterjee**, Asit Baran Biswas. Adsorptive removal of fluoride from aqueous solution using rice husk- effect of variables and kinetic studies. Ready to submit.
9. **Riya Chatterjee**, Baharak Sajjadi, Wei-Yin Chen. A comprehensive review on the activation of carbonaceous compounds for carbon dioxide capture. Under Preparation.

GRADUATE SEMINARS

1. Graduate Seminar, Faculty of Engineering, University of Mississippi (April, 2018)
Presentation Title: Activation of Biochar: A Feasible Strategy for CO₂ Capture.

2. **University of Mississippi, Graduate School 3-minute Thesis (October, 2017)**
Graduate Seminar, Faculty of Engineering, University of Mississippi (September, 2017)
Presentation Title: Ultrasound Activation Followed by Amine Functionalization: An Efficient Strategy for CO₂ Capture by Biochar.
3. **Graduate Seminar, Faculty of Engineering, University of Mississippi (March, 2017)**
Presentation Title: Carbon Dioxide Capture by Ultrasonicated Amine Functionalized Graphene Oxide.
4. **Graduate Seminar, Faculty of Engineering, University of Mississippi (November 2016)**
Presentation Title: Carbon Sequestration by Amine Functionalized Graphene Oxide.

CONFERENCE PRESENTATIONS

1. **Riya Chatterjee**, Baharak Sajjadi, Wei-Yin Chen, Daniell L. Mattern. Poster presentation on “Physico-Chemical Activation of Biochar using Acoustic Treatment and Amine Functionalization for Synthesizing Suitable Adsorbent towards the Application of Efficient CO₂ Adsorption” at 2019 AIChE Annual Meeting, Orlando, FL, Nov 10-15, 2019.
2. **Riya Chatterjee**, Baharak Sajjadi, Wei-Yin Chen, Daniell L. Mattern. Conference talk on “Modification of Biochar through Sono-Chemical Activation Method for Efficient CO₂ Adsorption” at “19th Southern School on Chemistry and Engineering Conference” at The University of Delaware, August 8-9, 2019.
3. **Riya Chatterjee**, Baharak Sajjadi, Wei-Yin Chen, Daniell L. Mattern. Conference talk on “Ultrasound assisted dual stage amination of biochar: efficient adsorbent for intensified CO₂ adsorption” at “9th Annual Research Symposium of Graduate Student Council (GSC)”, The University of Mississippi, March 26, 2019
4. **Riya Chatterjee**, Baharak Sajjadi, Wei-Yin Chen, Daniell L. Mattern. Poster presentation on “Activation of biochar through acoustic treatment and dual stage amination for efficient CO₂ adsorption” at “Conference on Current Trends in Computational Chemistry” at Jackson State University, Jackson, MS, November 9-10, 2018
5. **Riya Chatterjee**, Baharak Sajjadi, Wei-Yin Chen, Daniell L. Mattern. Conference talk on “Two Step Modification of Biochar using Ultrasonic Irradiation and Amine Functionalization for Enhanced CO₂ Adsorption” at “Southern School on Chemistry and Engineering Conference” at The University of Mississippi, August 2-3, 2018
6. **Riya Chatterjee**, Baharak Sajjadi, Wei-Yin Chen, Daniell L. Mattern. Conference talk on “Ultrasound Activation Followed by Amine Functionalization: An Efficient Strategy for CO₂ Capture by Biochar” at 255th ACS National Meeting and Exposition, New Orleans, LA, March 18-22, 2018.

7. **Riya Chatterjee**, Baharak Sajjadi, Wei-Yin Chen, Daniell L. Mattern. Poster presentation on “CO₂ Capture by Amine-Functionalized Graphene Oxide” at “Annual Research Symposium of the University of Mississippi Graduate Student Council” held during March 2017 at University of Mississippi.
8. **Riya Chatterjee**, Asit Baran Biswas. Conference talk on "Adsorptive removal of fluoride using rice husk" at "23rd West Bengal State Science and Technology Congress" held during February 2016 at Presidency University, West Bengal, India
9. **Riya Chatterjee**. Conference talk on “Polymer hydrogel: A unique material for drug delivery” at “International Conference on Recent Developments in Chemical and Biochemical Engineering”, 2015 at National Institute of Technology, Durgapur, India.
10. **Riya Chatterjee**. Conference talk on “Arsenic toxicity and its remediation: A general overview” was published at the “National Conference on Advanced Pollution Control Systems for Better Environmental Management” held during April 2011 at Durgapur Institute of Advanced Technology and Management, India.
11. **Riya Chatterjee**. Conference talk on “Decolourisation of Melanoidin pigments in synthetic and spent wash using fungi *phanerochaete chrysosporium*” was published at the “National Conference on Advanced Pollution Control Systems for Better Environmental Management” held during April 2011 at Durgapur Institute of Advanced Technology and Management, India.